Simulation of Two-Dimensional Steady State Boundary Layers Applied to Nonideal Gas Flows

Dominic Dyon Dijkshoorn

Report No. 3026

TU Delft Delft University of Technology

Mechanical, Maritime and Materials Engineering

The work in this report was supported by the Propulsion and Power group at the TU Delft Aerospace Department. Their cooperation is hereby gratefully acknowledged.

Delft University of Technology
Department of
Process & Energy

The undersigned hereby certify that they have read and recommend to the Faculty of Mechanical, Maritime and Materials Engineering (3ME) for acceptance a thesis entitled

Simulation of Two-Dimensional Steady State Boundary Layers Applied to Nonideal Gas Flows

by

Dominic Dyon Dijkshoorn

in partial fulfillment of the requirements for the degree of

Master of Science Mechanical Engineering: Sustainable Process and Energy Technology

Dated: August 10, 2020

Supervisor(s):

Ir. Adam Joseph Head

Dr. Carlo De Servi

Assoc. Prof. Dr. Rene Pecnik

Reader(s):

Prof. Dr. Bendiks Jan Boersma

Abstract

Organic Rankine Cycle (ORC) Power Plants can be of great importance in the energy transition as they are suitable for converting waste heat to power, and can utilize renewable energy for their operation. To improve the efficiency of ORC Power Plants, the physical phenomena inside these machines must be understood. Understanding the boundary layer of complex organic fluid flows in these systems is crucial, as it is estimated to be responsible for one-third of the losses in turbomachinery [1].

In this thesis, two-dimensional steady state boundary layer flows of nonideal gas have been investigated numerically. The objective was to find the influence of complex fluid nonideality, characterized by ideal gas departure, on boundary layer flows. In particular, a high-speed dense vapour expansion of organic fluid Hexamethyldisiloxane (MM) inside a de Laval nozzle test section has been studied. The nozzle is part of a measurement campaign to collect experimental data with the purpose of validation and calibration of Non-Ideal Compressible Fluid Dynamics (NICFD) software.

A MATLAB program was developed for solving the two-dimensional steady state boundary layer equations including general thermophysical properties. Transition prediction methods, the algebraic Cebeci-Smith turbulence model (CS-model), and state-of-the-art thermophysical models were implemented. The program was verified and validated against literature with test cases for air. The turbulence model was validated with experimental data of large-scale zero pressure gradient adiabatic flows. The results match for the entire Mach-number range from 0.2 up to 2.8. The program also proved to be capable of predicting the turbulent boundary layer along a flat wall inside a de Laval nozzle expanding air.

Deterministic simulations of the boundary layer along the curved wall surface of the aforementioned nozzle expanding MM were performed. The results showed a larger decrease in the newly defined property $C_{\mathrm{e}} = \frac{\rho_{\mathrm{e}}\mu_{\mathrm{e}}}{\rho_0\mu_0}$ in the core flow along expansion compared to air. In contrast, the property gradients; namely density ratio c and Chapman-Rubesin

parameter C, inside the boundary layer were found to be negligible. Furthermore, the results show that the influence of the pressure history upstream of the nozzle throat is relatively small or even negligible in the diverging nozzle section. The boundary layer displacement thickness for both laminar and turbulent flow was found to be negligible compared to the nozzle cross section, which results in a negligible effect on the nozzle core flow.

The program needs further validation for flows departing from ideal gas. First, the flow condition in de Laval nozzles, laminar or turbulent, needs to be obtained by conducting experiments. Then, sensitivity studies need to prove if the inviscid nozzle design is a robust design for viscous flows too; namely, being insensitive to changes in total input conditions, uncertainties in closure coefficients, and variations in upstream pressure history.

Table of Contents

List of Figures

List of Tables

Acknowledgments

Throughout the thesis process I have developed myself in multiple ways. I organized activities and camps being part of the NJN, I worked on my personal development, skills and qualities in life, and I worked on my thesis.

I have seen a lot of students come and go. Some of them unnoticed, others more on the foreground. I would like to thank the following former students, Engineers now, for the discussions during the breaks and sometimes when we should have worked but got stuck. I want to thank Adam, Yorick, Merijn, Luc, Tom, Anne-Liza and Rishikesh.

During the process of 'finishing the code', Federico Pizzi came from Italy (Politecnico di Milano) as a thesis student to work on the same topic, and who I regard to as a friend now. I will remember the interesting discussions we had about progressive rock and the physical meaning of the boundary layers characteristics, of which some of them were quite difficult to interpret and understand. Thanks to the strong theoretical and analytical skills of Federico, I was able to include more boundary layer characteristics in the program presented in this thesis.

Even more I would like to thank the people who tried to help me find my way: Evert, as always inspiring me, Lourdes, Monique, Adam Head, Rosalie, Nicolai and finally Kim and Rajat who helped me find the path. Even more, my housemates were a very important stable factor in my life. Besides them, I would like to thank Ferdinand and Anne for helping me restart. Most importantly, my daily supervisor Adam Head was always there to help, being a coach enabling me to get the best out of myself and my thesis and supporting me to develop myself. Without his help I would probably not have finished. In addition, I want to thank him for his impressive amount of patience.

The thesis process came a long way. I want to thank my parents for supporting me, and for sponsoring me. Although they never really understood what I was doing, or what I was going through, they kept their belief and trust in me and were very patient. Without their support it would not have been possible to finish.

The process has not always been easy. Sometimes I just lost my horizon, found myself drowning in an ocean of details, without a compass, not knowing where to go, not

knowing the difference between top and bottom, and I just kept swirling around. Finding solid ground below your feet is great, and this started when I finally wrote down my work.

Looking back on my work, the thesis which is in front of you now, I need to say that I feel proud of it, which is quite an achievement for a perfectionist. Working on something complex requires skills to bring it down into something more simple. Being a perfectionist meant to me that I did not make things more simple, but more complex instead. Therefore, the dedication on the next page has been a life-saver.

Delft, May 17th 2019

Dominic Dyon Dijkshoorn

"Simplicity is the ultimate form of sophistication." — *Leonardo da Vinci*

Nomenclature

Latin Symbols

a	Speed of Sound (SoS)	m^2/s
a_{0-4}	Constants in c_p polynomial	
A	Area	m^2
A	Van Driest damping-length factor	m
A^+	Van Driest damping constant	-
b	Coefficient in the transformed ME 3-1	-
B	Heat transfer damping-length factor	m
B^+	Second heat transfer damping-length factor	-
B^{++}	Third heat transfer damping-length factor	-
c	Density ratio: $c = \frac{\rho_e}{\rho}$; coefficient in transformed SoE	-
c_p	Specific heat at constant pressure	J/(kg K)
c_v	Specific heat at constant volume	J/(kg K)
C	Chapman-Rubesin parameter $C = \frac{\rho\mu}{\rho_e\mu_e}$ [2]	-
C_{1-5}	Constants in fluid specific third heat transfer damping-length factor	-
C_d	Denton's loss coefficient [1] (see dimensionless groups)	-
C_e	Fluid property change along isentropic expansion $C = \frac{\rho_e\mu_e}{\rho_0\mu_0}$	-
C_f	Local skin friction coefficient (see dimensionless groups)	-
d	Coefficient in the transformed EE 3-4	-
e	Specific internal energy (per unit mass)	J/kg
e	Coefficient in the transformed EE 3-4	-
E	Internal energy	J
f	Dimensionless stream function (eq. 3-1 and 3-4): $f' = u/u_e$ (differential parameter)	[-]
f	Force per unit mass	N/kg

g	Total enthalpy ratio inside BL $g = \frac{h_0}{h_{0,\mathrm{e}}}$ 3-4 (differential parameter)	-
g	Gravitational constant	$\mathrm{m/s^2}$
G_{tr}	Spot-formation-rate parameter (CS-model)	$\mathrm{m/(s\,m^2)}$
h	Specific enthalpy (per unit mass)	J/kg
h_0	Specific total enthalpy (per unit mass)	J/kg
h_{c}	Convective heat transfer coefficient (see dimensionless groups)	$\mathrm{W/(m^2\,K)}$
H	Shape factor (see dimensionless groups)	-
I	Integral of c over η inside the boundary layer	-
k	Thermal conductivity	$\mathrm{W/(m\,K)}$
l	Mixing-length (CS-model)	m
L	Corrected mixing-length (CS-model)	m
L	Length scale (for scaling surface coordinate)	m
m_1	Pressure Gradient parameter (eq. **??**) in transformed ME and EE 3-1 and 3-4	-
m_2	Second PG parameter (eq. **??**) in transformed ME and in m_1 (eq. 3-1)	-
m_3	Third PG parameter (eq. 3-15), inside m_1, measure of property variation along BL edge	-
m_4	Fourth PG parameter (eq. 3-16), inside m_2	-
m_5	Fifth PG parameter (eq. 3-17), inside m_2	-
$\dot{m}$	Mass flow rate	kg/s
N	Parameter for extension of Van Driest damping-length factor to include variable pressure gradient, heat transfer and mass transfer	-
p	Thermodynamic pressure	$\mathrm{N/m^2}$
p	Coefficient in the transformed EE 3-1 (differential parameter) $p = g'$	-
$\bar{p}$	Mechanical pressure	$\mathrm{N/m^2}$
p^+	Dimensionless Pressure Gradient parameter	-
$\dot{q}$	Heat flux	$\mathrm{J/(m^2\,s)}$
R_0	Molar or universal or Ideal Gas constant	$\mathrm{J/(mol\,K)}$
R_{c}	Radius of (surface) curvature	m
R_{sp}	Specific gas constant	$\mathrm{J/(kg\,K)}$
s	Entropy per unit mass	$\mathrm{J/(kg\,K)}$
S	Entropy	J/K
S	Sutherland's constant (Sutherland's Law)	K
t	Time	s
T	Temperature	K
u	Instantaneous velocity	m/s
u	Dimensionless velocity ratio inside BL $u = f' = u/u_{\mathrm{e}}$ (differential parameter)	-

U	Free stream velocity	m/s
v	Instantaneous velocity in y-coordinate direction	m/s
v	Specific volume	m/kg^3
v	Shear parameter $v = f''$ (differential parameter)	-
x	x-coordinate	m
X	Surface coordinate	m
y	y-coordinate	m
z	z-coordinate	m
Z	Compressibility factor	-

Greek Symbols

α	Thermal diffusivity	m^2/s
α	Clauser('s) (outer eddy viscosity) constant	-
α	Specific (nondimensionalized) Helmholtz energy	-
α_T	Turbulent thermal diffusivity	m^2/s
β	Pressure Gradient parameter (conventional)	-
γ	Ratio of specific heats	-
γ_{int}	Intermittency factor (CS-model)	-
γ_{tr}	Transition region intermittency factor	-
δ	Boundary layer velocity thickness	m
δ	Reduced density $\delta = \rho/\rho_c$	-
δ^*	Displacement thickness	m
η	Transformed y-coordinate	-
θ	Momentum thickness	m
ϵ_h	Eddy conductivity (heat transfer) (CS-model)	m^2/s
ϵ_m	Eddy viscosity (momentum) (CS-model)	m^2/s
ρ	Density	kg/m
κ	(Von) Kármán constant	-
κ_h	Heat transfer mixing-length constant	-
λ	Second coefficient of viscosity	kg/(m s)
λ^+	Nondimensional second coefficient of viscosity (ratio): $\lambda^+ = \lambda_e/\mu_e$	[-]
μ	Dynamic viscosity	kg/(m s)
μ_b	Bulk viscosity ratio $\mu_b = \frac{\mu_v}{\mu}$	[-]
μ_v	Bulk viscosity $\mu_v = \frac{\lambda_e + \frac{2}{3}\mu_e}{\mu_e}$	[-]
μ^λ	Ratio of Viscosities, relative size of 2^{nd} coefficient of viscosity $\mu^\lambda = \frac{\lambda_e}{\mu_e}$	[-]
μ_T	Eddy/Turbulent/Apparent (dynamic) viscosity	kg/(m s)
μ_T^+	Nondimensional Eddy/Turbulent/Apparent (dynamic) viscosity: $\mu_T^+ = \mu_T/\mu$	[-]
ν	Kinematic viscosity μ/ρ	m^2/s
ν_T	Eddy/Turbulent/Apparent (kinematic) viscosity μ_T/ρ	m^2/s

ν_{T}^{+}	Nondimensional turbulent (kinematic) viscosity $\nu_{\mathrm{T}}^{+} = \nu_{\mathrm{T}}/\nu$	[-]
σ	Stress tensor (including pressure)	$\mathrm{N/m^2}$
τ	Shear stress	$\mathrm{N/m^2}$
τ	Reduced temperature $\tau = T/T_{\mathrm{c}}$	-
τ_{ij}	Viscous stress tensor	$\mathrm{N/m^2}$
ψ	Stream function	-

Dimensionless Groups and Coefficients

Br	Brinkman-number: $\mathrm{Br} = \mathrm{Ec}\,\mathrm{Pr} = \frac{\text{viscous dissipation}}{\text{thermal conduction}}$	
C_{d}	Loss coefficient [1]: $C_{\mathrm{d}} = \frac{T\dot{S}_{\mathrm{A}}}{\rho U^3}$	
C_{f}	Local skin fiction coefficient: $C_{\mathrm{f}} = \frac{2\tau_{\mathrm{w}}}{\rho U^2} = \frac{\text{wall shear stress}}{\text{dynamic pressure}}$	
Ec	Eckert-number: $\mathrm{Ec} = \frac{U^2}{\Delta h} = \frac{\text{flow kinetic energy}}{\text{enthalpy driving force}}$; or, $\mathrm{Ec} = \frac{U^2}{h}$ (reference Ec-number)	
h_{c}	Convective heat transfer coefficient	$\mathrm{W/(m^2\,K)}$
H	Shape factor: $H = \frac{\delta^*}{\theta} = \frac{\text{displacement thickness}}{\text{momentum thickness}}$	
Ma	Mach-number: $\mathrm{Ma} = \frac{U}{a} = \frac{\text{flow kinetic energy}}{\text{molecule kinetic (internal) energy}} = \frac{\text{directed kinetic energy}}{\text{random kinetic energy}}$	
Nu	Nusselt-number: $\mathrm{Nu} = \mathrm{St}\,\mathrm{Re}\,\mathrm{Pr} = \frac{h_{\mathrm{c}}L}{k} = \frac{\text{convective heat transfer}}{\text{thermal conduction}}$	
Pe	Peclet-number: $\mathrm{Pe} = \mathrm{Re}\,\mathrm{Pr} = \frac{UL}{k} = \frac{\text{convective heat transfer}}{\text{thermal conduction}}$	
Pr	Prandtl-number: $\frac{\nu}{\alpha} = \frac{\mu c_{\mathrm{p}}}{k} = \frac{\text{momentum diffusion}}{\text{thermal diffusion}}$ (only dimensionless fluid property)	
$\mathrm{Pr_T}$	Turbulent Prandtl-number: $\mathrm{Pr_T} = \frac{\nu_{\mathrm{T}}}{\alpha_{\mathrm{T}}} = \frac{\epsilon_{\mathrm{m}}}{\epsilon_{\mathrm{h}}} = \frac{\text{convective momentum transport}}{\text{convective heat transfer}}$	
Re	Reynolds-number: $\mathrm{Re}_x = \frac{\rho UL}{\mu} = \frac{\text{momentum}}{\text{viscous forces}}$	
St	Stanton-number: $\mathrm{St} = \frac{\dot{q}_{\mathrm{w}}}{\rho U \Delta h} = \frac{\text{convective heat transfer}}{\text{thermal capacity}}$	

Subscripts

0	Total quantity
0	Reference state
aw	Adiabatic wall value
cr	Critical point value
dyn	Dynamic
e	Boundary layer edge
f	Free stream
h	Related to heat transfer
i	Index
j	Index
k	Index
m	Index
r	reduced quantity
sg	Specific gas
t	Total quantity
T	Turbulent quantity
tr	Transition (start of)

w	Wall quantity

Superscripts

+	Nondimensional
0	Ideal gas
IG or ig	Ideal gas
NIG or nig	Non-Ideal gas
r	Real gas
r	Reduced quantity

Symbols

+	Dimensionless
$*$	Dimensionless
$-$	Conventional time averaged
$\sim$	Mass-weighted time averaged
$'$	Time fluctuation (Schlichting [3]: Fluctuation quantity, conventional time averaged)
$''$	Mass-weighted fluctuation (Schlichting [3]: Fluctuation quantity, mass-weighted time averaged)
∞	Far field/free stream, infinity

Acronyms

2D	Two-Dimensional
3ME	Faculty of Mechanical, Maritime and Materials Engineering
APG	Adverse Pressure Gradient
AW	Adiabatic Wall
BL	Boundary Layer
BLC	Boundary Layer Characteristics
BLE(s)	Boundary Layer Equation(s)
CARE	Climate and Energy Package (EU)
CFD	Computational Fluid Dynamics
CPIG	Calorically Perfect Ideal Gas
CIIG	Calorically Imperfect Ideal Gas
CS	Cebeci-Smith turbulence model (introduced as CS-model in Cebeci and Smith (1974) [4])
CSM	Cebeci-Smith-method (introduced as CS-method in Cebeci and Smith (1974) [4])
D_6	Dodecamethylcyclohexasiloxane
DoE	Design of Experiment
DUT	Delft University of Technology
EE	Energy Equation
EIA	Energy Information Administration (US)
EU	European Union
EoS	Equation of State

FP	Flat Plate
FPP	Flight Propulsion and Performance (DUT)
FPG	Favourable Pressure Gradient
GHE	Greenhouse Gas Emissions
HMC	High Molecular Complex (fluid)
HT	Heat Transfer
iPRSV	Improved Peng-Robinson Stryjek-Vera (EoS)
IG	Ideal Gas
KBM	Keller's Box-Method
LE	Leading Edge
MDM	Octamethyltrisiloxane
MD2M	Decamethyltetrasiloxane
ME	Momentum Equation
MM	Hexamethyldisiloxane
MoC	Method of Characteristics
NICFD	Non-Ideal Compressible Fluid Dynamics
NIG	Non-Ideal Gas (departing from IG)
NGV	Nozzle Guide Vane
NS	Navier-Stokes
ODE	Ordinary Differential Equation
ORC	Organic Rankine Cycle
ORCHID	Organic Rankine Cycle Hybrid Integrated Device
PDE	Partial Differential Equation
PG	Pressure Gradient
PP2	Perfluoromethylcyclohexane
PP80	Perfluoro-2-methyl-3-ethylpentane
PP90	Perfluoro-2,4-dimethyl-3-ethylpentane
PRSV	Peng-Robinson Stryjek-Vera
PS	Pressure Side (of blade)
RANS	Reynolds Averaged Navier-Stokes
RE	Richardson Extrapolation
RG	Real Gas (departure from IG, and including dissociation and ionization)
SoE	System of Equations
SoS	Speed of Sound a
SP	Stagnation Point
SS	Suction Side (of blade)
SU2	Stanford University Unstructured (squared: SU^2)
SW	Span-Wagner
TE	Trailing edge
TPIG	Thermally Perfect Ideal Gas
TROVA	Test Rig for Organic Vapors
UQ	Uncertainty Quantification
WF	Working Fluid

ZPG	Zero Pressure Gradient

Chapter 1

Introduction

1-1 Background

Climate change is detrimental to the environment and is expected to cause severe problems and big challenges in the near future. The problem has been globally recognised and the call for a more sustainable future and society grew louder during the last decade. Governments and international organizations have been called and forced to action to combat climate change. For example, the Paris Agreement signed in 2016 by 189 parties [5] aimed at limiting the temperature increase on earth by reducing Greenhouse Gas Emissions (GHE) from fossil fuels (in CO_2 equivalents). In parallel, the European Union (EU) has set ambitious goals for reducing its inhabitants footprint on earth by setting the EU climate and energy (CARE) Package, also known as the 20-20-20 goals [6, 7]. These goals entail to reach by the end of 2020:

1. A 20% reduction in greenhouse gas emissions;
2. A 20% share of renewables in the total amount of energy used in the EU; and,
3. A 20% overall improvement in energy efficiency.

On top of that, the EU has adopted The Green Deal strategy for the years to come *Striving to be the first climate-neutral continent* [8] aiming at a climate-neutral and circular economy by 2050. Altogether, due to these objectives renewables are expected to become the world's primary energy source by 2050, as predicted by the US Energy Information Administration (EIA) in their International Energy Outlook, currently being already the fastest growing source of electricity.

The use of renewable energy technology will help ensure that the goals set out by the governments can be reached. The Organic Rankine Cycle (ORC) Power Plant is one of the promising technological solutions. Its biggest advantage is its capability to utilize any external heat source of relatively low capacity and low temperature, making it suitable for both converting low grade waste heat to power; and, utilizing renewables [9]. Therefore, ORC technology is especially interesting at the moment, since it covers both sides of the coin: on the one hand by reducing fossil-fuel use and improving energy efficiency and, on the other hand, by utilizing renewable energy sources.

An ORC based Power Plant contains a thermodynamic cycle with carbon-based working fluids. These working fluids are chosen due to their smaller specific enthalpy of evaporation, resulting in higher volume flows and thus in more efficient turbine designs at small scale. This makes ORC technology suitable for small scale plants utilizing low temperature and low capacity heat sources [9]. However, the low specific enthalpy also results in a highly supersonic stator design which therefore needs to be carefully considered. Other attractive features of the ORC Power Plant are for example:

1. Lubricative properties of some ORC working fluids;
2. Dry expansion process (for most ORC working fluids) avoiding blade erosion;
3. The possibility of effective thermal energy regeneration; and,
4. Simple construction of the Power Plant.

However, ORC Power Plant technology has not matured yet from a technical point of view. Improving the efficiency of these systems can make this technology more interesting and competitive.

Nonideal gas flows are one of the challenging research topics [10] that still need to be investigated. This is the realm of Non-Ideal Compressible Fluid Dynamics (NICFD)[1]. NICFD deals with complex fluids, meaning fluids that have high molecular complexity, refering to the structure of the molecule [12], that includes the arrangement of the atoms and the special bond-types between them. Molecular complexity includes both the capacity of the molecule to store energy, and the interaction between the molecules [13]. The range of nonideal gas behaviour is situated in the thermodynamic regions where the compressibility factor $Z = pv/R_{sp}T$ [14], a measure of the interaction between the molecules, deviates from one. The ideal gas-Law states that an ideal gas adheres to: $pv = R_{sp}T$, whereas a nonideal gas does not. The volume departure function $1 - Z$ quantifies the departure from ideal gas, where a value of zero indicates zero departure, or ideal gas.

[1] See Head [11] for a history and complete overview of NICFD.

1-2 Motivation

Improving the efficiency of ORC Power Plants entails understanding of the physical phenomena inside these machines. An important area is the study of the phenomena inside the boundary layer. Despite the fact that the boundary layer accounts for significant efficiency losses in turbomachinery (appr. 1/3 as claimed by Denton [1]), it has not been investigated thoroughly yet. Research into boundary layer theory for complex organic fluids can lead to improvements in efficiency, not only for the turbine but also for heat exchangers. So far, only a few authors have published research on fluid-dynamic losses in ORC turbomachines, and on the effects of complex fluids in boundary layer flows [10]. However, the influence of molecular complexity on the boundary layer characteristics and thus on profile losses is yet largely unknown. Better design of turbomachinery for higher efficiencies therefore requires fundamental understanding of the boundary layer, and thus bridging the current knowledge gap.

1-3 Scope and Objectives

To bridge this gap a facility or test-rig for the investigation of working fluids for ORC applications is being commissioned at the moment at Delft University of Technology (DUT) section Flight Propulsion and Performance (FPP). The facility, called Organic Rankine Cycle Hybrid Integrated Device (ORCHID) [15,16], is meant to reveal nonideal behaviour of vapours promising for ORC technology. It consists of two test-sections: a turbine test-section for novel blade designs, and a nozzle test-section which features a two-dimensional converging-diverging de Laval nozzle for investigating the flow physics of nonideal vapours. The 2D de Laval nozzle is designed to accelerate the working fluid up to Mach 2.0. The envisaged experiments are devoted to validation and calibration of NICFD software [11,17].

The design of the ORCHID nozzle requires knowledge about the boundary layer characteristics. The Method of Characteristics (MoC) is an inviscid method taking into account the supersonic flow properties of expanding gases to design a nozzle for a smooth and shockless expansion. Guardone [18] extended the use of the MoC with complex thermodynamic models, replacing the Ideal Gas model. The next step is a design taking into account the viscous effects in the region close to the wall, which is called the boundary layer. To the authors knowledge Goldman [19] is the first to introduce the concept of a viscous nozzle design. He presents a computer program for the design of sharp-edged throat nozzles for calorically perfect ideal gas by adding the predicted boundary layer displacement thickness to the inviscid nozzle design obtained with the MoC. This work aims at a preliminary prediction of the boundary layer displacement thickness based on the design operating conditions of the ORCHID nozzle test section.

A model capturing the relevant phenomena is needed for a prediction of the boundary layer characteristics, such as boundary layer displacement thickness, for the aforementioned viscid design of the nozzle. The model is required to be simple enough to interpret

and understand the effect of fluid complexity on the results. For this, existing methods and sub-models can be combined which are required to be valid for the range of operation of the ORCHID nozzle. A suitable program structure needs to be implemented in designing the program and with selection of the sub-models, such that Design of Experiments (DoE) or sensitivity studies, such as Uncertainty Quantification (UQ), can be performed in future by allowing closure coefficients and input conditions to be adjusted in between calculations for studying their effects. The knowledge developed by studying boundary layer theory through simulations with complex thermophysical models will aid the design of nozzles and stator vanes, the development of physically-based loss models, and the selection of working fluids for ORC technology. The main objective of this work is the verification and validation of a computer program for the simulation of two-dimensional steady state boundary layers generalized for complex organic fluids.

1-4 Literature Review

The development of boundary layer models has a long history, going back to Prandtl [20]. In the sixties and seventies of the previous century a successful approach to two-dimensional steady state laminar and turbulent boundary layer flows was developed by Clutter, Smith and Cebeci. Clutter and Smith started developing a laminar boundary layer program [21] and [22] which was improved and extended to include a simple algebraic turbulence model by Cebeci and Smith [4], called the CS-model. This zero-equation turbulence model was based on the Eddy Viscosity concept, and it includes a turbulent Prandtl-number model based on the Eddy Conductivity concept. Since then, the successful approach to boundary layer flows introduced by Cebeci and Smith [4] is referred to as the CS-method, which includes Keller's Box-method [23] to solve the system of equations. The method is extensively discussed in their book *Analysis of Turbulent Flows*, from which a second [24], and a third [25] edition included further improvements and model extensions, such as for example laminar-turbulent transition, but also closure coefficient corrections for strong adverse pressure gradients, low Reynolds-number flows and curvature. Wilcox [26] puts this model into perspective by discussing all different types of turbulence models and their pros and cons. The book *Convective Heat Transfer* by Cebeci from 2002 [27] contains a DVD with a FORTRAN program for solving the compressible two-dimensional steady state boundary layer equations including heat transfer for a calorically perfect ideal gas, with the dynamic viscosity obtained with Sutherland's Law. A more recent version of the CS-model was implemented here, and the program includes an Eddy Conductivity model in the form of a constant turbulent Prandtl-number (= 0.9). The FORTRAN program is shown being capable of simulating low Mach-number incompressible stagnation point flow over a NACA0012 airfoil. The case includes transition from laminar to turbulent flow with a predefined transition location and, finally, separation close to the leading edge.

For accurate prediction of boundary layers in physically based loss models it is important to know whether the flow is laminar or turbulent. In addition, the location of

laminar-turbulent flow transition, the transition region, and possibly relaminarization and re-transition are important to predict accurately, which is supported by Basha [28] and shown with, for example the experiments of Bader [29–31]. For estimation of the transition point from laminar to turbulent flow in compressible flow regimes, Wazzan [32] introduced an empirical correlation called the H-Re_x-method including mild heat transfer. Alternatively, Cebeci [25, 33] extended Michel's method for prediction of the transition point in adiabtic flows along curved surfaces. Cebeci [27] implemented a correlation based on an intermittency factor taking into account turbulent spots for prediction of the laminar-turbulent transition region in compressible adiabatic flows below Mach 5. Finally, Nash-Webber [34] introduced a simple engineering approach for the prediction of relaminarization in compressible adiabatic air flows, i.e. (re-)transition from turbulent to laminar flow.

Denton [1] introduced a physically based loss model for the prediction of losses in two-dimensional steady state boundary layer flows. The loss model supports the observation that proper simulation of turbulence is required to predict the amount of losses accurately, since turbulence contributes significantly to the total amount of losses. The loss coefficient derived was used to predict losses in zero, adverse and favourable pressure gradient boundary layer flows for air modeled as incompressible calorically perfect ideal gas. Denton and coworkers expect similar trends for compressible flows.

Regarding state-of-the-art complex thermophysical models, Setzmann and Wagner [35] developed a new multiparameter Equation of State (EoS) *in the form of a fundamental equation explicit in the Helmholtz free energy* [35]. In the meantime, the multiparameter EoS has been improved such that the coefficients can be fitted easily to restricted data sets [36–38], and extended to a range of (industrial) fluids [36–42]. Colonna and coworkers [43, 44] applied the multiparameter EoS to a selected range of siloxane fluids, which are promising for ORC applications. In response to this, Thol and coworkers [45] presented an improved multiparameter EoS for hexamethyldisiloxane (MM) which is considered highly accurate. The qubic EoS is a different type of EoS and more conventional. Van der Stelt [46] devised the qubic improved Peng-Robinson-Stryjek-Vera (iPRSV) EoS, removing numerical discontinuities from the PRSV EoS. Both the multiparameter and qubic EoS take into account molecular complexity and are implemented in the program FluidProp [47], a program for thermophysical property retrieval.

Regarding the design of a de Laval nozzle for supersonic flows, Goldman [19] introduced the viscous design of supersonic nozzles for calorically perfect ideal gas by adding the predicted boundary layer displacement thickness [48] to the inviscid nozzle design [49] obtained by applying the MoC. Guardone [18] extended the use of the MoC with complex thermodynamic models replacing the calorically perfect ideal gas model. He studied the effect of molecular complexity on the inviscid nozzle design for several ORC working fluid candidates by comparing the resulting designs with their ideal gas counterparts. Concerning profile loss predictions, Pizzi [50] and Pini [51] applied the loss coefficient introduced by Denton [1] to nonideal gas flows in a preliminary study using a preliminary version of the program introduced in this work. Kluwick [10, 52] investigated boundary

layers in fluid flows of complex gases and points out some interesting nonideal effects on boundary layer characteristics that can be utilized in power generation equipment such as ORC systems. Furthermore, Kluwick states that fluids of high molecular complexity are characterized by low Eckert-numbers, meaning that dissipation by internal friction and thermal conduction are negligible up to moderately large supersonic Mach-numbers, resulting in nearly constant temperature and density profiles inside adiabatic boundary layer flows. To the best knowledge of the author only Duff [53] acquired experimental data of nonideal gas boundary layer flows by measuring the boundary layer thickness at only four points inside a two-dimensional de Laval nozzle expanding CO2.

1-5 Outline

The following research question resulted from the literature study above:

What is the influence of the nonideal thermophysical properties of a complex fluid on two-dimensional steady state boundary layer flows?

The research objectives and the main research question led to the following key research sub-questions:

1. What is a suitable turbulence model for studying the effect of complex fluid thermophysical properties on boundary layer characteristics?
2. Are the closure coefficients and the range of validity of the boundary layer program suitable to predict accurately the physics of complex organic fluid flows?
3. How can a boundary layer in a complex organic fluid be characterized?
4. How does presence of the boundary layer influence the expansion of complex organic fluid MM in the ORCHID nozzle?
5. What factors need to be considered for a future robust viscous ORCHID nozzle design?

The research question will be answered by using the boundary layer program, the main deliverable of this work, that was specifically designed for this purpose. The structure of the program enables future sensitivity studies, such as UQ, and DoE studies which entail many simulations.

The structure of the report is as follows. First, the equations for laminar and turbulent two-dimensional steady state boundary layer flows are derived in Chap. 2. Furthermore, the equations are reported for general fluid properties predicted with state-of-the-art thermophysical models. Chapter 3 focuses on the implementation of the system of

equations in combination with these models into a computer program. Specifically, the limitations and capabilities of the program are discussed. Chapter 4 addresses numerical characteristics, and the validity of the program through an extensive verification and validation study for ideal gas air. The next chapter, Chap. 5, investigates how the nonideal gas properties affect the boundary layer characteristics inside the ORCHID nozzle. Lastly, in Chapt. 6 conclusions are drawn upon the preliminary predictions of the boundary layer flow inside the ORCHID nozzle for complex organic fluid MM, followed by recommendations for ongoing work, suggestions for future research and an outlook into the future.

Chapter 2

Boundary Layer Equations with General Thermophysical Properties

This chapter introduces the background theory of two-dimensional steady state compressible boundary layer flows with variable fluid properties, which is the basis of this work and the foundation of the computer program. The chapter starts with the conservation laws for mass, momentum and energy in Sec. 2-1. Then, this system of equations is simplified by using Prandtl's approach for capturing the important flow characteristics in the boundary layer in Sec. 2-2. Turbulent flow phenomena are captured by Reynolds-averaging (RANS) discussed in Sec. 2-3-3, which is applied to simplify the system of equations even further. Thereafter, the Cebeci-Smith algebraic turbulence model is then introduced for modelling the single Reynolds stress that is left (Eddy Viscosity concept), and the turbulent Prandtl-number for modelling turbulent heat transfer (Eddy Conductivity concept). This altogether results in a simplified system of the averaged boundary layer equations. Boundary layer characteristics and parameters to quantify them are discussed in Sec. 2-4. Section 2-5 discusses a few simple transition predicton methods. At last, Sec. 2-6 discusses thermophysical models for simulation with different thermophysical models for any choice of fluid including variable fluid properties.

2-1 Conservation of Mass, Momentum and Energy

In this section the conservation equations are introduced for mass, momentum and energy. These conservation equations form the basis of any fluid flow model. The resulting system of equations can be rewritten to a suitable form for the case at hand. The derivation of the following equations is based on the work of Schlichting, Cebeci, White and Kundu [3, 4, 27, 54, 55].

2-1-1 Continuity Equation

The conservation of mass results in the three-dimensional continuity equation, in tensor notation

$$\frac{\partial \rho}{\partial t} + \frac{\partial}{\partial x_i}\left(\rho u_i\right) = 0. \tag{2-1}$$

2-1-2 Navier-Stokes Equations

The conservation of momentum results in the three general momentum equations in the Cartesian coordinate directions, which are, written in general form in tensor notation

$$\rho \frac{\mathrm{D}u_i}{\mathrm{D}t} = \rho f_i + \frac{\partial \sigma_{ij}}{\partial x_i}, \tag{2-2}$$

where a capital D denotes the material derivative and the term f_i is defined as the body force(s) in the i-direction. Body forces can be for example gravity, e.g. $f_x = f_y = 0, f_z = -g$ or centrifugal and Coriolis forces in the flow field of a rotating turbine. The stress tensor σ_{ij} is equal to

$$\sigma_{ij} = -p\delta_{ij} + \tau_{ij}, \tag{2-3}$$

where σ_{ij} is the stress tensor, and τ_{ij} is the viscous stress tensor, with dynamic viscosity μ and second coefficient of viscosity λ

$$\tau_{ij} = \mu\left(\frac{\partial u_i}{\partial x_j} + \frac{\partial u_j}{\partial x_i}\right) + \lambda \frac{\partial u_m}{\partial x_m}\delta_{ij}, \tag{2-4}$$

such that the momentum equations can be written as

$$\rho\left(\frac{\partial u_i}{\partial t} + u_j \frac{\partial u_i}{\partial x_j}\right) = -\frac{\partial p}{\partial x_i} + \rho f_i + \frac{\partial}{\partial x_j}\left[\mu\left(\frac{\partial u_i}{\partial x_j} + \frac{\partial u_j}{\partial x_i}\right) + \lambda \frac{\partial u_m}{\partial x_m}\delta_{ij}\right]. \tag{2-5}$$

A mechanical pressure $\bar{p}$ can be defined as opposed to (in direction) and equal to one-third of the sum of all three normal stresses (see White [54])

$$\bar{p} = -\frac{1}{3}\sigma_{mm} = p - \left(\lambda + \frac{2}{3}\mu\right)\frac{\partial u_m}{\partial x_m}, \tag{2-6}$$

such that a *bulk viscosity* μ_v can be defined[1]. That is, a viscosity that counteracts dilatation (volume changes), which can be written in terms of second coefficient of viscosity λ and dynamic viscosity μ as

$$p - \bar{p} = \left(\lambda + \frac{2}{3}\mu\right)\frac{\partial u_m}{\partial x_m} = \mu_{\mathrm{v}}\frac{\partial u_m}{\partial x_m}. \tag{2-7}$$

The momentum equations can then be rewritten to

$$\rho\left(\frac{\partial u_i}{\partial t} + u_j\frac{\partial u_i}{\partial x_j}\right) = -\frac{\partial p}{\partial x_i} + \rho f_i + \frac{\partial}{\partial x_j}\left[\mu\left(\frac{\partial u_i}{\partial x_j} + \frac{\partial u_j}{\partial x_i}\right) + \left(\mu_{\mathrm{v}} - \frac{2}{3}\mu\right)\frac{\partial u_m}{\partial x_m}\delta_{ij}\right]. \tag{2-8}$$

Stokes' hypothesis states that $\mu_{\mathrm{v}} = \lambda + \frac{2}{3}\mu = 0$, which gives $\lambda = -\frac{2}{3}\mu$ and thus removes the difference between mechanical and thermodynamic pressure. Therefore, the second coefficient of viscosity can be written in terms of dynamic viscosity μ, which allows the momentum equations to be rewritten such that the viscous stress tensor is only a function of the dynamic viscosity μ. When written in this form, the momentum equations are called the Navier-Stokes equations

$$\rho\left(\frac{\partial u_i}{\partial t} + u_j\frac{\partial u_i}{\partial x_j}\right) = -\frac{\partial p}{\partial x_i} + \rho f_i + \frac{\partial}{\partial x_j}\left[\mu\left(\frac{\partial u_i}{\partial x_j} + \frac{\partial u_j}{\partial x_i}\right) - \frac{2}{3}\mu\frac{\partial u_m}{\partial x_m}\delta_{ij}\right]. \tag{2-9}$$

Generally however, the divergence term is neglected (it is zero for incompressible flow, which follows from continuity), and the Navier-Stokes equations can be rewritten to

$$\rho\left(\frac{\partial u_i}{\partial t} + u_j\frac{\partial u_i}{\partial x_j}\right) = -\frac{\partial p}{\partial x_i} + \rho f_i + \frac{\partial}{\partial x_j}\left[\mu\left(\frac{\partial u_i}{\partial x_j} + \frac{\partial u_j}{\partial x_i}\right)\right]. \tag{2-10}$$

2-1-3 Energy Equation

The conservation of energy results in

$$\rho\left(\frac{\partial h_0}{\partial t} + u_j\frac{\partial h_0}{\partial x_j}\right) = \frac{\partial p}{\partial t} - \frac{\partial \dot{q}_i}{\partial x_i} + \rho u_i f_i + \frac{\partial}{\partial x_j}\left(u_i\tau_{ij}\right), \tag{2-11}$$

where the total enthalpy is defined as $h_0 = h + \frac{1}{2}u_i^2$ with static enthalpy $h = e + \frac{p}{\rho}$.

[1] A derivation and explanation of the concept of bulk viscosity is given by Schlichting [3, p. 66]. Kundu [55] and White [54] present a short derivation, whereas Gad-el-Hak [56] gives an explanation and historical perspective on the topic in *Unanswered Questions in Fluid Mechanics*.

2-2 The Boundary Layer

The boundary layer is a thin layer close to a wall surface where the effect of viscosity cannot be neglected compared to the free stream. The flow interacts with the wall by friction forces. The size of these forces depends, among others, on the local value of viscosity. The flow velocity at the wall surface is required to be zero for a frictional flow. This is referred to as the *zero* or *no slip condition*. Figure 2-1 shows the development of a boundary layer on a smooth flat plate with typical velocity profiles for laminar (parabolic-shape) and turbulent (flat-shape) flow. The viscosity is small (high Reynolds-number), which results in a high velocity gradient close to the wall. Far from the wall surface, in the free stream, these gradients disappear and viscosity can be neglected.

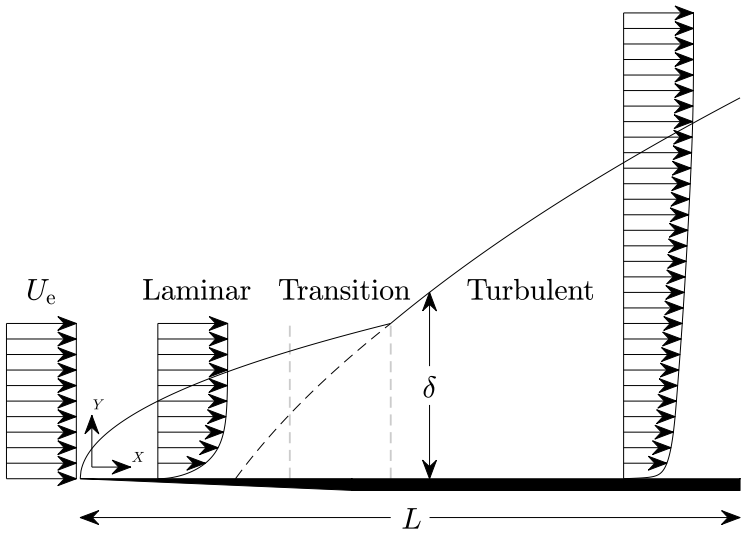

Figure 2-1: Boundary layer on a flat plate (zero pressure gradient) with free stream velocity U_e and plate length L: laminar flow, transition and turbulent flow. δ denotes the boundary layer velocity thickness. The grey vertical dashed lines represent the onset of transition and fully turbulent flow respectively. Euler's equations can be applied to the inviscid free stream where the flow is unaffected ($U = U_e$), whereas the boundary layer equations need to be applied close to the wall surface where $U < U_e$ due to the frictional forces induced by viscosity. The Y-coordinate has been stretched to illustrate the principles.

2-2-1 Free stream Euler Equations

The Navier-Stokes equations reduce to the Euler equations when viscosity can be neglected. This is the case far from the wall surface, outside the viscous region in the free stream, where the gradients in velocity disappear. The Euler equations in compressible form are

$$\rho\left(\frac{\partial u_i}{\partial t}+u_j\frac{\partial u_i}{\partial x_j}\right)=-\frac{\partial p}{\partial x_i}+\rho f_i. \tag{2-12}$$

2-2-2 Prandtl's Laminar Boundary Layer Equations

Prandtl published a famous paper [20] in 1904 in which he dealt with flows of *very low friction*. He showed that a very thin boundary layer exists close to a wall surface due to high velocity gradients, by considering low viscosity high Reynolds-number flows around objects with zero wall slip. With a scaling procedure he arrived at his celebrated boundary layer equations for incompressible flows with constant fluid properties

$$\frac{\partial u}{\partial x}+\frac{\partial v}{\partial y}=0, \tag{2-13}$$

$$u\frac{\partial u}{\partial x}+v\frac{\partial u}{\partial y}=-\frac{1}{\rho}\frac{\partial p}{\partial x}+\nu\frac{\partial^2 u}{\partial y^2}, \tag{2-14}$$

$$\frac{\partial p}{\partial y}=0. \tag{2-15}$$

This system of equations is easier to solve than the full Navier-Stokes equations, since a nonlinear term has disappeared. Rogers [57] gives an elaborate derivation and explanation of a scaling procedure to obtain these boundary layer equations. In short, the following property relations are obtained when assuming a very thin boundary layer δ due to low viscosity in high Reynolds-number flows, compared to the length-scale of the problem L, e.g. plate length:

1. $\delta \ll L$ or $\frac{\delta}{L} \ll 1$;
2. $\mathrm{Re} \gg 1$;
3. $\frac{\delta}{L} \sim \sqrt{\nu} \sim \frac{1}{\sqrt{\mathrm{Re}}}$;
4. $\frac{\partial}{\partial x} \ll \frac{\partial}{\partial y}$; and,
5. $\frac{\partial p}{\partial y}=0$, and thus $\frac{\partial p}{\partial x}=\frac{\partial p_\mathrm{e}}{\partial x}=-\rho_\mathrm{e}u_\mathrm{e}\frac{\partial u_\mathrm{e}}{\partial x}$ (compressible Euler equations).

A very thin boundary layer thus means that diffusion in the x-direction can be neglected compared to diffusion in the y-direction. From the scaling procedure it is found that the laminar boundary layer thickness scales with the inverse of the square root of the Reynolds-number. The most important result is that the free stream imposes the pressure on the boundary layer, since the pressure in the y-direction does not vary. Therefore, the pressure derivative can be substituted in x-direction with the derivative

of the velocity at the boundary layer edge obtained from the compressible Euler equations. Note that these results are only valid for high Reynolds-numbers. In this analysis second-order effects are neglected, such as centrifugal forces induced by wall curvature. Wall curvature can be neglected if the boundary layer thickness is much smaller than the radius of curvature: $\frac{\delta}{R_c} \ll 1$).

2-2-3 Coordinate Transformation

Transformed coordinates $(x, y) \rightarrow (\xi, \eta)$ have been introduced in boundary layer flows to obtain a system of equations that can be solved more easily, and thus reduce computational time [58]. The advantages of a coordinate transformation in boundary layer flow calculations are [4, pp. 260-261,295]:

1. Calculations can be started more easily at a stagnation point or at the leading edge of a flat plate, since the singularity at this point is removed by the transformation;
2. The variation of boundary layer thickness along the surface is removed in zero pressure gradient laminar flows by using the scaling parameter found under item 3 in Sec. 2-2-2 above. It is virtually constant for similar and most nonsimilar laminar flows, but it still changes fast in turbulent flows;
3. Compressibility effects are reduced, or in certain cases completely removed [33,58];
4. A high grid resolution close to the wall is realized by stretching [3] of the y-coordinate close to the wall to capture boundary layer effects in detail, while at the same time reducing the large property gradients; and,
5. The system of partial differential equations is reduced to a system of ordinary differential equations for similar flow cases, e.g. the Falkner-Skan wedge flows [54, 59].

In his later work Cebeci [25, 27, 33, 60, 61], uses a transformation which he refers to as the *compressible Falkner-Skan transformation*, which is therefore also adopted here

$$\mathrm{d}\eta = \sqrt{\frac{u_e}{\nu_e x}}\frac{\rho}{\rho_e}\mathrm{d}y, \tag{2-16}$$

$$\psi(x, y) = \sqrt{\rho_e \mu_e u_e x} f(x, \eta). \tag{2-17}$$

This is a simple and elegant transformation only applying to the y-direction, incorporating all benefits listed above, except for taking into account the flow's pressure gradient (item 5). Similar cases such as the Falkner-Skan wedge flows will hardly ever be encountered in practical situations. Therefore, the system of equations will almost always

be nonsimilar, and thus remain a system of partial differential equations. Leaving the pressure gradient from the coordinate transformation then results in a simpler and easier applicable coordinate transformation for transforming the turbulence model equations, while still retaining the other advantages of the transformation listed above.

By definition, the stream function ψ satisfies continuity and thus for compressible laminar flows this results in

$$\rho u = \frac{\partial \psi}{\partial y} \qquad \text{and} \qquad \rho v = -\frac{\partial \psi}{\partial x}, \tag{2-18}$$

and for turbulent flows (see the derivation of system of equations in section 2-3-3 and section 3-2-1)

$$\bar{\rho}\bar{u} = \frac{\partial \psi}{\partial y} \qquad \text{and} \qquad \overline{\rho v} = -\frac{\partial \psi}{\partial x}. \tag{2-19}$$

The dimensionless stream function f represents the mass flux, its derivative f' is equal to the nondimensional velocity ratio u/u_e inside the boundary layer, and the second derivative f'', called the shear parameter, represents the shear stresses inside the boundary layer. Section 3-2-1 will show the transformed system of equations, and section 3-2-3 will refer to a suitable method for solving this system of equations.

For an overview of coordinate transformations see reference [58]. For descriptions and examples of applications, see references [33, 54, 62]. Appendix E gives an overview of the coordinate transformations used in this thesis.

2-3 Turbulence

The Navier-Stokes equations are the most general equations to describe fluid motion. However, in this general form they cannot be solved in their entire form for most large-scale turbulent flows [63]. Therefore, simplifications need to be made to find a solution. One of the methods to achieve this is by averaging the NS-equations and devising a model for the newly appearing terms that result from it, the Reynolds stresses.

2-3-1 Reynolds-Averaged Navier-Stokes Equations

Assuming all velocity and property terms consist of an average and fluctuating term, substituting these in the NS-equations and then taking the average, one arrives at the Reynolds-averaged Navier-Stokes (RANS) equations. For the compressible case, mass-weighted averaging, also called Favre-averaging, is applied to the velocity and enthalpy

terms, which appear inside the differentials together with the density in the conservative form. The other terms, such as density, pressure, viscosity, heat flux and the stress tensor are time averaged. Fluctuations in the fluid properties viscosity μ, λ, thermal conductivity k, heat capacity c_p and thus the Prandtl-number Pr, are neglected [3, 54]. A time-averaged quantity $\bar{q}$ can be calculated on a time interval Δt starting at reference time t_0 with the integral

$$\bar{q} = \frac{1}{\Delta t} \int_{t_0}^{t_0+\Delta t} q(x_i, t)\, dt. \tag{2-20}$$

The time averaged density and mass-weighted averaged velocity then become for example[2]

$$\rho\,(x_i, t) = \bar{\rho}(x_i) + \rho'(x_i, t), \tag{2-21}$$
$$u\,(x_i, t) = \tilde{u}_i(x_i) + u_i''(x_i, t), \tag{2-22}$$
$$\tilde{u}_i = \frac{\overline{\rho u_i}}{\bar{\rho}}. \tag{2-23}$$

In tensor notation the continuity equation, the Navier-Stokes equations, and the total enthalpy based energy equation, become in conservative form

$$\frac{\partial \bar{\rho}}{\partial t} + \frac{\partial}{\partial x_i}\left(\bar{\rho}\tilde{u}_i\right) = 0, \tag{2-24}$$
$$\frac{\partial}{\partial t}\left(\bar{\rho}\tilde{u}_i\right) + \frac{\partial}{\partial x_j}\left(\bar{\rho}\tilde{u}_i\tilde{u}_j\right) = -\frac{\partial \bar{p}}{\partial x_i} + \frac{\partial}{\partial x_j}\left[\bar{\tau}_{ij} - \overline{\rho u_i'' u_j''}\right], \tag{2-25}$$
$$\frac{\partial}{\partial t}\left(\bar{\rho}\tilde{h}_0\right) + \frac{\partial}{\partial x_j}\left(\bar{\rho}\tilde{h}_0\tilde{u}_j\right) = \frac{\partial \bar{p}}{\partial t} - \frac{\partial \bar{\dot{q}}_i}{\partial x_i} + \frac{\partial}{\partial x_j}\left[\tilde{u}_i\bar{\tau}_{ij} + \overline{u_i''\tau_{ij}} - \overline{\rho h_0'' u_j''}\right]. \tag{2-26}$$

2-3-2 Turbulent Boundary Layer Equations

Following the detailed derivation of Cebeci [4] one arrives at the two-dimensional steady state compressible turbulent boundary layer equations for variable fluid properties in nonconservative form

[2] Notation adopted from Schlichting [3], Cebeci [4, 25, 27, 33, 60, 61] uses a different nomenclature (see footnote on p. 611 in Schlichting [3])

$$\frac{\partial}{\partial x}\left(\bar{\rho}\bar{u}\right)+\frac{\partial}{\partial y}\left(\overline{\rho v}\right)=0, \tag{2-27}$$

$$\bar{\rho}\bar{u}\frac{\partial\bar{u}}{\partial x}+\overline{\rho v}\frac{\partial\bar{u}}{\partial y}=-\frac{\partial\bar{p}}{\partial x}+\frac{\partial}{\partial y}\left[\bar{\mu}\frac{\partial\bar{u}}{\partial y}-\bar{\rho}\overline{u'v'}\right], \tag{2-28}$$

$$\frac{\partial\bar{p}}{\partial y}=0, \tag{2-29}$$

$$\bar{\rho}\bar{u}\frac{\partial\bar{h}_0}{\partial x}+\overline{\rho v}\frac{\partial\bar{h}_0}{\partial y}=\frac{\partial}{\partial y}\left[-\bar{\dot{q}}_{\mathrm{y}}+\bar{u}\bar{\mu}\frac{\partial\bar{u}}{\partial y}-\bar{\rho}\overline{h_0'v'}\right]. \tag{2-30}$$

Recall that it was assumed already that fluid property fluctuations can be neglected in section 2-3-1. Furthermore, Morkovin's hypothesis [3] results in negligible density variations: $\left|\overline{\rho' u' v'}\right| \ll \left|\bar{\rho}\overline{u'v'}\right|$, such that the apparent turbulent stress and conductivity can be rewritten into simpler forms: $\bar{\rho}\overline{u'v'}$ and $\bar{\rho}\overline{h_0'v'}$. Inside the boundary layer it follows from a scaling analysis [4] that the difference between $\tilde{u}$ and $\bar{v}$ can be neglected, but not between $\tilde{v}$ and $\bar{v}$, since the fluctuations v'' are of the same order $O(\delta)$ as v itself, resulting in

$$\bar{\rho}\tilde{v}\equiv\overline{\rho v}=\bar{\rho}\bar{v}+\overline{\rho' v'}=\bar{\rho}\tilde{v}. \tag{2-31}$$

The y-momentum relation for turbulent boundary layer flows reduces to

$$\frac{\partial\bar{p}}{\partial y}=-\frac{\partial}{\partial y}\left(\bar{\rho}\overline{v'v'}\right), \tag{2-32}$$

where the pressure variation $\frac{\partial\bar{p}}{\partial y}$ in the y-coordinate direction is of order 1 ($O(1)$) this time, compared to the laminar case where it is of order $O(\delta)$. Integration gives the pressure variation across the boundary layer to be of order $O(\delta)$, which can still be neglected [4]. Appendix C gives an overview of all assumptions.

The energy equation expressed in total enthalpy (eq. 2-30) then needs to be rewritten in terms of Prandtl- and turbulent Prandtl-number, because the eddy conductivity and the heat flux are defined in terms of static state variable gradients, see references [4, 27]. Rewriting the total enthalpy fluctuation, and substituting for μ_{T} and Pr_{T} gives

$$\bar{\rho}\bar{u}\frac{\partial\bar{h}_0}{\partial x}+\overline{\rho v}\frac{\partial\bar{h}_0}{\partial y}=\frac{\partial}{\partial y}\left[\left(\frac{\mu}{\mathrm{Pr}}+\frac{\mu_{\mathrm{T}}}{\mathrm{Pr}_{\mathrm{T}}}\right)\frac{\partial\bar{h}_0}{\partial y}+\left(\mu\left(1-\frac{1}{\mathrm{Pr}}\right)+\mu_{\mathrm{T}}\left(1-\frac{1}{\mathrm{Pr}_{\mathrm{T}}}\right)\right)\bar{u}\frac{\partial\bar{u}}{\partial y}\right], \tag{2-33}$$

where the static enthalpy is written as

$$\frac{\partial \bar{h}}{\partial y} = \frac{\partial \bar{h}_0}{\partial y} - \bar{u}\frac{\partial \bar{u}}{\partial y}. \tag{2-34}$$

Note that the normal velocity term in the y-direction is neglected here as a consequence of the boundary layer assumptions. Appendix C gives a complete overview of the assumptions made.

2-3-3 Turbulence Model: the Cebeci-Smith Model

A closure model is needed to find a solution for the unknown stress term and the turbulent Prandtl-number in the system of Reynolds averaged boundary layer equations. Such a closure model is called a turbulence model and it consists of several equations and closure coefficients, which can be based both on empirical and theoretical models. The different turbulence models are categorized by the amount of differential equations present. Zero-equation or algebraic models contain zero differential equations and thus consist of algebraic relations only. These models are generally based on the Boussinesq Eddy Viscosity hypothesis and often implement the mixing-length hypothesis [26]. The zero-equation turbulence model developed by Cebeci and Smith [4], the CS-model, is one of these models. This closure model is a semi-empirical system of equations calibrated for two-dimensional steady state turbulent boundary layer flows based on the Eddy Viscosity concept. It also includes an Eddy Conductivity model which is expressed in turbulent Prandtl-number for turbulent convective heat transfer. The turbulent Prandtl-number model is calibrated and validated for different fluids of low, medium and high Prandtl-numbers; namely liquid metals, air and water with additives [4, 64, 65].

2-3-3-1 Eddy Viscosity Model

Eddy viscosity is a term for the apparent viscosity, or turbulent viscosity in analogy with molecular viscosity, with which convective momentum transport can be modeled according to Boussinesq's hypothesis. The transport term that appears on the left side in the RANS equations can be interpreted dimensionally as a stress, and thus it can be added to the stress tensor (eq. 2-25 and 2-28). Boussinesq's hypothesis thus results in

$$-\bar{\rho}\overline{u'v'} = \mu_{\mathrm{T}}\frac{\partial \bar{u}}{\partial y} = \bar{\rho}\nu_{\mathrm{T}}\frac{\partial \bar{u}}{\partial y}. \tag{2-35}$$

The model has been improved and extended several times by Cebeci [25, 27, 33, 60, 61]. The model equations for the eddy viscosity below are taken from Cebeci (2002)[3] [27],

[3] *Convective Heat Transfer* is an excellent book to discover this subject. Unfortunately it contains a few deficiencies in, for example, the eddy viscosity model equations which might confuse the reader. Appendix D gives an explanation and a few corrections. Furthermore, Cebeci uses different nomenclature throughout his texts and thus, for simplicity, the conventional notation used by Schlichting [3] is adopted here as much as possible.

since it gives the most complete description, and the most simple model version suitable for the purpose of this work

$$(\nu_{\mathrm{T}})_{\mathrm{inner}} = L^2 \left|\frac{\partial u}{\partial y}\right| \gamma_{\mathrm{int}}\gamma_{\mathrm{tr}}, \qquad 0 \leq y \leq y_{\mathrm{c}}, \tag{2-36}$$

$$(\nu_{\mathrm{T}})_{\mathrm{outer}} = \alpha \left|\int_0^{\infty} (u_{\mathrm{e}} - u)\,\mathrm{d}y\right| \gamma_{\mathrm{int}}\gamma_{\mathrm{tr}}, \qquad y_{\mathrm{c}} \leq y \leq \infty, \tag{2-37}$$

where $\mu_{\mathrm{T}} = \rho\nu_{\mathrm{T}}$, and all fluid properties and transport properties are averaged local variables, leaving out the bars that indicate averaged properties for clarity. Furthermore,

$$L = l\left[1 - \exp\left(-y/A\right)\right], \qquad l = \kappa y, \tag{2-38}$$

$$A = A^{+}\frac{\nu}{N}\left(\frac{\tau_{\mathrm{w}}}{\rho_{\mathrm{w}}}\right)^{-1/2}\left(\frac{\rho}{\rho_{\mathrm{w}}}\right)^{1/2}, \qquad \tau_{\mathrm{w}} = \mu_{\mathrm{w}}\left.\frac{\partial u}{\partial y}\right|_{\mathrm{w}}, \tag{2-39}$$

$$N = \left[1 - 11.8\left(\frac{\mu_{\mathrm{w}}}{\mu_{\mathrm{e}}}\right)\left(\frac{\rho_{\mathrm{e}}}{\rho_{\mathrm{w}}}\right)^2 p^{+}\right]^{1/2}, \tag{2-40}$$

$$p^{+} = \frac{\nu_{\mathrm{e}}u_{\mathrm{e}}}{u_{\tau}^3}\frac{\mathrm{d}u_{\mathrm{e}}}{\mathrm{d}x}, \qquad u_{\tau} = \sqrt{\frac{\tau_{\mathrm{w}}}{\rho_{\mathrm{w}}}}, \tag{2-41}$$

$$\gamma_{\mathrm{int}} = \left[1 + 5.5(y/\delta)^6\right]^{-1}, \tag{2-42}$$

with closure coefficients (obtained from measurements, see section 3-3)

$$\kappa = 0.40, \qquad A^{+} = 26, \qquad \alpha = 0.0168. \tag{2-43}$$

For prediction of the transition region, while at the same time establishing a numerically smooth transition, the eddy viscosity is gradually increased from zero to one along the transition region by introducing a transitional intermittency factor γ_{tr} that takes into account turbulent formation spots

$$\gamma_{\mathrm{tr}} = 1 - \exp\left[-G_{\mathrm{tr}}\left(x - x_{\mathrm{tr}}\right)\int_{x_{\mathrm{tr}}}^{x}\frac{dx}{u_{\mathrm{e}}}\right], \tag{2-44}$$

$$G_{\mathrm{tr}} = 8.33 \times 10^{-4}\frac{u_{\mathrm{e}}^3}{\nu_{\mathrm{e}}}\mathrm{Re}_x^{-1.34}, \qquad \mathrm{Re}_x = \frac{u_{\mathrm{e}}x}{\nu_{\mathrm{e}}}. \tag{2-45}$$

The closure coefficients; namely 8.33×10^{-4} and -1.34 in equations 2-44 and 2-45, have been calibrated for adiabatic flows only [27].

2-3-3-2 Eddy Conductivity Model

Similar to Boussinesq's hypothesis an eddy conductivity model can be defined for turbulent convective heat transport as function of **static** enthalpy [4]

$$-\bar{\rho}\overline{h'v'} = \bar{\rho}\alpha_{\mathrm{T}}\frac{\partial \bar{h}}{\partial y}. \tag{2-46}$$

This model is rewritten [27] into a more convenient form[4] expressed in the turbulent Prandtl-number $\mathrm{Pr_T} = \nu_{\mathrm{T}}/\alpha_{\mathrm{T}}$ for a general fluid [4, 64, 65]

$$\mathrm{Pr_T} = \frac{\kappa\left[1-\exp\left(-y/A\right)\right]}{\kappa_{\mathrm{h}}\left[1-\exp\left(-y/B\right)\right]}, \tag{2-47}$$

with the turbulent Prandtl-number at the wall defined as

$$\mathrm{Pr_T}\big|_{\mathrm{w}} = \frac{\kappa}{\kappa_{\mathrm{h}}}\frac{B}{A}. \tag{2-48}$$

The turbulent Prandtl-number is a function of molecular (also called laminar) Prandtl-number close to the wall surface, whereas it is a function of turbulent phenomena only further away from the wall

$$B = B^{+}\frac{\nu}{N}\left(\frac{\tau_{\mathrm{w}}}{\rho_{\mathrm{w}}}\right)^{-1/2}\left(\frac{\rho}{\rho_{\mathrm{w}}}\right)^{1/2}, \tag{2-49}$$

$$B^{+} = \frac{B^{++}}{\mathrm{Pr}^{1/2}}, \tag{2-50}$$

$$B^{++} = \sum_{i=1}^{5} C_i\left(\log_{10}\mathrm{Pr}\right)^{i-1}, \tag{2-51}$$

with closure coefficients

$$\kappa_{\mathrm{h}} = 0.44, \quad C_1 = 34.96, \quad C_2 = 28.79, \quad C_3 = 33.95, \quad C_4 = 6.33, \quad C_5 = -1.186, \tag{2-52}$$

where C_1 to C_5 were found by Na and Habib [65] through measurements.

[4] See reference [4] section 6.4 pages 256-257 for a proposed eddy conductivity model similar in form to that of the eddy viscosity model.

2-4 Boundary Layer Characteristics

Boundary layer flows can be characterized by parameters which are referred to as boundary layer characteristics in this thesis. The properties can roughly be divided into three classes: local properties, integral properties and dimensionless groups and coefficients. All are used to characterize the boundary layer for comparison and monitoring of boundary layer behaviour.

2-4-1 Local Boundary Layer Properties

Local properties include the differential parameters in the system of PDEs, fluid properties, transport properties or parameters derived from them. The term local refers to a single specific point inside the boundary layer, including wall surface and boundary layer edge, or to a single station. These properties include:

1. Differential parameters f, u, v, g, p;
2. Fluid and transport properties, e.g. ρ, μ, k, c_{p}, μ_{T};
3. Parameters derived from the above properties, e.g. Chapman-Rubesin parameter C, density ratio c and Pr-number;
4. Pressure Gradient parameters m_i (single value per specific station);
5. Heat Transfer; enthalpy ratio g, or heat flux p at the wall; and,
6. Shear τ, or local skin friction coefficient C_{f}.

2-4-2 Boundary Layer Integral Properties

Integral properties or integral parameters are obtained by integration of a combination of the velocity and density profiles, or in some cases in combination with the enthalpy or temperature profiles, inside the boundary layer and thus represent a single value at each station. These properties generally represent a so-called *boundary layer thickness*, which expresses the losses of a specific property in terms of a shift of the undisturbed free stream from the wall surface. This shift of stream lines along the wall surface hence represents the accumulated losses generated by the surface along the entire upstream flow. The amount of losses generated locally is influenced directly by the free stream conditions at that location, which altogether along the entire wall surface result in the so-called *pressure history*. The local thickness, e.g. the shift, can thus be interpreted as a measure of the accumulated total losses generated by the boundary layer along the flow under the influence of the free stream conditions. The following boundary layer thicknesses are the most common for two-dimensional steady state compressible flows:

$$\delta = y\,(u = 0.99u_\mathrm{e}) \qquad \text{(the only nonintegral thickness)} \tag{2-53}$$

$$\delta^* = \int_0^\infty \left[1 - \frac{\rho u}{\rho_\mathrm{e} u_\mathrm{e}}\right] \mathrm{d}y \qquad (\delta_1) \tag{2-54}$$

$$\theta = \int_0^\infty \left[\frac{\rho u}{\rho_\mathrm{e} u_\mathrm{e}}\left(1 - \frac{u}{u_\mathrm{e}}\right)\right] \mathrm{d}y \qquad (\delta_2) \tag{2-55}$$

$$\delta_\mathrm{kin} = \int_0^\infty \left[\frac{\rho u}{\rho_\mathrm{e} u_\mathrm{e}}\left(1 - \frac{u^2}{u_\mathrm{e}^2}\right)\right] \mathrm{d}y \qquad (\delta_3) \tag{2-56}$$

$$\delta_s = \frac{T_\mathrm{e}}{u_\mathrm{e}^2} \int_0^\delta \left[\frac{\rho u}{\rho_\mathrm{e} u_\mathrm{e}}\,(s - s_\delta)\right] \mathrm{d}y \tag{2-57}$$

which can be characterized as: velocity thickness δ, shift in undisturbed core flow regarding velocity; displacement thickness δ^* or δ_1 (effective shift in streamlines of undisturbed core flow; momentum thickness θ or δ_2, shift in undisturbed core flow regarding momentum; and so on regarding kinetic energy δ_3, entropy δ_s, etc.

The shape factors H_{ij} are derived from these integral properties. H_{12} is the most applied shape factor, often written as $H = \delta^*/\theta$. The form factor H is said to be the most sensitive boundary layer parameter [66]. Future sensitivity studies need to prove if this is also the case for complex organic fluids (see recommendations in Chap. 6).

2-4-3 Dimensionless Groups and Coefficients

Dimensionless groups form a useful tool to characterize and compare physical phenomena. In boundary layer theory discussed in this thesis the following dimensionless groups are of importance:

- $\mathrm{Ec} = \frac{u^2}{h} = \frac{\text{flow kinetic energy}}{\text{enthalpy}}$ Eckert-number;
- $\mathrm{Ma} = \frac{U}{a} = \frac{\text{flow kinetic energy}}{\text{molecule kinetic/internal energy}} = \frac{\text{directed kinetic energy}}{\text{random kinetic energy}}$ Mach-number;
- $\mathrm{Pr} = \frac{\mu c_\mathrm{p}}{k} = \frac{\text{momentum diffusion}}{\text{thermal diffusion}}$ Prandtl-number;
- $\mathrm{Re} = \frac{\rho u}{\mu}$ $[1/\mathrm{m}]$ unit Reynolds-number;
- $\mathrm{Re}_x = \frac{\rho u x}{\mu} = \frac{\text{momentum}}{\text{viscous forces}}$ Reynolds-number;
- $\mathrm{Re}_\theta = \frac{\rho u \theta}{\mu}$ momentum thickness Reynolds-number;
- $\mathrm{St}_x = \frac{\dot{q}_\mathrm{w}}{\rho u \Delta h} = \frac{\text{convective heat transfer}}{\text{thermal capacity}}$ Stanton-number.

And the following coefficients:

- $C_\mathrm{f} = \frac{2\tau_\mathrm{w}}{\rho U^2}$ Local skin fiction coefficient;
- $C_\mathrm{d} = \frac{T\dot{S}_\mathrm{A}}{\rho u^3}$ Loss coefficient [1]; and,
- $r = \frac{T_\mathrm{w} - T_\mathrm{e}}{T_0 - T_\mathrm{e}}$ Recovery factor.

The loss coefficient introduced by Denton [1] expresses the total entropy generated locally, scaled with local properties, for which temperature and density can be chosen at the wall surface or at the boundary layer edge

$$C_\mathrm{d} = \frac{T\dot{S}_\mathrm{A}}{\rho u_\mathrm{e}^3}, \tag{2-58}$$

where

$$\dot{S}_\mathrm{A} = \int_0^\delta \dot{S}_\mathrm{V}\,\mathrm{d}y = \int_0^\delta \frac{1}{T}\tau\frac{\mathrm{d}u}{\mathrm{d}y}\,\mathrm{d}y. \tag{2-59}$$

Denton [1] suggests to choose the wall surface temperature and density since most of the losses are generated close to the wall.

2-5 Transition Prediction Methods

Three gross engineering transition prediction methods are discussed here. Wazzan's H-Re_x-method and Michel's method adapted by Cebeci for gross engineering predictions of transition from laminar to turbulent flow. Finally, Nash-Webber's method for estimating relaminarization: transition back from turbulent to laminar flow.

2-5-1 Wazzan's H-Re_x-method

Wazzan and coworkers [32] introduced an engineering estimate method for the prediction of laminar-turbulent transition location called the H-Re_x-method

$$\log_{10}\left(\mathrm{Re}_{x_\mathrm{tr}}\right) = -40.4557 + 64.8066H - 26.7538H^2 + 3.3819H^3, \qquad 2.1 < H < 2.8. \tag{2-60}$$

When Re_x exceeds $\mathrm{Re}_{x_\mathrm{tr}}$ transition is predicted at that station. The method is based on a theoretical derivation that simplifies the e^9-method. It should be checked with the e^9-method outside the range mentioned above. The correlation is a function of shape factor

H only, and therefore, it takes into account conditions that influence both transition phenomena and shape factor, such as heat transfer, albeit for small variations. The method is applicable to flows with relatively small changes along the surface coordinate (local similarity). The temperature difference $T_\mathrm{w} - T_\mathrm{e}$ should not exceed 23 K in case of heat transfer. Importantly, the method is not valid for large property variations along the surface coordinate, which is typical for airfoils and turbine blades.

2-5-2 Michel's Extended Method

Michel's extended method is introduced as a combination of two methods by Cebeci [4, 33], where the range of Michel's method was extended by Cebeci [67] to arrive at the following correlation

$$\mathrm{Re}_{\theta_\mathrm{tr}} = 1.174\left(1 + \frac{22400}{\mathrm{Re}_{x_\mathrm{tr}}}\right)\mathrm{Re}_{x_\mathrm{tr}}^{0.46}, \qquad 0.1 \times 10^6 < \mathrm{Re}_x < 40 \times 10^6, \tag{2-61}$$

which is the point of intersection of two curves. When Re_θ exceeds $\mathrm{Re}_{\theta_\mathrm{tr}}$ transition is predicted at that station. The method is developed by Cebeci and coworkers [67] for two-dimenional incompressible flows over curved bodies. Note that this is thus a useful correlation for airfoils and turbine blades, which are characterized by strong property variations along the surface coordinate.

2-5-3 Nash-Webber's Relaminarization Prediction Method

Nash-Webber [34] introduced an engineering prediction method for the prediction of relaminarization inside nozzles expanding air

$$K = \frac{\mu_\mathrm{w}}{\rho_\mathrm{w} u_\mathrm{e}^2}\frac{\mathrm{d}u_\mathrm{e}}{\mathrm{d}x}, \tag{2-62}$$

$$\mathrm{Re}_{\theta,\mathrm{w}} = \frac{\rho_\mathrm{e} u_\mathrm{e}\theta}{\mu_\mathrm{w}}, \tag{2-63}$$

$$K = 1.2 \times 10^{-6} + 1.1 \times 10^{-10}\mathrm{Re}_{\theta,\mathrm{w}} + 10^{-13}\mathrm{Re}_{\theta,\mathrm{w}}^2. \tag{2-64}$$

Relaminarization is likely to occur when the value of the pressure gradient K is larger than the value predicted by the correlation above. Despite the method is based on a wide range of measurements, the method only gives a gross estimate, since the phenomena behind relaminarization were, and still are, not yet understood[5]. The method is valid for compressible adiabatic air flows along surfaces with negligible curvature. The applicability of the method to flows including heat transfer was not investigated yet by Nash-Webberat and Oates at the time of publication.

[5] See recent work of Bader [31].

2-6 Thermophysical Model

A thermophysical model describes the thermodynamic state variables, transport properties and fluid properties for variable fluid property flows with the Equation of State (EoS), transport property models and fluid property models or relations respectively. The EoS relates the state variables, such that the density can be related to the pressure and temperature field. Transport models and fluid property relations also predict properties based on state variables, mostly on the temperature field alone. The velocity field is said to be coupled to the temperature field when the fluid properties are a function of one or more thermodynamic state variables. That is, the solution of the momentum equation, the velocity field, is coupled with the solution of the energy equation, the temperature, or here, the total enthalpy field, through the fluid and transport properties. Variable fluid property flows are considered compressible flows when changes in density become larger than 5% [68]. This section discusses a selection of thermophysical models. First, the microscopic scale at molecular level is discussed shortly. From this, the ideal gas model follows together with complementing transport and fluid property models. Lastly, more general models are treated which take into account the behaviour of complex organic fluids.

2-6-1 The Molecular Model

On a microscopic level molecules randomly move around and collide with each other in binary or even group collisions. The collisions are not perfect and they occur randomly, causing the molecules to deform, spin and engage with other molecules. Along their path they are being attracted to or repelled from each other through intermolecular forces. The different degrees of freedom; namely translational, rotational and vibrational, store the molecule's kinetic energy in the form of internal energy. This internal energy is *communicated* by the collisions between molecules. The pressure intensity is the average force exerted by the molecular collisions with the wall, and it is proportional to the translational molecular kinetic energy. It is lowered by attractive intermolecular forces. The absolute temperature is a measure of the average random velocity of the molecules, and it is proportional to their translational kinetic energy.

In order to work with a fluid without considering its molecular properties a model is needed capturing the *average* behaviour of the molecules as a group. The continuum hypothesis states that the microscopic molecular structure may be replaced by a continuum that makes it possible to deal with the fluid on a macroscopic scale [69]. This holds true as long as the amount of molecules is large enough and the intermolecular distance is not too large. Namely, both factors cause frequent collisions such that equilibrium is reached fast according to the principle of quasi-equilibrium or local state: departures from equilibrium are small. The fluid properties are then assumed to be represented by the average statistical properties inside an elementary fluid volume which size is taken in the lower limit, with Knudsen-number close to zero. In other words, the mean free

path of the molecules is much smaller than the size of the volume: $\mathrm{Kn} = l_{\mathrm{mfp}}/L \sim 0$.

2-6-2 The Ideal Gas Model

The ideal gas model is a simplified model representing the behaviour of a gas. In addition to the continuum hypothesis, the kinetic theory of gases forms the basis of the ideal gas model by making further simplifying assumptions on the behaviour of the molecules in a gas on a microscopic level. The theory states [70]:

1. Size of molecules is small relative to their distance apart;
2. Molecules are in constant random motion;
3. Frequent collisions occur between molecules; and,
4. Ordered motion can be superimposed on random motion.

In the ideal case the molecules do not occupy space and hence their volume can be neglected relative to their distances apart. Due to their large distance apart, there is no interaction between the molecules in the form of intermolecular forces, and hence molecules move in straight lines. The only interactions present are perfectly elastic binary collisions which take place instantaneously. In reality these assumptions are approached in the limit of a low pressure and high temperature gas. A low density gas has large intermolecular distances, and in a high temperature gas intermolecular forces become smaller compared to the kinetic energy of the molecules [71]. The internal energy is a function of translational energy only, and thus it is linear. Therefore, the internal energy depends on temperature only, and the temperature is a measure of the average random motion kinetic energy of the molecules.

2-6-2-1 Equation of State for an Ideal Gas

The state variables are related through an Equation of State (EoS). The EoS hence relates the state variables pressure and density, which is needed to complement the ME and EE. With the previous assumptions, of which the two most important are: molecules do not occupy space and only interact through perfect binary collisions, the following relation between state variables can be found, which turns out to be valid in practice for low pressure and high temperature limits [71]

$$pv = R_{\mathrm{sp}}T \qquad \text{or} \qquad p = \rho R_{\mathrm{sp}}T, \tag{2-65}$$

with $R_{\mathrm{sp}} = R_0/M$, where R_0 is the universal gas constant and M is the molecular weight. From this *ideal* gas model it follows that the internal energy and enthalpy become functions of temperature only [72]

$$e = e\left(T\right) \qquad \text{and} \qquad h = h\left(T\right). \tag{2-66}$$

This can also be explained as follows [73]: the internal energy is a function of the translational, rotational and vibrational energy stored in the molecule. Since the molecules are far apart, the intermolecular forces can be neglected and thus do not contribute to the internal energy, leaving the internal energy as a linear function of temperature only.

2-6-2-2 Transport Property Models

Transport properties are the coefficients related to transport of momentum, dynamic viscosity μ; heat, thermal conductivity k; or mass (not considered here). These coefficients relate the diffusivity to a property gradient. These properties are not state properties, and thus transport models are needed to determine their values.

Sutherland's Law is such a model which was devised to predict the transport properties viscosity and thermal conductivity

$$\frac{\mu}{\mu_0} \approx \left(\frac{T}{T_0}\right)^{3/2} \frac{T_0 + S_\mu}{T + S_\mu}, \tag{2-67}$$

$$\frac{k}{k_0} \approx \left(\frac{T}{T_0}\right)^{3/2} \frac{T_0 + S_k}{T + S_k}. \tag{2-68}$$

The equations and closure coefficients were taken from White [54]. Note that the reference temperature T_0 for viscosity and thermal conductivity can differ for a fluid.

2-6-2-3 Fluid Property Relations

The thermophysical model is further complemented with relations to model fluid properties. In the case of an ideal gas, two assumptions can be made in relation to the constant pressure heat capacity $c_\mathrm{p} = \left.\frac{\partial h}{\partial T}\right|_p$ resulting in the definitions of:

1. Calorically perfect ideal gas: $c_\mathrm{p} = \text{constant}$; and,
2. Calorically imperfect (thermally perfect) ideal gas: $c_\mathrm{p} = c_\mathrm{p}(T)$.

Case 1 assumes constant specific heats, whereas case 2 considers both specific heats as function of temperature alone, since $R_\mathrm{sp} = c_\mathrm{p} - c_\mathrm{v} = \text{constant}$. The specific heat at constant pressure can be expressed in temperature through a polynomial, which allows the specific heat ratio γ to be calculated from c_p only

$$c_{\mathrm{p}}(T) = a_1 + a_2 T + a_3 T^2 + a_4 T^3, \qquad \gamma = \frac{c_{\mathrm{p}}}{c_{\mathrm{v}}} = \frac{c_{\mathrm{p}}}{(c_{\mathrm{p}} - R_{\mathrm{sp}})}. \tag{2-69}$$

The Speed of Sound (SoS) can be determined from

$$a(T) = \sqrt{\gamma(T) R_{\mathrm{sp}} T}. \tag{2-70}$$

Note that γ is a constant in case of assumption 1, or a function of temperature in case of assumption 2.

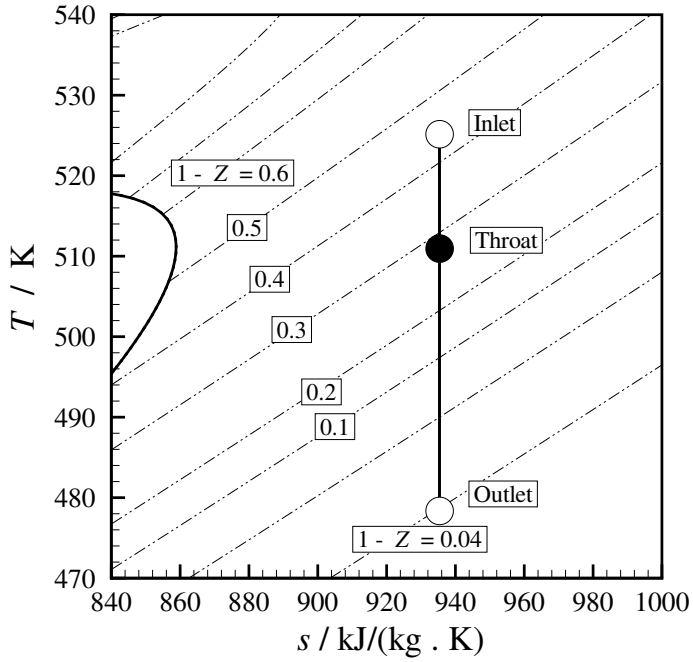

Figure 2-2: The volume departure function $1 - Z$, with compressibility factor $Z = \frac{pv}{RT}$, depicting the departure from ideal gas behaviour of MM plotted as contours in the Ts-diagram. The lower-right region represents the ideal gas range, whereas the departure from ideal gas increases towards the area in the vicinity of the critical point. An isentrope is shown along which an expansion takes place from the dense gas region, or nonideal gas range, towards ideal gas. Taken from Ref. [11].

2-6-3 Nonideal Gas

Contrary to an ideal gas, the molecules of a nonideal gas do occupy space and do interact with each other through intermolecular forces. These forces can be of repulsive or attractive nature. Instead of collisions between rigid molecules, there are *encounters* of two or multiple nonrigid molecules [74], hitting each other generally off-center. These

phenomena result in departure from the ideal gas Law. The resulting *nonideality* can be characterized by several parameters. One of them is the Fundamental derivative of Gas Dynamics [75]

$$\Gamma \equiv 1 + \frac{\rho}{a}\left(\frac{\partial a}{\partial \rho}\right)_s, \tag{2-71}$$

where a is the Speed of Sound and defined as

$$a \equiv \sqrt{\left(\frac{\partial p}{\partial \rho}\right)_s}. \tag{2-72}$$

For an ideal gas the Fundamental derivative reduces to $\Gamma = \frac{\gamma+1}{2}$, where γ is the specific heat ratio (eq. 2-69).

The Fundamental derivative is a measure of nonideality expressed in the behaviour of the constant entropy contours close to the critical point. A more practical parameter which directly indicates ideal gas departure is the compressibility factor

$$Z = \frac{v}{v_0} = \frac{p_0 v}{R_{\text{sp}} T_0} = \frac{pv}{R_{\text{sp}} T}, \tag{2-73}$$

where the subscript '0' denotes the two state variables in an ideal gas, and R_{sp} is the specific gas constant defined by $R_{\text{sp}} = R_0/M$, with R_0 the universal gas constant and the molecular weight M. Z relates the volume of a nonideal gas to the ideal gas volume considering the same state variables p and T. Departure from one means that attractive or repulsive intermolecular forces influence the volume of the gas. Thus, by definition Z is equal to one for an ideal gas without intermolecular interaction other than perfect binary collisions. The departure function $1 - Z$ then indicates the amount of departure from ideal gas, where zero indicates zero departure ($Z = 1$). Figure 2-2 depicts contour lines of the departure function $1 - Z$, where the dark blue area between 0 and 0.1 represents the ideal gas range. $1 - Z$ decreases closer to the critical point where departure is the highest.

The denser the gas, the larger the departure, which results in the commonly accepted term *dense gas*. A majority of gases in reality behave in a more complex way than ideal gas air. Next to the departure from ideal gas this also includes molecular dissociation and ionization at higher temperatures in, for example, the hypersonic flow regime. However, this thesis considers ideal gas departure only which is caused by molecular interactions. In addition, large changes in transport properties close to the critical point are considered. Hence, the term nonideal gas introduced here refers especially to departure from ideal gas and large changes in fluid properties.

2-6-3-1 Equations of State for a Nonideal Gas

For the simulation of flows in the dense gas region the EoS is required to take into account departure from ideal gas. Van der Waals introduced the first cubic equation of state (third-degree in volume) by adding two factors to the ideal gas equation of state: the volume b occupied by the molecules, and an attraction factor a for intermolecular forces

$$p = \frac{R_{\text{sp}}T}{v-b} - \frac{a}{v^2}. \tag{2-74}$$

2-6-3-2 Peng-Robinson-Stryjek-Vera Equation of State

Modern cubic equations of state based on this principal are for example the Peng-Robinson-Stryjek-Vera (PRSV) equation of state, where a consists of several functions to describe molecular properties

$$p = \frac{R_{\text{sp}}T}{v-b} - \frac{a}{v^2+2bv-b^2}, \tag{2-75}$$

$$a = \left(\frac{0.457235R_{\text{sp}}^2T_{\text{c}}^2}{p_{\text{c}}}\right)\alpha, \tag{2-76}$$

$$b = \frac{0.077796R_{\text{sp}}T_{\text{c}}}{p_{\text{c}}}, \tag{2-77}$$

$$\alpha = \left[1+\kappa\left(1-\sqrt{T_{\text{r}}}\right)\right]^2, \tag{2-78}$$

$$\kappa = \kappa_0 + \kappa_1\left(1+\sqrt{T_{\text{r}}}\right)(0.7-T_{\text{r}}), \tag{2-79}$$

$$\kappa_0 = 0.378893 + 1.4897153\omega - 0.17131848\omega^2 + 0.0196554\omega^3. \tag{2-80}$$

This EoS has been improved by Van der Stelt [46] for numerical smoothness by substitution of κ by

$$\kappa = \kappa_0 + \kappa_1\left(\sqrt{[A-D(T_{\text{r}}+B)]+E} + A - D(T_{\text{r}}+B)\right)\sqrt{T_{\text{r}}+C}. \tag{2-81}$$

Departure functions can be derived from the fundamental thermodynamic relations that estimate the departure from ideal gas for nonideal gas fluid properties or state variables with the given EoS. Differentiating between ideal gas and the contribution of nonideal gas phenomena, the following departure functions can be derived in the most suitable form for use with the iPRSV EoS [14, 76, 77]. The departure functions are for volume, enthalpy, isobaric specific heat and entropy respectively

$$1 - Z, \tag{2-82}$$

$$h(P,T) - h^{\mathrm{IG}}(P,T) = R_{\mathrm{sp}}T(Z-1) + \int_{v=\infty}^{v=v(P,T)} \left[T\left(\frac{\partial P}{\partial T}\right)_v - P \right] \mathrm{d}v, \tag{2-83}$$

$$c_{\mathrm{p}}(P,T) - c_{\mathrm{p}}^{IG}(P,T) = R_{\mathrm{sp}}T \int_{v=\infty}^{v=v(P,T)} \left[T\left(\frac{\partial^2 P}{\partial T^2}\right)_v \right]_T \mathrm{d}v - \frac{T\left(\frac{\partial P}{\partial T}\right)_v^2}{\left(\frac{\partial P}{\partial v}\right)_T} - R_{\mathrm{sp}}, \tag{2-84}$$

$$s(P,T) - s^{\mathrm{IG}}(P,T) = R_{\mathrm{sp}} \ln Z + \int_{v=\infty}^{v=v(P,T)} \left[T\left(\frac{\partial P}{\partial T}\right)_v - \frac{R_{\mathrm{sp}}}{v} \right] \mathrm{d}v. \tag{2-85}$$

The transport properties can be predicted by, for example, a multiparameter method introduced by Chung and coworkers [78], which takes into account molecular properties that influence departure. The constant pressure specific heat c_{p} can be modelled by a (more complex) polynomial, as in the case of an ideal gas.

2-6-3-3 Span-Wagner Multiparameter Equation of State

The Span-Wagner multiparameter EoS [35–38] is a different type of EoS based on the departure function for specific Helmholtz free energy

$$\alpha(\delta,\tau) = \alpha^0(\delta,\tau) + \alpha^{\mathrm{r}}(\delta,\tau), \tag{2-86}$$

with reduced density $\delta = \rho/\rho_{\mathrm{c}}$ and inverse reduced temperature $\tau = T_{\mathrm{c}}/T$. The superscripts '0' and 'r' denote *ideal gas* and *real gas* respectively. The *real gas* term is an empirical relation that consists of a summation of terms fitted to experimental data. The state variables and fluid properties are all obtained by derivatives and functions of the specific Helmholtz free energy.

2-7 Summary

Summarizing, the SoE is derived for two-dimensional steady state boundary layer flows for general thermophysical properties. The SoE consists of the Reynolds-Averaged boundary layer equations for two-dimensional geometries immersed in steady state flows. Recall that the fluctuations in fluid properties and transport properties have been neglected, and that the Mach fluctuations were assumed to be smaller than 1 (Morkovin's hypothesis). The simplified SoE resulting from the conservation of mass, momentum and energy is

$$\frac{\partial}{\partial x}\left(\bar{\rho}\bar{u}\right) + \frac{\partial}{\partial y}\left(\overline{\rho v}\right) = 0, \tag{2-27}$$

$$\bar{\rho}\bar{u}\frac{\partial \bar{u}}{\partial x} + \overline{\rho v}\frac{\partial \bar{u}}{\partial y} = -\frac{\partial \bar{p}}{\partial x} + \frac{\partial}{\partial y}\left[\bar{\mu}\frac{\partial \bar{u}}{\partial y} - \bar{\rho}\overline{u'v'}\right], \tag{2-28}$$

$$\frac{\partial \bar{p}}{\partial y} = 0, \tag{2-29}$$

$$\bar{\rho}\bar{u}\frac{\partial \bar{h}_0}{\partial x} + \overline{\rho v}\frac{\partial \bar{h}_0}{\partial y} = \frac{\partial}{\partial y}\left[\left(\frac{\mu}{\mathrm{Pr}} + \frac{\mu_\mathrm{T}}{\mathrm{Pr}_\mathrm{T}}\right)\frac{\partial \bar{h}_0}{\partial y} + \left(\mu\left(1 - \frac{1}{\mathrm{Pr}}\right) + \mu_\mathrm{T}\left(1 - \frac{1}{\mathrm{Pr}_\mathrm{T}}\right)\right)\bar{u}\frac{\partial \bar{u}}{\partial y}\right]. \tag{2-33}$$

An algebraic turbulence model, the CS-model, was added to solve for the, in this case, single turbulent shear stress. The model also includes a turbulent Prandtl-number model for modelling the Eddy Conductivity. Fluid property models, transport property models and equations of state were discussed, ranging from simple ideal gas to state-of-the-art models including ideal gas departure and complex fluid and transport property models. The implementation of a combination of these models in a computer program will be the topic of next chapter. The combination(s) of models will be used in the chapters thereafter for several verification and validation test cases, and for deterministic preliminary predictive simulations.

Chapter 3

A Program for Simulation of Two-Dimensional Steady State Boundary Layers

In the previous chapter the underlining theory was discussed which resulted in the SoE (eq. 2-27 to 2-29 and 2-33) to be solved for two-dimensional steady state boundary layer flows with variable fluid properties. This chapter introduces the computer program that was developed and used in this work for the solution of this SoE. The structure is as follows. First, in Sec. 3-1 the method chosen is explained, including the choice of turbulence model. Second, Sec. 3-2-1 introduces the SoE in transformed form using the coordinate transformation from Sec. 2-2-3. The next section, Sec. 3-2-2 analyzes the coupling of the ME and EE equations, and the characteristics of this transformed SoE. Section 3-2 discusses the solution method that was implemented. Then, Sec. 3-3-1 lists important assumptions and simplifications made, their consequences, and an evaluation of the turbulence model's closure coefficients. Lastly, the structure of the computer program and its various input types, output and simulation options is presented in Sec. 3-4.

3-1 Choice of Turbulence Model and Solution Method

According to Cho & Aessopos [58] no analytical solutions are available for the boundary layer equations with heat transfer and variable fluid properties, and therefore numerical methods are required for their solution. Wilcox [26] states that by definition a compressible flow is one in which significant density changes occur, even when pressure changes

are small. The CS-method [27] is the solution method adopted here, which includes Keller's Box-method [23] for the solution of the discretized SoE (eq. 3-1 to 3-5).

To investigate the effects of fluid properties on the boundary layer in compressible flows, especially complex molecular fluid properties, a model is needed that is detailed enough to capture the physical phenomena encountered, and at the same time simple enough to understand how these properties influence the boundary layer behaviour. Specifically, a simple model is required to understand the effects of fluid properties on turbulence properties, which also makes fast calculations possible.

Wilcox [26] states than an ideal model should introduce the minimum amount of complexity while capturing the essence of the relevant physics. Furthermore, if known how much detail is needed, the level of complexity of the model follows. In other words, *simplicity is the ultimate form of sophistication.*

Wilcox [26] also states that algebraic models are the simplest and easiest to implement of all turbulence models. Since they are conceptually very simple and rarely cause unexpected numerical difficulties. In addition, they are easy to implement in existing laminar codes, since no new ODE's or PDE's need to be solved. Because algebraic models are so easy to use, they should be replaced only where superior alternatives are available.

Therefore, an algebraic turbulence model should be utilized first for the simulation of boundary layer flows of complex molecular fluids. There are many algebraic turbulence models. Since this type of turbulence model is incomplete [26,63] a length-scale based on the mixing-length must be chosen which characterizes the type of flow, e.g. wall-bounded flows. In this case, 2D steady state boundary layer flows.

Wilcox [26] discusses three different algebraic turbulence models for wall-bounded flows: The Cebeci-Smith model (CS-model), the Baldwin-Lomax model, and the Johnson-King model. The Baldwin-Lomax model is designed to calculate boundary layer properties in complex wall-bounded flows without the need to know the boundary layer thickness beforehand, which is beneficial in Finite Volume Methods. The Johnson-King model was developed to predict the boundary layer in strong adverse PG flows[1]. The Cebeci-Smith model was specifically designed for predicting the boundary layer and contains the least amount of closure coefficients required.

The CS-model is the most popular algebraic turbulence model to the best knowledge of the author. It was developed for incompressible flows first [79], and later extended to compressible flows [80]. Many publications for its use and applications have followed since, amongst others references [4, 24, 25, 27, 33, 60, 61, 64, 67, 81, 82]. Several specific flow types, within steady state 2D flows, were taken into account by (re)calibrating the closure coefficients, or even fitting them to separate relations [4, 24, 25]. Even more interesting is the Eddy Conductivity model [64], which was calibrated for a large range

[1]Note that the term *strong pressure gradient* always refers to adverse pressure gradients that in the end cause flow separation. High pressure gradients inside highly supersonic nozzle expansions have not been considered in general.

of fluids of different (molecular) Prandtl-numbers [4,65]. Therefore, the author does not know of any model that is more suitable for simulation of turbulent boundary layers in complex fluid flows than the CS-model.

Wilcox [26] supports the popularity of the CS-model. He specifically mentions that the Cebeci-Smith model has been applied to a *wide range of boundary layer flows* and that it *has enjoyed a great deal of success*. Furthermore, he quantifies the performance of the model by calling it *reasonably accurate* for favorable pressure gradients and for mild adverse pressure gradients. And by stating that "because the model has been fine tuned for boundary layer flows, differences between computed and measured velocity profiles generally are small. However, integral parameters such as momentum thickness and shape factor often show 10% differences from measured values." Furthermore, he mentions that the CS-model is capable of reproducing skin friction and velocity profiles *faithfully* for incompressible turbulent boundary layers provided the pressure gradient is not too strong[1]. Velocity profiles are generally accurate within 2% compared with measured profiles.

Users need to be aware of the limitations when using algebraic turbulence models, because of their incompleteness [26]. Since they have been fine tuned for specific flow types, e.g. steady state boundary layers along smooth surfaces, the use of these models is bounded to these types of flows. Furthermore, the models are bounded to the range of flows for which the closure coefficients are calibrated. This points out the need of validation of the turbulence model for the highly supersonic and highly compressible flows discussed in this work.

If validation points out that the region of interest is (too) far from the flow range used to calibrate the closure coefficients, the model is simple enough to be recalibrated with sufficient data of high quality. In addition, recalibration is possible specifically for fluids other than air, such as MM, if needed. Another advantage of the CS-model used here, is that there are only few closure coefficients, of which the current closure coefficients rely on a large and reliable database already (see Sec. 3-3-3). The mathematical form of the CS-model has proven to be suitable already for the flow type at hand. In addition, many publications are available, and many easily reproducible test cases are available that have already proven its capabilities, e.g. Coles [83].

However, no proven validation cases were yet found in literature that cover the entire boundary layer development on the curved-wall surface of a supersonic nozzle. Therefore, this will be addressed in Chap. 4. Furthermore, all test cases deal with ideal gas, and most test cases deal with incompressible flows. Although the model has been proven to work for compressible flows, its basis originates from incompressible flow theory and model development. In addition, only one highly supersonic test case measured inside a nozzle is known to the author. Smith and Cebeci [80, Fig. 25] validated the state-of-the-art model in 1967 with experimental data obtained from a flat wall inside a 2D nozzle, and showed that the skin friction was predicted with *very good agreement* for Mach-number 2.8. This stresses the need of thorough validation and quantification of the turbulence model for highly supersonic and highly compressible flows, characterized

by large property gradients.

For the above mentioned reasons the CS-model was chosen and adopted here. Cebeci and Smith [4] not only introduced a succesful turbulunce model, but also a successful approach to the numerical solution of the laminar and turbulent boundary layer equations, which they called the CS-method. The method includes Keller's Box-method [23] for discretizing and solving the SoE. The CS-method is extensively discussed in *Analysis of Turbulent Flows* [4] including an Eddy Viscosity model, the algebraic turbulence model called the CS-model, and an Eddy Conductivity model in the form of a Turbulent Prandtl-number. Cebeci [27] presents in the book *Convective Heat Transfer* a FORTRAN program, included on a DVD, for solving the compressible two-dimensional steady state boundary layer equations including heat transfer for calorically perfect ideal gas air. The dynamic viscosity is calculated with Sutherland's Law. Furthermore, the program includes an Eddy Conductivity model in the form of a constant turbulent Prandtl-number (= 0.9). Also here, the Keller's Box-method is used to solve the discretized SoE, but now in a more effective and efficient way. The FORTRAN program is shown being capable of simulating low Mach-number incompressible stagnation point flow over a NACA0012 airfoil. The test case includes transition from laminar to turbulent flow with a predefined transition location and, finally, separation close to the leading edge.

This FORTRAN program has been chosen to be adopted here. The code is simple, easy and efficient and therefore it can readily be adapted and tailored to the specific needs in this work. It has been implemented in MATLAB and modified. Above all, its capabilities have been extended, as described in Sec. 3-4, and adapted to meet the current objectives.

3-2 Solution Method

The CS-method, implementing the CS-model, introduced in the previous section is further described here for the solution of the laminar and turbulent boundary layer equations with general fluid properties. First, the complete mathematical model is derived in Sec. 3-2-1. Second, the model's characteristics are derived and interpreted on a physical basis in Sec. 3-2-2. Last, Sec. 3-2-3 gives a detailed description of the solution method.

3-2-1 Mathematical Model: System of Equations

The resulting SoE as obtained in Sec. 2-3-2 for the conservation of mass (eq. 2-27), momentum (eq. 2-28 and 2-29) and energy (eq. 2-33), is a system of parabolic partial differential equations (PDE's). This means that it is characterized as a mixed problem of boundary conditions and initial values. Such a problem is solved using a so-called *marching method*. Initial values need to be prescribed at the start (first station), and

boundary conditions need to be prescribed along the path on both sides (wall and edge in this case), leaving the *end* open towards which is being *marched*.

This SoE and its boundary conditions are transformed using the coordinate transformation from section 2-2-3 into a third-order PDE system. The initial values at the leading edge are calculated by the program itself, directly in transformed form. The resulting system can be rewritten by defining differential parameters $u = f'$, $v = f''$ and $p = g'^2$ into the following system of two PDE's and three ODE's

$$\left(bf''\right)' + m_1 f f'' + m_2\left[c - \left(f'\right)^2\right] = x\left(f'\frac{\partial f'}{\partial x} - f''\frac{\partial f}{\partial x}\right), \tag{3-1}$$

$$f'' = v, \tag{3-2}$$

$$f' = u, \tag{3-3}$$

$$\left(eg' + df'f''\right)' + m_1 f g' = x\left(f'\frac{\partial g}{\partial x} - g'\frac{\partial f}{\partial x}\right), \tag{3-4}$$

$$g' = p, \tag{3-5}$$

$$\tag{3-6}$$

where u is the differenttial parameter defined as the velocity ratio with respect to the boundary layer edge $u = \frac{u}{u_e}$. The parameters and coefficients are defined as [27, 33][3]

[2]It needs to be stressed that the differential parameters u, v and p are different from the velocities in the x- and y-direction, or the pressure. This notation is still adopted, because it is used by Cebeci in this way consistently.

[3]The last two equations (3-13 and 3-14) were obtained from reference [33, p. 359], since they were omitted in reference [27].

$$b = C\left(1+\nu^{+}\right), \qquad \nu^{+} = \frac{\nu_{\mathrm{T}}}{\nu}, \tag{3-7}$$

$$c = \frac{\rho_{\mathrm{e}}}{\rho}, \qquad C = \frac{\rho\mu}{\rho_{\mathrm{e}}\mu_{\mathrm{e}}}, \qquad C_{\mathrm{e}} = \frac{\rho_{\mathrm{e}}\mu_{\mathrm{e}}}{\rho_0\mu_0}, \tag{3-8}$$

$$d = \frac{Cu_{\mathrm{e}}^2}{h_{0,\mathrm{e}}}\left[1-\frac{1}{\mathrm{Pr}}+\nu^{+}\left(1-\frac{1}{\mathrm{Pr}_{\mathrm{T}}}\right)\right], \tag{3-9}$$

$$e = \frac{C}{\mathrm{Pr}}\left(1+\nu^{+}\frac{\mathrm{Pr}}{\mathrm{Pr}_{\mathrm{T}}}\right), \tag{3-10}$$

$$f' = \frac{u}{u_{\mathrm{e}}}, \tag{3-11}$$

$$g = \frac{h_0}{h_{0,\mathrm{e}}}, \tag{3-12}$$

$$m_1 = \frac{1}{2}\left[1+m_2+m_3\right] = \frac{1}{2}\left[1+m_3+m_4+m_5\right], \tag{3-13}$$

$$m_2 = \frac{x}{u_{\mathrm{e}}}\frac{\mathrm{d}u_{\mathrm{e}}}{\mathrm{d}x} = m_4+m_5 = \frac{m_4}{1+(\Gamma-1)\,\mathrm{Ma}_{\mathrm{e}}^2}, \tag{3-14}$$

$$m_3 = \frac{x}{C_{\mathrm{e}}}\frac{\mathrm{d}C_{\mathrm{e}}}{\mathrm{d}x}, \tag{3-15}$$

$$m_4 = \frac{x}{\mathrm{Ma}_{\mathrm{e}}}\frac{\mathrm{dMa}_{\mathrm{e}}}{\mathrm{d}x}, \tag{3-16}$$

$$m_5 = \frac{x}{a_{\mathrm{e}}}\frac{\mathrm{d}a_{\mathrm{e}}}{\mathrm{d}x}. \tag{3-17}$$

Note that m_3 to m_5 and C_{e} are newly introduced in this work, which will be clarified later. In addition, the parameter u is multiple defined, which is confusing and therefore deserves the special attention of the reader.

The boundary conditions for the ME and the energy equation for a flow along a solid surface with an isentropic free stream or core flow are

$$u(x,0) = u_{\mathrm{w}}(x) = 0, \tag{3-18}$$

$$v(x,0) = v_{\mathrm{w}}(x) = 0, \tag{3-19}$$

$$u(x,y_{\mathrm{e}}) = u_{\mathrm{e}}(x), \tag{3-20}$$

which includes zero velocity (zero slip condition) and zero mass transfer at the wall. And for the EE

$$h_0(x,0) = h_{0,\mathrm{w}}(x) \qquad \text{or} \qquad \frac{\partial h_0(x,0)}{\partial y} = -\dot{q}_{\mathrm{w}}(x)\frac{\mathrm{Pr}_{\mathrm{w}}(x)}{\mu_{\mathrm{w}}(x)}, \tag{3-21}$$

$$h_0(x,y_{\mathrm{e}}) = h_{0,\mathrm{e}}(x), \tag{3-22}$$

where the wall enthalpy or the wall heat flux can be given as an input. These boundary conditions become in transformed form for the complete transformed SoE

$$f(x,0) = 0, \tag{3-23}$$
$$u(x,0) = 0, \tag{3-24}$$
$$u(x,\eta_\mathrm{e}(x)) = 1, \tag{3-25}$$
$$g(x,0) = g_\mathrm{w}(x), \qquad \text{or} \qquad p(x,0) = p_\mathrm{w}(x), \tag{3-26}$$
$$g(x,\eta_\mathrm{e}(x)) = 1. \tag{3-27}$$

Recall that $p = g'$ and $g = h_0/h_{0,\mathrm{e}}$, and that we use the velocity ratio $u = \frac{u}{u_\mathrm{e}}$ here once again. The initial conditions in transformed form include (a guess of) the initial profiles of all of the differential parameters for the first station[4]

$$f(0,\eta) = f_0(\eta), \tag{3-28}$$
$$u(0,\eta) = u_0(\eta), \tag{3-29}$$
$$v(0,\eta) = v_0(\eta), \tag{3-30}$$
$$g(0,\eta) = g_0(\eta), \tag{3-31}$$
$$p(0,\eta) = p_0(\eta). \tag{3-32}$$

The CS-model from section 2-3-3 is a function of the velocity field and the fluid property coefficients c and C and the Reynolds-number along the boundary layer edge. It becomes in dimensionless form after transformation[5]

$$\left(\nu^+\right)_\mathrm{inner} = \kappa^2 \frac{1}{C}\frac{1}{c^3}\sqrt{\mathrm{Re}_x} I^2 v \left[1 - \exp\left(-y/A\right)\right]^2 \gamma_\mathrm{tr}\gamma, \qquad 0 \le \eta \le \eta_\mathrm{c}, \tag{3-33}$$
$$\left(\nu^+\right)_\mathrm{outer} = \alpha \frac{1}{C}\frac{1}{c^2}\sqrt{\mathrm{Re}_x}\left[\int_0^{\eta_\mathrm{e}} c\,(1-u)\,\mathrm{d}\eta\right]\gamma_\mathrm{tr}\gamma, \qquad \eta_\mathrm{c} \le \eta \le \eta_\mathrm{e}, \tag{3-34}$$

where $\nu^+ = \nu_\mathrm{T}/\nu$ is the nondimensionalized eddy viscosity, made dimensionless with the local kinematic viscosity, and furthermore

[4] For all following stations the solution of the previous station suffices when using a marching method.

[5] The transformed eddy viscosity relations and the relation for turbulent Prandtl-number are rewritten to contain only nondimensional quantities, and thus are equal to, but differ in expression from the equations listed in reference [27, p. 289]. A few deficiencies in these equations listed in this reference have been corrected for, see also App. D).

$$y/A = \frac{N}{A^+} c^{-3/2} \frac{\sqrt{C_\mathrm{w}}}{C} \mathrm{Re}_x^{1/4} I v_\mathrm{w}^{1/2}, \qquad I = \int_0^\eta c \, \mathrm{d}\eta, \qquad I_\mathrm{e} = \int_0^{\eta_\mathrm{e}} c \, \mathrm{d}\eta, \tag{3-35}$$

$$N^2 = 1 - 11.8 C_\mathrm{w} c_\mathrm{w}^3 p^+, \qquad p^+ = \frac{m_2}{\mathrm{Re}_x^{1/4}} \left(C_\mathrm{w} c_\mathrm{w} v_\mathrm{w} \right)^{-3/2}, \tag{3-36}$$

$$\gamma = \left(1 + 5.5 \left(I / I_\mathrm{e} \right)^6 \right)^{-1}. \tag{3-37}$$

With the closure coefficients repeated from Sec. 2-3-3-1

$$\kappa = 0.40, \qquad A^+ = 26, \qquad \alpha = 0.0168. \tag{2-43}$$

And the turbulent Prandtl-number model

$$\mathrm{Pr_T} = \frac{\kappa \left[1 - \exp\left(-y/A \right) \right]}{\kappa_\mathrm{h} \left[1 - \exp\left(-y/B \right) \right]}, \tag{3-38}$$

$$y/B = \frac{N}{B^+} c^{-3/2} \frac{\sqrt{C_\mathrm{w}}}{C} \mathrm{Re}_x^{1/4} I v_\mathrm{w}^{1/2}, \tag{3-39}$$

$$B^+ = \frac{B^{++}}{\mathrm{Pr}^{1/2}}, \tag{3-40}$$

$$B^{++} = \sum_{i=1}^{5} C_i \left(\log_{10} \mathrm{Pr} \right)^{i-1}. \tag{3-41}$$

With $\mathrm{Pr_T}|_\mathrm{w} = \frac{\kappa}{\kappa_\mathrm{h}} \frac{B}{A}$ (eq. 2-48) and the closure coefficients repeated from Sec. 2-3-3-2

$$\kappa_\mathrm{h} = 0.44, \quad C_1 = 34.96, \quad C_2 = 28.79, \quad C_3 = 33.95, \quad C_4 = 6.33, \quad C_5 = -1.186. \tag{2-52}$$

Note that only properties which are a function of the y-coordinate, or its derivatives, need to be transformed. The fluid property variables are either obtained from ideal gas fluid property relations (see section 3-4-1) or from FluidProp [47].

3-2-2 Influence of Fluid Properties on the Boundary Layer Characteristics

This section reports how fluid properties influence the shape and development of a two-dimensional steady state boundary layer by analyzing the SoE from Sec. 3-2-1 in transformed form. The velocity profile will be the main focus of this analysis since it forms the basis of most parameters of interest as was shown in Sec. 2-4. The most relevant fluid properties that affect the velocity profile will be identified. For simplicity,

only laminar flows will be considered, but extension to turbulent flows is relatively simple and straightforward.

The relative boundary layer thickness in a laminar flow is proportional to

$$\frac{\delta}{L} \sim \sqrt{\nu} \sim \frac{1}{\sqrt{\mathrm{Re}}}, \tag{??}$$

for large Reynolds-numbers (see Sec. 2-2-2). The laminar boundary layer thickness hence is proportional to the length of the surface and the inverse of the size of the square root of the kinematic viscosity. The relative thickness decreases with increasing Reynolds-number. In other words, the size of the kinematic viscosity influences the shape of the velocity profile.

Recall from Sec. 2 that the ME and EE are *coupled* when the fluid and transport properties inside the ME are a function of the temperature or enthalpy profile, which results from the EE. Therefore, compressible flows *always* have a *coupled* ME and EE. From the equations in Chap. 2, such as eq. 2-10, it can be seen that the ME and EE are coupled through fluid property density ρ and transport property dynamic viscosity μ respectively.

Next, consider the ME from Sec. 3-1 and its coefficients which give the velocity field in the form of differential parameter f'

$$\left(C\left(1+\nu^{+}\right)f''\right)' + m_1 f f'' + m_2\left[c-\left(f'\right)^2\right] = x\left(f'\frac{\partial f'}{\partial x} - f''\frac{\partial f}{\partial x}\right). \tag{3-1}$$

From the ME it can be observed that the boundary layer flow parameters influencing the velocity profile are the density ratio $c = \frac{\rho_e}{\rho}$, the Chapman-Rubesin parameter $C = \frac{\rho\mu}{\rho_e\mu_e}$, the dimensionless Eddy Viscosity ratio ν^+, and the dimensionless PG parameters m_1 and m_2 respectively. When considering laminar flow, the ME is influenced only by the parameters c and C, which are functions of density and dynamic viscosity inside the boundary layer only. In addition, the Eddy Viscosity is a function of density, dynamic viscosity and the velocity field at any arbitrary station.

From the ME it can also be observed that the EE influences the ME only indirectly through the relevant fluid properties density ρ and viscosity μ in the form of the parameters c and C. There is no direct influence of the EE on the ME, since the total enthalpy ratio profile g and its derivative p (differential parameters) are not present inside the ME.

When considering nonzero PG flow, the PG parameters m_1 and m_2 influence the ME and thus the velocity profile. It is important to realize that the PG parameters are a function of free stream conditions only, and hence they remain constant along the

vertical coordinate direction inside the boundary layer at an any arbitrary station. By its definition, m_1 is a function of the velocity based PG parameter m_2 and the fluid property based PG parameter m_3 in case of compressible flows

$$m_1 = \frac{1}{2}\left[1 + m_2 + m_3\right], \tag{3-13}$$

with

$$m_3 = \frac{x}{C_\mathrm{e}} \frac{\mathrm{d}C_\mathrm{e}}{\mathrm{d}x}, \tag{3-15}$$

which is defined as function of the here newly introduced core flow parameter

$$C_\mathrm{e} = \frac{\rho_\mathrm{e}\mu_\mathrm{e}}{\rho_0\mu_0}, \tag{3-8}$$

which is useful as a measure of the relative change in free stream fluid properties along the flow by scaling the local edge properties with the the unchanging total properties. It is convenient for comparing the change in fluid properties along nozzle expansions since the total conditions do not change along the isentropic expansion. This is in contrast to the similar Chapman-Rubesin parameter C which is a measure of the relative change of fluid properties inside the boundary layer locally. The formulation of the core flow property C_e follows from the derivation of the SoE. By definition, $C_\mathrm{e} = 1$ at stagnation conditions, where $C = 1$ at the boundary layer edge along the flow in compressible flows. Both parameters are equal to one in the entire flow field for incompressible flows ($\mathrm{Ma} = 0$). Note again that C_e and thus m_3 too, are functions of density and dynamic viscosity only.

Concluding, fluid property changes along an isentropic nozzle expansion can be quantified and compared with the newly introduced dimensionless fluid property C_e, and the fluid property based PG parameter m_3 which represents the contribution of fluid property changes along the flow direction in the ME. Thus, fluid property changes are only present inside the ME through parameters c, C and m_3, which are all a function of density and dynamic viscosity only. Therefore, c, C and m_3 are important parameters in characterizing the boundary layer in compressible fluid flows, with the SoE in transformed coordinates. The coordinate transformation results in dimensionless variables, which makes comparison with other fluids possible.

Furthermore, note that the velocity based PG parameter m_2 can be rewritten in terms of the Mach-number, which is a more convenient form when considering supersonic nozzle design cases where the focus is on the Mach-number along the expansion

$$m_2 = \frac{x}{u_e}\frac{\mathrm{d}u_e}{\mathrm{d}x} \tag{3-14}$$
$$= \frac{x}{\mathrm{Ma}_e}\frac{\mathrm{dMa}_e}{\mathrm{d}x} + \frac{x}{a_e}\frac{\mathrm{d}a_e}{\mathrm{d}x} \tag{3-42}$$
$$= m_4 + m_5 \tag{3-43}$$
$$= \frac{m_4}{1 + (\Gamma - 1)\,\mathrm{Ma}_e^2}. \tag{3-44}$$

Notice here that the Fundamental Derivative of Gas Dynamics appears in the last relation, since it relates the changes in SoS with density at constant entropy, in this case along an isentropic nozzle expansion, and the SoS relates the velocity with the Mach-number.

3-2-3 Numerical Solution Method: Keller's Box-Method

Keller's Box-method [23, 25], is an implicit numerical method which is (extremely) simple, efficient and easy to program [4, 23, 84]. This method [23] is implemented in the FORTRAN computer program [27] to solve the system of equations, and hence this routine has been implemented in the same form in the MATLAB boundary layer program considered here. The Keller's Box-method is an implicit method, meaning that it is unconditionally stable. The discretized SoE equations is ordered in an effective and efficient way, and as such the coefficient matrix does not become singular. In fact, Keller states [23] that the equations are discretized in such a way that it becomes the most efficient implicit numerical scheme for solving the type of parabolic partial differential equations under consideration.

Recall that the SoE as listed in the previous section was expressed as a first-order system of partial differential equations by introducing the variables f, u, v, g and p which are called differential parameters here. This is the form of the SoE which is discretized according to Keller's Box-method. Figure 3-1 illustrates (a) the rectangular mesh-grid, or *net*, and (b) one of the mesh-grid rectangles, which is referred to as the *box* around which the equations are discretized.

The three first-order ODE's are discretized around the midpoint $(x_n, \eta_{j-1/2})$, and the two first order PDE's around midpoint $(x_{n-1/2}, \eta_{j-1/2})$. Consider any net quantity w substituting for f, u, v, g or p, which is discretized as follows

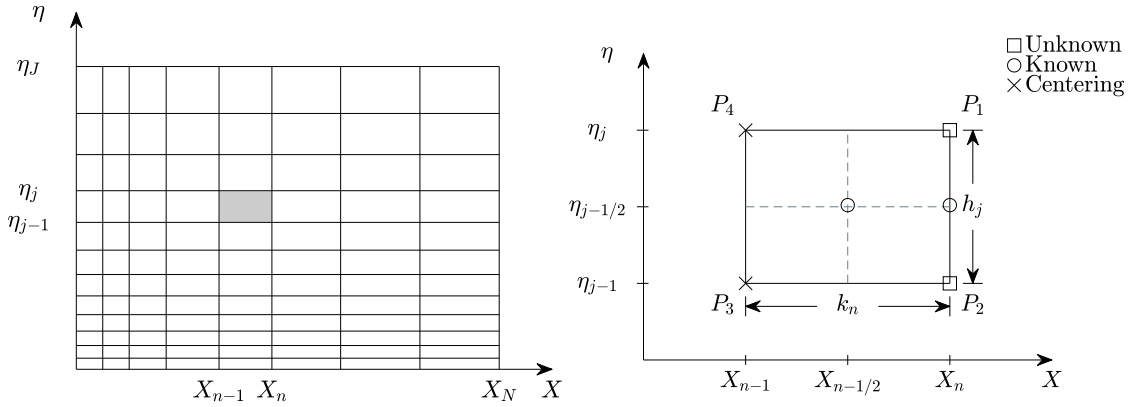

Figure 3-1: Keller's Box-method, illustrating: (a) The mesh-grid with nonuniform spacing in the x- and y-coordinate directions, and (b) A single *box* as part of the net to illustrate the box-type discretization scheme. The equations are centered about the two points which are marked with a cross-symbol $\times$.

$$[w]^n_{j-1/2} = \frac{1}{2}\left(w^n_j + w^n_{j-1}\right), \tag{3-45}$$

$$\left[\frac{\partial w}{\partial \eta}\right]^n_{j-1/2} = \frac{1}{h_j}\left(w^n_j - w^n_{j-1}\right), \tag{3-46}$$

$$\left[\frac{\partial w}{\partial x}\right]^{n-1/2}_{j-1/2} = \frac{1}{k_n}\left([w]^n_{j-1/2} - [w]^{n-1}_{j-1/2}\right), \tag{3-47}$$

$$\left[\frac{\partial w}{\partial \eta}\right]^{n-1/2}_{j-1/2} = \frac{1}{2}\left(\left[\frac{\partial w}{\partial \eta}\right]^n_{j-1/2} + \left[\frac{\partial w}{\partial \eta}\right]^{n-1}_{j-1/2}\right), \tag{3-48}$$

$$[w]^{n-1/2}_{j-1/2} = \frac{1}{2}\left([w]^n_{j-1/2} + [w]^{n-1}_{j-1/2}\right). \tag{3-49}$$

The resulting first-order equations are hence approximated on the arbitrary rectangular net (the spacing of this grid can vary arbitrarily) with centered differences of the net rectangle difference equations [25]. The resulting system of equations is nonlinear and implicit. Writing the discretized SoE complemented with the boundary conditions results in a nonlinear system of $5J + 5$ equations and $5J + 5$ unknowns. The discretized system can be grouped such that the unknowns (see Fig. 3-1 (a)) are collected on the left-hand side, and the knowns are collected on the righ-hand side. Cebeci [27] gives an elaborate explanation of this derivation and lists finally the complete discretized SoE.

Newton's method [23, 85] is applied to linearize and solve this discretized nonlinear system. The approach adopted is to find the corrections δw in the 5 *Newton iterates* defined as

$$w^{(i+1)}_j = w^{(i)}_j + \delta w^{(i)}_j, \tag{3-50}$$

at a certain station n, where the indices i and j denote the iteration number and the vertical grid node respectively. The right-hand side of these iterates is substituted in the discretized nonlinear system. After which the terms quadratic in δ are dropped, resulting in a linear system. The boundary conditions for the corrections δ in this system become

$$\delta f_0 = 0, \qquad \delta u_0 = 0, \qquad \delta u_J = 0, \tag{3-51}$$

$$\alpha_0 \delta g_0 + \alpha_1 \delta p_0 = 0, \qquad \delta g_J = 0, \tag{3-52}$$

where α_0 or α_1 equals one, while the other equals zero depending on the boundary conditions prescribed for the EE. This linear system $\mathbf{A}\boldsymbol{\delta} = \mathbf{r}$ can be written as a linear block-tridiagonal system with block-matrices $\mathbf{A}$, $\mathbf{B}$ and $\mathbf{C}$, as follows

$$\mathbf{A}_j^{n,i} \boldsymbol{\delta}_{j-1}^{n,i+1} - \mathbf{B}_j^{n,i} \boldsymbol{\delta}_j^{n,i+1} - \mathbf{C}_j^{n,i} \boldsymbol{\delta}_{j+1}^{n,i+1} - r_j^{n,i}, j = 0, 1, ..., J. \tag{3-53}$$

Where the *blocks* are 5×5 in size, following the amount of first-order differential equations, and vector $\boldsymbol{\delta}$ consists of vectors $\boldsymbol{\delta}_j^n$ of length 5. Again, Cebeci [27] gives an elaborate explanation of this derivation and lists the matrix-blocks graphically. The resulting linear system in block-tridiagonal matrix form is solved by the block-elimination method (see also reference [27, 85]). The solution procedure for the block-tridiagonal matrix is similar to the procedure for solving tridiagonal matrices (see also [85]). First, in a so-called *forward sweep*, the coefficients are calculated by substitution of the previous row into the next row, from top to bottom, with the *recursion formulas*. Then, the solution of the last row can be found from the boundary conditions, and all row solutions can be found by back substitution from bottom to top, again using *recursion formulas*. Theoretically it would take about two iterations to find the solution. In practice however, it will take about three to four iterations to reach second-order accuracy, since boundary layers are nonsimilar in general [23].

The method is second-order accurate in both x- and η-coordinate directions on mesh grids with nonuniform grid spacing. The Lagrange interpolation scheme implemented allows for calculation of derivatives on the variable grid coordinates accurately in both directions. The coordinate transformation which is implemented here removes the singularity at the wall at the start of the calculations, and reduces or completely removes the boundary layer growth in most nonsimilar laminar flow cases. At the same time, it stretches the mesh-grid close to the wall and thereby reduces the large property gradients. Hence, it improves computational accuracy and speed, and allows for larger steps in the x-coordinate stream-wise direction. Next, the combination of the implemented transformation and stream function forces mass conservation by definition. Since the integral of the shear parameter is always equal to 1.

Furthermore, Keller [23] adds that since the boundary layer equations have been formulated as a first-order system, all derivatives can be approximated by simple centered

differences and two-point averages, using only values at the corners of the *box*. He further states, that this type of differencing is as compact as possible and is one of the most attractive features of the Box-scheme. On top of that, a nonuniform mesh grid spacing in both x- and y-coordinate direction can be used, e.g. a stretched grid in case of turbulent flows, which is beneficial for reducing computational time even further.

Cebeci [4, p. 270] and Keller [23] state that there is a slight departure from the implementation of Newton's method in compressible laminar and turbulent flows, but that this is observed not to have any noticeable effects on the second-order convergence of the iterations. The departure is due to the b-coefficient (eq. 3-7) which is a function of the velocity and enthalpy field, and therefore it's value is taken from the previous calculation in order not to destroy the block-tridiagonal structure. For further details of the simplification, see references [4, p. 270] and [23].

Summarized, the Keller's Box-method entails [27]:

1. Reducing the system of equations to a first-order system;
2. Discretize the system of equations with central differences for each *box*;
3. Linearize the discretized system with Newton's method; and,
4. Solve the linearized system by a block-tridiagonal-elimination method.

A general mathematical description of Keller's box-method can be found in reference [23]. A detailed and complete explanation of how this method is applied to the current problem can be found in [27, Chap. 9 & 10].

3-3 Range of Application

The CS-method is specifically developed for two-dimensional boundary layer flows. Only first-order boundary layer effects are considered. The current program can take into account general boundary layers in two-dimensional steady state flows. General is defined here as variable fluid property (compressible) boundary layers including nonzero pressure gradient and heat transfer (including nonsimilar free stream and wall conditions) for laminar and turbulent flows up to separation. Transition can be forced at a predetermined location for example based on measurements, or roughly estimated with one out of two implemented transition prediction methods by Wazzan [32] or Michel's extended method [33, p. 117] (see Sec. 2-5). Separation can be predicted, but is not relevant in this case of highly accelerated nozzle flows.

The capabilities of the computer program will be discussed here. This will lead to the need for validation, which will be dealt with in the next chapter.

3-3-1 Assumptions and Simplifications

The CS-method was developed for predicting two-dimensional steady state compressible boundary layers developing along solid and smooth wall surfaces of bodies placed in external flows, including nonzero pressure gradient and heat transfer. Single-phase fluid flows, e.g. gas, liquid or supercritical state[6], of uniform composition can be simulated with varying fluid properties for laminar and turbulent flows, as long as the thermo-physical model is appropriate for the case at hand. Fluctuations in fluid properties due to turbulence are neglected (see Sec. 2-3-2). Other important assumptions and simplifications are:

1. Continuum hypothesis;
2. Principle of local state;
3. Isotropic fluid;
4. Newtonian fluid (linear stress-strain relationship);
5. Stokes' hypothesis;
6. Prandtl's boundary layer assumptions (no second-order boundary layer effects);
7. The flow field properties can be split in an average and fluctuating part (RANS);
8. Fluctuations in fluid properties due to turbulence are small and can be neglected
9. Morkovin's hypothesis: density variations do not influence or affect the turbulence structure; and,
10. No losses in free stream (isentropic free stream; laminar or isotropic low level turbulence).

Appendix C gives a more elaborate and complete list of assumptions in chronological order including an explanation of the hypotheses.

3-3-2 Limitations

Due to the assumptions and simplifications as described in the previous section (3-2-1), the following phenomena **cannot** be taken into account by the current boundary layer program:

1. Fluid dissociation/recombination, ionization and chemical reactions;

[6] Liquid and supercritical fluids can be modelled through gas model option 3, which uses FluidProp [47] for retrieval of the thermophysical properties.

2. Bulk viscosity;
3. Body forces (centrifugal, Coriolis, gravitational, etc.);
4. Boundary layer flow beyond point of separation;
5. Longitudinal and transverse wall surface curvature (curvature is a second-order boundary layer effect);
6. Shock waves and expansion fans (sudden large accelerations);

Furthermore, notice that prediction of separation is not reliable [26, p. 68]; and the transition methods used are for global estimates of the transition location for air only. The transition region model is valid for adiabatic air flows only (see Sec. 2-3-3-1).

In the future the model can be extended to include the simulation of low Reynolds-number boundary layer flows, strong adverse pressure gradient flows, pipe and duct flows, and second-order boundary layer effects. Second-order boundary layer effects include for example wall-surface curvature along turbine blades and nozzle guide vanes expressed as centrifugal forces; centrifugal and Coriolis forces respectively; and rotational coordinate systems, see Sec. A-13.

3-3-3 Closure Coefficients

The CS-model was developed first for the incompressible turbulent boundary layer [79], where the pressure gradient was not taken into account in the eddy viscosity model. Later it was extended to compressible flows including nonzero pressure gradient and for the first time including a turbulent Prandtl-number equal to one [80]. Na and Habib [65] have extended the turbulent Prandtl-number model for pipe flows to a range of fluids with molecular Prandtl-numbers ranging from 0.02 to 14.3. Cebeci [64] has adopted this model for use in two-dimensional boundary layer flows. The CS-model has been refined for different specific flow types, such as high adverse pressure gradients, low Reynolds-numbers, etc. For an overview of these specific case refinements, see references [4] and [25].

Recall from Sec. 3-1 that the mathematical form of the CS-model has proven to be suitable for the flow type at hand. In addition, Wilcox [26] stresses that the models are bounded to the range of flows for which the closure coefficients were calibrated. Furthermore, he states that the CS-model has been applied to a *wide range of boundary layer flows* successfully. Since the model is calibrated with the *measurable* velocity profiles, velocity profiles are predicted most accurately, in general within 2% accuracy. Properties derived from the velocity profile are generally predicted with less accuracy. Integral parameters such as momentum thickness and shape factor often show 10% differences from measured values.

The closure coefficients of the Eddy Viscosity model as part of the implemented CS-model [27], e.g. κ, A^+, α, 11.8 as listed in Sec. 2-3-3-1 (2-43) were determined from large sets of experimental data obtained from renowned measurement campaigns of zero pressure gradient (flat plate) incompressible flows in air. Opposite to the other constants, Clauser's constant (α) was measured for different pressure gradients, but was found to be independent of pressure gradient [86]. A weaker part of the turbulence model is the intersection location (involving the factor 11.8) of the linear laminar sublayer with the logarithmic law of the wall, since it is based on a more approximate approach.

The closure coefficients of the turbulent Prandtl-number model [4] as part of the implemented CS-model, e.g. κ_h, C_{1-5} as listed in Sec. 2-3-3-2 (2-52) were obtained from measurements of fully developed pipe flows [65]. The turbulent Prandtl-number is also a function of the turbulent flow characteristics, except for the region in close proximity to the wall surface where it is a function of the molecular Prandtl-number. The turbulent Prandtl-number model, as part of the CS-model, was calibrated with a wide variety of fluids ranging in Prandtl-numbers making it suitable for different types of fluid flows. The coefficients C_{1-5} for the fluid dependent heat transfer damping factor B were obtained from measurements of fully developed pipe flows [65]. The closure coefficients are listed in table 3-1 together with a short description and the value taken from literature as generally accepted including its reference.

In general, flow properties of turbulent flows are a function of turbulent characteristics and do not depend on fluid properties. Furthermore, the characteristics seem universal, e.g. the Von Kármán constant. Therefore, it is expected that fluid flows that behave near incompressible can be simulated using these closure coefficients. Note however, that in complex fluid flows close to the critical point changes in fluid properties are believed to stabilize the flow possibly leading to relaminarization [87–89]. This possibly requires the introduction of a new damping- or intermittency factor to reduce the turbulence intensity based on thermodynamic property changes close to the critical point.

There is a need to verify the validity of these closure coefficients in case of nonideal boundary layer flows. Since the model is empirical, the validity of the current closure coefficients needs to be studied first by experiments. If needed the model can easily be (re)calibrated for the case at hand. This highlights the need for finding suitable experimental data for validation of the program in the operational range of the ORCHID nozzle [15] for Mach-numbers ranging from 0.1 up to 2.0; and high Reynolds-numbers. Chapter 4 reports the validation of the currently implemented model for boundary layer flows in air.

Table 3-1: The CS-model closure coefficients as obtained from reference [27] and implemented in the current boundary layer program.

Closure coefficient	**Value** [-]	**Source**	**Description**	**Range/Note**
κ	0.40	Coles (1969) [83]	(Von) Kármán constant	Supported by more recent work, considered as universal constant
A^+	26	Van Driest (1956) [90]	Van Driest damping constant/factor	$\mathrm{Re}_\theta > 5000$ [25, p. 159]
α	0.0168	Clauser (1956) [86]	Clauser('s)/outer eddy viscosity constant	Independent of PG [86]
-	11.8	Cebeci (1974) [4]	Assumed intersection of viscous sublayer with (intermediate) log layer	
γ_{int}	eq. 2-42	Klebanoff (1955) [91], Corrsin & Kistler (1955) [92]	Intermittency factor	
κ_{h}	0.44	Cebeci (1973) [64]	Heat transfer mixing-length constant	
C_{1-5}	eq. 2-52	Na & Habib (1973) [65]	Constants in fluid specific eddy conductivity damping factor	$0.02 < \mathrm{Pr} < 14.3$ and accurate for $\mathrm{Re} > 10^4$

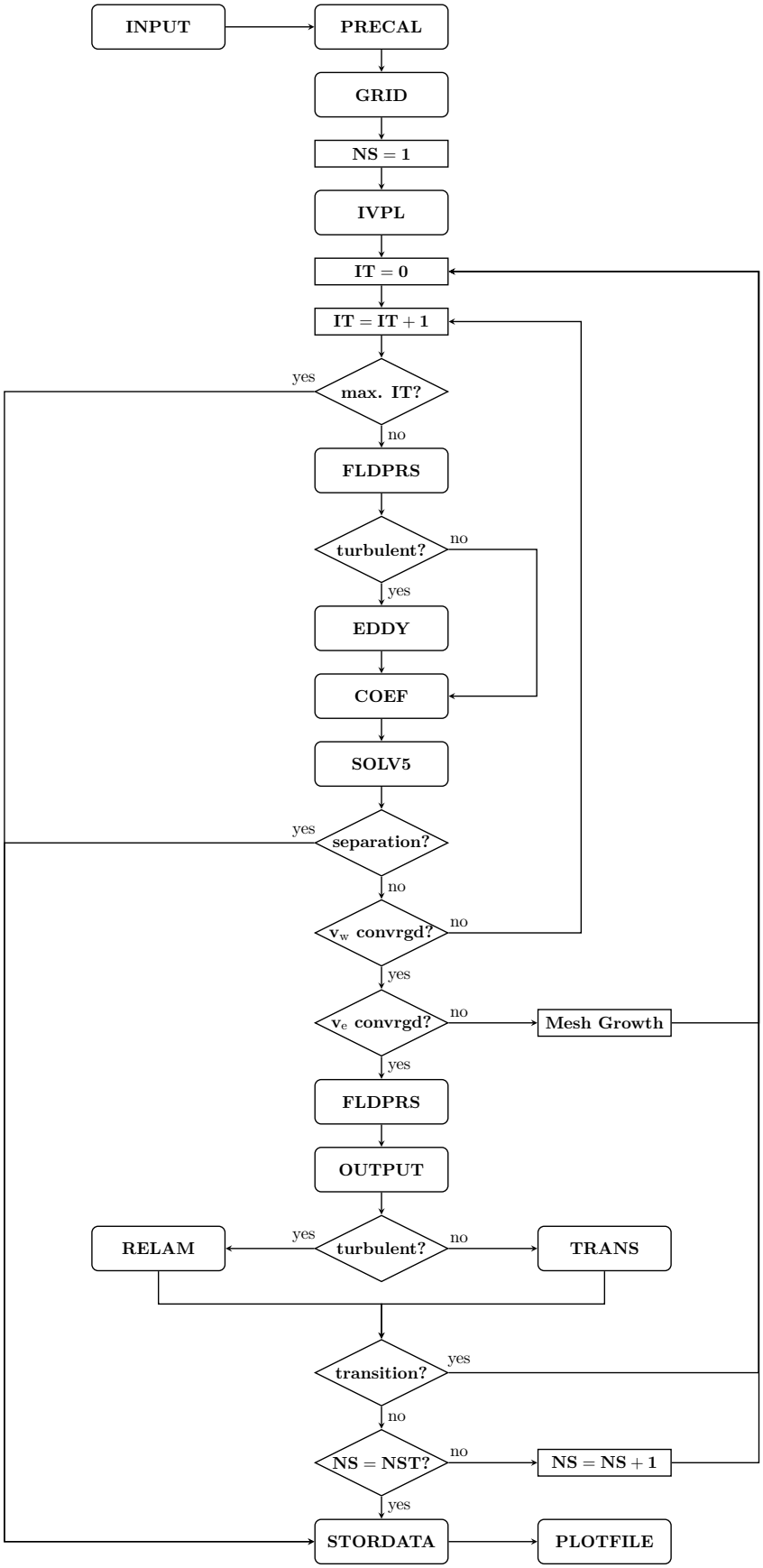

Figure 3-2: Flow-chart of the boundary layer program including the functions and main criteria.

3-4 Structure of the Program

The computer program is largely taken from the book *Convective Heat Transfer* by [27]. The FORTRAN code accompanying this book was rewritten to MATLAB code, and coupled with an external fluid property library to consider a wide variety of fluids and variations in the thermodynamic properties within the boundary layer. The structure and handling of variables was adapted where needed to fulfill MATLAB criteria. In addition, the structure was adapted to meet the current simulation objectives of general fluid property boundary layer flows. The current code therefore entails several function-files based on several other sources (with references included in these files). The main structure of the program is still largely based on Cebeci [27], but also on the structure obtained from the FORTRAN programs presented in McNally [48] and Goldman [19].

Figure 3-2 shows the overall structure of the program. The overarching MAIN-file (caller file) is used to load the case specific input first from a case specific INPUT-file. Then, it calls the other files one by one according to the flow-chart, starting with the PRECAL-file. PRECAL stands for precalculation, which entails the calculation of all properties that can be obtained beforehand through the boundary conditions (edge and wall). The PRECAL-file includes the calculation of the boundary layer edge velocity along the flow and its derivative. Several differencing techniques are available, but LAGRANGE interpolation gives the best results in terms of numerical noise due to sudden changes in geometry or boundary layer edge input. Then, a mesh-grid is calculated by the GRID-file which size and shape is predefined by several grid parameters defined in the INPUT-file. Next, the station counter `NS` is set equal to one `NS = 1` for use in the IVPL-file (Initial Value ProbLem) which calculates the initial conditions. The initial conditions are the initial profiles of the differential parameters at the first station. To calculate these profiles, the IVPL-file contains calls to the COEF-file, for calculation of the COEFficients in the coefficient matrix, and to the SOLV5-file for calculation of its solution, where SOLV5 stands for SOLVing the 5 first-order differential equations (eq. 3-1 to eq. 3-5) all at the same time. Now all conditions are set, and the boundary layer calculations can start for which the overarching CSM-file is called. This file contains the rest of the functions, except for the functions STORDATA and PLOTFILE which handle the results in case the calculation has been ended.

The CSM-file starts with setting the iteration counter to zero `IT = 0`. The calculations are performed inside a while-loop, while the convergence criteria are monitored until convergence has occurred. These convergence criteria are

$$\mathrm{d}v_\mathrm{w} < 1 \times 10^{-5}, \tag{3-54}$$

$$\left| \frac{\mathrm{d}v_\mathrm{w}}{v_\mathrm{w} + 0.5\mathrm{d}v_\mathrm{w}} \right| > 0.02, \tag{3-55}$$

for laminar and turbulent flow respectively. Note that the turbulent convergence criterion

is the less stringent one [27]. Cebeci [4, 27] states that the shear parameter at the wall is the most sensitive parameter, and it is the last parameter to converge.

Regarding the calculations, first, it is checked whether the number of iterations has already exceeded the predefined maximum number of iterations `IT_MAX = 6`. If not, the FLuiD PRopertieS, in the form of dimensionless parameters, are calculated with the FLDPRS-file. According to whether the flow is laminar or turbulent, the dimensionless EDDY Viscosity and turbulent Prandtl-number are calculated with the EDDY-file. Then, the COEF-file calculates the **A**-matrix coefficients, which are used in the SOLV5-file to solve the system of discretized equations as discussed in Sec. 3-2-3.

After a single calculation has been finished, it is first checked whether the wall shear obtained is still greater than zero. If it is smaller than zero $v_w < 0$, separation has likely occurred and the calculation is stopped by proceeding to the STORDATA-file storing the results obtained, and plotted by the PLOTFILE. If the wall shear, as in most cases, is larger than zero, two other checks follow: 1) does the change in wall shear compared with the previous calculation result meet the convergence criterion (eq. 3-54)? If not, the calculation is proceeded, and the iteration counter `IT` is increased with one, `IT = IT + 1`. If so, then convergence is reached and the program proceeds to the next check: 2) did the shear at the boundary layer edge become lower than the predefined threshold of $\mathrm{d}v_w < 1 \times 10^{-3}$? If not, this means that the solution is about to exceed the current mesh-grid, and therefore the grid is extended, including the size of the solution vector variables. However, if the shear at the edge is lower than the threshold value, the calculation proceeds with updating the fluid properties (FLDPRS-file) for the converged solution. And followed by the OUTPUT-file, which calculates the boundary layer characteristics based on the solution and fluid properties found for that current station. When the boundary layer characteristics are determined, another check is done to see whether the flow is laminar or turbulent. When the flow is laminar, a laminar-turbulent transition check is done if predefined, with the methods described in Sec. 2-5. When the flow is turbulent, the same is done for turbulent-laminar transition (relaminarization) with the method described in Sec. 2-5. If transition has occurred according to one of these methods, the calculation is restarted at the same station while resetting the iteration counter `IT` (the total amount of iterations pets station is stored though). When transition did not occur, a last check is done to see if the final station has been reached already. If not, the station counter `NS` is increased with one, `NS = NS + 1`, and the calculation is started at the next station by setting the iteration counter back to zero, `IT = 0`, and using the final calculation results from the previous station as initial values. If the the final station has been reached though, the solution is stored by the STORDATA-file and the results are plotted by the PLOT-file. STORDATA stores the MATLAB structures obtained in a separate folder, such that they can be loaded anytime plotted with the PLOT-file function without the need of re-running simulations.

Appendix A lists all code functions with a short explanation of their function and methods implemented. The files SOLV5, COEF, GRID, IVPL have been copied from reference [27], although one missing coefficient was added to the COEF-file (see App. D). In

addition, App. A includes a table with all variables and structures contained in these functions. Furthermore, some nuances (Sec. A-12) on the implementation of several methods. Section A-2 contains a list of changes and additions made to the original FORTRAN code. Appendix F gives a complete listing of the computer code. Where possible, comments were inserted in the code for the interested reader to clarify the methods implemented and the units of variables used.

3-4-1 Program Options: Input and Fluid Property Models

In order to simulate a test case it must contain initial values, boundary conditions and fluid properties. There are several options a user can specify depending on the available information and the required output. For example, the boundary layer edge condition can be prescribed with three different parameters, which gives the option to use the variable at hand, e.g. velocity, Mach-number or pressure. The advantage lies in the simulation case at hand. For experimental data the velocity is mostly measured. In case of the ORCHID nozzle the static pressure and Mach-number are measured. Regarding numerical methods, such as CFD or the design of a nozzle with the Method of Characteristics, other outputs might be available or more relevant such as the Mach-number. Functions are available to smooth experimental data, if needed.

Regarding the *boundary conditions* the following options are available in combination with the mentioned inlet conditions:

1. Regarding the boundary layer edge:
   (a) Free stream velocity ratio $u_\mathrm{e} = \frac{u_\mathrm{e}}{u_\mathrm{I}}$, with P, T and u_I;
   (b) Free stream Mach-number Ma_e, with P_0, T_0 and Ma_I; or,
   (c) Free stream (static) pressure distribution $p_\mathrm{e} = \frac{P_\mathrm{e}}{P_\mathrm{I}}$ or $C_\mathrm{p} = \frac{p_\mathrm{e} - p_\infty}{\frac{1}{2}\rho_\mathrm{e} u_\mathrm{e}^2}$, with P_0, T_0 and Ma_I.
2. And regarding the wall surface:
   (a) Total enthalpy ratio: $g_\mathrm{w}(x) = \frac{h_{0,\mathrm{w}}(x)}{h_{0,\mathrm{e}}(x)}$; or,
   (b) Heat flux: $\dot{q}_\mathrm{w} = -k_\mathrm{w} \left.\frac{\mathrm{d}T}{\mathrm{d}y}\right|_\mathrm{w} = -\frac{\mu_\mathrm{w}}{\mathrm{Pr}_\mathrm{w}} \left.\frac{\mathrm{d}h_0}{\mathrm{d}y}\right|_\mathrm{w}$, or expressed as derivative of enthalpy ratio $p_\mathrm{w}(x) = g'_\mathrm{w}(x)$, which is zero for an adiabatic wall.

Regarding the initial values, these are calculated by the program itself for the first station, directly in transformed form. The initial values are polynomials which are a function of the transformed η-coordinate, and match the adiabatic incompressible Blasius' profile solution.

Regarding the *thermophysical properties*, e.g. state variables, fluid properties and transport properties, three *gas models* are available:

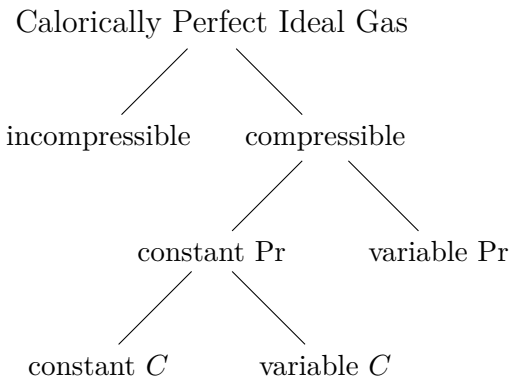

Figure 3-3: Fluid and transport property modelling options for the Calorically Perfect Ideal Gas model (CPIG). Note that the most general fluid property model still has constant isobaric specific heat, but is compressible because all other properties depend on temperature, including the Pr-number. The options are used for the verification and validation cases in chapter 4.

1. Calorically perfect ideal gas, with constant heat capacities;
2. Thermally perfect ideal gas (calorically imperfect), with fluid properties as function of temperature only; or,
3. Nonideal gas, with general variable fluid properties.

The first *gas model* assumes ideal gas and both specific heats constant. The fluid and transport properties can be chosen to be constants, or to vary with temperature. Figure 3-3 depicts the options available. The second *gas model* considers thermophysical properties as function of temperature only. The specific heats are a function of temperature, and therefore this ideal gas model is called calorically imperfect or thermally perfect. Both models can be used in the ideal gas range where values of the compressibility factor Z are close to one.

In contrast, the *nonideal gas model* takes into account departure from ideal gas, meaning Z departs from one. Do note that this model can also be used in the ideal gas region (see Fig. 2-2 for the range of compressibility factor Z for MM). The model uses the program FluidProp [47] for thermophysical property data retrieval. This program has several options for implementing different fluids which can be modelled with various thermodynamic and transport models. Both ideal and nonideal. However, the pittfall is that thermodynamic properties are calculated using complex equations of state and this increases the computational cost.

3-4-2 Selection of Output Variables

The program generates a number of output parameters (boundary layer characteristics). The most important output parameters from Sec. 2-4 are listed here with their defini-

tion and in transformed form. Among them are velocity, displacement and momentum thickness and a few dimensionless groups which are used in this work:

$$\delta = y\left(u = 0.99u_\mathrm{e}\right) = y\left(f' = 0.99\right), \tag{3-56}$$

$$\delta^* = \int_0^\infty \left[1 - \frac{\rho u}{\rho_\mathrm{e} u_\mathrm{e}}\right] \mathrm{d}y = \frac{x}{\sqrt{\mathrm{Re}_x}} \int_0^{\eta_\mathrm{e}} \left[c - f'\right] \mathrm{d}\eta, \tag{3-57}$$

$$\theta = \int_0^\infty \left[\frac{\rho u}{\rho_\mathrm{e} u_\mathrm{e}}\left(1 - \frac{u}{u_\mathrm{e}}\right)\right] \mathrm{d}y = \frac{x}{\sqrt{\mathrm{Re}_x}} \int_0^{\eta_\mathrm{e}} \left[f'\left(1 - f'\right)\right] \mathrm{d}\eta, \tag{3-58}$$

$$\mathrm{Re}_x = \frac{u_\mathrm{e} x}{\nu_\mathrm{e}}, \qquad \mathrm{Re}_\theta = \frac{u_\mathrm{e}\theta}{\nu_\mathrm{e}}, \tag{3-59}$$

$$\mathrm{Pr}_x = \frac{c_{\mathrm{p,e}}\mu_\mathrm{e}}{k_\mathrm{e}}, \tag{3-60}$$

$$\mathrm{St}_x = \frac{\dot{q}_\mathrm{w}}{\rho_\mathrm{e} u_\mathrm{e} \Delta H} = \frac{C_\mathrm{w} p(1)}{\mathrm{Pr}_\mathrm{w}\sqrt{\mathrm{Re}_x}\left(g_{aw} - g(1)\right)}, \tag{3-61}$$

$$\mathrm{Nu}_x = \mathrm{Pr}_x\,\mathrm{Re}_x\,\mathrm{St}_x = \frac{\mathrm{Pr}}{\mathrm{Pr}_\mathrm{w}} \frac{C_\mathrm{w}\sqrt{\mathrm{Re}_x}}{1 - g(1)} p(1), \tag{3-62}$$

$$C_\mathrm{f} = \frac{\tau_\mathrm{w}}{\frac{1}{2}\rho_\mathrm{e} u_\mathrm{e}^2} = \frac{2C_\mathrm{w}}{\sqrt{\mathrm{Re}_x}} f''_\mathrm{w}, \tag{3-63}$$

$$C_\mathrm{d} = \frac{T}{\rho}\frac{1}{u_\mathrm{e}^3} \int_0^\infty \left[\frac{1}{T}\mu\left(\frac{\partial u}{\partial y}\right)^2\right] \mathrm{d}y = \frac{T}{T_\mathrm{e}} c \frac{1}{\sqrt{\mathrm{Re}_x}} \int_0^{\eta_\mathrm{e}} \left[\frac{T_\mathrm{e}}{T} C v^2\right] \mathrm{d}\eta. \tag{3-64}$$

Note that the loss coefficient C_d can be scaled with the wall density and temperature, or with the boundary layer edge density and temperature which is implemented in the current computer program and results in

$$C_\mathrm{d} = \frac{1}{\sqrt{\mathrm{Re}_x}} \int_0^\infty \left[\frac{T_\mathrm{e}}{T} C v^2\right] \mathrm{d}\eta. \tag{3-65}$$

Importantly, the user should be aware of the decreasing trend of C_d in the flow direction while, in contrast, the trend of the total entropy generation per surface area for an accelerating flow is generally increasing along the flow

$$\dot{S}_\mathrm{A} = k_\mathrm{e} \frac{1}{x}\sqrt{\mathrm{Re}_x}\mathrm{Pr}_\mathrm{e}\mathrm{Ec}_\mathrm{e} \int_0^\infty \left[\frac{T_\mathrm{e}}{T} C v^2\right] \mathrm{d}\eta. \tag{3-66}$$

3-5 Summary

The CS-method, including the CS-model, was chosen for the simulation of two-dimensional steady state boundary layers in flows of complex molecular fluids for the following reasons:

1. Validated and proven for numerous cases in literature.
2. Semi-empirical (partly based on physical phenomena);
3. Algebraic (zero-equation) turbulence model, and thus no further differential equations need to be solved;
4. High mesh-grid resolution and appropriate relations for accurate results close to the wall surface;
5. Low amount of closure coefficients for possibly later calibration of the model;
6. Including an eddy conductivity model, expressed as turbulent Prandtl-number model, for turbulent (convective) heat transfer; and,
7. Turbulent Prandtl-number has been validated and found to agree well with experimental data of fluids with low, medium and high Prandtl-numbers [4].

The CS-model is considered as a simple model which is detailed enough to capture the relevant physical phenomena and to understand their effects on and inside the boundary layer. Keller's Box-method is the numerical solution method included in the CS-method. Keller's Box-method entails:

1. Reducing the system of equations to a first-order system;
2. Discretize the system of equations with central differences for each *box*;
3. Linearize the discretized system with Newton's method; and,
4. Solve the linearized system by a block-tridiagonal-elimination method.

The structure of the program allows for simulation of boundary layers with different input conditions and thermophysical models. The thermodynamic models available are:

1. Calorically Perfect Ideal Gas;
2. Thermally Perfect Ideal Gas; and,
3. Nonideal Gas.

FluidProp [47] is used for fluid property simulations of complex molecular fluids including ideal gas departure, for any fluid available. The input options available are:

1. P, T, u_{I} and u_{e} at the boundary layer edge;

2. P_0, T_0, $\mathrm{Ma_I}$ and $\mathrm{Ma_e}$; and,
3. P_0, T_0, $\mathrm{Ma_I}$ and $\mathrm{p_e}$.

Where u_e and $\mathrm{p_e}$ are the dimensionless properties velocity ratio $\frac{u_\mathrm{e}}{u_\mathrm{I}}$, and the (static) pressure ratio $\frac{P_\mathrm{e}}{P_0}$ respectively.

Chapter 4

Verification and Validation Cases for Ideal Gas Air

The extent of the program's capabilities was described by the previous chapter. This chapter reports a number of test cases which allow to assess the range of applicability of the program. First, the performance and results of the program are compared with other programs in Sec. 4-1-1. Second, in Sec. 4-1-2 the solver is verified thoroughly by comparison with solutions obtained from literature to the system of equations implemented. Third, the accuracy of the program is studied by studying the discretization error with a basic grid convergence study, and the influence of the iterative error is studied by comparison with solutions from literature in Sec. 4-1-3. The results listed can be used to choose a suitable grid-spacing for the case at hand. Fourth, Sec. 4-2 presents the verification of the program output, the boundary layer characteristics, with solutions from other programs. Last, the turbulence model is validated extensively in Sec. 4-4 with experimental data obtained from literature.

4-1 Solution Verification

A summary of the solution verification process is given here. Detailed information, such as comparison with tabulated solutions, is given in App. A. The program is compared with four other programs as discussed later on in this section.

First, it is important that the reader is aware of the terminology used in modelling and the process of verification and validation, or in short: V&V. In physical modelling, a mathematical model of a physical phenomenon is obtained by making assumptions to simplify the real world. Verification is verifying if the solution obtained is the right

solution to the mathematical model. Validation is to find out if the right mathematical model is solved with respect to representing physics [93, 94].

Verification can be divided in *code verification* and *solution verification*. These comprise error evaluation and error estimation respectively. Code verification (debugging and verifying the correct implementation of (pieces of) code) has been finished successfully and is not considered here, except for one important finding[1].

Error estimation, see Sec. 4-1-3, is the quantification of the numerical error. Three sources of numerical error can be distinguished, which are: round-off error; iterative error; and discretization error. The objective of validation is to find modelling errors and to quantify them. Modelling errors are deviations in the mathematical model from the physical phenomenon.

The system of partial differential equations solved by the boundary layer program from Chap. 3 is listed here again

$$\left(bf''\right)' + m_1 f f'' + m_2\left[c - \left(f'\right)^2\right] = x\left(f'\frac{\partial f'}{\partial x} - f''\frac{\partial f}{\partial x}\right) \tag{3-1}$$

$$f'' = v \tag{3-2}$$

$$f' = u \tag{3-3}$$

$$\left(eg' + df'f''\right)' + m_1 f g' = x\left(f'\frac{\partial g}{\partial x} - g'\frac{\partial f}{\partial x}\right), \tag{3-4}$$

$$g' = p. \tag{3-5}$$

The coefficients are omitted, but can also be found in Sec. 3-2-1.

The two partial differential equations above are dependent on the X-coordinate and vertical η-coordinate. The terms dependent on the X-coordinate are moved to the right. A solution independent of X is called a similar solution, and the system of PDE's is reduced to a system of ODE's. This solution is the same along X for all values of X in the transformed coordinate system, but varies in the real XY-coordinate system due to the coordinate transformation. The advantage of working with similar solutions is that they can be tabulated for comparison. Real flows are generally nonsimilar. Notice that similar flows are the exception but easier to calculate and thus often used as reference case.

The program was verified and the system of equations mentioned above were found to be solved correctly. The System of Equations (SoE) above is verified with a variety of cases increasing the complexity, divided into the categories similar and nonsimilar. Table 4-1 lists the cases distinguishing in similar and nonsimilar cases. The numerical characteristics of the solver can be found by studying similarity cases by increasing the

[1] One of the coefficients was found to be missing in the FORTRAN program by Cebeci [27] and added to the boundary layer program coefficient-file. See App. D.

complexity step-by-step, case by case, by inducing more terms in the SoE every time. Starting with adiabatic incompressible flows (solution to the energy equation is zero), towards compressible flows with nonzero Pressure Gradient (PG) and Heat Transfer (HT), inducing more and more terms step-by-step. First, the Blasius' solution was compared, which only consists of the following equation: $f''' + \frac{1}{2}ff'' = 0$. Then, the PG is added with the Falkner-Skan wedge flows, followed by HT with unit Prandtl-number, heat transfer with Prandtl-number equal to one combined with zero or infinte Mach-number, and lastly adiabatic flow with Prandtl-number equal to one and infinite Mach-number.

The convergence criterion used by the CS-method for all cases is 1×10^{-5} for changes in the shear parameter at the wall between consecutive iterations. This convergence criterion was recommended by Cebeci [27]. The uniform mesh-grid spacing is listed for each case. Laminar flows utilize a uniform mesh-grid spacing where turbulent flows implement a stretched mesh-grid with smaller spacing close to the wall to capture the laminar sublayer.

Table 4-1: A concise overview of the verification cases (all of which for air) and their characteristics for verification of the boundary layer program. The flow is considered incompressible when the density is constant, i.e. $c = \frac{\rho_e}{\rho} = 1$ (and in this case fluid properties and transport properties also). The flow can be considered compressible when the dynamic viscosity is allowed to vary with density (and thus temperature) while keeping the Chapman-Rubesin parameter constant: $C = \frac{\rho\mu}{\rho_e\mu_e}$. Cases NACA0012 and Giepman include transition to fully turbulent flow. Note that similar cases span only one single station, while nonsimilar cases span multiple stations.

Similar-flow cases						
Case \Variable	c	C	PG	Pr	HT	Ma
Blasius [95]	1	1	zero	NA	adiabatic	NA
Falkner-Skan [59]	1	1	favourable, zero, adverse	NA	adiabatic	NA
C-25 [57]	var.	1	favourable, adverse	1.0	nonadiabatic	NA
C-26 [57]	var.	1	favourable, zero, adverse	0.723	nonadiabatic	0
C-27 [57]	var.	1	favourable, zero, adverse	0.723	nonadiabatic	$\infty^{\diamond}$
C-28 [57]	var.	1	favourable, zero, adverse	0.723	adiabatic	$\infty^{\diamond}$
Nonsimilar-flow cases						
Case \Variable	c	C	PG	Pr	HT	Ma
Howarth [96]	1	1	adverse	NA	adiabatic	NA
NACA0012 [27]	var.*	var.*	favourable-adverse	0.72	adiabatic	< 0.016
Giepman [97]	var.	var.	zero	variable	nonadiabatic	1.7

* Variable, but due to low Mach-number it is effectively a constant equal to 1.

$^{\diamond}$ NB In the simulations a value of Ma = 1000 is taken which is considered as large enough, since infinity is numerically impossible.

4-1-1 Comparison with Other Boundary Layer Programs

The program is compared with two other programs in terms of performance and accuracy of the results: a MATLAB program solving the same set of nonlinear boundary layer equations with the MATLAB bvp4c-solver, from now on called the bvp4c-solver; and a MATLAB program solving the full Navier-Stokes equations in nondimensionalized form using the Chebyshev spectral collocation method. The last program will be referred to as the spectral-solver. The comparison with the spectral-solver is especially interesting because this program is not bounded to the boundary layer assumptions. The problem definition of the following test case is modelled with boundary conditions, i.e., dimensions, and inlet/outlet Mach-numbers similar to those of the ORCHID nozzle. A flat plate flow, i.e. Zero Pressure Gradient (ZPG) flow, with length $L = 0.1$m is simulated for air with: 1) incompressible flow: Mach 0.1, and 2) compressible flow: Mach 2.0. The simulation results obtained with the CS-method are compared with the spectral-solver and the bvp4c-solver in tables 4-2 and 4-3.

Table 4-2: General verification of the program utilizing the CS-method (CSM) [27] by comparison with program characteristics and a few relevant boundary layer characteristics for adiabatic flat plate flow (zero pressure gradient) at $P_0 = 7.8244 \times 10^5$ Pa and $T_0 = 500$K with Mach-number 0.1 and Reynolds-number 9.1e5 for a flat plate with length of 0.10 m for the following MATLAB programs: spectral solver [98], bvp4c-solver [99] and the CS-method (CSM) [27]. Values of the shear parameter $f''(0)$ are listed in compressible Falkner-Skan transformed coordinates.

\Parameter Method	n_x [-]	n_y [-]	Time s	$f''(0)$ [-]	H [-]	δ^* [m]	C_f [-]	r [-]
spectral	9900	40	72	0.332 19	2.5983	1.8128e−4	6.9589e−4	0.8171
bvp4c	111	30 \103*	184	0.332 17	2.5975	1.8075e−4	6.9584e−4	0.8159
CSM	111	81	0.45	0.332 15	2.5989	1.8082e−4	6.9580e−4	0.8158

* NB 30 points for the momentum equation and 103 points for the energy equation.

Table 4-3: General verification of the program utilizing the CS-method (CSM) [27] by comparison with program characteristics and a few relevant boundary layer characteristics for adiabatic flat plate flow (zero pressure gradient) at $P_0 = 7.8244 \times 10^5$ Pa and $T_0 = 500$K with Mach-number 2.0 and Reynolds-number 4.8e6 for a flat plate with length of 0.10 m for the following MATLAB programs: spectral solver [98], bvp4c-solver [99] and the CS-method (CSM) [27]. Values of the shear parameter $f''(0)$ are listed in compressible Falkner-Skan transformed coordinates.

\Parameter Method	n_x [-]	n_y [-]	Time s	$f''(0)$ [-]	H [-]	δ^* [m]	C_f [-]	r [-]
spectral	9900	40	85	0.383 48	5.2060	1.3775e−4	3.0598e−4	0.8205
bvp4c	111	29 \49*	101	0.361 43	5.1679	1.4895e−4	2.8822e−4	0.8243
CSM	111	81	0.67	0.361 40	5.1698	1.4899e−4	2.8820e−4	0.8243

* NB 29 points for the momentum equation and 49 points for the energy equation.

The results show that the CS-method (CSM) is the fastest method for both incompressible and compressible flow. The time taken is around two orders of magnitude lower. The CSM calculation time is of the order of 1 second, while both the spectral- and bvp4c-solver calculation time are of the order of 100 seconds calculated with an Intel i7-6700HQ processor at 2.60 GHz. The mesh grid varies due to constraints of

the spectral-solver, and due to the fact that the bvp4c-solver chooses its own η-grid for improving the accuracy of the solution. At low Mach numbers all three solvers predict the same values for the shear parameter, displacement and momentum thickness. Thus it can be concluded that the same solution is found for the same mathematical model by two different methods. The spectral-solver gives a slightly different solution for Mach-number 2.0. The skin friction coefficient is predicted to be about 6% higher while the displacement thickness is predicted to be about 7.5% lower. The boundary layer equations only consider the losses induced by shear, whereas the spectral-solver program is more general. A possible explanation is that next to shear also other losses become important at higher Mach-numbers which increase the total dissipation inside the boundary layer as modelled by the boundary layer equations.

Concluding, the CS-method calculation time is two orders-of-magnitude lower for about the same accuracy of results. The CS-method is preferred since it can be applied to design and optimisation studies in ORC turbomachinery which would entail many simulations. In addition, the simulation of complex fluid flows is time consuming.

4-1-2 Verification of the Solver

The solver has been verified extensively for a wide range of test cases as discussed above. The Momentum Equation (ME) and Energy Equation (EE) were verified to be solved correctly. The complexity of the test cases was increased step-by-step and case-by-case to study the numerical characteristics of the program. The solver was capable of simulating almost all test cases with accurate results. The solver was not able to find solutions for the test cases characterized by Prandtl-numbers equal to one with infinite Mach-number in combination with high (infinite) heat transfer rates from the flow to the wall. The two most complex test cases are included here: 1) compressible adiabatic similar flow with several pressure gradients (Tab. 4-4, see Rogers [57] Tab. C28) and 2) the nonsimilar decelerating, i.e. Adverse Pressure Gradient (APG) Howarth's flow case (Fig. 4-1 and 4-2).

Rogers [57] claims that his fixed-step size fourth-order Runge-Kutta numerical integration scheme including a Nachtsheim-Swigert iteration scheme reaches an absolute accuracy of within $\pm 5 \times 10^{-5}$. A fixed-step size of $\mathrm{d}\eta = 0.01$ is implemented with a default grid-height of $\eta_e = 6.0$ and an absolute convergence criterion of 5×10^{-6} is used for $f''(\eta \to \infty)$ and $g'(\eta \to \infty)$, whereas an absolute convergence criterion of 5×10^{-7} is used for $f'(\eta \to \infty) - 1$ and $g(\eta \to \infty) - 1$.

Howarth's incompressible adverse PG flow case was verified with several sources [4, 21]. Figures 4-1 and 4-2 illustrate the results of the comparison. The current method is shown to be at least as accurate as the most accurate results considered by Smith [21] and Cebeci [4]. A more extensive comparison is given in Sec. A-5-4 which includes tables with the data plotted in the graphs for reference.

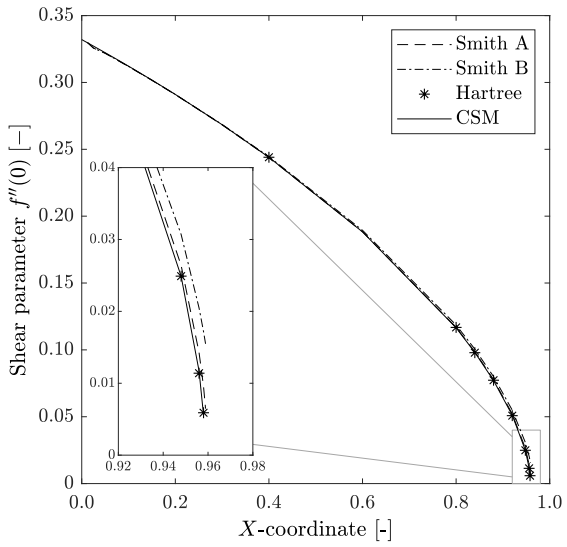

Figure 4-1: Comparison of program with the results obtained from several other programs for an incompressible flow of air as listed in Smith [21]. The sensitive shear parameter is plotted as function of the surface coordinate.

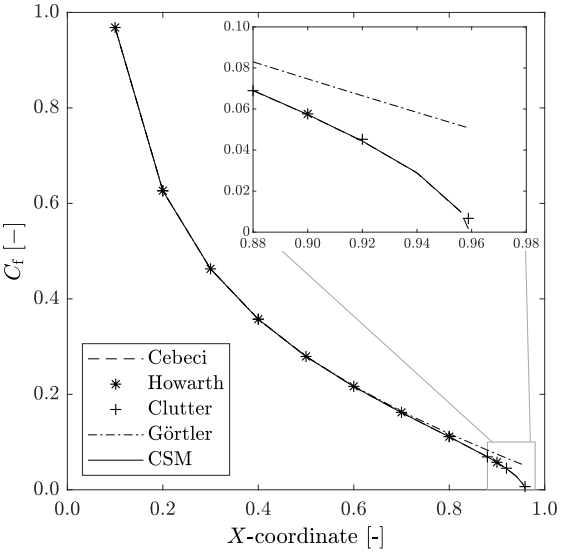

Figure 4-2: Comparison of program with the results obtained from several other programs for an incompressible flow of air as listed in Cebeci [4]. The local skin friction coefficient is plotted as function of the surface coordinate.

Table 4-4: Comparison with tabulated data of adiabatic laminar compressible similar flows with constant nonzero pressure gradients for calorically perfect ideal gas with $C = 1$ (constant) and $\mathrm{Pr} = 0.723$ and $\bar{\sigma} = 2.0 \quad (\mathrm{Ma} = \infty)$ taken from Rogers [57] table C-28. The values obtained with the CS-method (CSM) are transformed from the compressible Falkner-Skan transformed y-coordinate with uniform (vertical) grid spacing of $\mathrm{d}\eta = \sqrt{\frac{2C}{m_2+1}}0.0001$ and height of $\eta_\mathrm{e} = \sqrt{\frac{2C}{m_2+1}}8.0$ to the Illingworth-Levy coordinates ($\mathrm{d}\eta = 0.0001$ and $\eta_\mathrm{e} = 8.0$). Note that separation occurred when the table entry shows 'sep'.

$\hat{\beta}$	m_2	g_aw		$f''(0)$		**Rogers**	**CSM**	**Rogers**	**CSM**
		Rogers	**CSM**	**Rogers**	**CSM**	J_1	$2J_1$	J_2	$2J_2$
1.00	2.499 994e−6	0.814 388	sep	1.152 95	sep	0.866 815	sep	0.286 134	sep
0.50	1.249 995e−6	0.826 698	0.826 691	0.881 723	0.881 713	1.071 83	1.071 785	0.345 808	0.345 823
0.10	2.499 988e−7	0.843 270	0.843 233	0.575 496	0.575 486	1.412 975	1.412 747	0.434 199	0.434 209
0	0.000 000	0.849 464	0.849 389	0.469 600	0.469 603	1.570 195	1.569 703	0.465 967	0.469 585
−0.10	−2.499 987e−7	0.857 375	0.857 094	0.335 283	0.335 395	1.810 908	1.808 755	0.516 373	0.516 197
−0.15	−3.749 980e−7	0.862 319	0.861 761	0.246 432	0.246 848	2.002 835	1.997 853	0.546 857	0.546 338
−0.20	−4.999 973e−7	0.868 479	0.866 773	0.114 397	0.117 393	2.359 336	2.336 963	0.586 263	0.584 018
−0.215 957	−5.398 895e−7	0.870 973	0.867 209	0.01	0.038 176	2.745 153	2.597 303	0.602 836	0.597 049
−0.216 103	−5.402 545e−7	0.871 000	0.867 186	0	0.036 978	2.790 413	2.601 652	0.603 017	0.597 136

4-1-3 Accuracy Study

The first source of numerical error, i.e., the round-off error can be neglected since the simulations are conducted with double-precision variables. The iterative and discretization errors remain. A basic grid refinement study following next will show what minimum grid-spacing must be applied to significantly reduce or remove the influence of the discretization error. The iterative error will be discussed thereafter.

The iterative error can not be determined, but an indication of its magnitude can be obtained by comparison with other codes that use different solution methods. The iterative error is due to the solution method involving linearization applied to the nonlinear differential equations. The tables of comparion with Rogers' tabulated data show the highest accuracy of the current method for zero pressure gradients. However, the more complex the system of equations becomes (with increasing pressure gradient, and heat transfer), the larger the deviations, and thus the larger the iterative error. The iterative error is more pronounced for adverse pressure gradients. Generally it is shown to be small. Knowing the effect of step-sizes on the discretization error, and obtaining an indication of the magnitude of iterative error from Tables A-1 to A-6, it can concluded that their influence is only small. Therefore, considerable deviations in simulation results for real flow cases can be attributed safely to modelling errors.

Concluding, it can be said that the CS-method as applied here gives satisfying results for the solution of the problem using a uniform grid with spacing of $d\eta = 0.01$ for laminar flows, for which the discretization error has been minimized. All studies have been performed with a convergence criterion of 1×10^{-5} for changes in the shear parameter at the wall between consecutive iterations. The reader should be aware that these results are not directly applicable to turbulent flows. The characteristics of the turbulence model allow for a less stringent convergence criterion for turbulent flow in combination with a stretched grid (see eq. 3-54). A smaller grid-spacing close to the wall is needed to resolve for the laminar sublayer close to the wall. A stretched grid is applied to reduce the calculation time while preserving the same accuracy.

Finally, an overview of the solver test cases is given here. The complete solver verification process is included in Sec. A-5. In Sec. A-6 basic grid refinement studies are listed that were performed for the following test cases:

1. Falkner-Skan wedge flows, effect of increasing number of grid points in uniformly spaced grid on shear parameter at wall;

2. Falkner-Skan wedge flows, effect of increasing number of grid points in uniformly spaced grid on form factor;

3. Adiabatic similar flows of several pressure gradients at infinite Mach-number, effect of increasing number of grid points in uniformly spaced grid on wall enthalpy ratio;

4. Adiabatic similar flows of several pressure gradients at infinite Mach-number, effect of increasing number of grid points in uniformly spaced grid on shear parameter at wall;

5. Nonsimilar Howarth's flow case with decelerating flow, effect on shear parameter at wall for:

   (a) grid-refinement of η-coordinate;

   (b) grid-refinement of X-coordinate;

   (c) Combination of both η- and X-coordinate grid refinement.

A uniformly spaced (vertical) grid was taken for the similar cases in which the spacing was refined step-wise. Tables A-10 to A-13 list the refined η-coordinate together with the obtained solution. Table A-13 is included below as Table 4-5. For the nonsimilar case of Howarth both X-coordinate and η-coordinate were refined to find the dependence on both grid parameters. Tables A-15 to A-16 show a refinement in η-coordinate, X-coordinate and a refinement in both coordinates respectively. The last table thus combines both and is included below as Tab. 4-6. From these tables it can be seen that choosing a uniform η-coordinate spacing of $\mathrm{d}\eta = 0.01$ and a uniform X-coordinate spacing of $\mathrm{d}X = 0.001$ guarantees a negligible discretization error for Howarth's flow case. Notice however that the grid spacing in the X-coordinate direction is strongly dependent on the geometry and type of flow. Table 4-5 below can be used to set the grid parameters at hand to tailor them to the user's specific needs.

Table 4-5: Accuracy study with adiabatic laminar compressible similar flows with constant nonzero pressure gradients for calorically perfect ideal gas with $C = 1$ (constant) and $\mathrm{Pr} = 0.723$ and $\bar{\sigma} = 2.0 \quad (\mathrm{Ma} = \infty)$ based on tabulated data obtained from Rogers [57] table C-28 and the method following the example of Cebeci [4] table 8-3. The convergence criterion used was $|\mathrm{d}f''(0)| < 1e-5$. The values obtained with the CS-method (CSM) are in transformed compressible Falkner-Skan coordinates with grid height of $\eta_\mathrm{e} = 8.0$. Note that separation occurred when the table entry shows 'sep'.

$\hat{\beta}$	m_2	f_0'' [-]						
		$\mathrm{d}\eta = 1.0$	$\mathrm{d}\eta = 0.5$	$\mathrm{d}\eta = 0.2$	$\mathrm{d}\eta = 0.1$	$\mathrm{d}\eta = 0.01$	$\mathrm{d}\eta = 0.001$	$\mathrm{d}\eta = 0.0001$
1.00	2.499 994e−6	sep	sep	sep	sep	sep	sep	sep
0.50	1.249 995e−6	0.614 389	0.621 157	0.623 095	0.623 373	0.623 465	0.623 466	0.623 466
0.10	2.499 988e−7	0.403 793	0.406 173	0.406 811	0.406 901	0.406 930	0.406 930	0.406 930
0	0.000 000	0.330 122	0.331 604	0.331 988	0.332 041	0.332 059	0.332 059	0.332 059
−0.10	−2.499 987e−7	0.236 303	0.236 982	0.237 134	0.237 154	0.237 160	0.237 160	0.237 160
−0.15	−3.749 980e−7	0.174 324	0.174 542	0.174 550	0.174 549	0.174 548	0.174 548	0.174 548
−0.20	−4.999 973e−7	0.084 756	0.083 560	0.083 103	0.083 033	0.083 009	0.083 009	0.083 009
−0.215 957	−5.398 895e−7	0.034 723	0.029 419	0.027 409	0.027 099	0.026 996	0.026 995	0.026 995
−0.216 103	−5.402 545e−7	0.034 076	0.028 635	0.026 575	0.026 255	0.026 148	0.026 147	0.026 147

Table 4-6: Accuracy study with nonsimilar Howarth's Flow: incompressible adiabatic decelarating flow (adverse pressure gradient) following the example of Cebeci [4] table 8-4. The convergence criterion used was $|\mathrm{d}f''(0)| < 1e-5$. The values obtained with the CS-method (CSM) are in transformed compressible Falkner-Skan coordinates with grid height of $\eta_\mathrm{e} = 9.0$.

X [-]	$f''(0)$ [-]						
	$\mathrm{d}\eta = 1.0$ $\mathrm{d}X$	$\mathrm{d}\eta = 0.5$ $\mathrm{d}X/2$	$\mathrm{d}\eta = 0.2$ $\mathrm{d}X/4$	$\mathrm{d}\eta = 0.1$ $\mathrm{d}X/8$	$\mathrm{d}\eta = 0.01$ $\mathrm{d}X/16$	$\mathrm{d}\eta = 0.001$ $\mathrm{d}X/32$	$\mathrm{d}\eta = 0.0001$ $\mathrm{d}X/64$
0	0.330 121	0.331 604	0.331 986	0.332 040	0.332 057	0.332 057	0.332 057
0.0125	0.327 878	0.329 231	0.329 574	0.329 622	0.329 638	0.329 638	0.329 638
0.025	0.325 621	0.326 842	0.327 145	0.327 187	0.327 200	0.327 201	0.327 201
0.050	0.321 057	0.322 011	0.322 232	0.322 262	0.322 272	0.322 272	0.322 272
0.075	0.316 427	0.317 107	0.317 246	0.317 264	0.317 270	0.317 270	0.317 270
0.100	0.311 729	0.312 130	0.312 184	0.312 189	0.312 191	0.312 191	0.312 191
0.150	0.302 114	0.301 941	0.301 820	0.301 800	0.301 793	0.301 793	0.301 793
0.200	0.292 200	0.291 423	0.291 117	0.291 070	0.291 055	0.291 055	0.291 055
0.300	0.271 358	0.269 286	0.268 582	0.268 477	0.268 442	0.268 441	0.268 441
0.400	0.249 009	0.245 463	0.244 302	0.244 131	0.244 074	0.244 073	0.244 073
0.600	0.198 419	0.191 113	0.188 744	0.188 393	0.188 276	0.188 275	0.188 275
0.800	0.135 991	0.121 994	0.117 212	0.116 479	0.116 236	0.116 232	0.116 232
0.840	0.121 132	0.104 822	0.099 108	0.098 228	0.097 935	0.097 931	0.097 931
0.880	0.105 076	0.085 611	0.078 453	0.077 329	0.076 952	0.076 948	0.076 947
0.920	0.087 432	0.063 138	0.053 180	0.051 517	0.050 951	0.050 945	0.050 944
0.948	0.073 784	0.043 792	0.028 576	0.025 471	0.024 338	0.024 324	0.024 323
0.956	0.069 628	0.037 241	0.018 112	0.012 957	0.010 652	0.010 621	0.010 620
0.958	0.068 569	0.035 493	0.014 744	0.007 909	0.003 203	0.003 104	0.003 099
0.9589	0.068 089	0.034 689	0.013 034	0.000 000	sep	sep	sep
n_{η_points}	10	19	46	91	901	9001	90001
$n_{\mathrm{X}_\mathrm{stations}}$	19	37	73	145	289	577	1153

4-2 Verification Test Cases

This section proves the successful transformation and implementation of the FORTRAN code obtained from Cebeci [27] to MATLAB, by verification with the NACA0012 airfoil case obtained from the same reference. Furthermore, it proves the successful implementation of the turbulent Prandtl-number model obtained from Cebeci [4] in supersonic laminar-turbulent flows with heat transfer obtained from Giepman [97].

4-2-1 NACA0012 Airfoil: Laminar, Transitional and Turbulent Flow

The NACA0012 airfoil test-case obtained from Cebeci [27] is a highly suitable test-case for the verification of the boundary layer program. It includes a variety of phenomena in adiabatic flow: stagnation point flow (leading edge), laminar flow, priorly fixed (forced) point of transition, transitional flow, turbulent flow, and prediction of separation close to the trailing edge. Therefore, it was used by Cebeci [27] to prove the functionality of his enclosed FORTRAN program. The current MATLAB computer program was verified with the results from this FORTRAN program included in the book *Convective Heat Transfer* by Cebeci (2002) [27] from which the currently implemented solver was copied. Both program solutions coincide in Fig. 4-3 up to the 4th or 5th digit, which is the amount of digits printed as output by the FORTRAN program. Therefore, only the solution obtained with the MATLAB boundary layer program is shown. These results prove a correct transformation from FORTRAN code to MATLAB code, and a correct mathematical solution of the problem. The program takes around 1 second for the calculation of this stagnation point airfoil with 105 stations including laminar flow, transition, turbulent flow and prediction of separation for calorically perfect ideal gas air.

Calorically perfect ideal gas was assumed, a constant Prandtl-number of 0.72 was taken and the dynamic viscosity was determined with Sutherland's Law for air. The maximum Mach-number reached is almost 0.016 and thus the flow is effectively incompressible. Figure 4-3 shows three important boundary layer characteristics. The shape factor, which is considered to be the most sensitive boundary layer parameter [66]). Furthermore, the displacement thickness, which is important for viscous nozzle designs. And, the local skin friction coefficient, which can be measured directly and which is related to the losses induced by the boundary layer. Further details, such as the geometry, are included in Sec. A-7.

Note that Coles [83] lists many suitable cases for adiabatic incompressible two-dimensional steady state boundary layer flows. Cebeci [27,61] has shown that the program is capable of simulating a selection of these cases. According to the author, it can be assumed safely that these cases are also predicted accurately by the current MATLAB program since the program code and the (CS-)method implemented are essentially the same for incompressible flows, and especially since the NACA0012 case is simulated with the same accuracy as the FORTRAN program from Cebeci [27].

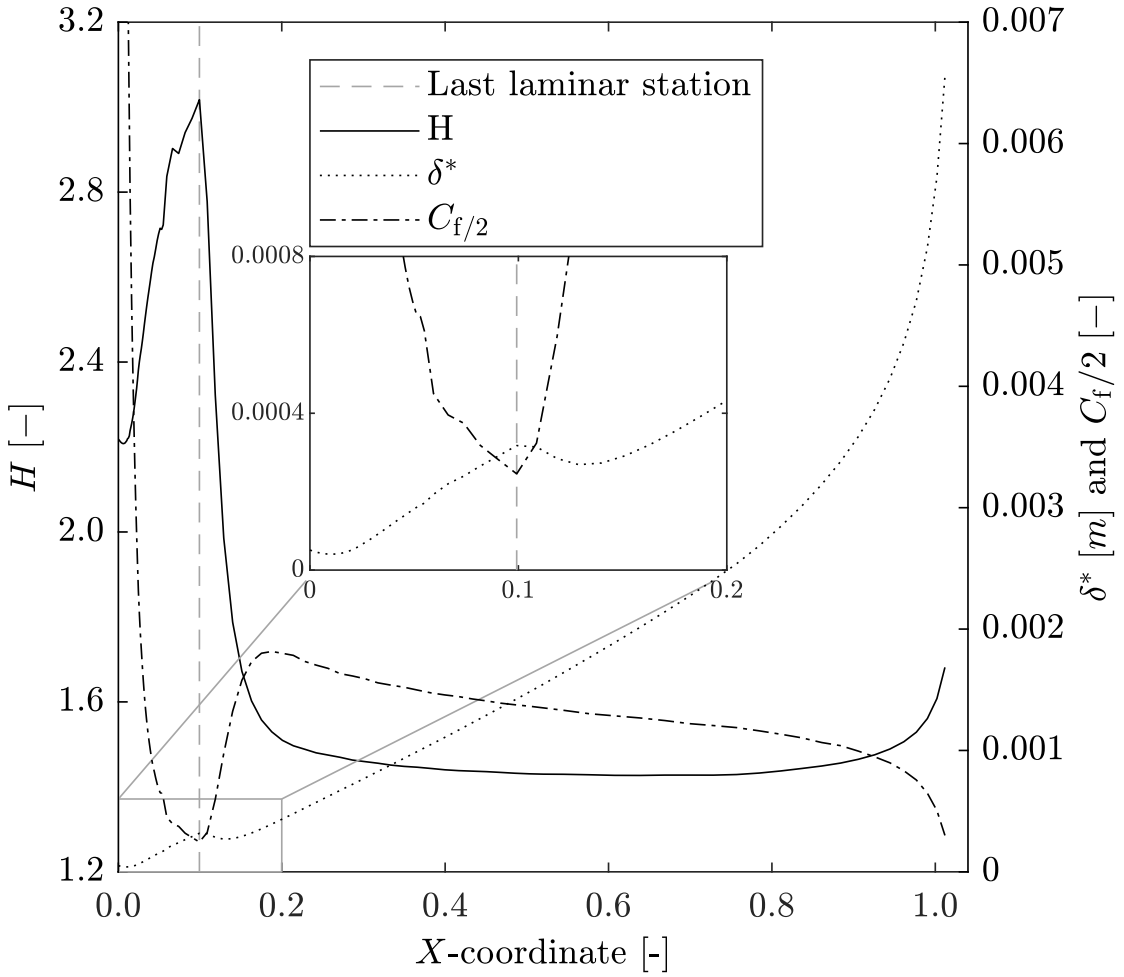

Figure 4-3: Shape factor, boundary layer displacement thickness and skin friction coefficient for the NACA0012 airfoil test-case from Cebeci [27]. This test-case includes: stagnation point flow, laminar flow, transitional flow, turbulent flow, and separation close to the trailing edge. Only the results obtained from the MATLAB boundary layer program are shown, since the results superpose with those obtained from the FORTRAN program [27].

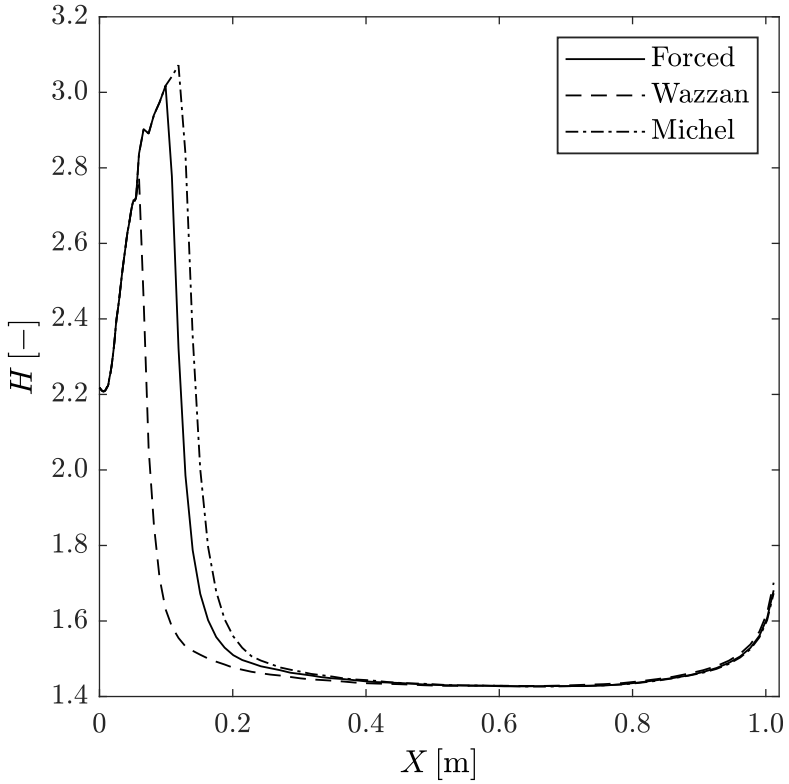

Figure 4-4: Comparison of Wazzan's H-Re_x-method [32] and modified Michel's method [33] for prediction of transition discussed in Ch. 2 compared with the forced transition location from Cebeci [27] using the NACA0012 test case.

4-2-1-1 Engineering Transition Prediction Methods

The NACA0012 airfoil test-case with its known transition location can also be used to verify if the transition prediction methods have been implemented correctly, and how they perform. Figure 4-4 shows the prediction of transition location with two methods, using Wazzan's H-Re_x-method [32] and the modified Michel's method [33]. The predicted transition locations are considered to be sufficiently close by the author for engineering estimate methods.

4-2-2 Simulation of a Cooling Flat Plate

A cooling flat plate is an appropriate test case for assessing if the energy equation has been successfully implemented. The program is verified on basis of Stanton-numbers for steady state heat transfer in laminar flow of Mach-number 1.7 with an isothermal wall with the spectral-solver written by Groot [98] mentioned in Sec. 4-1-1 of this chapter. The isothermal wall input for these simulations was obtained from measurements by Giepman [97].

4-2-2-1 Description of Case

Giepman [97] studied the shift in transition front downstream on a cooling flat plate in supersonic flow of Mach-number 1.7 at a unit Reynolds-number of around 3.5×10^7. The flat plate was heated prior to the test run with a lamp, after it was cooled down by the flow. Through infrared thermography measurements the plate's wall temperature was measured. The heat flux was determined by solving the unsteady heat conduction equation inside a two-dimensional slice of the plate, using the measured wall temperatures from the top surface of the plate and assuming the wall temperature of the bottom of the plate equal in value. The last assumption, meaning that the heat transfer coefficient on the top and bottom of the plate were the same, turned out not to be the case. It turned out that the heat transfer on the bottom of the plate was probably higher, inducing a heat flux inside the plate towards the bottom, resulting in different Stanton-numbers. For the experiment of Giepman this was not a problem, since the Stanton-numbers were used as indication for the point of transition. The spectral-solver was used to verify the measured values for laminar flow, since the Reynolds analogy is not valid here which was used to calculate the laminar reference solution shown also in Fig. 4-5. For the calculation of the experimentally derived Stanton-numbers conservative values for the recovery factor were assumed to calculate the adiabtaic wall temperature in the laminar ($r_{\mathrm{L}} = 0.84$) and turbulent ($r_{\mathrm{T}} = 0.89$) flow regions respectively. The time scales of the transient cooling process were such that the experimental results can be considered as steady state [66].

4-2-2-2 Implementation

The inlet total conditions and the free stream conditions were set as input together with an adiabatic wall (zero heat flux condition) to calculate the adiabatic wall temperature with the boundary layer program first. In a second calculation the measured wall temperature for each time was set as input and the previously adiabatic wall temperature distribution was used for calculation of the Stanton-number for comparison. The point of transition was forced for each calculation at the minimum Stanton-number (dip) in the experimental data as shown in Fig. 4-5. The results of the simulation were plotted in the same graph together with the experimentally derived Stanton-numbers, the laminar and turbulent reference solutions, and the simulation results obtained from the spectral-solver.

4-2-2-3 Results

The steady state solutions of Stanton-numbers for isothermal wall calculations with the spectral-solver where used for the verification of laminar heat transfer predicted by the program. Figure 4-5 shows that the Stanton-numbers predicted by the boundary layer program match with those obtained from the spectral-solver. The boundary program predicts values that are only slightly smaller, but the difference is negligible.

The experimentally derived Stanton-numbers by Giepman are considered by the author as not reliable enough for a sound validation of the program, due to uncertainties in the numerical and physical values of recovery factors[2]. Note however, that for the first profiles the angle of the transition regions match, and that this angle decreases with time which is also predicted by the program. This is an interesting result. Remember that the intermittency relation applied here for the prediction of transitional flow was explicitly stated to be calibrated only for adiabatic flows. Furthermore, notice that the turbulent values of the reference and the experiment are both influenced by a conservative estimate of the recovery factor. On top of that, the real heat flux might be different due to slightly different conditions on the bottom of the plate.

[2]The recovery factor is a function of 1) The flow condition; 2) the Prandtl-number; and 3) The geometry probably, which is the uncertain factor, since it is unknown to the author how it is related exactly to the recovery factor.

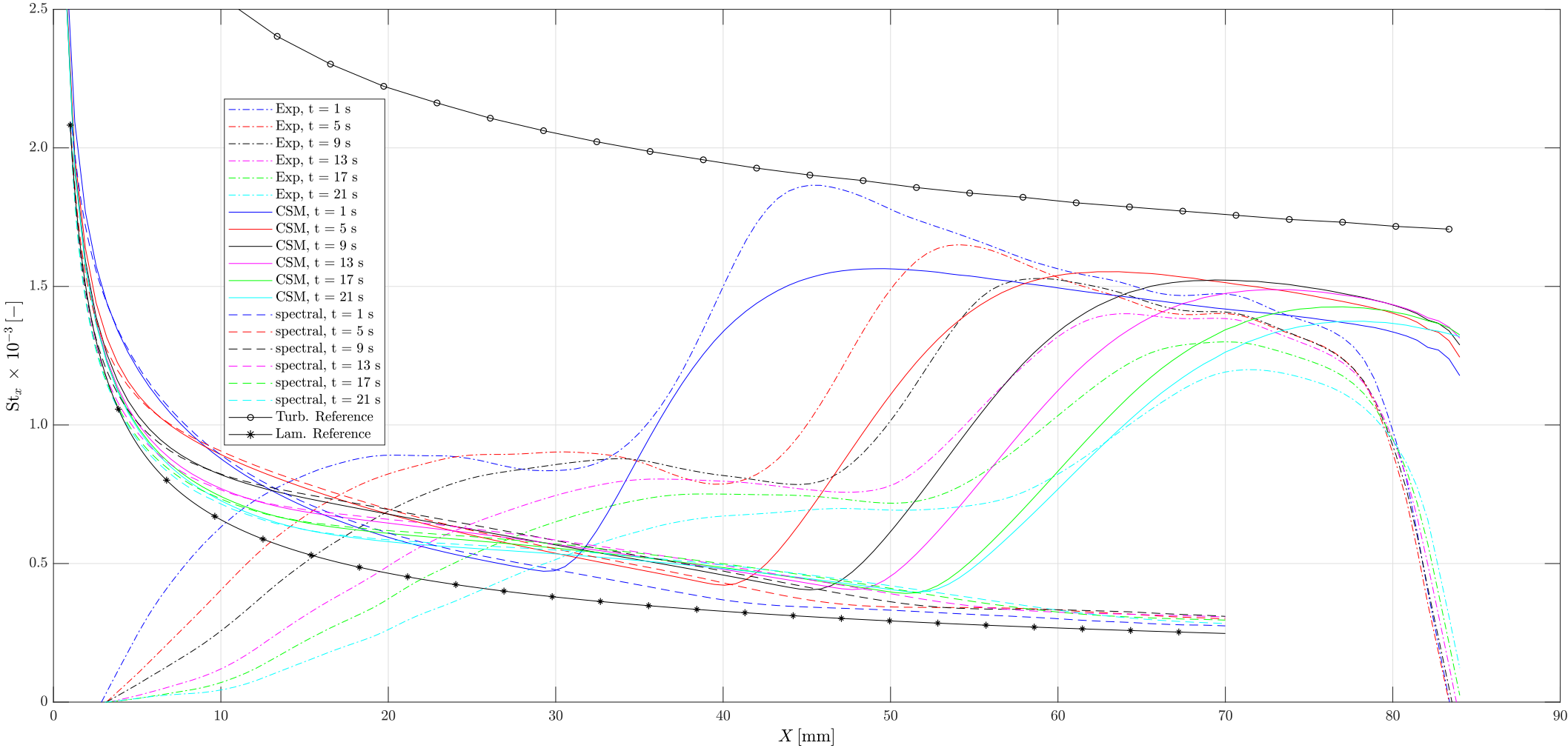

Figure 4-5: Comparison of steady state simulations of a cooled flat plate boundary layer flow at Mach-number 1.7 with forced transition location with steady state laminar simulations and transient experimental data of Stanton-number. Note that laminar and turbulent recovery factors were estimated for both experimental and simulated Stanton-numbers by the spectral-solver. Obtained from Giepman [97].

4-3 Validation Test Cases

The computer program needs to be compared with experimental data to learn about its validity and to add to its credibility. The objective of validation [93], following (numerical) verification, is to find and quantify physical modelling errors. Physical modelling errors are a result of the assumptions made to simplify the physical phenomenon to a mathematical model. Therefore, evaluating the capabilities of the program with experimental data is needed before any predictive simulations can be made.

Table 4-7 presents the cases chosen for validation of the boundary layer program. The experimental data of these cases have the following characteristics:

1. BL thickness, starting from Stagnation Point (SP), laminar, transition and turbulent flow (NACA0012 airfoil);
2. Turbulent boundary layer development on flat wall in supersonic nozzle;
3. Turbulent boundary layer development on curved wall in supersonic nozzle; and,
4. Detailed turbulent boundary layer characteristics in zero PG at a single station for a range of Mach-numbers.

The NACA0012 airfoil serves as validation case for laminar, transitional and turbulent stagnation point flow. It is the only case containing measured laminar boundary layer characteristics as far as known by the author. The combination of these flow types is the importance of this case, and the complete pressure history is known. The next step is proving the predictive capacity of the boundary layer program by comparison with the (turbulent) boundary layer development on a flat wall inside a supersonic nozzle. In addition, the same case contains a curved wall for comparison. Last, and most important, an extensive validation case is needed to evaluate the predictive capacity of the algebraic turbulence model in supersonic flows.

Table 4-7: Validation of the boundary layer program with several adiabatic cases obtained from literature. A flexible-walled converging-diverging de Laval nozzle with a length of around $20\,\mathrm{m}$, where boundary layer charcteristics were measured at the last station only. The case was found in Fernholz & Finley [101] and the experimental data was obtained from the original work by Winter & Gaudet [100] complemented with estimated data by Fernholz & Finley [101]. Furthermore, two cases obtained from McNally [48] contain the full range of measured displacement and momentum thicknesses. The Reynolds-numbers in the table belong to the last station only.

Experimental data of turbulent flows							
Case \Variable	Geometry	PG	HT	Ma $[-]$	$\mathrm{Re_e}$ $\times 10^7\,[\mathrm{m^{-1}}]$	Re_x $\times 10^7\,[-]$	Re_θ $\times 10^3\,[-]$
McNally [48] NACA0012	airfoil	fav.-adv.	isothermal	< 0.34	0.6	1.0	17
McNally [48] Flat-wall	nozzle	favourable	isothermal	$0.49 - 1.10$	1.5	1.5	4.4
McNally [48] Curved-wall	nozzle	favourable	isothermal	$0.48 - 2.02$	1.2	1.2	2.4
Winter & Gaudet [100, 101] profile 2	flat plate	zero	adiabatic	0.2	0.7	23	96
Winter & Gaudet [100, 101] profile 12	flat plate	zero	adiabatic	1.4	0.7	22	58
Winter & Gaudet [100, 101] profile 19	flat plate	zero	adiabatic	2.2	0.4	13	30
Winter & Gaudet [100, 101] profile 26	flat plate	zero	adiabatic	2.8	0.7	22	38

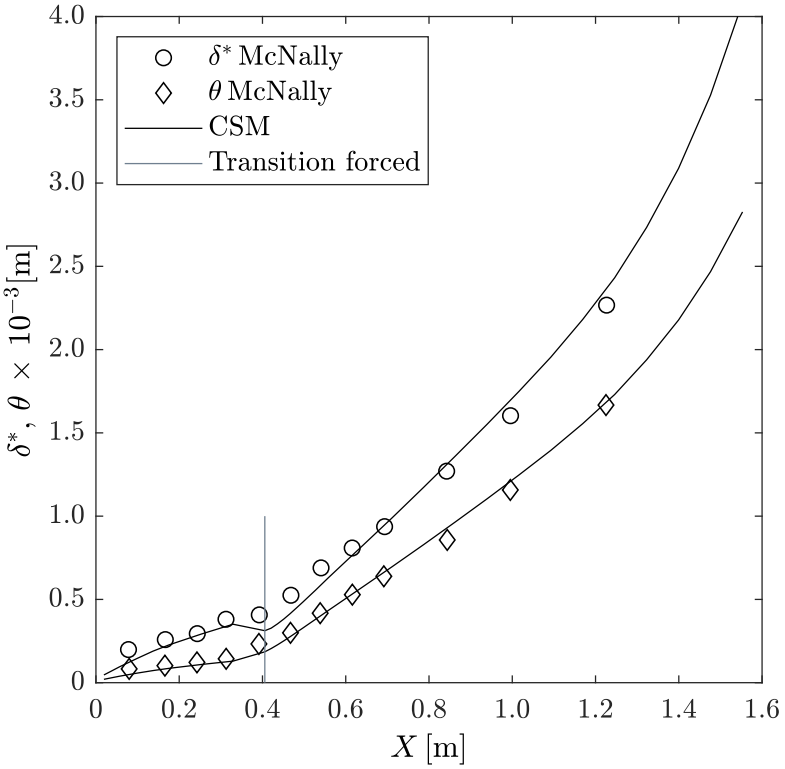

Figure 4-6: Comparison between the experimental data of McNally [48] and the prediction from the CSM. δ^*: displacement thickness, θ: momentum thickness. The vertical grey line indicates the station where transition from laminar to turbulent flow has been forced.

4-3-1 Boundary Layer Thickness along a NACA0012 Airfoil

The program is validated here with experimental data of a NACA0012 airfoil at zero angle of attack in a free stream flow with Mach-number 0.284. The experimental data was obtained from McNally [48] and includes the boundary layer displacement and momentum thicknesses. The free stream conditions (surface pressure), total (inlet) conditions and the isothermal wall temperature were listed, and taken as program input. The point of transition was estimated from plotted data in McNally [48], and the transition station was set (forced) beforehand at station 10 ($X = 0.41\,\mathrm{m}$). Figure 4-6 depicts the simulation results compared with the experimental data. The vertical line indicates where transition was forced. The test case was also simulated with the transition methods of Michel and Wazzan (not shown). Michel's method gives a closer prediction to the point of transition when compared with the method of Wazzan, which predicts the transition point too early. The author speculates that this is related to the curvature of the airfoil, for which Michel's method was developed (see Sec. 2-5 for more details on both methods).

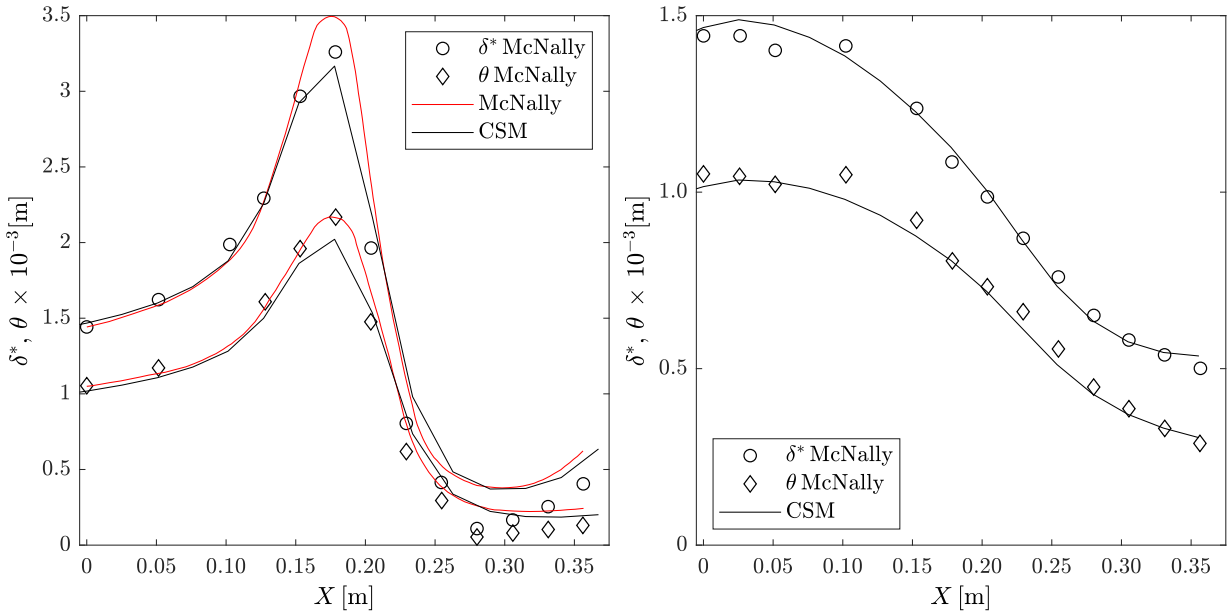

Figure 4-7: Comparison with boundary layer displacement and momentum thickness derived from velocity profile measurement along the walls of an asymmetric two-dimensional nozzle: (left) Curved wall and (right) flat wall. Data obtained from McNally [48]. The results for the flat walled nozzle match around the throat region (right), whereas the results for the curved wall (left) deviate significantly.

4-3-2 Boundary Layer Thickness along Supersonic Nozzle Walls

The program is validated here with experimental data obtained from McNally [48] and includes the boundary layer displacement and momentum thicknesses. The free stream conditions (surface pressure), total (inlet) conditions and initial boundary layer displacement and momentum thicknesses, and the isothermal wall temperature were listed, and taken as program input. The data was referred to as not reported before, and no reference was mentioned except that the measurements were taken at the Glenn Research Center at Lewis. An inlet length under zero pressure gradient conditions had to be calculated and was added to the geometry to arrive at the initial boundary layer thicknesses as listed by McNally.

The two-dimensional nozzle was asymmetric and contained a flat wall and a curved wall. The curved wall induced a pressure gradient, which was stronger on the curved wall than on the flat wall. The flow was considered fully turbulent. McNally reports that the agreement of prediction and measurements on the flat wall is extremely good, but that there are some doubts about the experimental data on the converging-diverging section of the curved wall. He attributes the differences between prediction and measurements to the difficulty of determining the boundary layer edge from the velocity profiles due to the curvature of streamlines.

Figure 4-7-a and 4-7-b present the experimental data together with the prediction by

McNally and by the boundary layer program implemented in this thesis. McNally succesfully predicts both displacement and momentum thickness up to and including their maxima for the curved wall, Fig. 4-7-a. After the maxima McNally overpredicts the experimental data. The boundary layer program uses a coarser grid and thus predicts the trends with lower accuracy. Nevertheless, the results for fully turbulent flow are close to those found by McNally. The boundary layer program almost superposes the prediction by McNally (based on momentum integral method) when the curved nozzle wall and the free stream pressure distribution are interpolated (Fig. A-7 in App. A). In addition, Fig. 4-7-b shows that the predicted momentum thickness results of the flat wall correspond within a maximum 5% deviation of the experimental values.

The results of the curved wall are over predicted by both programs after the maxima in thicknesses. For the curved wall the trend after the throat predicted by both programs and the experimental data is the same, showing an increase in thicknesses, but the sizes of the predicted thicknesses do not correspond with the measurements. The measured values become lower already after the maxima in thicknesses, where the pressure starts to decrease rapidly. Therefore, the author expects that relaminarization occurs shortly after the maxima for the curved wall. In addition, the trend of the last three measured flat wall stations indicates further decreasing thicknesses on the flat wall in contrast to both programs which predict a trend back to horizontal.

The author speculates that the low values of measured boundary layer thicknesses might be attributed to relaminarization, the re-transition from turbulent to laminar flow. The engineering estimate of Nash & Webber [34] was not able to predict this. Furthermore, to investigate the influence of wall curvature on the boundary layer, the radius of curvature R was estimated to be 0.09 m and the boundary layer velocity thickness $\delta = 0.005$ which results in the ratio

$$\frac{\delta}{R} = \frac{0.005}{0.09} = 0.06 < 1.0. \tag{4-1}$$

This value is small, but not much smaller than one. In this case, the velocity profiles might be affected by the curvature indeed. Note that δ is predicted by the boundary layer program for fully turbulent flow. The velocity thickness will become lower when relaminarization takes place. For laminar flow the effect of curvature is negligible since the velocity thickness then is much smaller compared to the radius of curvature.

The complete results for the flat wall and curved wall are presented in App. A section A-8, including the added inlet length. The results of the flat wall comparison match, but the results of the curved wall deviate considerably towards the nozzle throat. The pressure input is also shown. Note that the wall surface pressure ratio along the curved wall shows an increase in pressure, just before the converging section starts, resulting in a maximum.

4-4 Validation of the Algebraic Turbulence Model

The algebraic turbulence model is validated here with experimental data of zero pressure gradient adiabatic flows obtained from Winter & Gaudet [100] by comparison of Mach-number, velocity and density profiles, and boundary layer characteristics for a range of Mach-numbers in adiabatic flow varying from low Mach-number incompressible flow to highly compressible supersonic flow of zero pressure gradient. The objective is to show that the algebraic turbulence model is capable of simulating the compressibility effects present in supersonic nozzles. First, the selection criteria of a suitable test case are discussed. Then, the test set-up is discussed together with the accompanied uncertainties in collecting the data. The methods and assumptions were listed which were used to arrive at the tabulated data. Then the implementation is described followed by the results of the comparison.

4-4-1 Selection of a Detailed Turbulent Test-Case

Cebeci and Smith have calibrated their CS-model as discussed in Ch. 3. There it was concluded that the semi-empirical model has a suitable form for two-dimensional steady state boundary layer flows, and that there are not many coefficients to calibrate. Cebeci and Smith [79] developed their model first for incompressible flows, and later extended it to also include simulation of compressible flows [80]. Later, the model was validated [61] with a variety of cases obtained from the extensive library of incompressible adiabatic turbulent flows listed by Coles [83]. Validation of the currently implemented form of the CS-model with a similar extensive library of compressible flows from, for example the AGARD-library, is not known to the author. The currently implemented CS-model takes into account the change in density along the nozzle expansion, since the relations are scaled with the local boundary layer edge density, although it is unknown how the model performs in predicting the boundary layer in a de Laval nozzle. But first, let us see if the program is capable of predicting the large density gradient inside the boundary layer for highly compressible flows up to Mach-numbers just above Mach 2.0. To answer this question, a suitable experimental data set is needed for comparison. The requirements used for the test-case that was selected were based on the ORCHID nozzle geometry and conditions (similarity of dimensionless groups) as much as possible. The main criteria are listed here:

1. Steady state flow;
2. Two-dimensional (flow) geometry;
3. Mach-number in range of the ORCHID nozzle ($0.3 < \mathrm{Ma} < 2.0$);
4. Pressure history well documented (BL edge conditions); and,
5. Adiabatic flow, preferably complemented by heat transfer under same conditions.

The AGARD-library of compressible turbulent flows was studied and the listed test-cases were evaluated with above criteria. Appendix B gives a tabulated overview of all studied test-cases from Fernholz & Finley [101,102] and their properties. Of all, only one test-case was found that met above criteria sufficiently. Experimental data of measured boundary layer characteristics inside nozzles are unknown to the author, except for those by McNally [48], and Duff [53].

The case of Winter & Gaudet [100] was finally chosen since it met most criteria. Most importantly, it was well documented and included as one of the fewest cases an almost complete pressure history, which was believed to be necessary to predict the boundary layer thickness at the measurement station. On top of that it was a very consistent experimental measurement campaign in which the Mach-number was varied systematically from low (incompressible) to relatively high supersonic Mach-numbers (highly compressible flow) with the same measurement apparatus. Table 4-7 lists the four different profiles taken to validate the program.

4-4-2 Case Description

Zero pressure gradient steady state adiabatic supersonic flows at the outlet of a two-dimensional de Laval nozzle were studied for a range of Mach-numbers varying in steps of 0.2 from 0.2 up to 2.8. The objective of the experiment was to find a simple method for estimating the skin friction in compressible adiabatic flows. Therefore, the measured effects of increased compressibility on the boundary layer characteristics with increasing Mach-number was well documented. The Mach-number was increased systematically with a constant step and measurements were made in a consistent manner with the same measurement apparatus at a single station close to the outlet in zero pressure gradient adiabatic flow. The data is highly suitable for comparison and analyzing trends due to the consistent and systematic approach. These combined characteristics make this case very suitable for the validation of the algebraic turbulence model regarding the effects of compressibility.

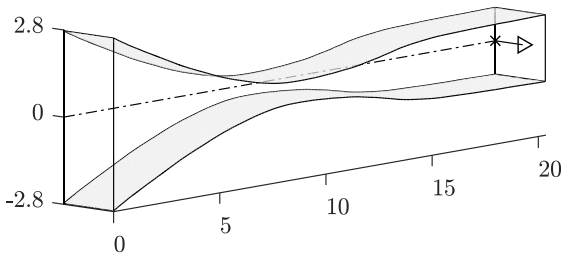

Figure 4-8: Flexible-walled nozzle geometry for Mach 2.8. Dimensions in meters.

4-4-3 Methods used in the Experiment

The wind tunnel was continuously operated and of the closed-circuit type. The two-dimensional nozzle (Fig. 4-8) was about 20 m long (diverging section about 10 m) and had a flexible-walled top and bottom actuated by hydraulic jacks. The Mach-number was varied from values of 0.2 to 0.8 and from 1.4 up to 2.8 in steps of 0.2 with about the same total conditions for constant unit Reynolds-number; and series of runs with Mach 0.2 and 2.2 while varying the total conditions for obtaining different unit Reynolds-numbers. The single measurement station was located at the end of the nozzle in the center of the flat back wall where the Mach-number converged to its final value within 1% for the last 25% of the nozzle diverging section resulting in an effectively zero pressure gradient flow.

Skin friction, total pressure profiles and total temperature profiles were measured at the same station, but for separate runs. The skin friction was measured by a large floating element balance plate which size made it possible to make pressure and temperature corrections for highly accurate results. Total temperature profiles were measured with 49 round pitot tubes, divided over columns to avoid interference. The total temperature profiles were measured with 13 stagnation temperature probes of the vented tube type. The profile data was matched by graphical interpolation based on the normal wall distance (Y-coordinate), and the skin friction and profile data were matched based on the unit Reynolds-number.

The data was listed in the report by tabulating for each profile number the measured Mach-number, unit Reynolds-number (iterated) and total temperature outside the boundary layer, and the skin friction at the wall, together with the Mach-number profile (based on total pressure measurements), velocity profile and density profile (inverse temperature ratio for Ideal Gas) both based on measured temperature. Velocity and density profiles calculated for a recovery factor of 1.00 and 0.89 were also listed for comparison. The Mach-number profiles were derived from total and static pressures with state-of-the-art[3] methods which are unknown to the author. The velocity profiles were also derived with state-of-the-art[3] methods unknown to the author. The patterns observed in the experimental values of absolute Mach-number and relative velocity suggest that both temperature and pressure measurements might have been used to arrive at the listed velocity profiles underneath the header *measured temperature*. Air was assumed to follow the ideal gas law. And the boundary layer assumption of zero pressure gradient in the Y-coorindate direction was applied. Combining both results in relating the density ratio with the temperature ratio by $\frac{\rho_e}{\rho} = \frac{T}{T_e}$. Sutherland's Law was applied for finding the dynamic viscosity.

[3]State-of-the-art 1970, while the first flight of the Concorde took place in 1969.

4-4-4 Uncertainties in the Experimental Data

Uncertainties could not be quantified by the researchers [100, 101], but they called their collected data self-consistent. Several indications were given that support the reliability of the test set-up and that of the experimental data. Accidental oil leakages for example were reported to indicate parallel streamlines. Measured temperatures related to the floating element balance indicated wall temperatures close to adiabatic values, and in some cases possibly with slight heat transfer to the flow. Wall temperatures were not measured as part of the experiment.

The point of transition from laminar to turbulent flow is unknown. However, Winter & Gaudet [100] could estimate the effective turbulent length successfully for the four Mach-numbers that were thus chosen in this validation study. The effective turbulent length was estimated by obtaining the length scale from the momentum integral using the measured skin friction and derived unit Reynolds-numbers for these cases. They showed graphically that the measurements and theory matched within 2% for this relationship. The onset of transition from laminar to turbulent flow however remains unknown.

Measured temperatures and pressures close to the wall are generally found to be higher due to wall interference, as discussed by Coles [83]. Fernholz & Finley [101] comment that substantial probe corrections can reasonably be applied to the points closest to the wall as indicated by the log-law plots. Furthermore, they note that measurements did not always extend within the momentum-deficit peak and thus integral values obtained from these profiles tabulated by Winter & Gaudet [100] should be treated with caution.

Out of the numerous profiles reported by Winter and Gaudet, number two should be considered with caution for validation purposes since it was considered by the authors to be the least accurate. The air bypass slots were used for Mach-numbers above 2.2. The authors mention that they do not know the effect of bypassing air on the total temperature downstream. The authors themselves consider the series of experiments for Mach 2.2 as the most accurate. Fernholz & Finley [101] did not list the Mach-number profiles based on the pressure measurements, but only the velocity and density profiles based on the temperature measurements which they considered the most consistent.

4-4-5 Implementation of the Validation Cases

The four Mach-number profiles were chosen since for these profiles Winter & Gaudet [100] had made estimates of the effective turbulent length successfully, and thus reported them in their report in Fig. 6 together with the pressure history along the nozzle in the form of Mach-number distributions for these cases.

The expansion was assumed to be fully isentropic and thus the total conditions at the boundary layer edge represent the total inlet conditions. The flow was assumed adiabatic. Furthermore, Ideal Gas was assumed and the boundary layer assumption of zero pressure gradient in the wall normal direction inside the boundary layer, resulting in the following

relation between density and temperature $\frac{T}{T_e} = \frac{\rho_e}{\rho} = c$. Sutherland's Law was applied for the prediction of dynamic viscosity.

The required input of the boundary layer program as discussed in Ch. 3 consists of inlet total pressure and temperature, initial conditions (velocity profile), wall conditions and edge conditions (pressure history), and (possibly) a predefined point of transition.

The total temperature was taken from Winter & Gaudet [100], while the total pressure was taken from Fernholz & Finley [101]. The last mentioned authors complemented the experimental data set obtained from Winter & Gaudet [100] with estimates and calculations, and formatted the whole into the standardized table entries of reference [101]. For example, they estimated the inlet total pressure per case, and they estimated the wall temperature per case with a single recovery factor for all cases based on the approximation $r_T = \mathrm{Pr}^{\frac{1}{3}} = 0.72^{\frac{1}{3}} = 0.896$. The flow and therefore also the wall are assumed adiabatic and thus a zero heat-flux boundary condition has been implemented.

The length of the pressure history remains constant for all cases, which is an advantage of measuring on the straight back-wall of the flexible-walled nozzle. However, the bypass slots influence the effective length of the pressure history if used or not. When air is bypassed for Mach-numbers above 2.2 the boundary layer presumably starts right after the bypass slots as if the wall acts as a leading edge of a plate. For cases with lower Mach-numbers the pressure history is expected to be effectively longer extending upstream towards an unknown point. Therefore, it was assumed for all cases that the boundary layer started right after the bypass slots as if this was the leading edge of a flat plate. This assumption results in the initial conditions belonging to the leading edge of a flat plate. The sensitivity of the boundary layer characteristics to differences in position of the starting point (leading edge) are unknown to the author and should be studied further.

The boundary layer edge condition, or the so-called pressure history, was obtained in the form of a Mach-number distribution along the nozzle by combining Fig. 1 and Fig. 6 from Winter & Gaudet [100]. They depict respectively a schematic drawing of the wind tunnel working section and contraction; and of the Mach-number distribution inside the nozzle only, together with the location of measurement station and the estimated effective turbulent length of the four different Mach-numbers respectively. Lengths from the two figures were combined as accurately as possible. The Mach-number distribution was estimated partly by the isentropic relations and partly by graphical interpolation which resulted in a smooth curve suitable for numerical simulations. The result can be seen in Fig. 4-9. Also shown is the relative change in density of the free stream by scaling the local density at the boundary layer edge with the density at the nozzle outlet.

A predefined forced point of transition from laminar to turbulent flow was estimated from the estimated effective turbulent length for implementation of each of the simulation cases. The sensitivity of the boundary layer characteristics to differences in transition location, and length of transition region, remains unknown and should be studied further. The points of transition applied are indicated in Fig. 4-9 with an asterisk. The turbulent

Prandtl-number was taken as a constant equal to 0.9. The effect of variable turbulent Prandtl-number is negligible regarding the predicted wall temperature (maximum 1.5% larger wall density ratio c for Mach-number 2.8). However, note that the recovery factor becomes even higher, up to 0.958 for profile 2 of Mach 0.2, and decreases for the other profiles of increasing Mach-number. It is tentative to assume a relation between recovery factor and Mach-number, however, the recovery factor is not a function of Mach-number but instead it is a function of shear.

Because of the Log-Law plots a high grid resolution was chosen for the stretching grid. The first vertical grid-spacing was chosen to be 0.0001 1×10^{-4} where for most cases a value of 1×10^{-2} is taken. The variable grid parameter was kept at a value of 1.14.

Profile 19 should also be treated with care since the total pressure is lower compared to the other cases, which results in only half of the unit Reynolds-number compared to the other cases (Tab. 4-8 to 4-11). Therefore, it should be replaced ideally with profile 44 which has about the same unit Reynolds-number as the other selected cases. On top of that, profile 26 should also be considered with caution, since it is the only case considered here where the air bypass slots have been used.

4-4-6 Results

The simulation results of each profile were compared against all experimental data available for each profile. Dimensionless profiles of velocity and density were compared in the usual relative coordinates as function of the dimensional Y-coordinate, and in dimensionless Log-Law coordinates to appreciate the results close to the wall. Measured skin friction and integral properties derived from the velocity profiles were also compared and their values and trends as function of Mach-number are depicted in graph 4-16 a to b, and listed in tables 4-8 to 4-11 for completeness. Remember that the integral properties obtained from Winter & Gaudet [100] should be considered with caution, since the velocity profile measurements were not always close enough to the wall surface, i.e. not within the momentum deficit peak.

Fernholz & Finley [101] only considered the experimental data based on the temperature measurements for consistency. However, according to the author the absolute Mach-number profiles based on measured total pressure are highly suitable for a comparison of absolute values, in contrast to the dimensionless temperature-based profiles and thus they complement the validation. The absolute Mach-number profiles based on measured total pressure were compared in Fig. 4-10 showing a good correspondence, both in trends as in absolute values. Profile 26 with free stream Mach-number 2.8 shows an outlier, and, before the outlier a steeper increase than predicted. An offset is seen in all values close to the boundary layer edge. The values close to the boundary layer edge first seem to increase, after which there is suddenly a single lower outlier, and then the values converge again as expected. The origin of the offset was not discussed or explained by the authors and thus remains unknown. The increase cannot be explained, but is also seen in a comparison for high(er) Mach-number profiles by Smith [80] (Fig.

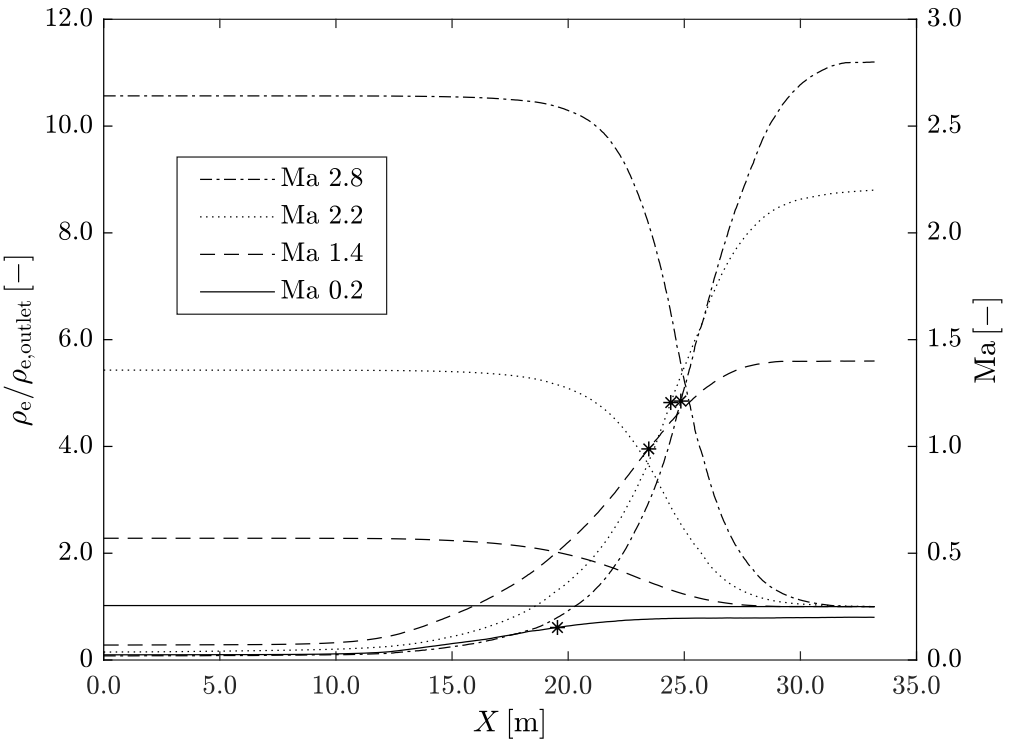

Figure 4-9: Mach-number curves (increasing to the right) serving as pressure history (input), and scaled density (decreasing to the right) along the nozzle geometry obtained from Winter & Gaudet ([100] for the four different test cases. Transition is forced at the $*$ marker. The compressibility increases in the direction of the arrow: higher Mach-number and lower density with expansion of the flow.

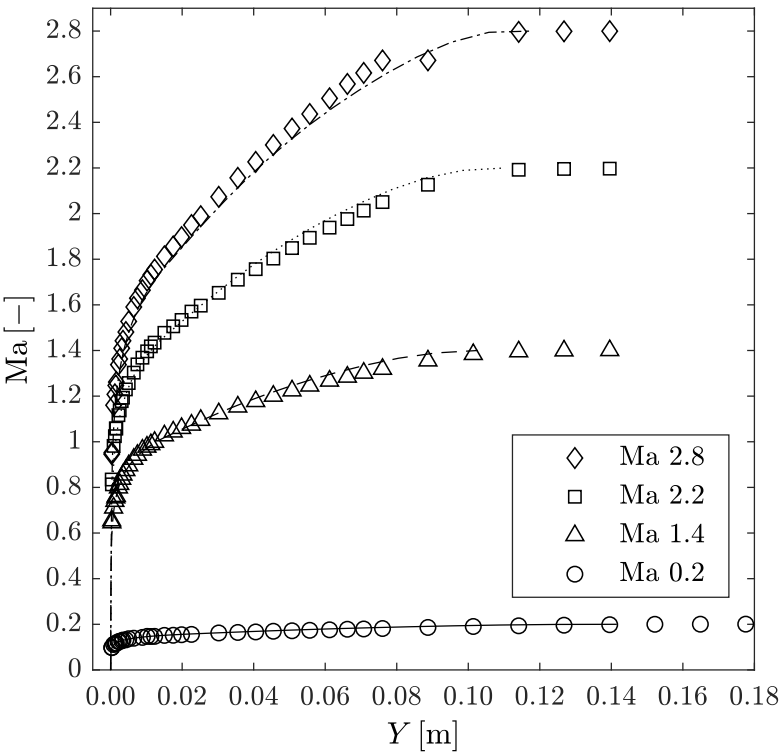

Figure 4-10: Measurements (markers) and simulations (solid lines) of absolute Mach-number profiles. Note that the higher the Mach-number becomes, the larger the difference in simulation and measurement in the region towards the boundary layer edge. The results close to the wall cannot be appreciated in this figure. Profiles based on measured pressures.

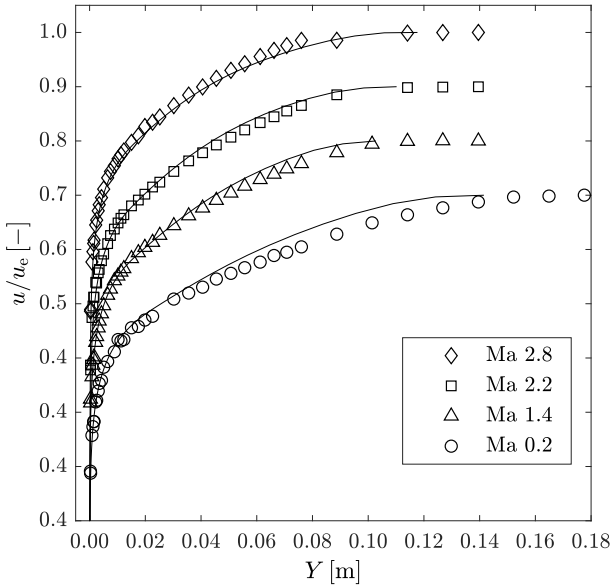

Figure 4-11: Dimensionless velocity profiles based on total temperature measurements.

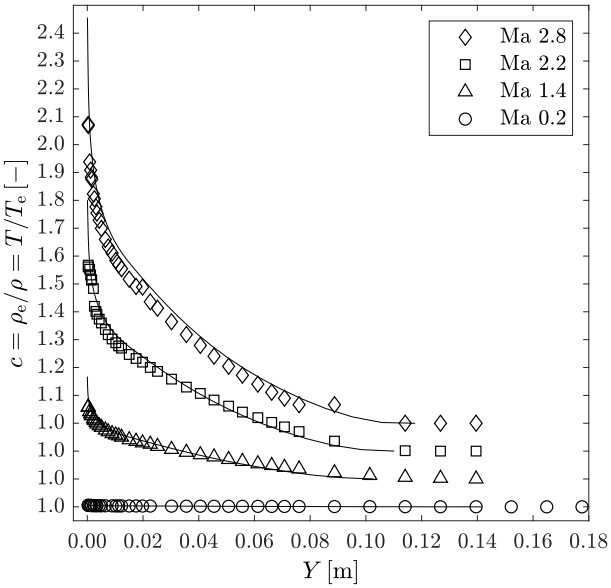

Figure 4-12: Dimensionless density profiles based on total temperature measurements.

28). Note that all measured Mach-number data points towards the boundary layer edge are slightly lower than the simulated profiles, except for profile 26 which shows slightly higher results.

The dimensionless velocity profiles in Fig. 4-11 also show a good correspondence in trends and values between measured data and simulated results. The patterns in the experimental data and the single outlier correspond with the absolute Mach-number profiles of Fig. 4-10 which suggests that the measured total pressure was also used to obtain the velocity profiles which were explicitly listed as based on measured temperature. The difference in profile 2 (Mach-number 0.2) seems larger in this graph relative to the other velocity profiles. Remember that the authors considered this case as the least accurate, and note that these differences cannot be appreciated in the absolute Mach-number profiles of the previous Fig. 4-10 due to their relatively low values. Note that also here the measured data points are slightly lower towards the boundary layer edge than the simulated profiles, except for profile 26 (Mach 2.8) again. This also holds for the density ratio in Fig. 4-12, which is plotted as the inverse density ratio $c = \frac{\rho_e}{\rho}$ in line with the boundary layer property definitions. Lastly, note that the density ratios close to the wall can be appreciated slightly better due to the definition.

Dimensionless Log-Law plots were made for velocity (Fig. 4-13) and density (Fig. 4-15) to appreciate the values close to the wall. The usual Log-Law coordintes are:

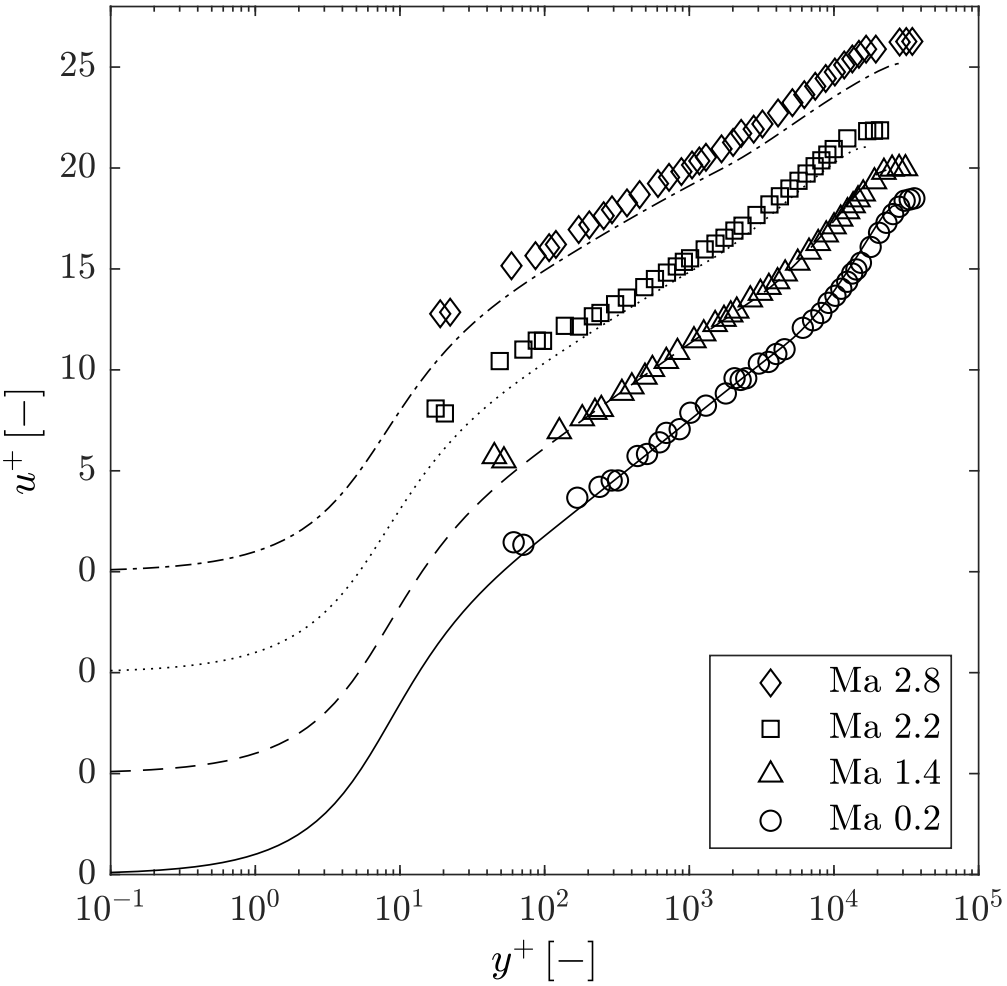

Figure 4-13: Measurements (markers) and simulations (solid lines) of the velocity profiles in the usual Log-Law coordinates. Note that the higher the Mach-number becomes, the larger the difference between simulation and measurement. Values measured close to the wall are always higher than predicted. Measured profiles for Mach 2.8 and Mach 2.2 are both entirely higher than predicted.

$$y^+ = \frac{y u_\tau}{\nu} \tag{4-2}$$

$$u^+ = \frac{u}{u_\tau} \tag{4-3}$$

$$u_\tau = \sqrt{\frac{\tau_\mathrm{w}}{\rho_\mathrm{w}}} \tag{4-4}$$

where the wall density was obtained from the wall temperature. The wall temperature was not measured but calculated by Fernholz & Finley [101] using a recovery factor obtained from the conservative approximation for turbulent flows of $r_\mathrm{T} = \mathrm{Pr}^{\frac{1}{3}} = 0.72^{\frac{1}{3}} = 0.896$ for all profiles. This approximation of the wall density influences both Log-Law coordinates through the scaling of wall shear with wall density. As we can see in Fig. 4-12, the wall density ratio c increases substantially for air, from 1.0 for Mach 0.2 up to 2.8 for Mach 2.8[4] according to the simulations. Therefore, the approximated recovery factor influences the usual wall coordinates used in Fig. 4-13 substantially, and therefore alters the comparison. In Fig. 4-14 the wall shear stress is scaled with the local density[5]. The Log-Law coordinates can now be rewritten to include measured data only, using all data listed by Winter & Gaudet [100], see App. A section E-3 for the derivation. The result is a pure comparison to avoid misleading conclusions from Fig. 4-13. Slightly higher values are found close to the wall as expected. The deviation is largest for Mach-number 2.8, for which the Log-Law profile is under predicted with a constant offset, which is attributed to a 6% higher predicted skin friction. For Mach-number 2.2 a slight and constant under prediction is visible, with a 4% higher predicted skin friction. The other profiles are in good agreement, as their predicted skin friction coefficients. Therefore, the accuracy of predicted skin friction coefficient is thought to be leading in this comparison.

The density was also plotted in Log-Law format, but still as function of the usual Y-coordinate and scaled such that the dimensionless density varied from zero at the wall to unity at the boundary layer edge. The added value of this graph is the fact that the values measured close to the wall and close to the boundary layer edge can be appreciated. The two lowest Mach-numbers show a substantial deviation in the last points close to the edge, which can also be seen in Fig. 4-11, but not in Fig. 4-12 due to the definition. The density values close to the wall are expected to be lower due to a higher measured temperature as can be seen in Fig. 4-12, but they are higher in fact. This is due to the estimate of the recovery factor through which the profiles shift to the left depending on the value of wall density, where the shift thus is higher for higher Mach-numbers. The shift towards the left also occurs in the velocity plot in Fig. 4-13, but is less obvious.

The trends and values of boundary layer characteristics predicted match with the experimental data. From Tab. 4-8 to 4-11 and Fig. 4-16 a to b, the most important boundary

[4] These values match coincidentally for this case only.

[5] Winter & Gaudet [100] introduce their *equivalent incompressib1e friction velocity* parameter by scaling the wall shear stress with the density at the boundary layer edge.

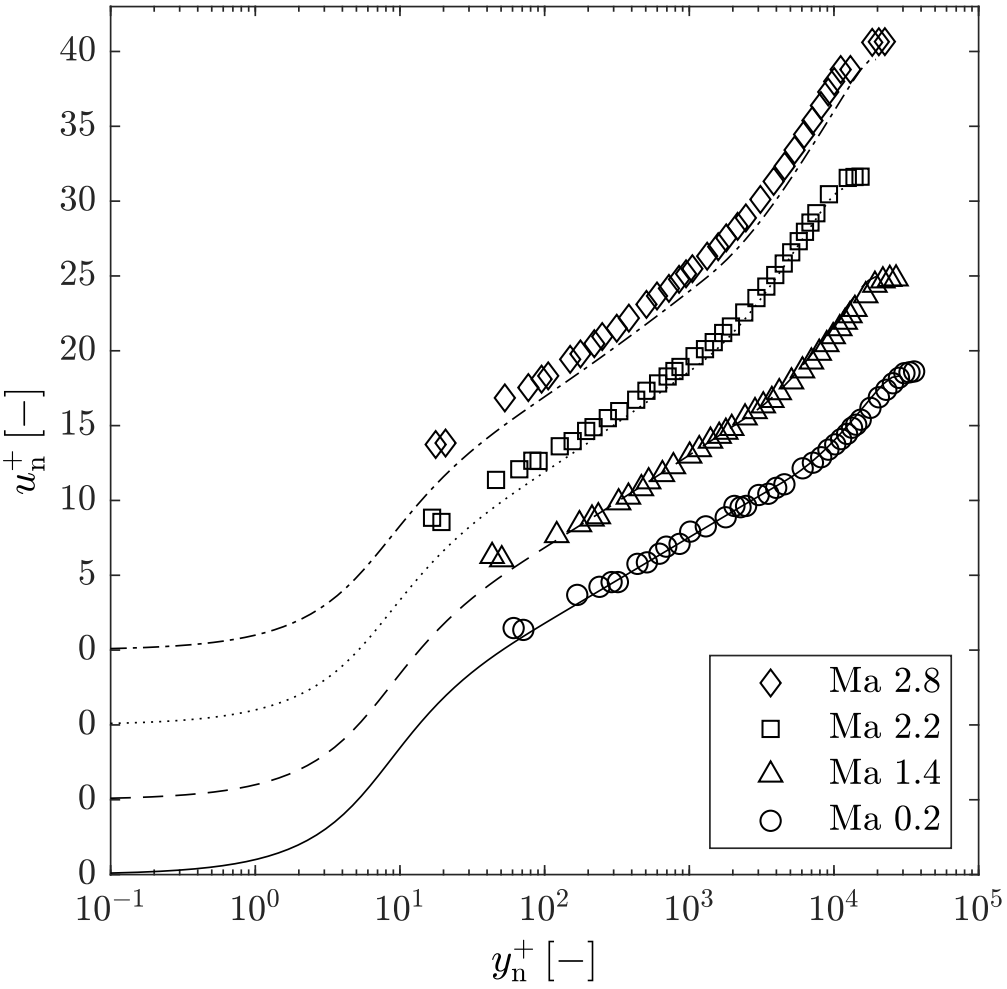

Figure 4-14: A pure comparison of the velocity profile measurements (markers) and simulations (solid lines) plotted as function of the slightly altered Log-Law coordinates where wall shear stress has been scaled with local density. Note that the differences between measured and simulated results are more subtle compared to Fig. 4-13. Values measured close to the wall are always higher than predicted. Profile 26 (Mach 2.8) is the only curve showing a noticable offset between prediction and measurement.

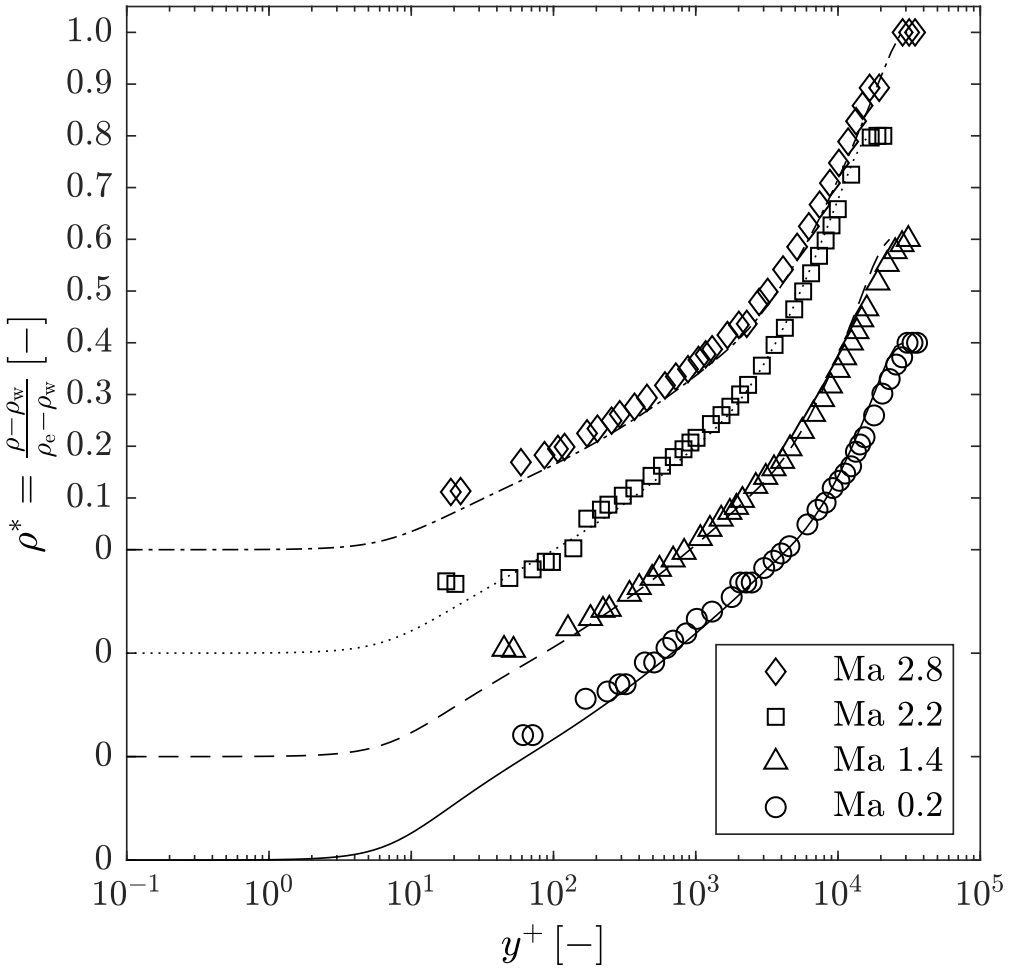

Figure 4-15: Measurements (markers) plotted versus simulations. Note that the higher the Mach-number becomes, the lower the difference in simulation and measurement towards the boundary layer edge.

layer characteristics are compared, showing trends as function of Mach-number and relative differences between measurements and predictions. A few trends are important to note. First, the wall density ratio increases with increasing Mach-number (decreasing density); at the same time the skin friction and momentum thickness decrease, while the displacement thickness and form factor increase. These trends are measured and predicted. The shape factor is considered as the most sensitive boundary layer parameter [66], and shows a very consistent trend, with small deviations for higher Mach-numbers. Although the integral properties should be treated with caution according to Fernholz & Finley [101] the results are in good agreement.

It can be concluded that the systematic and consistent measurements of Winter & Gaudet [100] serve as a useful validation source for zero pressure gradient compressible adiabatic flows. The predicted results match with the measurements over the entire range, both in terms of (absolute) values and trends. Absolute and relative profile properties were generally found to be accurate within 2%, and integral properties within 10%, as reported by Wilcox [26] discussing the performance of the CS-method. Figure 4-14 seems the most useful comparison since it combines all measured data in one graph, and it enables the reader to appreciate trend close to the wall and boundary layer edge due to the scaling Log-Law coordinates. The resulting comparison suggests only a slight under prediction for Mach-number 2.8. Regarding the comparison of absolute values and integral values one can speculate that pressure history, including point of transition from laminar to turbulent flow, is taken into account properly. However, one should first conduct a sensitivity study to make substantiate conclusions.

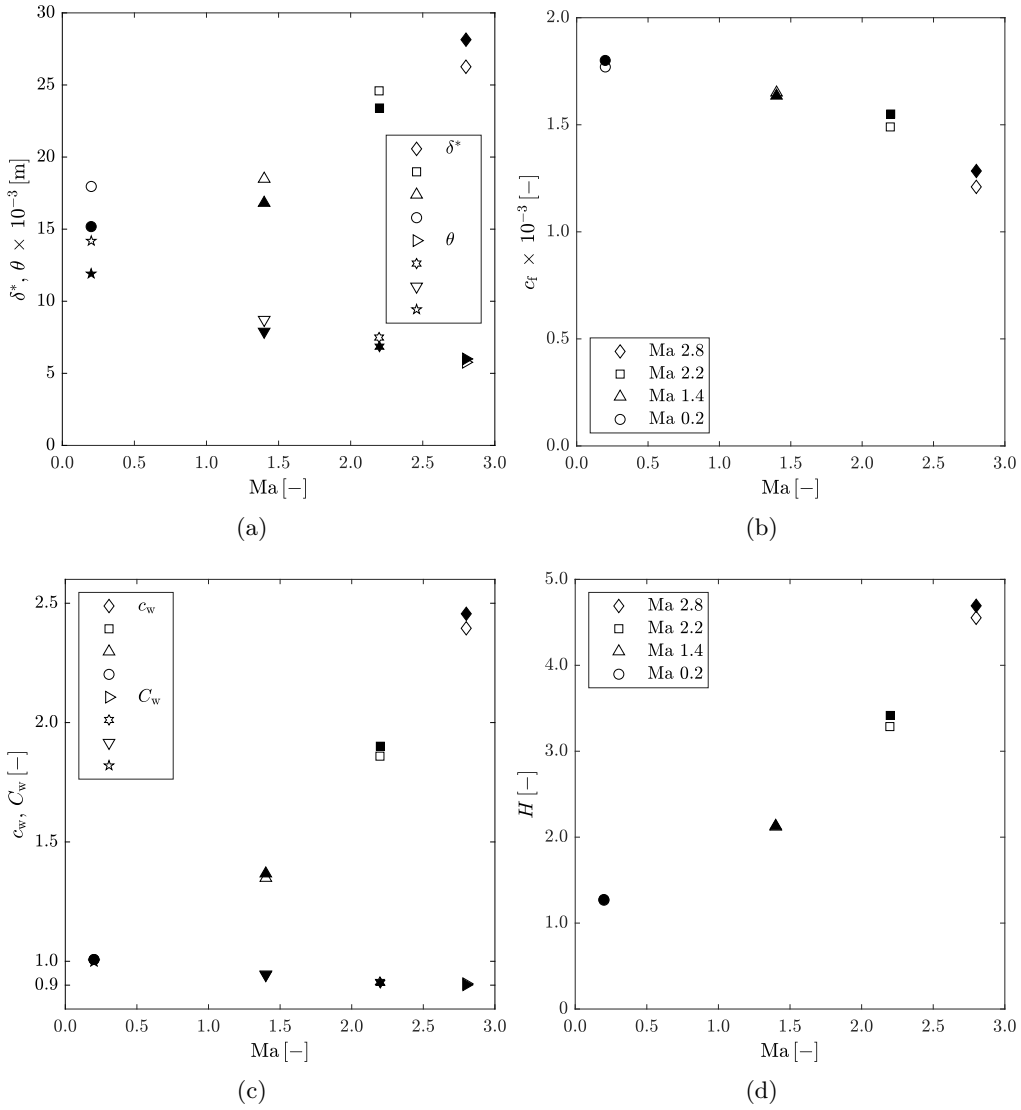

Figure 4-16: Boundary layer characteristics from Tab. 4-8 to 4-11: (a) Displacement and momentum thickness, (b) Skin friction, (c) Wall density ratio and wall Chapman-Rubesin parameter (estimated for the experimental data set), and (d) Shape factor. Note that the inlet total pressure for Mach 2.2 is lower, which cannot be seen from these results.

Table 4-8: Mach 2.8: Comparison of simulated results with experimental data of profile 26 with Mach-number 2.8 and initial total conditions $P_0^* = 0.76454 \times 10^5\,\mathrm{Pa}$ and $T_0 = 291.85\,\mathrm{K}$ from Winter & Gaudet [100] and complemented by Fernholz & Finley [101].

	$\boldsymbol{\delta}$ $\times 10^{-3}\,[\mathrm{m}]$	$\boldsymbol{\delta^*}$ $\times 10^{-3}\,[\mathrm{m}]$	$\boldsymbol{\theta}$ $\times 10^{-3}\,[\mathrm{m}]$	$\boldsymbol{H}$ $[-]$	$\mathbf{Re}$ $\times 10^{7}\,[\mathrm{m}^{-1}]$	$\mathbf{Re}_x$ $\times 10^{7}\,[-]$	$\mathbf{Re}_\theta$ $\times 10^{3}\,[-]$	$\boldsymbol{C_\mathrm{f}}$ $\times 10^{-3}\,[-]$	$\boldsymbol{r}$ $[-]$	$\boldsymbol{c_\mathrm{w}}$ $[-]$	$\boldsymbol{C_\mathrm{w}}$ $[-]$
Experimental data	97.31$^\diamond$	26.26	5.77	4.55	0.66	21.75	37.79	1.210	0.896*	2.40*	0.91*
Simulation	91.03	28.14	6.00	4.69	0.66	21.75	39.29	1.284	0.928	2.46	0.90
Deviation [%]	−6.45	7.15	3.97	3.07	0.00	0.00	3.97	6.13	NA	2.53	−0.53

$^\diamond$ Estimated by linear interpolation of the experimental data.
* Estimated by Fernholz & Finley [101].

Table 4-9: Mach 2.2: Comparison of simulated results with experimental data of profile 19 with Mach-number 2.2 and initial total conditions $P_0^* = 0.34522 \times 10^5\,\mathrm{Pa}$ and $T_0 = 291.65\,\mathrm{K}$ from Winter & Gaudet [100] and complemented by Fernholz & Finley [101].

	$\boldsymbol{\delta}$ $\times 10^{-3}\,[\mathrm{m}]$	$\boldsymbol{\delta^*}$ $\times 10^{-3}\,[\mathrm{m}]$	$\boldsymbol{\theta}$ $\times 10^{-3}\,[\mathrm{m}]$	$\boldsymbol{H}$ $[-]$	$\mathbf{Re}$ $\times 10^{7}\,[\mathrm{m}^{-1}]$	$\mathbf{Re}_x$ $\times 10^{7}\,[-]$	$\mathbf{Re}_\theta$ $\times 10^{3}\,[-]$	$\boldsymbol{C_\mathrm{f}}$ $\times 10^{-3}\,[-]$	$\boldsymbol{r}$ $[-]$	$\boldsymbol{c_\mathrm{w}}$ $[-]$	$\boldsymbol{C_\mathrm{w}}$ $[-]$
Experimental data	98.07$^\diamond$	24.59	7.48	3.29	0.40	13.31	30.00	1.490	0.896*	1.86*	0.91*
Simulation	87.97	23.40	6.85	3.42	0.40	13.29	27.43	1.550	0.931	1.90	0.91
Deviation [%]	−10.29	−4.84	−8.46	3.94	−0.11	−0.11	−8.56	4.04	NA	2.24	−0.46

$^\diamond$ Estimated by linear interpolation of the experimental data.
* Estimated by Fernholz & Finley [101].

Table 4-10: Mach 1.4: Comparison of simulated results with experimental data of profile 12 with Mach-number 1.4 and initial total conditions $P_0^* = 0.95936 \times 10^5\,\mathrm{Pa}$ and $T_0 = 291.75\,\mathrm{K}$ from Winter & Gaudet [100] and complemented by Fernholz & Finley [101].

	$\boldsymbol{\delta}$ $\times 10^{-3}\,[\mathrm{m}]$	$\boldsymbol{\delta^*}$ $\times 10^{-3}\,[\mathrm{m}]$	$\boldsymbol{\theta}$ $\times 10^{-3}\,[\mathrm{m}]$	$\boldsymbol{H}$ $[-]$	$\mathbf{Re}$ $\times 10^{7}\,[\mathrm{m}^{-1}]$	$\mathbf{Re}_x$ $\times 10^{7}\,[-]$	$\mathbf{Re}_\theta$ $\times 10^{3}\,[-]$	$\boldsymbol{C_\mathrm{f}}$ $\times 10^{-3}\,[-]$	$\boldsymbol{r}$ $[-]$	$\boldsymbol{c_\mathrm{w}}$ $[-]$	$\boldsymbol{C_\mathrm{w}}$ $[-]$
Experimental data	98.09$^\diamond$	18.49	8.71	2.12	0.67	22.25	58.41	1.650	0.896*	1.35*	0.95*
Simulation	85.97	16.82	7.89	2.13	0.67	22.25	52.92	1.636	0.938	1.37	0.94
Deviation [%]	−12.35	−9.03	−9.42	0.45	0.02	0.02	−9.40	−0.88	NA	1.37	−0.30

$^\diamond$ Estimated by linear interpolation of the experimental data.
* Estimated by Fernholz & Finley [101].

Table 4-11: Mach 0.2: Comparison of simulated results with experimental data of profile 2 with Mach-number 0.2 and initial total conditions $P_0^* = 1.46880 \times 10^5\,\mathrm{Pa}$ and $T_0 = 283.95\,\mathrm{K}$ from Winter & Gaudet [100] and complemented by Fernholz & Finley [101].

	$\boldsymbol{\delta}$ $\times 10^{-3}\,[\mathrm{m}]$	$\boldsymbol{\delta^*}$ $\times 10^{-3}\,[\mathrm{m}]$	$\boldsymbol{\theta}$ $\times 10^{-3}\,[\mathrm{m}]$	$\boldsymbol{H}$ $[-]$	$\mathbf{Re}$ $\times 10^{7}\,[\mathrm{m}^{-1}]$	$\mathbf{Re}_x$ $\times 10^{7}\,[-]$	$\mathbf{Re}_\theta$ $\times 10^{3}\,[-]$	$\boldsymbol{C_\mathrm{f}}$ $\times 10^{-3}\,[-]$	$\boldsymbol{r}$ $[-]$	$\boldsymbol{c_\mathrm{w}}$ $[-]$	$\boldsymbol{C_\mathrm{w}}$ $[-]$
Experimental data	142.91$^\diamond$	17.96	14.18	1.27	0.68	22.51	96.18	1.770	0.896*	1.01*	1.00*
Simulation	114.39	15.18	11.91	1.27	0.68	22.44	80.50	1.801	0.942	1.01	1.00
Deviation [%]	−19.96	−15.50	−16.03	0.66	−0.33	−0.33	−16.31	1.73	NA	0.04	−0.01

$^\diamond$ Estimated by linear interpolation of the experimental data.
* Estimated by Fernholz & Finley [101].

4-5 Discussion and Conclusions

This chapter presented several verification and validation test cases in air which were used to assess the capabilities of the BL program. The program was compared with two other solvers in order to assess the computational cost and accuracy.

The boundary layer computer program was found to be much faster in solving a flat plate flow of length $L = 0.1\,\mathrm{m}$ than the spectral-solver MATLAB program and the MATLAB bvp4c-solver program reaching the same accuracy for low Mach-numbers, and comparable accuracy for high Mach-numbers. Where the boundary layer program takes about 0.5 s for ideal gas, the other two programs take much more time for the same case, which is about two orders of magnitude. The program takes only 1 second for the NACA0012 verification case, which consists of 105 stations and includes laminar and turbulent ideal gas flow.

Importantly, the boundary layer program is much faster than the spectral-solver, for comparable accuracy. Note that the spectral-solver is not bound to the boundary layer assumptions, and at the same time it is considered as highly accurate. However, the computations take two orders of magnitude more time. The boundary layer program implementing the CS-method can reach similar levels of accuracy in much less time which allows Design of Experiment studies and sensitivity studies that entail many simulations.

The comparison with a highly accurate MATLAB bvp4c-solver justifies the correct solution is found for the system of equations. The comparison with the MATLAB spectral-solver proves high accuracy for incompressible flows, but shows a small deviation for the compressible flat plate flow case of Mach-number 2.0. This is an interesting comparison, since the spectral-solver is not bounded to the boundary layer assumptions.

The solver was verified with numerous cases obtained from literature, testing its capability. Howarth's flow case with nonlinear increasing pressure gradient, a highly suitable test case for testing codes, was implemented successfully. The point of flow separation was predicted with about the same accuracy as compared with the work of others.

An accuracy study implementing a simple grid refinement study showed that the discretization error and the iterative error become negligible when choosing a uniform η-coordinate spacing of $\mathrm{d}\eta = 0.01$ in case of laminar flow. The X-coordinate spacing is dependent on changes in the free stream and wall properties and the surface geometry. The reader can use Tab. 4-6 to find a suitable X-coordinate spacing for the case at hand.

The boundary layer program was verified with the FORTRAN program, from which it originated. The simulations of a NACA0012 airfoil superpose and thus prove that the FORTRAN code has been converted to MATLAB code successfully. This specific case of stagnation point flow is a comprehensive verification case since it includes: laminar flow, transition (forced by user), transitional flow, turbulent flow, and flow separation.

Heat transfer in flat plate supersonic laminar flow was verified with the spectral-solver program. Experimental data allowed to qualitatively assess the trends in Stanton-

number predicted by the simulation. Interestingly, the trend in angle and shape of the transition region predicted were in close agreement with the experimental results. Surprisingly, since the empirical relation used for transitional was explicitly stated to be calibrated for adiabatic flows only.

Validation with developing boundary layers along surfaces was performed with two cases. The first was again a highly suitable low Mach-number (incompressible) NACA0012 airfoil including experimental data of displacement and momentum thickness for laminar, transitional and turbulent flow. The results were in good agreement. The second case was an asymmetric nozzle including experimental data of displacement and momentum thickness measured along a flat wall and along a curved wall in the same supersonic nozzle. The results of the flat wall comparison were in good agreement. The results of the curved wall are in good agreement with the solution predicted by the program presented in the report, but not with the measured data. The results imply that there might be a small effect of wall curvature. In addition the current author speculates that relaminarization has occurred.

The algebraic turbulence model was validated successfully with an extensive experimental data base measuring several boundary layer characteristics at a single station in zero pressure gradient adiabatic flow over a wide range of Mach-numbers. The results matched and the CS-model implemented proved capable of predicting the compressible phenomena inside a boundary layer accurately up to and including a Mach-number of 2.8. Log-Law velocity profiles were plotted and compared and indicated minimal differences. Absolute and relative profile properties were generally found to be accurate within 2%, and integral properties within 10%, as reported by Wilcox [26] discussing the performance of the CS-method. At the highest Mach-number of value 2.8 the program under predicted slightly, due to a over prediction in skin friction of only 6%. The predicted skin friction seems a sensitive indicator for comparison in zero pressure gradient adiabatic turbulent flows, and it is suitable since it can be measured directly in contrast to integral properties.

Now the program is verified and validated for air, simulations can be performed for complex fluids such as MM to investigate the effect of their nonideal properties on the boundary layer characteristics. However, experimental campaigns, such as with the ORCHID, will be needed for establishing the validity of the program in the nonideal gas range. Experimental data of nonideal gas or vapour flows in the range of interest are currently still unavailable.

Chapter 5

Boundary Layer Simulations of a Supersonic Dense Organic Vapour

The objective of this chapter is to study the boundary layer development inside an existing two-dimensional supersonic de Laval nozzle expanding Hexamethyldisiloxane (MM). The nozzle under consideration was designed with the Method of Characteristics (MoC) for a test set-up called the ORCHID. The motivation is to find how the boundary layer inside the current nozzle influences its performance, e.g. the outlet Mach-number and loss generation. In addition, parameters c, C, C_e and m_3 are studied to quantify the characteristics of the boundary layer. The ultimate goal is to find what factors need to be considered for a future robust nozzle design. Hence, this chapter investigates the effects of laminar and turbulent flow, and the sensitivity of the results to different thermophysical models used, by means of preliminary deterministic simulations. First, the ORCHID nozzle design is introduced in Sec. 5-1. Section 5-2 discusses the numerical framework that was set up for the simulations, which results are presented in Sec. 5-3. Finally, Sec. 5-4 discusses the factors that need to be considered in a future robust design of the ORCHID nozzle.

5-1 The ORCHID Nozzle Design

At the moment of writing, a facility for studying Non-Ideal Compressible Fluid Dynamics (NICFD) and testing of Organic Rankine Cycle (ORC) expanders is commissioned at the Delft University of Technology [11,15]. MM (Hexamethyldisiloxane) is the first fluid chosen for studying departure from ideal gas. The test facility is similar to a small scale ORC Power Plant but includes two test-sections. The first is being commisioned at present: a 2D converging-diverging de Laval nozzle test section for supersonic flow with

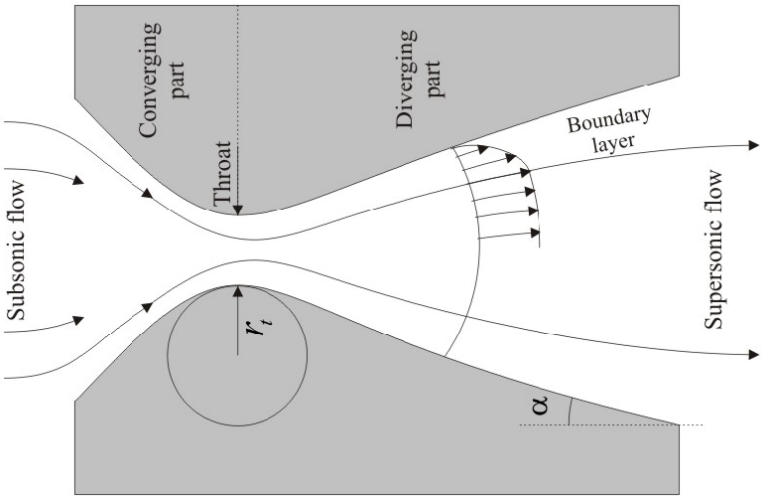

Figure 5-1: A de Laval Nozzle including boundary layer, which is exaggerated (not to scale) for clarity. First, a contraction accelerates the incoming subsonic flow ($\mathrm{Ma} < 1$) up to $\mathrm{Ma} = 1$ at the throat, after which it is further expanded (accelerated). The minimum radius of curvature is located at the throat in this example. Source: unknown.

optics to measure the nonideal gas behaviour during expansion from low Mach-number flow up to Mach-number 2.0. The second test-section will be designed and commissioned at a later stage for evaluating the performance of new turbines with novel Nozzle Guide Vane (NGV) designs. The current ORCHID test set-up supplies the necessary boundary conditions (P_0, T_0, P_b) for the nozzle expanding MM. The focus of this chapter is the development of the viscous boundary layer inside the current inviscid ORCHID nozzle design.

A de Laval nozzle has a converging-diverging nozzle shape for accelerating a subsonic gas to supersonic speeds and is named after the Swedish inventor de Laval. The nozzle can be axisymmetric or two-dimensional. Figure 5-1 depicts a typical two-dimensional de Laval nozzle shape including the formation of a boundary layer along the curved nozzle surface walls. First, a subsonic flow ($\mathrm{Ma} < 1$) is accelerated by the converging nozzle section up to the minimum contraction, called the nozzle throat. When the mass flow is high enough the flow reaches Mach 1, the Speed of Sound (SoS), at the throat section. From this point on, downstream influences cannot travel upstream anymore, and any further decrease in the nozzle back-pressure will no longer increase the mass flow. At this point, the throat is so-called *choked*. When $\mathrm{Ma} > 1$, the flow is supersonic, and expansion can only occur if the nozzle diverges after the throat according to the Mach-area relation [103]. This diverging section is designed with the MoC [68, 103, 104] for inviscid flows. It's design is critical, as entropy generation in the nozzle has to be minimized to preserve the experiments reliability. The reader is assumed to be familiar with the isentropic flow relations in supersonic flows (see for example Grossman [103]).

The flow inside a nozzle can be divided into two regions (Fig. 5-1): an inviscid core

flow, and a boundary layer flow induced by viscosity. The core flow is not affected by the walls, and viscosity does not play a role here since velocity gradients are negligible. In contrast, the boundary layer is a flow region close to the wall characterized by a high velocity gradient induced by viscosity that causes the frictional interaction with the wall, resulting in retarded flow close to the wall. The presence of the boundary layer will thus result in a shift of the flow streamlines from the wall surface inwards, with a value equal to the displacement thickness[1]. This shift inwards on both sides results in a smaller unaffected core flow of the originally inviscid nozzle design. The effective area for expansion hence has decreased compared to the critical MoC contour, which results in higher losses. The decrease in free stream Mach-number, which is of importance at the nozzle outlet, depends on the magnitude of the displacement thickness. A viscous nozzle design will thus add the resulting displacement thickness to the inviscid nozzle geometry [19] taking into account an unaltered total mass flow. The displacement thickness hence is a parameter that indicates the effect of viscosity on the inviscid nozzle core flow. Therefore, it will have our special interest in the following sections of this Chapter.

The ORCHID nozzle is a 2D de Laval nozzle, and thus converging-diverging in shape, designed for accelerating MM up to Mach-number 2.0. Figure 5-2 depicts the nozzle half-geometry contours and the results of a CFD simulation with SU2 [105] showing Mach-number contours. The nozzle design consists of several sections (Fig. 5-2): a straight inlet section; a converging section, first concave then convex; the throat, the smallest area; a diverging section, first convex then concave; and a straight outlet section. The converging section was designed with rules of thumb for wind tunnel design, see Ref. [106], and the ends were matched with interpolating polynomials matching the derivatives. The diverging section of the nozzle was designed with a high fidelity inviscid MoC program using RefProp [107] for obtaining the fluid properties through a multiparameter equation of state for MM [45]. The MoC [104, 108] is a method which solves the partial differential equations for expanding supersonic gas flows given several boundary conditions such as the total inlet conditions and the outlet static pressure, which together result in the outlet Mach-number aimed for. The nozzle was designed by Head [11] with inlet total conditions of 252 °C and 18.4 bar and a back pressure of 2.1 bar. Fifty characteristic lines were to guarantee a smooth diverging section of the nozzle profile. Figure 5-2 displays the resulting geometry and Mach distribution for the nozzle half-geometry. The minimum radius of curvature is about 0.017 m at the start of the converging section.

Considering the fact that the current ORCHID nozzle design is not taking into account viscosity, the question arises of how dynamic viscosity influences its performance. In other words, what is the magnitude of the boundary layer displacement thickness, and how is it expected to influence the expansion of MM and the outlet Mach-number? Furthermore, from Chap. 3 it followed that the parameters density ratio c, Chapman-Rubesin parameter C and fluid property gradient parameter m_3 are important factors

[1] According to the definition of displacement thickness, see also the derivation by White [54].

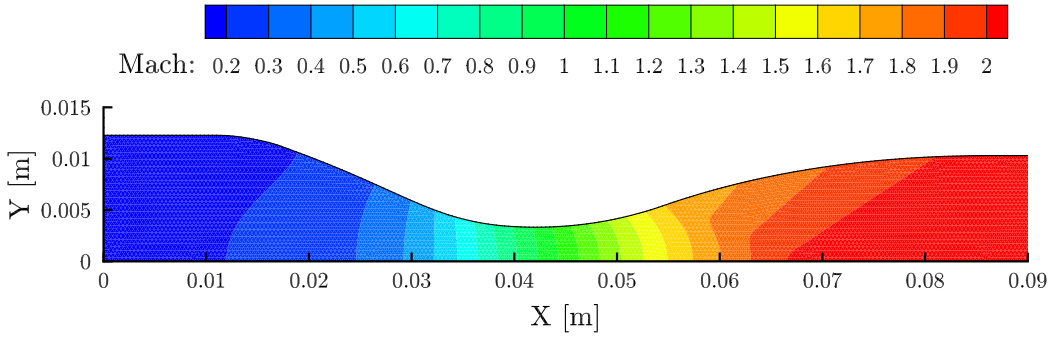

Figure 5-2: Nozzle half-geometry of the ORCHID nozzle for the expansion of MM (Hexamethyldisiloxane). The diverging section was designed with the Method of Characteristics (MoC) [11]. The colours and their contours depict the Mach-number distribution of the flow on its course expanding from left to right obtained from a second-order high fidelity inviscid (euler-solver) CFD simulation with SU2 [105]. RefProp was used for fluid property calculations.

influencing the velocity profile and thus the characteristic boundary layer thicknesses. In addition, Kluwick [10] states that High Molecular Complexity (HMC) fluids, which are defined by $0 < \Gamma < 1$ [13], are characterized by low Eckert-numbers. As a consequence, both dissipation caused by internal friction and heat conduction can be neglected, even at supersonic Mach-numbers. Adiabatic flows of complex fluids are therefore characterized by negligible temperature gradients, and thus low density gradients inside the boundary layer locally. This leads to the question of how this applies to the MM boundary layer.

5-2 Numerical Framework

This section discusses the model definition and setting up the numerical framework for simulation of the ORCHID nozzle. This includes conditioning of the model inputs.

Recall the required input data for the boundary layer program as discussed in Chap. 3. The following combination of input parameters was chosen for the ORCHID boundary

layer simulations:

Table 5-1: The input conditions used for the ORCHID nozzle boundary simulation.

Input	Value	Unit
P_0	18.360×10^5	Pa
T_0	525.85	K
$\mathrm{Ma_I}$	0.1862	-
P_e	From 18.183×10^5 to 1.942×10^5	Pa
$\left.\frac{\partial h_0}{\partial y}\right\|_\mathrm{w}$	0	J/(kg K m)

The nozzle total inlet conditions and static back pressure were determined by Head [15, 16] in designing the ORCHID test set-up, and were later also used in designing the ORCHID nozzle [11] with the MoC as discussed in the previous section. The wall surface was assumed adiabatic. These conditions were used for an Euler CFD simulation with SU2 [105] to obtain the Mach-number and pressure fields inside the nozzle neglecting viscosity which results in wall-slip. Since the problem is symmetric, only the nozzle half-geometry needed to be considered in the simulation. Figure 5-3 shows the resulting Mach-number $\mathrm{Ma_{in}}$ and pressure distribution along the curved nozzle wall surface taken from the SU2 CFD simulation results [105]. According to the definition of the displacement thickness, the curved wall surface with velocity slip can be considered as the boundary layer edge in a viscous simulation. Therefore, the static pressure along the curved wall surface can be taken as boundary layer edge input for the boundary layer program. The pressure was chosen since the total inlet and static outlet (back) pressure were chosen design conditions. Note here, that choosing the Mach- or velocity distribution possibly results in a mismatch in pressure at the in- or outlet depending on the thermodynamic model used.

However, taking the pressure along the curved nozzle wall surface with velocity slip directly as an input of the boundary layer program results in non-real solutions. For example, the shape factor is heavily influenced by sudden changes in the pressure distribution, were the pressure distribution in reality is expected to be smooth. Figures 5-4-a and 5-4-b zoom in at the wall surface pressure distribution (black solid lines) from Fig. 5-3. Figure 5-4-a shows a sudden pressure increase obtained from the SU2 simulation, which results in a relatively small but irregular pressure maximum at the start of the converging section. Furthermore, Fig. 5-4-b shows irregular oscillations at the nozzle outlet. These irregularities influence the boundary layer simulation results and thus they were smoothed. These irregularities are most probably caused by a non-smoothness in the derivatives of the ORCHID nozzle geometry, since they only appear at the interpolated section interfaces.

The pressure peak in Fig. 5-4-a is relatively small and accounts only for 0.3% of the static inlet pressure (5 kPa). Although its small in size it is not negligible, since it causes flow separation directly in case of simulating laminar flow. Hence it does not

allow the simulation of laminar flow. Therefore, the pressure peak was removed by interpolating the derivative of the pressure with a piecewise cubic hermite interpolating polynomial (PCHIP-function MATLAB). The smooth derivative was then integrated and a small correction was made for the numerical deviation introduced by the trapezoid method used to obtain the smooth curve (dashed grey line) depicted in Fig. 5-4-a. Note that McNally [48, p. 16, Fig. 2] shows a similar but measured pressure peak with a maximum of 5.1% of the static inlet pressure. Therefore, this pressure peak might not be a numerical phenomena, but true physics, and therefore it needs to be taken into account. This phenomenon will be further discussed in Sec. 5-4 of this Chapter. The ORCHID Scanivalve pressure tap T03 is located at the location of the (static) pressure peak [11].

The irregularities in the pressure distribution at the nozzle outlet location did appear clearly in preliminary boundary layer simulation results, where they were considered as numerical noise. Therefore, the pressure in the straight outlet section was also smoothed for the simulation results currently discussed by means of interpolation. Here a normal spline sufficed to arrive at a smooth pressure curve connecting the smooth diverging section with a chosen outlet pressure based on the pressure at the start of the outlet section in Fig. 5-4-b. Note that the outlet section in the SU2 CFD simulation [105] was extendend (not shown) to guarantee convergence. The straight inlet and outlet sections were assumed to have zero pressure drop. The differences in static pressure at the inlet and outlet of the ORCHID nozzle calculated with the MoC by using StanMix were only 0.003% and 0.4% respectively compared to those obtained with RefProp (Tab. 5-2). Therefore, the same static pressure curve obtained with RefProp was interpolated and then used as input for all simulations, including the simulations with the four different thermodynamic models adopted. In other words, all simulations adopt exactly the same input conditions.

The boundary layer program calculates a surface coordinate X from the x- and y-coordinate inputs obtained from the geometry of the curved wall surface. Recall that wall curvature is neglected. The grid parameters were chosen as advised by Cebeci [27] for both laminar and turbulent flow. The stretched grid starts with the smallest step-size at the wall of $d\eta = 0.01$ which is multiplied with a variable grid parameter (VGP) of 1.14. The maximum grid-heigth η_e was set at 8.0. Note that for solely laminar flow a VGP of 1.0 gives the best results. The current values give the best results for flows being both laminar and turbulent [27]. The same value of the convergence criterion was applied as suggested by Cebeci [27] (see Sec. 4-1-3), which compares the differences in the shear parameter at the wall between consecutive iterations. When the difference is smaller than 1.0×10^{-5} in case of laminar flow the solution is considered as converged. For turbulent flow the criterion is less stringent (see Cebeci [27]). The calculation is started as a plate. Namely, the first boundary layer edge condition, static pressure in this case, is equal to the free stream value.

The thermophysical properties are retrieved through FluidProp [47]. The first thermodynamic model used is a multiparameter equation of state for MM [45] implemented in

RefProp [107]. This model is currently considered as the most accurate model available. The second model is the iPRSV EoS [46] implemented in FluidProp [47]. There it is named the StanMix model, which implements the iPRSV and is complemented with a polynomial for the constant pressure specific heat together with Chung's method [78] for obtaining the transport properties dynamic viscosity and thermal conductivity. RefProp is considered as the most accurate and therefore it is taken as a reference. However, it is relatively slow. The second model in contrast, takes less time but is also less accurate. In the future, the StanMix model will be used in a Design of Experiment (DoE) which entails many simulations, and thus speed is a prerequisite. In the following, the differences between both models will be studied simulating the boundary layer for the expansion of MM in the ORCHID nozzle. The results of this study are relevant for future studies because it gives the opportunity to learn about both models shortcomings for a correct interpretation of the simulation results.

The ideal gas models, calorically perfect and thermally perfect, were both complemented with Sutherland's Law for calculation of the transport properties of MM. RefProp was used first to obtain values of these properties at the low pressure limit (ideal gas) of 0.1 bar for the entire temperature range of the ORCHID nozzle expansion. Then, the coefficients in Sutherland's Law were determined from these values by least-squares fitting with a Python routine [109]. The isobaric heat capacity of MM was obtained for the same conditions from RefProp and it was fitted to a fourth-order polynomial with MATLAB.

For air, the behaviour of the boundary layer (conditions and characteristics) is well known due to extensive experimental campaigns, which include for example the point of transition from laminar to turbulent flow (see the Agard catalogues [83, 101, 102, 110]). In contrast, for MM or other complex fluids, no such flow experiments have been done concerning the boundary layer as far as known by the author. On top of that, it is unknown if the highly accelerated MM flow will be fully laminar everywhere, or fully turbulent, or even a combination of both.

Therefore, deterministic simulations have been carried out to obtain an order-of-magnitude estimate of the boundary layer velocity and displacement thickness for fully laminar and fully turbulent flows as the two outer limits. Both simulation cases were performed with the two different types of thermophysical models to investigate their effect on the results. The resulting preliminary displacement thickness can be used for an estimate of the performance of the current nozzle, and if measurement results are available it can be used for comparison with experimental data obtained from the current ORCHID nozzle.

5-3 Results

The simulation results presented here aim to characterize the boundary layer inside the ORCHID nozzle. The boundary layer characteristics presented can be divided into two categories: integral properties expressing the influence of the boundary layer on the core

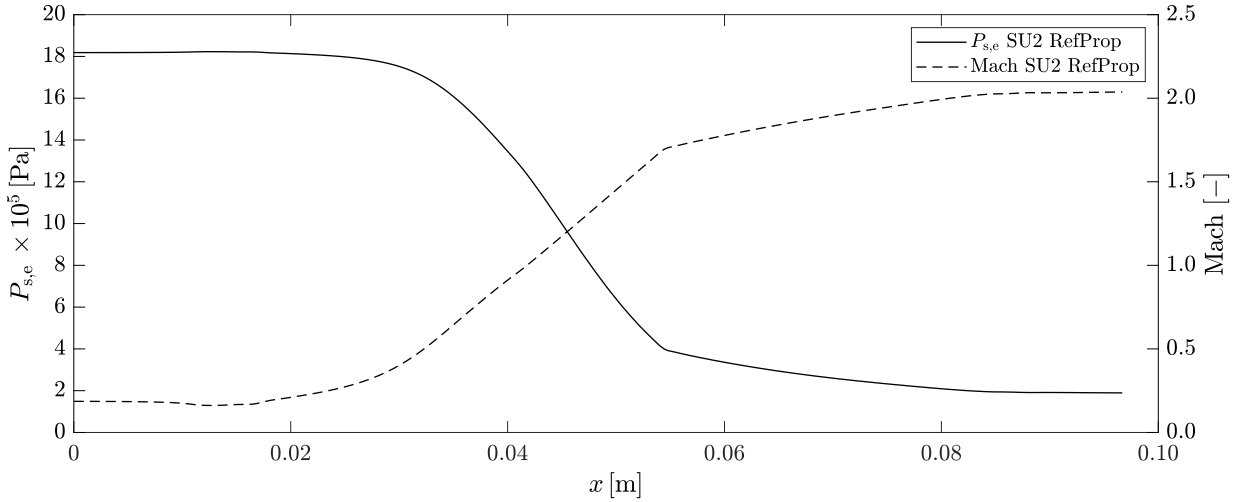

Figure 5-3: The solid line depicts the static pressure plotted as function of the nozzle x-coordinate obtained from the SU2 CFD simulation [105] using RefProp, which serves as input to the boundary layer program. The resulting boundary layer edge Mach-number calculated with the boundary layer program (RefProp) is also shown.

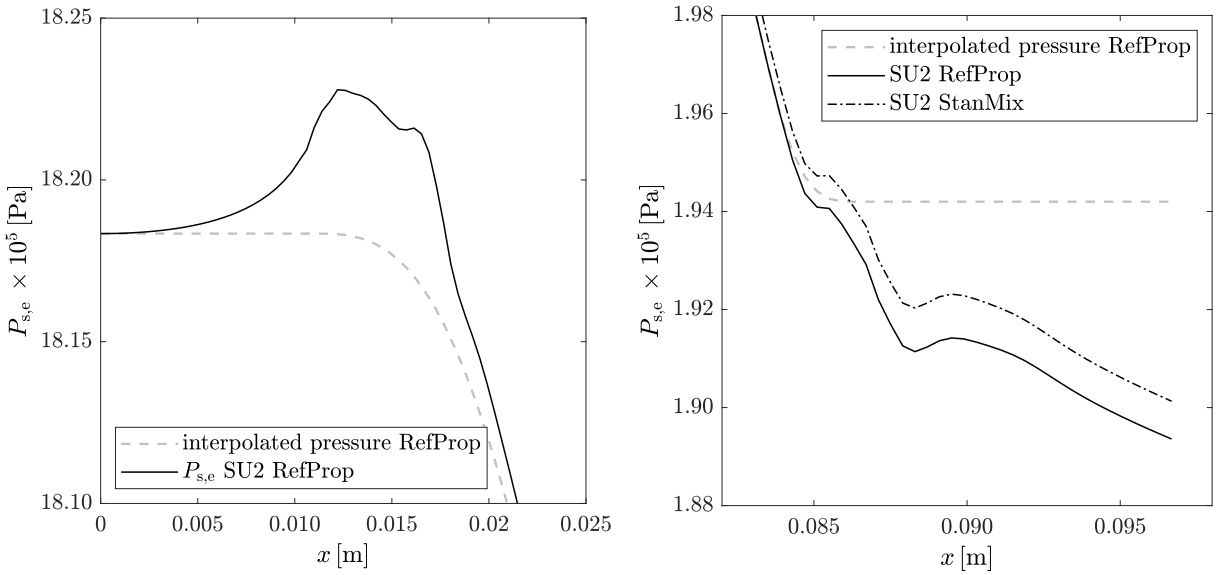

Figure 5-4: Zoom view of the static pressure from Fig. 5-3 plotted as function of the nozzle x-coordinate at the straight inlet section before the nozzle (left), and at the straight outlet section after the nozzle (right). Both are obtained from the SU2 CFD simulations [105] with RefProp and StanMix and show irregularities introduced by the numerical methods applied. The grey dashed lines substitute for these artifacts and were obtained by interpolation. The same interpolated pressure distribution is used as input for all four simulations, although they use different thermophysical models, due to the negligible deviation in the static pressure input (StanMix gives a 0.003% higher pressure at the inlet and 0.4% higher at the outlet compared to RefProp).

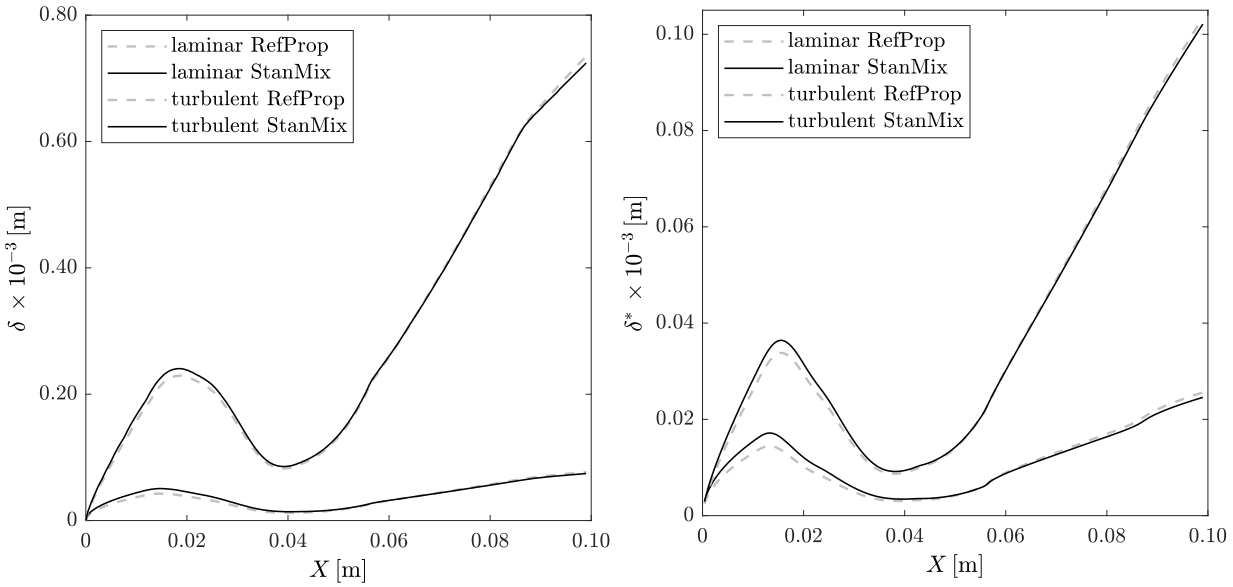

Figure 5-5: Velocity thickness (left) and displacement thickness (right) as function of the nozzle surface coordinate for simulations of laminar and turbulent flow with StanMix (solid line) and RefProp (grey dashed line) respectively. The velocity and displacement thicknesses for fully turbulent flow are one order-of-magnitude larger compared to laminar flow. Using StanMix compared to RefProp results in a higher velocity and displacement thickness up to and including the throat section, but the difference is smaller in the diverging section and straight outlet section (see table 5-3 and 5-4).

flow, such as the displacement thickness; and local properties influencing the velocity profile inside the boundary layer, in this case c, C and PG parameter m_3.

5-3-1 Boundary Layer Integral Properties: Displacement Thickness

Figures 5-5, 5-6 and 5-8 and Tables 5-2, 5-3 and 5-4 present the simulation results of four simulations for laminar and turbulent flow with RefProp and StanMix respectively. RefProp is considered as a reference, and therefore comparisons are always made in relation to the results obtained with RefProp. Velocity and displacement thickness are discussed together, due to their similarity.

Figures 5-5, left and right, show the behaviour of the boundary layer velocity (left) and displacement (right) thickness. First, both thicknesses increase fast in the straight inlet section and continue growing in the first part of the converging section until reaching a maximum. Notice that the maximum is reached earlier for laminar flow than for turbulent flow. From this point on, the thicknesses decrease fast towards a minimum just after the throat location. The point of inflection in the diverging section can be seen because it alters the constant growth rate of the boundary layers at this point to a slightly lower value. The end of the nozzle diverging section and start of the straight outlet section mark another point where the constant growth rate also changes suddenly

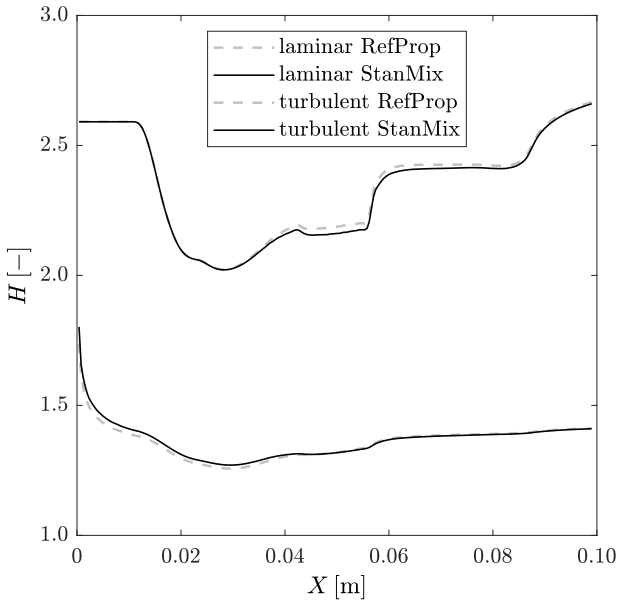

Figure 5-6: Shape factor as function of the nozzle surface coordinate for all four simulations: laminar (top) and turbulent (bottom) flow both with the StanMix and RefProp thermophysical models. For comparison: $H = 2.59$ for Blasius' (laminar) boundary layer, and $H = 1.3 - 1.4$ for a turbulent flat plate boundary layer in air. The shape factor is sensitive to sudden changes in the nozzle geometry.

to a slightly lower value.

The velocity and displacement thickness for turbulent flow are larger than in case of laminar flow as expected. From Tables 5-4 and 5-3 it can be seen that the velocity thickness at the outlet is about a factor 10 larger for turbulent flow compared to laminar flow. The displacement thickness is about a factor 5 larger for turbulent flow compared to laminar flow respectively. Figure 5-6 depicts the shape factor, which is considered as the most sensitive boundary layer characteristic. The shape factor values at the nozzle outlet for laminar flow are close to those for incompressible flat plate flow for air, around 2.6 (2.59 for Blasius' profile), and for turbulent flow around 1.4 (1.3 to 1.4 for air). The differences caused by the type of thermophysical model is small. However, it needs to be noticed that the shape factor is sensitive to the peaks in the derivative of the static pressure input caused by sudden changes in the geometry, which is another reason why this pressure peak in the boundary layer edge input was removed. Transitions between the different nozzle sections, e.g. inlet section, converging section, diverging section; can be appreciated in the shape factor plot by sudden changes. For example, the connection between the laminar inlet and converging section in Fig. 5-6 show a smooth course around $X = 0.012\,\mathrm{m}$ due to interpolation of the input pressure, but a dent around the minimum at $X = 0.023\,\mathrm{m}$ where the interpolation polynomial matches with the original curve.

The differences in velocity and displacement thickness caused by the type of thermophys-

ical model adopted are relatively small. The results of the simulations using StanMix show a higher velocity and displacement thickness up to and including the throat section, but slightly lower values in the diverging section and straight outlet section compared to RefProp (see table 5-3 and 5-4). Notice also the differences in maximum displacement thickness in the converging nozzle section: 19% higher for laminar flow, and 8% higher for turbulent flow using StanMix. The converging section is not crucial, but the diverging section is, and there the differences are smaller. From the throat on, the prediction will matter for the nozzle performance. The displacement thickness around the throat differs with 8.2% for laminar and 3.3% for turbulent flow. Notice that the throat, located at $X = 0.044\,\mathrm{m}$, is just after the minimum turbulent boundary layer thickness of $X = 0.038\,\mathrm{m}$ in both cases; and it is just after the minimum laminar boundary layer thickness of $X = 0.039\,\mathrm{m}$ in both cases. At the nozzle outlet the displacement thickness differs with -4% for laminar and -1.3% for turbulent flow. Interestingly, it can be seen that the relative differences in the simulation results are the smallest for the more critical diverging section. It would therefore be interesting for design purposes to find and quantify the sensitivity of the displacement thickness in the diverging section to the pressure history in the converging section.

The final displacement thickness predicted for the inviscid ORCHID nozzle design expanding MM using RefProp is estimated to be 1.0% of the outlet half-height (and thus also 1.0% of the total outlet cross section) for turbulent flows. For laminar flows this is 0.3%. The velocity thickness is 7% for turbulent flows and 0.7% for laminar flows. This order-of-magnitude of boundary layer displacement thickness for laminar and for turbulent flow is negligible, and hence it will barely influence the outlet Mach-number. In addition, it is not measurable with the current ORCHID test set-up. Because, from experience of others[references] it is expected that a velocity thickness for air of at least 1 mm should be visible in the Schlieren graphs, whereas the density gradient for a complex fluid is much less, and thus a much thicker boundary layer is needed to measure any differences in density compared to air. In case of laminar flow, the displacement thickness is of the order of 10^{-5} m, which is close to the machine tolerance.

Recall the relation for displacement thickness from Sec. 3-4-2

$$\delta^* = \int_0^\infty \left[1 - \frac{\rho u}{\rho_\mathrm{e} u_\mathrm{e}}\right] \mathrm{d}y = \frac{x}{\sqrt{\mathrm{Re}_x}} \int_0^{\eta_\mathrm{e}} \left[c - f'\right] \mathrm{d}\eta. \tag{3-57}$$

When considering the non-transformed relation it can be seen that a value of c closer to one results in a smaller displacement thickness. The next section will show that the parameter c is closer to one for MM as compared to air. This is a general trend for complex fluids. Therefore, the displacement thickness is smaller for HMC fluids.

5-3-2 Local Boundary Layer Properties

Local dimnesionless boundary layer properties that influence the velocity profile were identified in Sec. 3-2-2, and were found to be: c, C, m_3, m_2 and ν^+ in case of turbulent

flow (eq. 3-8, 3-15, 3-14 and 3-7). Where m_3 is a function of local property C_e. Recall that the Energy Equation (EE) influences the Momentum Equation (ME), and thus the velocity field, but only through parameters which are a function of density and dynamic viscosity: c, C, m_3 and ν^+ in case of turbulent flow. By definition, c and C are equal to one at the boundary layer edge, and they reach their largest deviation from this value at the wall surface. Therefore, only the wall values of these parameters are considered next: c_w and C_w. Also, recall that Kluwick [10] states that HMC fluids exhibit negligible changes in temperature inside the boundary layer, and thus c_w and C_w are expected to be close to one. However, the question remains how close, and whether small enough to be neglected in case of MM. This section aims to quantify the behaviour of MM along the expansion in the ORCHID nozzle.

Figure 5-7-a represents the simulated values of c_w along the nozzle wall for MM and air for comparison. For air, the value of c_w is about 1.7 for laminar and turbulent flows at Mach 2.0 inside the wind tunnel nozzle of Winter & Gaudet for profile 19, which validation case was extensively reported and discussed in Sec. 4-4. In large contrast, the value of c_w at Mach 2.0 is about 1.05 inside the ORCHID nozzle design according to the laminar and turbulent simulations using Refprop. Recall that a flow is considered incompressible when density changes are lower than 5%. Putting this in perspective, the density changes inside the MM boundary layer flow are small enough to be neglected. However, the density along the expansion changes strongly, even more than air, which is discussed next. Figure 5-7-b zooms into the results for MM and shows the small difference between laminar and turbulent flow, and the values resulting from an ideal gas simulation with thermally perfect and calorically perfect ideal gas for MM. Note that the prediction will be better when more details are added. In this case adding the temperature dependence of fluid properties.

Figure 5-7-c represents the simulated values of C_w along the nozzle wall for MM and air for comparison. For air, the value of c_w is about 0.92 at the outlet of the wind tunnel nozzle of Winter & Gaudet for laminar and turbulent flow at Mach 2.0. In contrast, the value of c_w at Mach 2.0 is about 0.99 according to the laminar and turbulent simulation results using Refprop. Also here, the difference between laminar and turbulent flow is relatively small. Figure 5-7-d zooms in into the MM simulation results from Fig. 5-7-c. First, notice the minimum in the curves for both laminar and turbulent flow. This minimum is not present in the wind tunnel nozzle simulations for air. Further simulations with air showed that this trend is influenced by the choice of total conditions. For example, taking the reduced total conditions for air in the wind tunnel nozzle equal to those of the ORCHID nozzle will result in same trend, but with the value of C_w at the outlet even approaching 1.02. Thus, a minimum will appear for ideal gas simulations with air when the total conditions are chosen closer to the critical point. In other words, the total inlet conditions of the ideal gas simulation with air in the current case shown in Fig. 5-7-c are further away from the critical point compared to MM. Furthermore, note the discontinuity in viscosity for MM obtained with RefProp which is located just after Mach 0.5. In contrast, ideal gas simulation results for MM in Fig. 5-7-d show a different trend. Important to note is that both predictions for MM, for nonideal and

for ideal gas, result in a value of C_w larger than 0.99 for the main part of the nozzle expansion.

Figure 5-9-a depicts the parameter C_e (eq. 3-8). Shown are boundary layer simulations of:

1. The ORCHID nozzle using RefProp for MM, allowing departure from ideal gas;
2. The ORCHID nozzle using thermally perfect ideal gas for MM; and,
3. The wind tunnel nozzle of Winter & Gaudet for profile 19 with calorically perfect ideal gas air.

Note that the value of C_e is independent of the flow condition, laminar or turbulent. From this figure it can be seen that the relative change of C_e as function of the Mach-number along the expansion is larger for MM compared to air, but with different reduced total conditions. Further simulations with the wind tunnel nozzle for air have shown that reduced total conditions equal to the ORCHID nozzle results in a value of C_e which is only about 10% lower at the nozzle outlet than in the previous case. For comparison, simulation of isentropic expansion of air with the same reduced total conditions as the ORCHID nozzle still result in a value of C_e for MM being two times lower compared to air at Mach 2.0. Furthermore, Fig. 5-9-a illustrates that ideal gas simulations with MM do not predict the larger change in density and dynamic viscosity along the nozzle expansion.

Figure 5-9-d depicts the PG parameter m_3 (eq. 3-15) together with the other PG parameters m_1 and m_2. In this figure it can be seen that m_3 is the largest PG parameter in terms of absolute values. In contrast, for an incompressible flow m_3 is equal to zero. m_3 is a function of C_e, which decreases along expansion, and therefore m_3 is smaller than zero. Since m_3 is smaller than zero along an expansion, it counteracts the effect of the velocity gradient m_2 in a compressible flow. Further simulations of air, with equal reduced total quantities and Mach-number distribution to ORCHID nozzle conditions, showed that m_3 for MM is also larger in absolute quantities compared to air. At the same time, m_2 is also larger. But the final contribution of both m_2 and m_3 on the velocity profile is in $m_1 = \frac{1}{2}[1 + m_2 + m_3]$, which depends strongly on the pressure gradient. For the current case, absolute values for m_1 are smaller in case of MM compared to air at the ORCHID conditions. At most, m_1 is 10% and 30% smaller compared to air for the two largest absolute pressure gradients respectively. In short, the effect of the PG on the velocity profile is smaller for compressible flows. Furthermore, the effect of the PG of a complex molecular fluid such as MM is slightly smaller compared to compressible air. This means that the effect of the PG on the velocity profile is smaller in compressible flows, and it reduces even more in case of compressible flows of complex fluids.

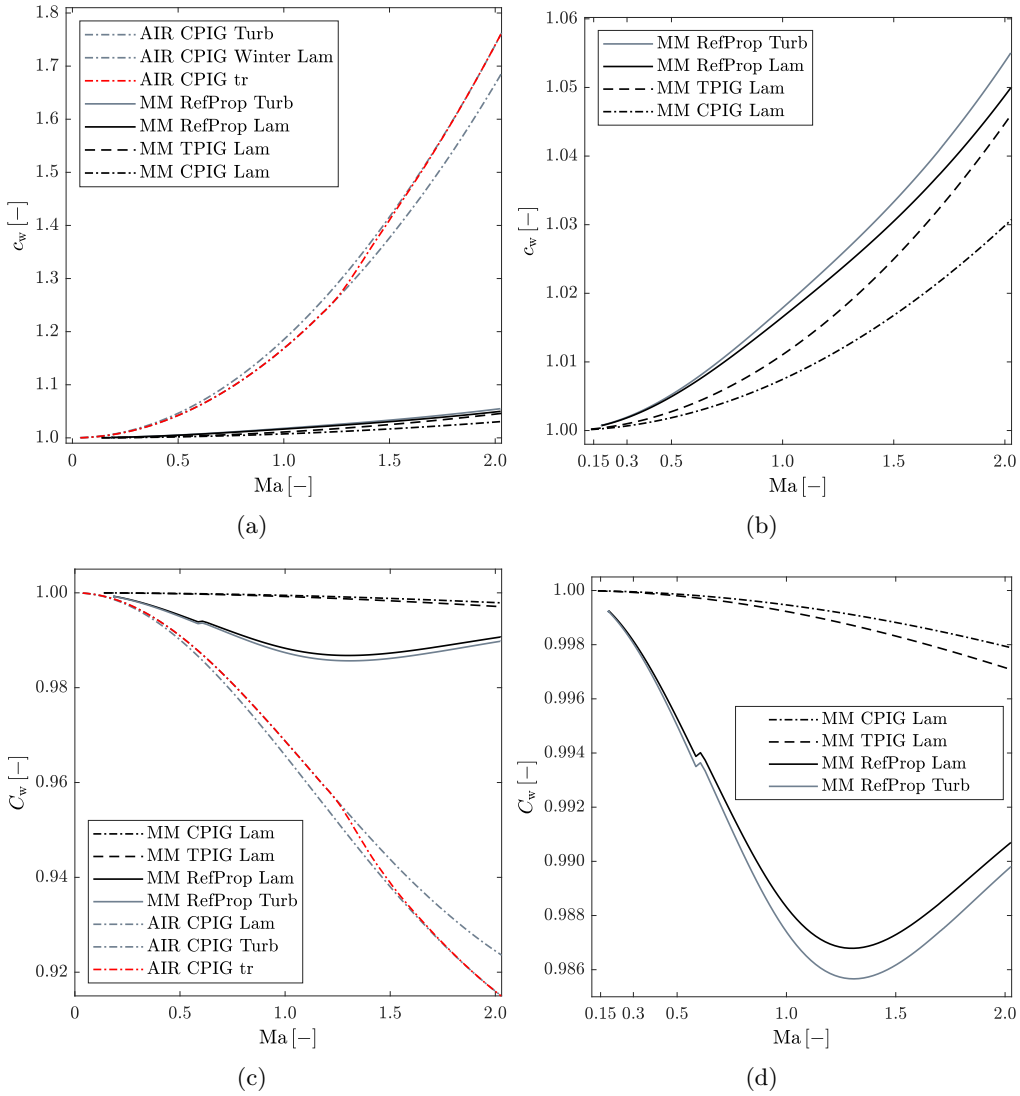

Figure 5-7: Boundary layer characteristics: local properties (a) Density ratio $c = \frac{\rho_e}{\rho}$ inside the boundary layer for MM and for Air (Winter [100] profile 19), (b) Result for MM only (Zoom of Fig. a), (c) Chapman-Rubesin parameter $C = \frac{\rho\mu}{\rho_e\mu_e}$ inside the boundary layer for MM and for Air (Winter [100] profile 19), and (d) Result for MM only (Zoom of Fig. c). Notice the discontinuities in dynamic viscosity after Mach 0.5 in the black and grey solid lines denoting the MM RefProp simulations.

5-3-3 Thermal Boundary Layer Characteristics

Other properties also characterize the boundary layer. Examples are the enthalpy recovery factor, the Prandtl-number and the turbulent Prandtl-number in case of turbulent flow.

Although the type of thermophysical model plays a minor role in predicting the displacement thickness, it does play a major role in heat transfer processes. Figure 5-8 shows several dimensionless parameters related to fluid properties along the boundary layer edge comparing their values obtained from RefProp and StanMix. It can be seen that the difference in predicted compressibility factor Z (eq. 2-73) is negligible. In contrast, the other properties show substantial differences (see table 5-2). Recall that the Prandtl-number is a function of the transport properties and isobaric specific heat. Notice also that the recovery factor is a function of the Prandtl-number, and thus of the transport properties and constant pressure specific heat. Therefore, StanMix is able to predict state variables within one percent along the nozzle expansion, but it is not able to predict dynamic viscosity μ, thermal conductivity k and constant pressure specific heat c_p accurately for lower values of Z, in the nonideal gas range (also see Fig. E-1 in Sec. E-4). Notice that all properties converge when Z approaches 1. The Prandtl-number predicted by StanMix is larger than one in the nonideal gas range (for lower values of Z), while a value of around 0.7 is expected for gases [54], and generally smaller than one. This results in a recovery factor larger than one as well. RefProp predicts a value higher than 0.7, but still smaller than one. The recovery factors obtained from the simulations with RefProp become larger compared to air, but remain below 1 as expected. The following relations can be used to approximate the recovery factor:

$$r_\mathrm{Lam} = \mathrm{Pr}^{\frac{1}{2}}, \tag{5-1}$$

$$r_\mathrm{Turb} = \mathrm{Pr}^{\frac{1}{3}}. \tag{5-2}$$

Note that the laminar recovery factor predicted by Refprop is close to the above relation, but that the turbulent recovery factor is slightly higher.

Figure 5-10-d presents the wall value of the turbulent Prandtl-number. This figure proves that the turbulent Prandtl-number model is a function of local properties close to the wall surface, and thus it also changes with the compressibility factor Z. Although the differences in wall values are small, the effect on the EE can be substantial. However, this needs further study, and especially validation with experimental data of 2D complex fluid flows, since the original model was developed for pipe flows.

5-3-4 Laminar-Turbulent Transition

The flow condition, e.g. laminar or turbulent, inside the ORCHID nozzle is yet unknown. Experiments with the test set-up have not revealed a boundary layer or turbulent phenomena. Therefore, both flow conditions have been modelled here. The engineering

estimates for prediction of transition from Sec. 2-5 were tested, and the results are discussed here.

The engineering estimate method of Wazzan [32] predicts transition just before the end of the divering nozzle section, such that the straight outlet section is fully turbulent. In contrast, Michel's extended method predicts transition in the straight inlet section already, just before the start of the converging section. Furthermore, Michel's extended method does not predict transition at all when starting the simulation at the start of the converging section. Wazzan's correlation did not predict transition from laminar to turbulent flow in a previous ORCHID nozzle design, which is not discussed here. These results are supported by Nash-Webber [34], who states that transition in these types of nozzles generally occurs in either the straight inlet, or the straight outlet sections. Experiments will have to clarify if, and where transition will take place inside the ORCHID nozzle.

Several factors play a role here. For example, one of them is the length of the straight inlet section. Depending on the method applied, transition is not predicted when the straight inlet section is left out and the flow starts to accelerate strongly almost immediately. Laminar flow then occurs in the simulation at least until the straight outlet section. When a straight inlet section is included, transition is predicted almost immediately within the inlet section. The shape of the nozzle also plays a role since it determines the acceleration of the flow which is an important factor in relaminarization and retransition [31, 34].

Furthermore, note that the simple engineering transition prediction methods where developed for incompressible flows originally. It is expected that these methods can also be applied to MM, considering the behaviour of MM as studied in the preceding sections.

5-3-5 Comparison of Results with different Thermophysical Models

Four different thermophysical models have been used for the simulations of laminar flow inside the ORCHID nozzle for comparison. Laminar flow was chosen in order to prevent the turbulence model from influencing the results. The models used were:

1. Span-Wagner (SW) multiparameter EoS (RefProp);
2. iPRSV (StanMix);
3. Calorically Perfect Ideal Gas (CPIG); and,
4. Thermally Perfect Ideal Gas (TPIG).

The first two therophysical models; namely, the SW and iPRSV take into account departure from ideal gas. The other two are ideal gas models ($Z = 1$). RefProp implements a, to the author unknown, complex model taking into account nonidealities of properties

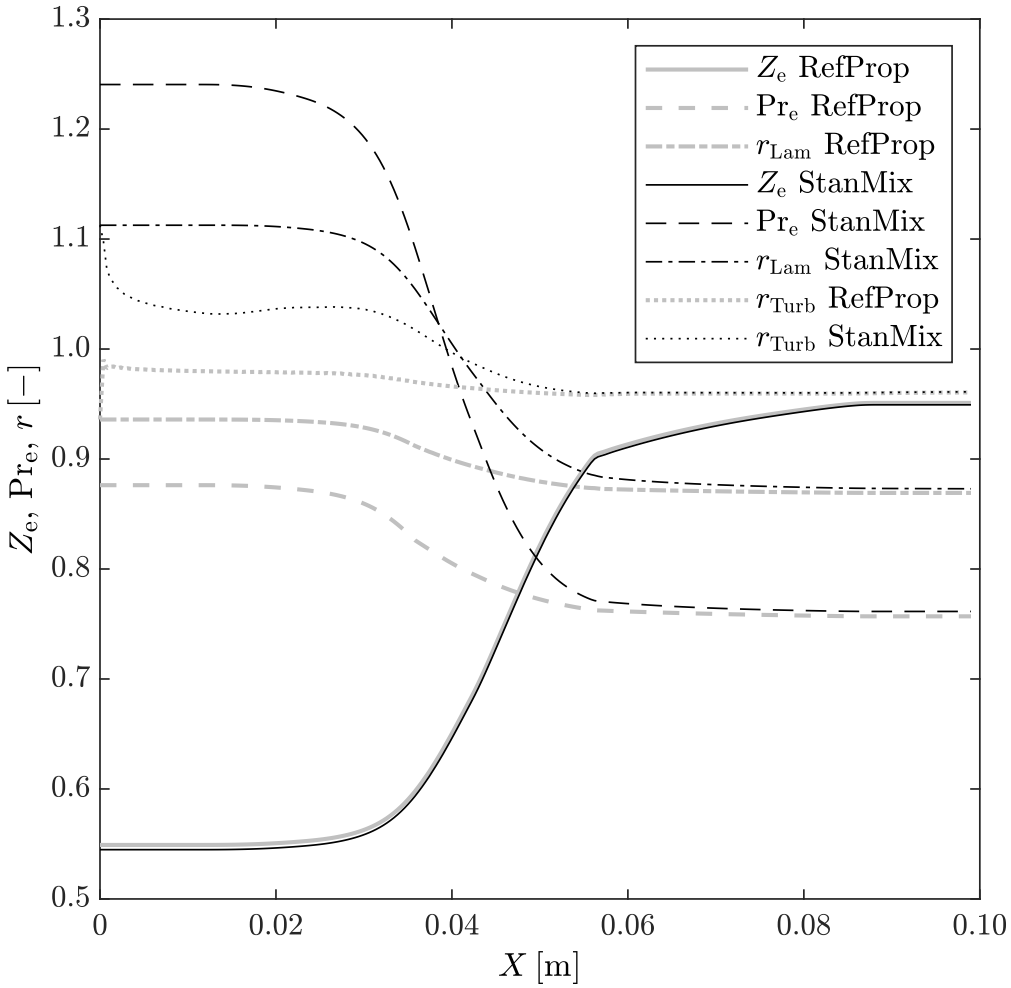

Figure 5-8: Compressibility-factor Z, Prandtl-number Pr, and enthalpy recovery factor r as function of the nozzle surface coordinate at the boundary layer edge for all four simulations. Notice that only the recovery factor changes depending on laminar or turbulent flow, proportional to: $r_{\mathrm{Lam}} = \mathrm{Pr}^{\frac{1}{2}}$ for laminar and $r_{\mathrm{Turb}} = \mathrm{Pr}^{\frac{1}{3}}$ for turbulent flow. Notice also the differences between the results obtained from RefProp and StanMix. The Prandtl-number predicted by StanMix is larger than 1 for both laminar and turbulent flow before the nozzle throat. This results in a recovery factor above one, which will affect heat transfer simulations. The differences are caused by substantial differences in predicted isobaric specific heat and the transport properties. Notice that the Prandtl-number predicted by StanMix is larger than one, while a value of around 0.7 is expected for gases. The values from StanMix converge to those of RefProp for Z approaching 1.

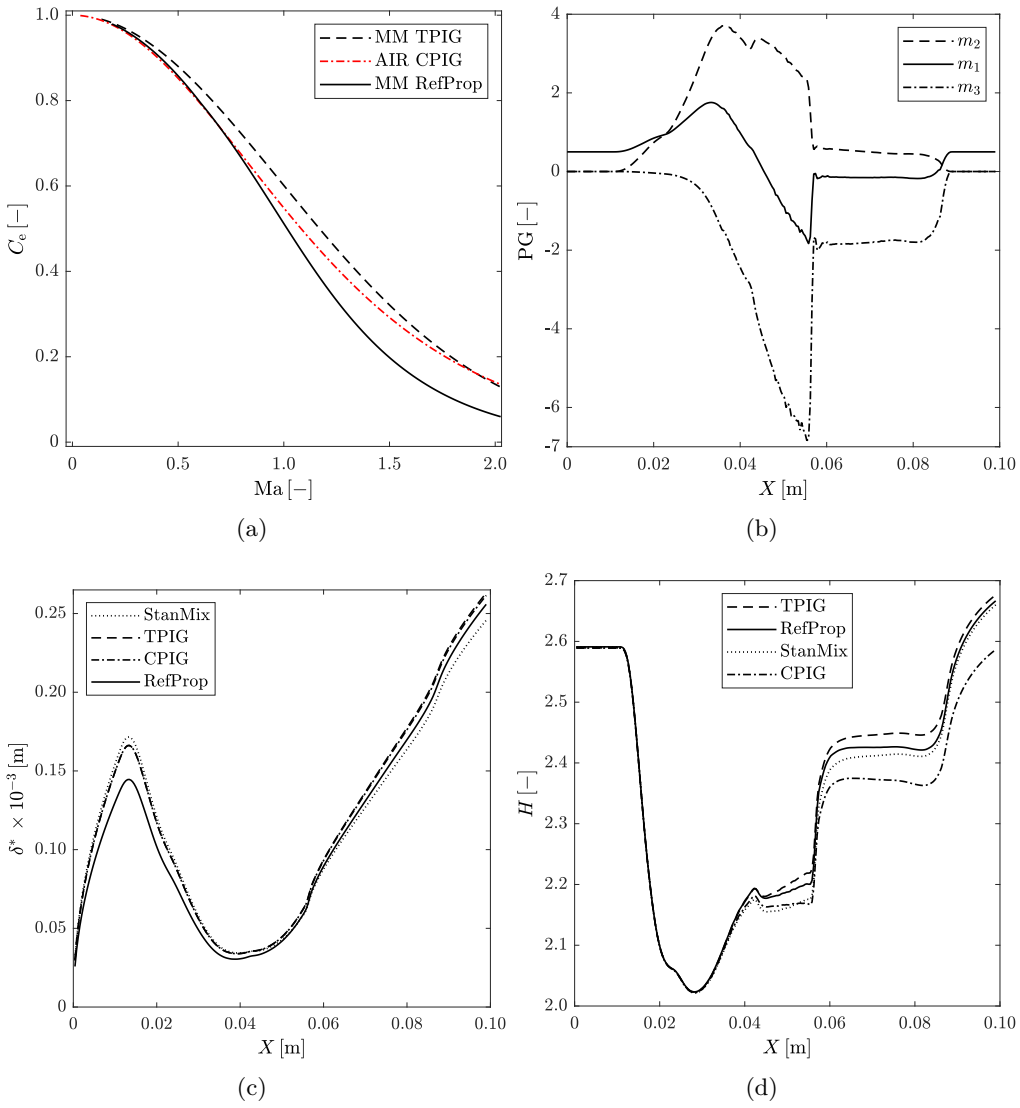

Figure 5-9: Boundary layer characteristics: integral properties (a) Parameter $C_e = \frac{\rho_e \mu_e}{\rho_0 \mu_0}$ for MM and for Air (Winter [100] profile 19), (b) Pressure Gradient parameters m_1 to m_3, (c) Displacement thickness with four different Thermophysical models, and (d) Shape factor with four different Thermophysical models.

such as the isobaric specific heat and the transport properties. The iPRSV and the ideal gas models are complemented with simple polynomials for modelling the isobaric heat capacity. The iPRSV implements Chung's method [78] for obtaining the transport properties, whereas the ideal gas models use Sutherland's Law. The combinations are referred to as, for example, the StanMix thermophysical model, which is the iPRSV complemented with relations for isobaric heat and transport properties. RefProps is considered as reference, since it is the most accurate model available.

Figures 5-9-c and 5-9-d show the predicted displacement thicknesses and shape factors for laminar flow of MM along the curved surface walls inside the ORCHID nozzle using these four different thermophysical models. Regarding the converging nozzle section it can be seen in Fig. 5-9-c that RefProp predicts a different and lower displacement thickness compared to the other thermophysical models used. This cannot be appreciated in the shape factor in Fig. 5-9-d. Furthermore, in the converging section the displacement thickness (Fig. 5-9-c) of both ideal gas models superimposes, and StanMix gives only a slightly higher value, which deviates the most from RefProp. In this case of laminar flow StanMix hence gives a displacement thickness prediction which is even further from the RefProp reference than the two ideal gas models in the converging section for values of $Z = 0.55$. Regarding the diverging section, the trends become different. The two ideal gas models still superimpose, but StanMix behaves differently, since it becomes lower than the RefProp reference, but it still deviates from it with about the same magnitude as the ideal gas models, and it shows even a slightly larger deviation at the nozzle outlet. The shape factor in Fig. 5-9-d gives a different result, showing that the result obtained with StanMix is the closest of all three to the RefProp reference, and the ideal gas models do not superimpose but show an opposite trend. Concluding, the faster StanMix thermophysical model can be used for the prediction of state variables, but the iPRSV needs to be complemented with better performing models for predicting the isobaric specific heat and transport properties.

5-3-6 Analysis of Boundary Layer Losses

Analyzing the losses generated inside the simulated boundary layer flows along the nozzle wall surface can assist in improving the nozzle design. The loss coefficient introduced by Denton [1] is a useful parameter to characterize the losses generated. However, it is difficult to interpret how these losses build-up, and where the highest amount of losses is generated.

Figure 5-10-c presents Denton's loss coefficient for laminar and turbulent flow for the ORCHID nozzle boundary layer using RefProp. As expected, the loss coefficient for turbulent flow is higher than that of laminar flow. The relative losses are higher at the start of this boundary layer, since the loss coefficient scales the amount of entropy generated within the local boundary layer with the local flow conditions. This results in higher relative losses at the start of this boundary layer in case of plate flow. Since the relative difference in velocity is highest at the leading edge, and thus the velocity

gradient is high. The thicker the boundary layer becomes, the lower the loss coefficient. Therefore, it is likely to interpret the loss coefficient in this case such, that the relative amount of losses generated at the start of the developing boundary layer is higher.

Figure 5-10-a presents the total accumulated entropy generated inside the boundary layer. The steepness of this curve represents the rate of entropy generated, which is shown in Fig. 5-10-b. The first thing that stands out is the large difference in losses generated by laminar and turbulent flow regarding equal free stream conditions. Clearly, one wants to design for laminar flow conditions when aiming for an efficient design. The second thing that should be noticed is the relatively small contribution of the subsonic nozzle sections to the total loss generated. For laminar flow this is 7%, and for turbulent flow this is only 5% upstream of the throat. The main part of the losses is generated inside the diverging section. Only a small fraction of the losses is generated around the leading edge, where the boundary layer starts to develop. These numbers explain why the simulation results of displacement thickness for the diverging section are closer, since the influence of the pressure history from the converging section is relatively small here. Decreasing the losses from the converging section even further, can therefore decrease the influence of the pressure history upstream of the throat on the boundary layer thickness inside the critical diverging section.

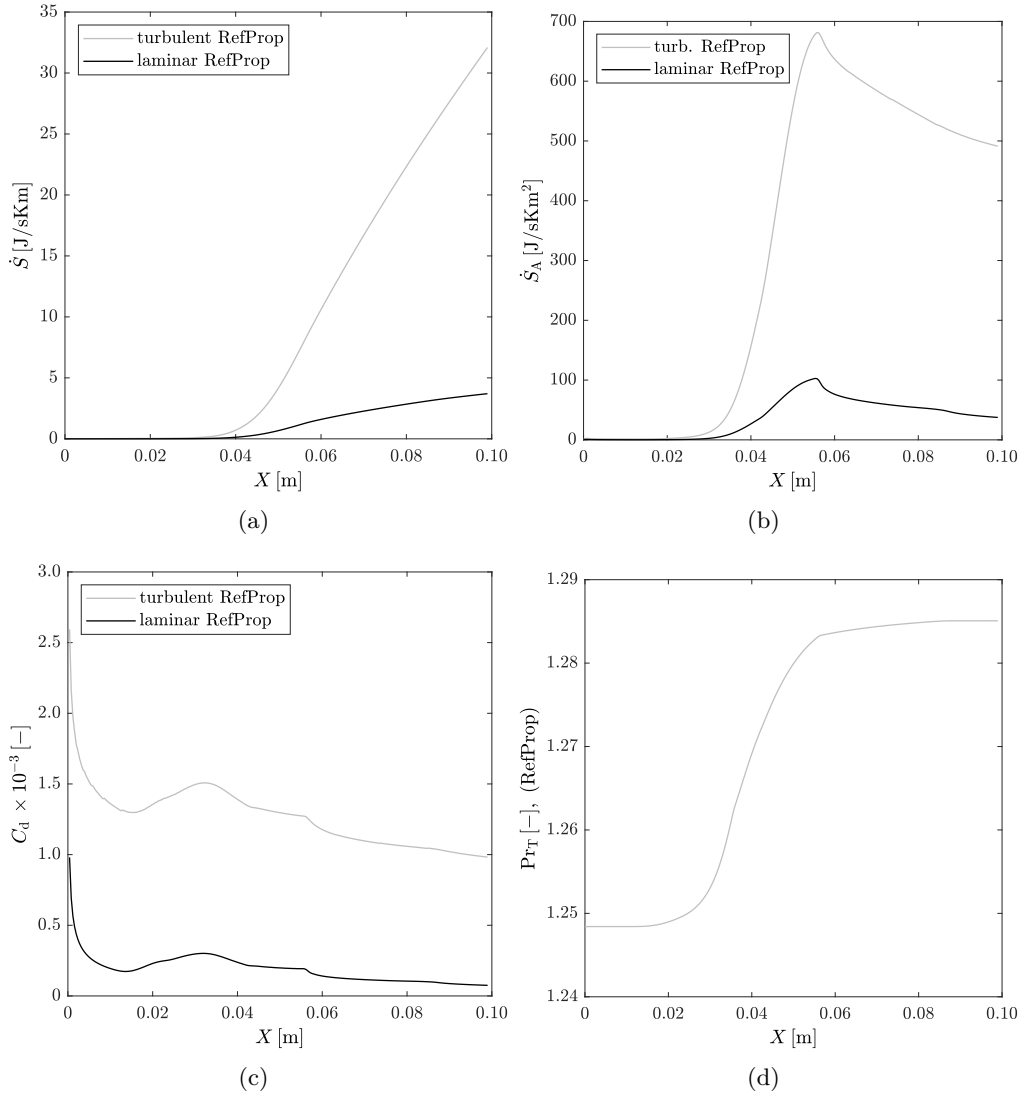

Figure 5-10: Boundary layer losses plotted, and nonrelated wall turbulent Prandtl-numbers: (a) Cumulative entropy generated inside the boundary layer, (b) Local entropy generation rate, (c) Loss coefficient by Denton [1], and (d) The turbulent Prandtl-number at the wall surface along the ORCHID nozzle. All results were calculated using RefProp. Notice that the loss coefficient C_d gives a different perspective on the total (absolute) losses generated.

Table 5-2: Comparison of ORCHID simulations with two different thermodynamic models: boundary layer edge properties. Results calculated using StanMix and RefProp. StanMix utilizes the iPRSV, whereas RefProp utilizes unknow industrial standards? StanMix is used here as starting point for convenience, since the fluid property retrieval is much faster, whereas RefProp is thought to be more accurate. Note also that edge properties are the same for laminar or turbulent flow. Static pressure obtained from SU2 CFD simulation second-order convergence is used as input.

Boundary layer edge	$P_{s,e}$ $\times 10^5$ [Pa]		Ma_e [-]		Z_e [-]		Pr_e [-]		$C_{p,e}$ $\times 10^3$ [J/kg/K]		μ_e $\times 10^{-5}$ [kg/m/s]		k_e $\times 10^{-2}$ [W/m/K]		Re_e $\times 10^7$ [1/m]	
properties	in	out	in	out	in	out	in	out	in	out	in	out	in	out	in	out
RefProp	18.183	1.894	0.2	2.0	0.55	0.95	0.88	0.76	2.890	1.990	1.161	1.045	3.829	2.747	18	24
StanMix	18.184	1.901	0.2	2.0	0.54	0.95	1.24	0.76	2.729	1.954	1.642	0.944	3.612	2.423	13	27
Deviation [%]	0.003	0.41	−0.03	−0.14	−0.78	−0.18	41.58	0.59	−5.58	−1.80	41.45	−9.66	−5.67	−11.81	−29.0	10.7

Table 5-3: Comparison of ORCHID laminar simulations with two different thermodynamic models: boundary layer edge properties. Results calculated using StanMix and RefProp. StanMix utilizes the iPRSV, whereas RefProp utilizes unknow industrial standards? StanMix is used here as starting point for convenience, since the fluid property retrieval is much faster, whereas RefProp is thought to be more accurate. Note also that edge properties are the same for laminar or turbulent flow. Static pressure obtained from SU2 CFD simulation second-order convergence is used as input.

Laminar flow	δ $\times 10^{-3}$ [m]	δ^* $\times 10^{-3}$ [m]	θ $\times 10^{-3}$ [m]	H [-]	Re_e $\times 10^7$ [1/m]	Re_x $\times 10^7$ [-]	Re_θ $\times 10^3$ [-]	C_f $\times 10^{-3}$ [-]	C_d $\times 10^{-3}$ [-]	r [-]	c_w [-]	C_w [-]
RefProp	0.077	0.026	0.010	2.67	24	2.4	2.34	4.593	0.075	0.869	1.050	0.991
StanMix	0.075	0.025	0.009	2.66	27	2.7	2.49	4.344	0.071	0.873	1.051	0.991
Deviation [%]	−3.12	−3.97	−3.73	−0.25	10.7	10.7	6.5	−5.41	−5.75	0.43	0.06	0.06

Table 5-4: Comparison of ORCHID turbulent simulations with two different thermodynamic models: boundary layer edge properties. Results calculated using StanMix and RefProp. StanMix utilizes the iPRSV, whereas RefProp utilizes unknow industrial standards? StanMix is used here as starting point for convenience, since the fluid property retrieval is much faster, whereas RefProp is thought to be more accurate. Note also that edge properties are the same for laminar or turbulent flow. Static pressure obtained from SU2 CFD simulation second-order convergence is used as input.

Turbulent flow	δ $\times 10^{-3}$ [m]	δ^* $\times 10^{-3}$ [m]	θ $\times 10^{-3}$ [m]	H [-]	Re_e $\times 10^7$ [1/m]	Re_x $\times 10^7$ [-]	Re_θ $\times 10^3$ [-]	C_f $\times 10^{-3}$ [-]	C_d $\times 10^{-3}$ [-]	r [-]	c_w [-]	C_w [-]
RefProp	0.735	0.103	0.073	1.41	24	2.4	17.87	51.009	0.982	0.961	1.055	0.990
StanMix	0.724	0.102	0.072	1.41	27	2.7	19.55	50.273	0.966	0.961	1.056	0.990
Deviation [%]	−1.46	−1.25	−1.15	−0.11	10.7	10.7	9.4	−1.44	−1.68	0.06	0.05	0.07

5-4 Factors to Consider in a Future Robust Viscous Nozzle Design

This section outlines a few factors for improving the (re)design of a nozzle used for highly nonideal expansions. The term *robust* in the title refers to a design by which fluctuations in performance caused by fluctuations of the surrounding factors are reduced to a minimum to guarantee stable operation.

From the results of the preceding deterministic simulations (Fig. 5-10-a and -b) it is clear that a more efficient nozzle design should aim at entirely laminar flow since its losses are significantly lower with an-order-of-magnitude compared to turbulent flow. Repeating the experiments of Bader [29–31] with the ORCHID can lead to the required knowledge.

Furthermore, the amount of losses can be lowered by changing minor things in the current ORCHID nozzle design. For example, recall the peak in static pressure at the start of the converging section, which is possibly caused by a too sudden contraction at the start of the converging section. Increasing this smallest radius of curvature results in a more gradual pressure decrease in the converging nozzle section. Designing more gradual connections between the different nozzle sections (see Sec. 5-2) results in lower losses and better predictability. Namely, the current sudden changes in the derivative of geometry cause fluctuations in the static pressure distribution obtained with the CFD simulation at some of these locations. These fluctuations result in larger numerical fluctuations in the pressure gradient parameters of the boundary layer program.

Figure 5-11 presents the ratio of velocity thickness to radius of curvature locally for the current ORCHID nozzle in case of turbulent flow and in case of laminar flow. The radius of curvature was calculated with the usual analytical relation for 2D geometries in a Cartesian coordinate system. This relation contains the first and second derivative of the geometry, which posed a problem immediately. Analytical functions of the ORCHID nozzle geometry were not available, and the numerical derivatives resulted in larger spikes than the actual radius of curvature. Therefore, a piecewise cubic hermite interpolating polynomial (PCHIP-function MATLAB) was used to fit the derivatives and to estimate curvature. The smooth results can be seen in Fig. 5-11. The current minimum radius of curvature is about 0.017 m, which results in a ratio of $\frac{\delta}{R_c} = 0.0026$ for laminar flow, and $\frac{\delta}{R_c} = 0.0124$ for turbulent flow. The peaks occur in Fig. 5-11 between the minimum in radius of curvature and the maximum velocity thickness in both cases. Notice that the ratio for turbulent flow is relatively large. When the ratio becomes too large, centrifugal forces cannot be neglected anymore changing the boundary layer behaviour and thus lowering its predictability.

Summarizing, both increasing the smallest radius of curvature and smoothing the derivatives of the current nozzle design results in a more gradual pressure decrease and thus a smoother expansion with lower losses. At the same time, this results in a higher predictability with the current method. On the one hand, because the relative amount

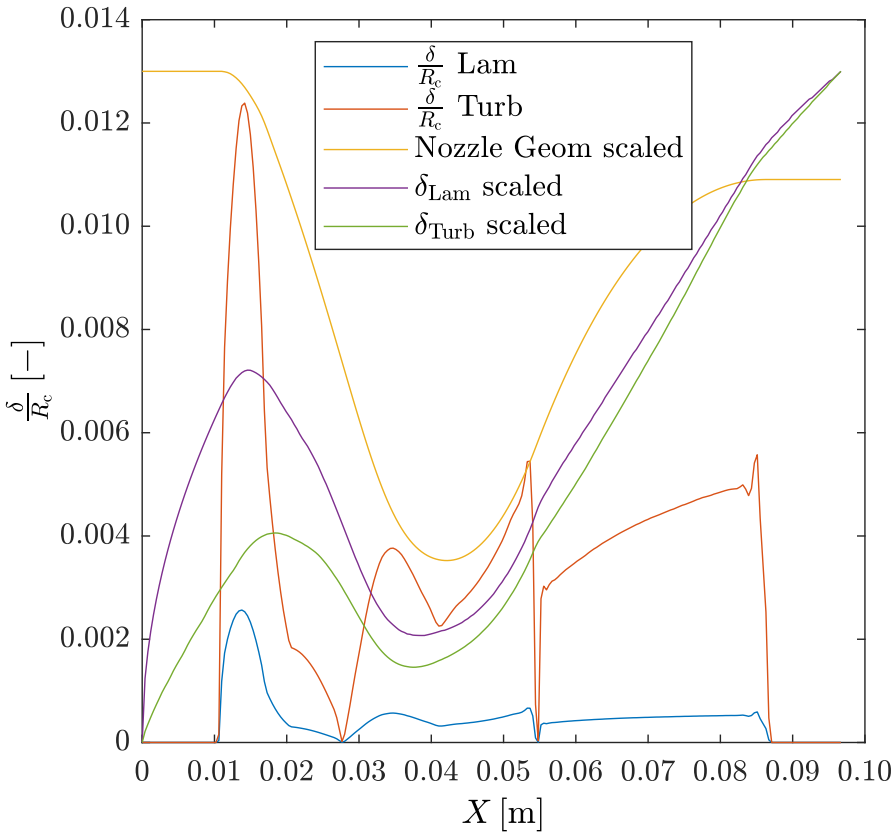

Figure 5-11: Ratios of laminar and turbulent velocity thickness over radius of curvature. Scaled nozzle geometry and laminar and turbulent velocity thicknesses are plotted for reference.

of losses inside the converging section is reduced, which reduces the influence of the converging section on the diverging section, e.g. pressure history. On the other hand, because a smoother geometry with larger radii of curvature not only results in less numerical noise, but it also reduces the effects of e.g. centrifugal forces caused by wall surface curvature.

For a robust nozzle design, first the validity of the boundary layer program for nozzle flows of complex fluids departing from ideal gas needs to be proven, such that the displacement thickness can be predicted with confidence. Preferably with experimental data obtained from the ORCHID nozzle test section. Second, the uncertainties and sensitivities of boundary layer characteristics to their surroundings and to the models used needs to be investigated, such as was done by Iyer [77]. Examples of these factors are the input total conditions, the pressure history and closure coefficients in the thermophysical and turbulence models. Sensitivity studies will need to be performed to quantify the influences of these factors.

The following uncertainties and knowledge gaps deserve attention for a future robust

design:

1. Validity of boundary layer program for accelerating complex organic fluids in dense gas regions (with departure from Ideal Gas);
2. Validity of thermophysical models;
3. Uncertainty in closure coefficients of thermophysical models;
4. Flow conditions for laminar and turbulent flow (transition and relaminarization);
5. Uncertainty in closure coefficients of turbulence model (in case of turbulent flow);
6. Sensitivity of boundary layer characteristics (especially displacement thickness) to:
   (a) Input conditions;
   (b) Thermophysical properties;
   (c) Closure coefficients of thermophysical models;
   (d) Closure coefficients of turbulence model(s);
   (e) Pressure history, including point of (re-)transition and transition region.

The calculation time taken by the boundary layer program can be decreased for sensitivity studies by, for example:

1. Implementing the entire program in FORTRAN or any other faster language;
2. Using StanMix supplemented with Sutherland's Law for transport properties and a polynomial for the isobaric heat capacity fitted to the ORCHID nozzle conditions; or,
3. Implementing table interpolation of thermophysical properties (LUT) [111, 112];
4. Removing calculations of output variables other than the displacement thickness; and,
5. Substituting MATLAB built-in functions for simple hard-coded algorithms.

For a complete robust ORCHID nozzle design, the sensitivity studies of Iyer [17] need to be repeated including shear viscosity. Iyer showed that in the case of an inviscid flow the nozzle design is barely influenced by variations in the total input conditions and thermophysical model closure coefficients. The variation in nozzle outlet half-height was on average 0.29 mm, which accounted for 1.1% of the nozzle outlet cross-sectional area (compared to 9.1% and 13.3% (Mach 0.2 only) for the four cases of Winter & Gaudet considered in Sec. 4-4). This variation has a negligible influence on the outlet Mach-number. Since the displacement thickness can be considered as the inviscid nozzle design, it might be sufficient to consider the effects of total input conditions, the thermophysical model closure coefficients and turbulence model closure coefficients on the boundary layer characteristics.

5-5 Summary

In this chapter preliminary results of deterministic simulations performed with state-of-the-art thermophysical models applied to the ORCHID nozzle were presented.

Simulations of fully laminar and fully turbulent flow showed that the displacement thickness in both cases is negligible compared to the cross-sectional area of the nozzle for MM. Simulations using RefProp resulted in a maximum displacement thickness at the nozzle outlet of 1% of the outlet cross-sectional area in case of turbulent flow. In case of laminar flow, the maximum displacement thickness at the nozzle outlet was 0.3% of the outlet cross-sectional area. The effect of a displacement thickness of this order-of-magnitude can be considered as negligible on the outlet Mach-number.

According to the simulations, the boundary layer flow of complex fluid MM can be characterized as close to incompressible locally, since the changes in the density ratio c do not exceed 5% relative to the free stream. In contrast, c_{w} exceeds 1.7 for air at Mach 2.0. This is supported by Kluwick [10] who claims that HMC fluids exhibit negligible changes in temperature and density inside the boundary layer. Also, the Chapman-Rubesin parameter C does not exceed 1.5% from the local edge value of one, along the entire nozzle wall surface. In contrast, the change in fluid property PG parameter C_{e} along expansion in the isentropic core flow is significant: it decreases from 0.98 to 0.06, and its decrease is larger compared to air. These effects result in higher absolute values of PG parameter m_3 relative to m_2 for MM, which results in a smaller influence of the PG on the velocity profile. Generalizing, the properties of HMC fluids decrease the effects of local compressibility and PG on the velocity profile in boundary layer flows inside nozzles expanding these complex fluids.

The transport property predictions were shown to influence the boundary layer characteristics by comparing StanMix with RefProp, which is considered to be the most accurate. The differences in velocity and displacement thickness, and shape factor are still within 10% comparing StanMix with RefProp. The differences are higher for the nozzle sections located upstream of the throat in the dense gas region where $1-Z = 0.45$. Interestingly, the predictions with both models for the diverging nozzle section almost superimpose. This is due to at least two effects: relative amount of losses, and departure from ideal gas. Regarding the first effect, Duff [53] derived a simple relation based on the momentum integral approach which he used to show that the thickness inside the diverging nozzle section is barely influenced by the thickness inside the section upstream of the throat. This supports the trends seen in Fig. 5-10-a and 5-10-b. The magnitude of losses generated inside the boundary layer is a function of boundary layer edge velocity and acceleration. The steeper the velocity profile, the higher the losses. The flow inside the ORCHID nozzle accelerates such that the losses generated upstream of the throat are only 7% of the total losses generated inside the boundary layer. For turbulent flow this accounts for 5%. Both are almost negligible compared to the losses generated around and downstream of the throat, and can even be reduced further by design. The second effect, that of accurate property prediction in the ideal gas region, is illustrated

in Figures 5-5-a to d. Which show a negligible influence of the thermophysical model used inside the diverging section where the ideal gas region is entered again and the fluid and transport properties predicted by both models converge.

Simulations of a laminar boundary layer flow inside the current ORCHID nozzle showed that ideal gas models are not suitable for the prediction of the boundary layer characteristics for MM. Interestingly, the results obtained with StanMix were comparable in predictive capacity regarding the calculated displacement thickness as the calorically perfect and imperfect ideal gas models due to low accuracy transport property predictions for the range considered. It is essential to predict fluid properties accurately though. Therefore, an interpolation table can be made with fluid property values obtained from RefProp. Implementing this for the range of the ORCHID nozzle only will make the fluid property retrieval even faster (estimated to be around 1 second per simulation) compared to the current action of calling FluidProp. It is also possible to use StanMix for obtaining state variables only, implementing Sutherland's Law for dynamic viscosity and thermal conductivity and a polynomial for constant specific heat. The computational time is then expected to be less than one minute per run for the ORCHID nozzle case.

Factors that need to be considered for a future robust viscous nozzle design are:

1. Design for a smooth and gradual expansion to reduce losses;
2. Design for a smooth geometry up to second derivative to increase numerical predictability;
3. Investigate laminar-turbulent transition and retransition for designing a completely laminar nozzle;
4. Validate the boundary layer program with experimental data obtained from the ORCHID test set-up; and,
5. Perform sensitivity studies to investigate the effect of uncertainties in closure coefficients in thermophysical and turbulence models, and variations in input conditions and pressure history, on the boundary layer displacement thickness.

The time taken for the calculations is another factor to take into account. A simulation with RefProp for accurate fluid property predictions takes about 80 minutes, whereas a simulation using StanMix takes only around 2 minutes, calculated with an Intel i7-6700HQ processor at 2.60 GHz. The calculation speed of the program can be increased for performing sensitivity studies. StanMix can be used for state variables only in sensitivity study calculations, supplemented by Sutherland's law for predicting dynamic viscosity and thermal conductivity, and a polynomial for predicting c_p fitted to the ORCHID nozzle conditions. It is expected that the time taken for one nozzle simulation can be reduced to less than 1 minute while keeping the same accuracy. A grid refinement

study can be performed to find a possible reduction in the number of stations without reducing accuracy.

The validity of the thermophysical models in combination with NICFD is part of the ORCHID research [17]. DoE studies together with the ORCHID experimental campaign might give answers to the uncertainty in closure coefficients of the thermophysical models used here. The current boundary layer program is designed for these kind of sensitivity studies. A thorough sensitivity study will be the next step in this research.

Chapter 6

Conclusions, Recommendations and Future Outlook

6-1 Conclusions

The influence of nonideal thermophysical properties on predictions of two-dimensional steady state boundary layer characteristics was investigated. A program was developed including a turbulence model and capable of using different thermophysical models. The program was verified and validated.

The main research question was:

What is the influence of the nonideal thermophysical properties of a complex fluid on two-dimensional steady state boundary layer flows?

This research question was answered by treating the following sub-research questions.

1. What is a suitable turbulence model for studying the effect of complex fluid thermophysical properties on boundary layer characteristics?

The Cebeci-Smith (CS) algebraic turbulence model was implemented. This semi-empirical zero-equation model was found to be sophisticated enough to capture the relevant physics while at the same time it was simple enough to gain an understanding of the influence of nonideal thermophysical properties on the boundary layer characteristics.

2. Are the closure coefficients and the range of validity of the boundary layer program suitable to predict accurately the physics of complex organic fluid flows?

The closure coefficients and the range of validity of the boundary layer program are expected to be suitable for flow simulations of complex organic fluid flows, altough there remains a need to verify this with experimental data. The closure coefficients of the CS-model are based on a sound approach and calibrated to large sets of experimental data obtained from renowned experiments of (close to) incompressible flows in air. In addition, flow properties of turbulent flows are a function of turbulent characteristics and do not depend on fluid properties. Furthermore, the characteristics seem universal, e.g. the Von Kármán constant. Therefore, it is expected that flows of complex molecular fluids can be simulated using these closure coefficients, since their behaviour is characterized as close to incompressible (see next item 3). Note however, that in complex fluid flows close to the critical point changes in fluid properties are believed to stabilize the flow possibly leading to relaminarization [87, 88].

3. How can a boundary layer in a complex organic fluid flow be characterized?

Deterministic simulations of the boundary layer along the curved wall surface of the aforementioned nozzle expanding MM were performed. The results showed a larger decrease in the newly defined property $C_\mathrm{e} = \frac{\rho_\mathrm{e}\mu_\mathrm{e}}{\rho_0\mu_0}$ in the core flow along expansion compared to air. In contrast, the property gradients inside the boundary layer; namely the density ratio c and Chapman-Rubesin parameter C, were found to be negligible, resulting in a locally incompressible boundary layer for MM. The velocity profile therefore converges to Blasius' solution for zero pressure gradient flows. The decrease in C_e along an isentropic expansion even reduces the effect of the pressure gradient on the velocity profile compared to incompressible flows, and it reduces the changes in velocity profiles along the X-coordinate direction. Hence, the effect of an arbitrary pressure gradient on the velocity profile in a complex fluid flow of MM is smaller compared to air for equal nondimensional pressure gradients.

4. How does presence of the boundary layer influence the expansion of complex organic fluid MM in the ORCHID nozzle?

Boundary layers in supersonic nozzles were found to be relatively thin according to experiments and simulations. They were found to be even thinner for complex fluid flows such as MM due to the aforementioned negligible gradient in c. The boundary layer displacement thickness is a measure of the shift in stream lines of the core flow caused by the retarded flow region close to the wall. The shift in stream lines decreases the effective core flow area which results in a lower expansion ratio and thus lower Mach-numbers at the nozzle outlet. The boundary layer displacement thicknesses for laminar and turbulent flow predicted for MM in the ORCHID nozzle were 0.25% and 1% of the outlet cross-sectional area respectively. These percentages have a negligible effect on the Mach-number.

5. What factors need to be considered in a future robust design of a viscous ORCHID nozzle?

Factors that need be considered in a future design include designing for entirely laminar flow and for a smooth pressure decrease. Both factors apply to the converging nozzle section and result in lower losses and higher predictability with the current method. Laminar flows generate lower losses and the inlet of the converging section is crucial in retaining laminar flow conditions throughout the rest of the nozzle. The predictability of the boundary layer in the most critical nozzle diverging section increases by reducing the already relatively low amount of losses of the converging section even further. For a robust design, detailed sensitivity studies need to be performed to quantify the influence of this so-called pressure history on boundary layer characteristics, and especially on the displacement thickness which is directly linked to the viscous nozzle design. Furthermore, the sensitivity of the displacement thickness to the total input conditions, thermophysical model closure coefficients and turbulence model closure coefficients needs to be investigated.

6-2 Recommendations

For a robust ORCHID nozzle design, the sensitivity studies of Iyer [17] need to be repeated including shear viscosity. Iyer showed that in the case of an inviscid flow the nozzle design is barely influenced by variations in the total input conditions and thermophysical model closure coefficients. The variation in nozzle outlet half-height was on average 0.29 mm, which accounted for 1.1% of the nozzle outlet cross-sectional area. This variation has a negligible influence on the outlet Mach-number. Since the displacement thickness contour along the nozzle wall can be considered as the inviscid nozzle design as obtained from the MoC, it is possibly sufficient to consider the effects of total input conditions, thermophysical model closure coefficients and turbulence model closure coefficients on the boundary layer characteristics only.

However, the validity of the boundary layer program has not been verified yet for MM. Obtaining experimental data with the purpose of validation and calibration of NICFD software is part of the ORCHID test facility [17]. The current test set-up consists of optics to capture the Mach flow field by means of schlieren images, and pressure taps to obtain the pressure distribution along the nozzle expansion. However, what boundary layer characteristics should be measured for a thorough validation is yet uncertain. Therefore, a DoE study needs to be performed first to find out what parameters are required for validation. The current boundary layer program is designed for these kind of sensitivity studies. To determine what parameters need to be measured it is required to:

1. Determine the sensitivity of boundary layer characteristics to variations in total input conditions, thermophysical model closure coefficients, and turbulence model closure coefficients to find the most sensitive properties; and,
2. Set up a framework for Design of Experiment studies to evaluate the measurability of boundary layer characteristics.

The deterministic simulations presented in Chap. 5 showed a negligible boundary layer thickness compared to the nozzle cross-section for both laminar and turbulent flow. Also, the fluid property gradients inside the boundary layer were found to be negligible. Furthermore, the current models are not capable of predicting whether the flow is laminar or turbulent. In addition, the first experimental results obtained with the current ORCHID test set-up did not reveal any boundary layer developing on the curved nozzle wall surfce. Furthermore, the uncertainty in measured Mach-number and density were found to be larger than the expected density gradient inside the boundary layer, and the effect of the boundary layer on the Mach-number in the free stream respectively. The measured uncertainty in the measured Mach-number was found to be ± 0.1 Mach [11, Chap. 6]. This also means that the flow condition along the nozzle wall surface; namely, laminar or turbulent, remains yet unknown. These results lead to the conclusion that the boundary layer cannot be measured with the current test set-up. Therefore, an extension of the measurement equipment is needed to determine the flow condition, e.g. laminar or turbulent, and to measure the boundary layer characteristics.

Duff [53] applied interferometric density measurements to measure subtle density gradients inside a two-dimensional nozzle expanding CO2 in its dense gas range close to the saturation curve. The measurement equipment was found to be capable of capturing small density gradients. The accuracy of density measurements was *probably* not exceeding 0.2%. This resulted in boundary layer thickness measurements of within $\pm 15\%$ for thicknesses as small as 0.1 mm around the throat. This experiment showed that the measurement technique used is suitable for the ORCHID test set-up to capture the relatively small density variations close to the wall, but also in the high density-gradient nozzle throat.

Regarding determining the flow condition, laminar or turbulent, different techniques can be used. For example, by measuring the adiabatic wall temperature or skin friction. The flow condition can be determined from measuring the adiabatic wall temperature along the flow path, since recovery factors for laminar and turbulent flow differ. At the same time, additional temperature measurements inside the nozzle wall, at a distance from the wall surface, need to prove that the wall is near adiabatic. In addition, skin friction can be measured. Both adiabatic wall temperature and skin friction differ substantially in value between laminar and turbulent flow. However, Bader [31] studied laminar-turbulent and turbulent-laminar transition phenomena. He proved by experiments that the skin friction is not a suitable parameter for determining the flow condition. In short, highly accelerated flow conditions can suppress turbulence creation, which leads to a laminar boundary layer inside the turbulent boundary layer close to the wall including characteristic laminar skin friction values. Laminar skin friction values thus also lead to laminar adiabatic wall temperatures locally, which makes the measured adiabatic wall temperature in combination with the recovery factor approximations also unsuitable to determine the flow condition. Hence, the experiments of Bader [31], which used LDV and LIV to determine the velocity profiles, can be performed in the ORCHID nozzle to study the flow state. Especially, to study if and where laminar-turbulent transition, and possibly relaminarization occurs.

Concluding, both the experiments by Duff [53] and Bader [31] should be repeated to obtain reliable and detailed experimental data of density profiles and velocity profiles inside the boundary layer for an extensive validation of the boundary layer program. Notice from Chap. 2 that the boundary layer characteristics are predominantly functions of the velocity and density profiles. Therefore, detailed measurements of these profiles should result in a reliable and thorough validation. Sensitivity studies will prove and quantify the influence of the pressure history and models closure coefficients on the boundary layer characteristics.

Regarding the test cases obtained from literature used in this work it can be recommended to place a flat plate inside the nozzle for boundary layer measurements. The advantages of a flat plate are:

1. Start of boundary layer growth from zero at known location;
2. No influence of wall curvature; and,
3. Test region of interest is located in the middle of the glass window, avoiding influences from the wall, such as interference or (slight) heat transfer (NB an asymmetric flat plate can also cause heat transfer [97]).

Regarding the extension of CFD codes to capture boundary layer flow physics in more detail for prediction and verification, the following work is relevant. First, Cebeci [61] describes how the CS-method including the CS-model can be implemented in CFD codes implementing higher-order turbulence models. In addition, Basha [28] discusses the implementation of transition models in CFD software packages for improving the predicted drag. Furthermore, Abid [113] presents an improved CS-model for 3D boundary layer flows, and Cebeci [81] discusses a general method for arbitrary wings utilizing an adopted form of the CS-model.

6-3 Future Outlook

The nature of high molecular complex fluids involves an unfamiliar fluid property that has been neglected in this work: the second coefficient of viscosity λ. Several authors state that fluids characterized by methyl-groups, complex atomic structures and bonds, and high molecular mass result in nonnegligible values of this property compared to the familiar dynamic shear viscosity μ. Shear viscosity counteracts differences in velocity, whereas bulk viscosity counteracts dilatation. Not much is known yet about values of bulk viscosity for different types of fluids. At present, CO2 is known for having the largest bulk viscosity to date [114]. Nothing is known about siloxanes, although they are expected to possess a considerable value due to their methyl-groups. Currently, the interest in bulk viscosity has increased, proved by the recent amount of publications. Also, bulk viscosity is expected to play an important role in the design of ORC systems

in the near future [114]. On top of that, fluid flows characterized by high values of bulk viscosity cannot be neglected, since bulk viscosity influences turbulence [89]. A near future version of the boundary layer program should therefore also include bulk viscosity. It is possible to measure the bulk viscosity of MM with the ORCHID by measuring the thickness of steady state normal shocks [115].

Losses in turbomachinery are roughly categorized into [1]:

1. Profile loss;
2. Endwall loss; and,
3. Leakage loss.

Which all account for about one-third of the total losses [1]. The main physical phenomena behind these categories, which form sources of entropy generation, are [1]:

1. Viscous effects in boundary layers;
2. Viscous effects in mixing processes;
3. Shock waves; and,
4. Heat (and mass) transfer.

Bulk viscosity is known to have a detrimental effect on the losses induced by shocks. Therefore, high molecular complexity fluids are likely to induce a larger amount of losses due to shocks in conventional bladed turbine designs. Reducing the losses is the main aim to increase performance and cost efficiency. Regarding organics, large leaps in efficiency can be made by optimizing the design and reducing the losses induced by shocks and the boundary layer. Improved turbine designs can realize this. More importantly, different types of turbine designs may need to be considered.

The Tesla Turbine is such a promising design for a high efficiency ORC expander [116]. Invented by Nikola Tesla, this turbine design is bladeless. Therefore, the turbine rotor is free of shocks, mixing processes and tip or clearance leakages. Due to the discs moving with the flow, low Reynolds-numbers are achieved which is expected to lead to laminar flow conditions. Its working principle is based on boundary layer formation, and therefore it is also called the *boundary layer turbine*. Expected advantages of the Tesla Turbine are:

1. Entirely shock-free turbine rotor;
2. No tip or clearance leakage loss (which is a major loss factor at small scale);
3. Relatively small surface inducing boundary layer losses (only outer wall);

4. Turbine discs move with the flow (low losses);
5. Gradual expansion (low losses);
6. Laminar flow (lower losses);
7. Low velocity of organic fluids for comparable Mach-numbers;
8. Simple construction (cheap manufacturing); and,
9. Efficient part-load performance (parallel stages).

Summarizing, this turbine design is expected to reduce losses significantly. And, losses induced by shocks, leakage and mixing are removed entirely inside the rotor, which is reducing turbine losses significantly compared to conventional multistage bladed turbine designs. The current interest in this type of turbine has increased, shown by the amount of recent publications [116–120]. Speculating, a proper design of the turbine can take advantage of the characteristics of fluids of high molecular complexity, reducing the losses even further. The author expects that future small-scale ORC Power Plants will utilize Tesla Turbine expanders for high molecular complex working fluids.

Bibliography

[1] J. D. Denton, "Loss mechanisms in turbomachines," in *ASME 1993 International Gas Turbine and Aeroengine Congress and Exposition*, pp. V002T14A001–V002T14A001, American Society of Mechanical Engineers, 1993.

[2] D. R. Chapman and M. W. Rubesin, "Temperature and velocity profiles in the compressible laminar boundary layer with arbitrary distribution of surface temperature," *Journal of the Aeronautical Sciences*, vol. 16, no. 9, pp. 547–565, 1949.

[3] H. Schlichting and K. Gersten, *Boundary layer theory*. Springer, 8 ed., 2001.

[4] T. Cebeci and A. Smith, *Analysis of turbulent boundary layers*. Academic Press, 1974.

[5] United Nations treaty collection, "Paris agreement," February 2020.

[6] European Commission, "2020 climate & energy package," February 2020.

[7] The European Environment Agency (EEA), "The eu climate and energy (care) package," February 2020.

[8] European Commission, "A european green deal," February 2020.

[9] P. Colonna, E. Casati, C. Trapp, T. Mathijssen, J. Larjola, T. Turunen-Saaresti, and A. Uusitalo, "Organic rankine cycle power systems: from the concept to current technology, applications, and an outlook to the future," *Journal of Engineering for Gas Turbines and Power*, vol. 137, no. 10, 2015.

[10] A. Kluwick, "Non-ideal compressible fluid dynamics: A challenge for theory," in *Journal of Physics: Conference Series*, vol. 821, IOP Publishing, 2017. 1st International Seminar on Non-Ideal Compressible-Fluid Dynamics for Propulsion & Power.

[11] A. Head, *Novel experiments for the investigation of Non-Ideal Compressible Fluid Dynamics: The ORCHID and First Results of Optical Measurements*. PhD thesis, Faculty of Aerospace Engineering, Delft University of Technology (DUT), Delft, The Netherlands, 2021.

[12] C. Invernizzi, P. Iora, and P. Silva, "Bottoming micro-rankine cycles for micro-gas turbines," *Applied thermal engineering*, vol. 27, no. 1, pp. 100–110, 2007.

[13] J. Harinck, A. Guardone, and P. Colonna, "The influence of molecular complexity on expanding flows of ideal and dense gases," *Physics of fluids*, vol. 21, no. 8, p. 086101, 2009.

[14] B. E. Poling, J. M. Prausnitz, J. P. O'connell, *et al.*, *The properties of gases and liquids*, vol. 5. Mcgraw-hill New York, 2001.

[15] A. J. Head, C. De Servi, E. Casati, M. Pini, and P. Colonna, "Preliminary design of the ORCHID: A facility for studying non-ideal compressible fluid dynamics and testing orc expanders," in *ASME Turbo Expo 2016: Turbomachinery Technical Conference and Exposition*, American Society of Mechanical Engineers, 2016.

[16] A. Head, C. De Servi, E. Casati, and P. Colonna, "Design specifications and requirements of the ORCHID set-up," tech. rep., Faculty of Aerospace Engineering, Delft University of Technology (DUT), Delft, The Netherlands, 2015.

[17] A. Head, S. Iyer, C. de Servi, and M. Pini, "Towards the validation of a CFD solver for non-ideal compressible flows," in *IV International Seminar on ORC Power Systems, ORC2017*, vol. 129, pp. 240–247, Elsevier, 2017.

[18] A. Guardone, A. Spinelli, and V. Dossena, "Influence of molecular complexity on nozzle design for an organic vapor wind tunnel," *Journal of engineering for gas turbines and power*, vol. 135, no. 4, 2013.

[19] L. J. Goldman and M. R. Vanco, "Computer program for design of two-dimensional sharp-edged-throat supersonic nozzle with boundary layer correction," tech. rep., National Aeronautics and Space Administration (NASA), Washington DC, 1971.

[20] L. Prandtl, "Uber flüssigkeitsgewegung bei sehr kleiner reibung," *Proc. 3rd Intern. Math. Congr*, 1904.

[21] A. M. O. Smith and D. W. Clutter, "Solution of the incompressible laminar boundary layer equations," tech. rep., Douglas Aircraft Company Inc. El Segundo California, 1961.

[22] D. W. Clutter and A. Smith, "Solution of the general boundary-layer equations for compressible laminar flow, including transverse curvature," tech. rep., DTIC Document, 1963.

[23] H. B. Keller, "Numerical methods in boundary-layer theory," *Annual Review of Fluid Mechanics*, vol. 10, no. 1, pp. 417–433, 1978.

[24] T. Cebeci, *Analysis of Turbulent Flows with Computer Programs*. Elsevier, 2004.

[25] T. Cebeci, *Analysis of turbulent flows with computer programs*. Butterworth-Heinemann, 3 ed., 2013.

[26] D. C. Wilcox, *Turbulence modeling for CFD*. DCW industries La Canada, CA, 2 ed., 1994.

[27] T. Cebeci, *Convective heat transfer*. Springer, 2 ed., 2002.

[28] W. A. Basha and W. S. Ghaly, "Drag prediction in transitional flow over airfoils," *Journal of aircraft*, vol. 44, no. 3, pp. 824–832, 2007.

[29] P. Bader and W. Sanz, "On the setup of a test bench for predicting laminar-to-turbulent transition on a flat plate," 2015.

[30] P. Bader, W. Sanz, J. Peterleithner, J. Woisetschläger, F. Heitmeir, W. Meile, and G. Brenn, "Detecting transition in flat plate flow with laser interferometric vibrometry (liv)," in *Turbo Expo: Power for Land, Sea, and Air*, vol. 49699, p. V02AT37A003, American Society of Mechanical Engineers, 2016.

[31] P. Bader, M. Pschernig, W. Sanz, J. Woisetschläger, F. Heitmeir, W. Meile, and G. Brenn, "Experimental investigation of boundary layer relaminarization in accelerated flow," *Journal of Fluids Engineering*, vol. 140, no. 8, 2018.

[32] A. Wazzan, C. Gazley Jr., and A. Smith, "Hr/x/method for predicting transition," *AIAA Journal*, vol. 19, no. 6, pp. 810–812, 1981.

[33] T. Cebeci and J. Cousteix, *Modeling and Computation of Boundary-Layer Flows*. Springer, 2 ed., 2005.

[34] J. Nash-Webber and G. Oates, "An engineering approach to the design of laminarizing nozzle flows," *American Society of Mechanical Engineers (ASME)*, 1972.

[35] U. Setzmann and W. Wagner, "A new equation of state and tables of thermodynamic properties for methane covering the range from the melting line to 625 k at pressures up to 100 mpa," *Journal of Physical and Chemical reference data*, vol. 20, no. 6, pp. 1061–1155, 1991.

[36] R. Span and W. Wagner, "Equations of state for technical applications. i. simultaneously optimized functional forms for nonpolar and polar fluids," *International journal of thermophysics*, vol. 24, no. 1, pp. 1–39, 2003.

[37] R. Span and W. Wagner, "Equations of state for technical applications. ii. results for nonpolar fluids," *International Journal of Thermophysics*, vol. 24, no. 1, pp. 41–109, 2003.

[38] R. Span and W. Wagner, "Equations of state for technical applications. iii. results for polar fluids," *International Journal of Thermophysics*, vol. 24, no. 1, pp. 111–162, 2003.

[39] W. Wagner and A. Pruß, "The iapws formulation 1995 for the thermodynamic properties of ordinary water substance for general and scientific use," *Journal of physical and chemical reference data*, vol. 31, no. 2, pp. 387–535, 2002.

[40] R. Span and W. Wagner, "A new equation of state for carbon dioxide covering the fluid region from the triple-point temperature to 1100 k at pressures up to 800 mpa," *Journal of physical and chemical reference data*, vol. 25, no. 6, pp. 1509–1596, 1996.

[41] C. Tegeler, R. Span, and W. Wagner, "A new equation of state for argon covering the fluid region for temperatures from the melting line to 700 k at pressures up to 1000 mpa," *Journal of Physical and Chemical Reference Data*, vol. 28, no. 3, pp. 779–850, 1999.

[42] E. W. Lemmon and R. Span, "Short fundamental equations of state for 20 industrial fluids," *Journal of Chemical & Engineering Data*, vol. 51, no. 3, pp. 785–850, 2006.

[43] P. Colonna, N. Nannan, A. Guardone, and E. W. Lemmon, "Multiparameter equations of state for selected siloxanes," *Fluid Phase Equilibria*, vol. 244, no. 2, pp. 193–211, 2006.

[44] P. Colonna, N. Nannan, and A. Guardone, "Multiparameter equations of state for siloxanes:[(ch3) 3-si-o1/2] 2-[o-si-(ch3) 2] i= 1,. . . , 3, and [o-si-(ch3) 2] 6," *Fluid Phase Equilibria*, vol. 263, no. 2, pp. 115–130, 2008.

[45] M. Thol, F. H. Dubberke, G. Rutkai, T. Windmann, A. Köster, R. Span, and J. Vrabec, "Fundamental equation of state correlation for hexamethyldisiloxane based on experimental and molecular simulation data," *Fluid Phase Equilibria*, vol. 418, pp. 133–151, 2016.

[46] T. Van der Stelt, N. Nannan, and P. Colonna, "The iprsv equation of state," *Fluid Phase Equilibria*, vol. 330, pp. 24–35, 2012.

[47] P. Colonna and van der Stelt TP, *FluidProp: a program for the estimation of thermo physical properties of fluids*. Energy Technology Section, Delft University of Technology, The Netherlands, 2004.

[48] W. D. Mc Nally, "Fortran program for calculating compressible laminar and turbulent boundary layers in arbitrary pressure gradients," tech. rep., National Aeronautics and Space Administration (NASA), Washington DC, 1970.

[49] L. Goldman and M. Vanco, "Computer program for design of two dimensional supersonic nozzle with sharp edged throat," tech. rep., National Aeronautics and Space Administration (NASA), Washington DC, 1968.

[50] F. Pizzi, "Development and assessment of physical based profile loss model for orc turbine based on boundary layer analysis," Master's thesis, Politecnico di Milano, Italy, 2018.

[51] M. Pini and C. De Servi, "Entropy generation in laminar and turbulent adiabatic boundary layers of non-ideal fluid flows." Unpublished.

[52] D. Vimercati, A. Kluwick, and A. Guardone, "Shock interactions in two-dimensional steady flows of Bethe–Zel'dovich-Thompson fluids," *Journal of Fluid Mechanics*, vol. 887, 2020.

[53] K. M. Duff, *Non-equilibrium condensation of carbon dioxide in supersonic nozzles.* PhD thesis, Massachusetts Institute of Technology, 1966.

[54] F. M. White, *Viscous fluid flow*, vol. 3. McGraw-Hill New York, 2006.

[55] P. Kundu, I. Cohen, and D. Dowling, *Fluid mechanics.* Academic Press, 5 ed., 2012.

[56] M. Gad-el Hak, "Stokes' hypothesis for a newtonian, isotropic fluid," *Journal of Fluids Engineering*, vol. 117, no. 1, pp. 3–5, 1995.

[57] D. F. Rogers, *Laminar flow analysis.* Cambridge University Press, 1992.

[58] Y. Cho and A. Aessopos, "Similarity transformation methods in the analysis of the two dimensional steady compressible laminar boundary layer," *Term paper*, vol. 2, 2004.

[59] V. Falkner and S. W. Skan, "Solutions of the boundary-layer equations," *The London, Edinburgh, and Dublin Philosophical Magazine and Journal of Science*, vol. 12, no. 80, pp. 865–896, 1931.

[60] T. Cebeci, *An engineering approach to the calculation of aerodynamic flows.* Springer Science & Business Media, 1999.

[61] T. Cebeci, *Turbulence models and their application: efficient numerical methods with computer programs.* Springer Science & Business Media, 2004.

[62] C. B. Cohen and E. Reshotko, "Similar solutions for the compressible laminar boundary layer with heat transfer and pressure gradient," Tech. Rep. Report 1293, Flight Propulsion Research Lab Cleveland Ohio, 1956. Supersedes NACA TN3325, 'Similar solutions for the compressible laminar boundary layer with heat transfer and pressure gradient', by Clarence B. Cohen and Eli Reshotko, 1955 [121].

[63] F. T. Nieuwstadt, J. Westerweel, and B. J. Boersma, *Turbulence: introduction to theory and applications of turbulent flows*. Springer, 2016.

[64] T. Cebeci, "A model for eddy conductivity and turbulent prandtl number," *Journal of Heat Transfer*, vol. 95, no. 2, pp. 227–234, 1973.

[65] T. Na and I. Habib, "Heat transfer in turbulent pipe flow based on a new mixing length model," *Applied Scientific Research*, vol. 28, no. 1, pp. 302–314, 1973.

[66] K. Groot. personal communication, December 2016.

[67] T. Cebeci, G. Mosinskis, and A. Smith, "Calculation of viscous drag and turbulent boundary-layer separation on two-dimensional and axisymetric bodies in incompressible flows," tech. rep., DOUGLAS AIRCRAFT CO LONG BEACH CA, 1970.

[68] J. D. Anderson, *Modern compressible flow: with historical perspective*. McGraw-Hill New York, 3 ed., 1990.

[69] M. J. Zucrow and J. D. Hoffman, *Gas dynamics*, vol. 1. Wiley, 1976.

[70] NASA, "Kinetic theory of gases." Retrieved February 1, 2019, from https://www.grc.nasa.gov/www/k-12/airplane/kinth.html, February 2019.

[71] Y. A. Cengel and M. A. Boles, *Thermodynamics: an engineering approach*. McGraw-Hill, 5 ed., 2006.

[72] M. J. Moran, H. N. Shapiro, D. D. Boettner, and M. B. Bailey, *Fundamentals of engineering thermodynamics*. John Wiley & Sons, 2010.

[73] W. C. Reynolds and P. Colonna, *Thermodynamics*. Cambridge University Press, 2018.

[74] S. Chapman, T. G. Cowling, and D. Burnett, *The mathematical theory of non-uniform gases: an account of the kinetic theory of viscosity, thermal conduction and diffusion in gases*. Cambridge university press, 2 ed., 1953.

[75] P. Colonna, N. Nannan, A. Guardone, and T. Van der Stelt, "On the computation of the fundamental derivative of gas dynamics using equations of state," *Fluid phase equilibria*, vol. 286, no. 1, pp. 43–54, 2009.

[76] S. I. Sandler, *Chemical, biochemical, and engineering thermodynamics*. John Wiley & Sons, 4 ed., 2006.

[77] S. Iyer, "Influence of thermodynamic property perturbations on nozzle design and non-ideal compressible flow," Master's thesis, Delft University of Technology, The Netherlands, 2015.

[78] T. H. Chung, M. Ajlan, L. L. Lee, and K. E. Starling, "Generalized multiparameter correlation for nonpolar and polar fluid transport properties," *Industrial & engineering chemistry research*, vol. 27, no. 4, pp. 671–679, 1988.

[79] A. Smith, N. Jaffe, and R. Lind, "Study of a general method of solution to the incompressible turbulent boundary-layer equations," tech. rep., Douglas Aircraft Company Long Beach California Aircraft Division, 1965.

[80] A. Smith and T. Cebeci, "Numerical solution of the turbulent-boundary-layer equations," tech. rep., Douglas Aircraft Company Long Beach California Aircraft Division, 1967.

[81] T. Cebeci, K. Kaups, and J. A. Ramsey, "A general method for calculating three-dimensional compressible laminar and turbulent boundary layers on arbitrary wings," tech. rep., National Aeronautics and Space Administration (NASA), Washington DC, 1977.

[82] T. Cebeci and L. Carr, "A computer program for calculating laminar and turbulent boundary layers for two-dimensional time-dependent flows," tech. rep., 1978.

[83] D. Coles, "Computation of turbulent boundary layers," in *1968 AFOSR-IFP-Stanford Conference*, Stanford Univ. Press, 1969.

[84] H. B. Keller, "A new difference scheme for parabolic problems," in *Numerical Solution of Partial Differential Equations–II*, pp. 327–350, Elsevier, 1971.

[85] E. Isaacson and H. B. Keller, *Analysis of numerical methods*. Dover Publications Inc., 2 ed., 1996.

[86] F. H. Clauser, "The turbulent boundary layer," in *Advances in applied mechanics*, vol. 4, pp. 1–51, Elsevier, 1956.

[87] *Turbulent Flows of Supercritical Fluids with Heat Transfer*, 1 2020. Department colloquium Process & Energy TU-Delft.

[88] J. Y. Yoo, "The turbulent flows of supercritical fluids with heat transfer," *Annual review of fluid mechanics*, vol. 45, pp. 495–525, 2013.

[89] S. Pan and E. Johnsen, "The role of bulk viscosity on the decay of compressible, homogeneous, isotropic turbulence," *Journal of Fluid Mechanics*, vol. 833, pp. 717–744, 2017.

[90] E. V. Driest, "On turbulent flow near a wall," *Journal of the aeronautical sciences*, vol. 23, no. 11, pp. 1007–1011, 1956.

[91] P. Klebanoff, "Characteristics of turbulence in a boundary layer with zero pressure gradient," tech. rep., National Bureau of Standards Gaithersburg MD, 1955.

[92] S. Corrsin and A. L. Kistler, "Free-stream boundaries of turbulent flows," tech. rep., National Advisory Committee for Aeronautics (NACA), 1955.

[93] L. Eça and M. Hoekstra, "Verification and validation for marine applications of CFD," *International Shipbuilding Progress*, vol. 60, no. 1-4, pp. 107–141, 2013.

[94] AIAA, "Guide for the verification and validation of computational fluid dynamics simulations," Tech. Rep. G-077-1998, American Institute of Aeronautics and Astronautics (AIAA), 1998.

[95] H. Blasius, "Grenzschichten in flüssigkeiten mit kleiner reibung," *Zeitschrift für angewandte Mathematik und Physik*, vol. 56, pp. 1–37, 1908.

[96] L. Howarth, "On the solution of the laminar boundary layer equations," *Proceedings of the Royal Society of London. Series A, Mathematical and Physical Sciences*, pp. 547–579, 1938.

[97] R. H. Giepman, F. F. Schrijer, and B. W. van Oudheusden, "Infrared thermography measurements on a moving boundary-layer transition front in supersonic flow," *AIAA Journal*, vol. 53, no. 7, pp. 2056–2061, 2015.

[98] K. Groot, *Biglobal stability of shear flows*. PhD thesis, Faculty of Aerospace Engineering, Delft University of Technology (DUT), Delft, The Netherlands, 2018.

[99] C. De Servi, "A MATLAB program for solving the laminar boundary layer equations." Unpublished.

[100] K. G. Winter and L. Gaudet, "Turbulent boundary-layer studies at high reynolds numbers at mach numbers between 0.2 and 2.8," tech. rep., Ministry of Aviation Supply, Royal Aircraft Establishment, RAE, 1970.

[101] H.-H. Fernholz and P. Finley, "A critical compilation of compressible turbulent boundary layer data," tech. rep., Avisory Group for Aerospace Research and Development (AGARD) Neuilly-sur-Seine (France), 1977.

[102] H.-H. Fernholz, P. Finley, and V. Mikulla, "A further compilation of compressible boundary layer data with a survey of turbulence data," tech. rep., Avisory Group for Aerospace Research and Development (AGARD) Neuilly-sur-Seine (France), 1981.

[103] B. Grossman, "Fundamental concepts of real gas dynamics." Lecture notes, Department of Aerospace and Ocean Engineering, Virginia Polytechnic Institute and State University, January 2000.

[104] J. D. Anderson Jr, *Fundamentals of aerodynamics*. McGraw-Hill Higher Education, 3 ed., 2001.

[105] L. Bills, "Validation of the SU2 solver for classical non-ideal compressible fluid dynamics," Master's thesis, Faculty of Aerospace Engineering, Delft University of Technology (DUT), Delft, The Netherlands, 2020.

[106] J. B. Barlow, W. H. Rae, and A. Pope, *Low-speed wind tunnel testing*. John Wiley & Sons, 1999.

[107] E. W. Lemmon, , I. H. Bell, M. L. Huber, and M. O. McLinden, "NIST Standard Reference Database 23: Reference Fluid Thermodynamic and Transport Properties-REFPROP, Version 10.0, National Institute of Standards and Technology," 2018.

[108] M. J. Zucrow and J. D. Hoffman, *Gas dynamics*, vol. 2. Wiley, 1977.

[109] STF Solutions, "Solving for your own sutherland coefficients using python," March 2020.

[110] S. Kline, "The 1980-81 afosr-httm-stanford conference on complex turbulent flows: Comparison of computation & experiment.," tech. rep., Stanford University, California, Department of Mechanical Engineering, 1982.

[111] E. Rinaldi, R. Pecnik, and P. Colonna, "Accurate and efficient look-up table approach for dense gas flow simulations," in *6th European Congress on Computational Methods in Applied Sciences and Engineering (ECCOMAS 2012)*, no. 12630386, pp. 8690–8704, 2012.

[112] M. Pini, A. Spinelli, G. Persico, and S. Rebay, "Consistent look-up table interpolation method for real-gas flow simulations," *Computers & Fluids*, vol. 107, pp. 178–188, 2015.

[113] R. Abid, "An eddy viscosity for three-dimensional boundary-layer flows," in *1st National Fluid Dynamics Conference*, p. 3748, 1988.

[114] M. S. Cramer, "Numerical estimates for the bulk viscosity of ideal gases," *Physics of fluids*, vol. 24, no. 6, p. 066102, 2012.

[115] G. Emanuel and B. M. Argrow, "Linear dependence of the bulk viscosity on shock wave thickness," *Physics of Fluids*, vol. 6, no. 9, pp. 3203–3205, 1994.

[116] L. Talluri, O. Dumont, G. Manfrida, V. Lemort, and D. Fiaschi, "Experimental investigation of an organic rankine cycle tesla turbine working with r1233zd (e)," *Applied Thermal Engineering*, p. 115293, 2020.

[117] F. Ji, Y. Bao, Y. Zhou, F. Du, H. Zhu, S. Zhao, G. Li, X. Zhu, and S. Ding, "Investigation on performance and implementation of tesla turbine in engine waste heat recovery," *Energy Conversion and Management*, vol. 179, pp. 326–338, 2019.

[118] K. Rusin, W. Wróblewski, and M. Strozik, "Experimental and numerical investigations of tesla turbine," in *J. Phys.: Conf. Series*, vol. 1101, p. 012029, 2018.

[119] G. Manfrida, L. Pacini, and L. Talluri, "An upgraded tesla turbine concept for ORC applications," *Energy*, vol. 158, pp. 33–40, 2018.

[120] G. Manfrida, L. Pacini, and L. Talluri, "A revised tesla turbine concept for ORC applications," *Energy Procedia*, vol. 129, pp. 1055–1062, 2017.

[121] C. B. Cohen and E. Reshotko, "Similar solutions for the compressible laminar boundary layer with heat transfer and pressure gradient," Tech. Rep. TN3325, Flight Propulsion Research Lab Cleveland Ohio, 1955. Superseded by Report 1293 [62].

[122] D. J. Collins, D. E. Coles, and J. W. Hicks, "Measurements in the turbulent boundary layer at constant pressure in subsonic and supersonic flow. part 1. mean flow," tech. rep., California Institute of Technology Pasadena Jet Propulsion Lab, 1978.

[123] P. E. Dimotakis, D. J. Collins, and D. B. Lang, "Measurements in the turbulent boundary layer at constant pressure in subsonic and supersonic flow. part 2. laser-doppler velocity measurements," tech. rep., California Institute of Technology Pasadena Jet Propulsion Lab, 1979.

[124] P. Bradshaw, "Effects of streamline curvature on turbulent flow.," tech. rep., Avisory Group for Aerospace Research and Development (AGARD) Neuilly-sur-Seine (France), 1973.

[125] K. Stewartson, *The theory of laminar boundary layers in compressible fluids*. Clarendon Press Oxford, 1964.

Appendix A

Description of the Computer Program

Include full code, description of derivation/composition, use etc.

This appendix aims to be a complete code documentation.

NB (2023-03-06) not all sections in this Appendix have been completed.

A-1 Description of Program

A-2 Differences Between the Current MATLAB Program and the Original FORTRAN Program

This appendix lists the changes made to the original FORTRAN code obtained from reference [27].

1. Choice of working fluid is made possible;
2. Choice of gas model for simulating working fluid is made possible. Choice out of three different gas models (previously only calorically perfect ideal gas):
   (a) Ideal gas, calorically perfect;
   (b) Ideal gas, calorically imperfect (thermally perfect); and,
   (c) Nonideal gas (variable fluid properties as function of two state variables through FluidProp [47]).

3. Variable fluid properties were added through adding the FluidProp library [47];
4. Transition calculation moved to a separate file (thereby introducing a small deviation in the first calculated turbulent velocity profile after transition, since more laminar iterations (previously transition occured and velocity profile was calculated with previous laminar profile, now laminar profile is calculated until convergence and then transition occurs, thus turbulent profile is calculated with converged laminar profile));
5. Two transition methods added (Wazzan[source] and Michel[source]);
6. Relaminarisation method added;
7. Turbulent Prandtl model added (from reference [4] according to [65]);
8. A plot-file was added for visualizing the results immediately;
9.

Changes to program structure:

1. Added another call to FLDPRS to update fluid properties after last iteration. I found one example (don't remember which one) which indicated the need for this.
2. order of separation check, other checks.
3. implementation of Eddy Conductivity model (instead of constant PrT model).
4. implementation of general fluid property models and choice of input options.

A-3 Derivation of Equations and System of equations solved

A-4 Verification

Include here:

1. Blasius profile table (high grid resolution KBM compared with table from Rogers);
2. Falkner-Skan cases: adiabatic flow (only ME solved), nonzero PG;
3. Comparison of above results with other authors;
4. Table from Rogers (C-?) comparing with Pr1;
5. Table from Rogers (C-?) comparing with Pr0723: Mach0 and Mach inf (last is not exactly infinte);

6. high resolution grid with different spacings (VGP equal and unequal to one), compare with Rogers' accurate Blasius solution;
7. compare form factor H with different grid resolutions and compare speed;
8. compare accuracy and speed (at least table from word-doc comparing Spectral, bvp4c and KBM);
9. compare spectral and KBM for varying Reynolds-number and see if solution converges with higher Re as expected;
10. Verification and validation of heat transfer (Stanton-number) with spectral code (verification) and Rogier's data (qualitative validation), note that these are steady state simulations for transient proces. The tip of the plate is thin and does not contain much mass, therefore the amount of heat transferred from the tip and the region close to the tip is negligible or small, and thus the measured St gives zero heat flux, while the simulation gives a heat flux (since temperature is not stable but changing in time and thus not representative).
11. plot δ^* correlation based on Reynolds-number Re or Re_θ? for verifying BL integral parameters. Analytic solution available for laminar flow!

A-4-1 Results

For zpg adiabatic flow with conv criterion $1e-5$ we find 7 acurate digits compared with Rogers. The same applies for favourable pressure gradients for FS wedge flows. The integral values don't seem affected, and thus the entire solution must be this accurate (abs diff Blasius below). For adverse pressure gradients the accuracy decreases only slowly to suddenly about 1 digit at the separation pg, which is the most difficult to predict accurately. Including heat transfer and nonunit Pr -numbers in Tab. X and Y and Z it is already more difficult to reach the same accuracy, especially for adverse pressure gradients. The program is not able to find solutions for the highest pressure gradients (sep) in tables l and k. The EE gives satisfying results too in tables (C-28 adiabatic!). The deviations are thought to be caused by the iterative error, which is shown to be small, and only becomes larger for highly adverse pressure gradients, which the program will not be used for.

Blasius table solution gives all data to make following graphs. absolute errors and relative errors. fpp is said to be most sensitive parameter.

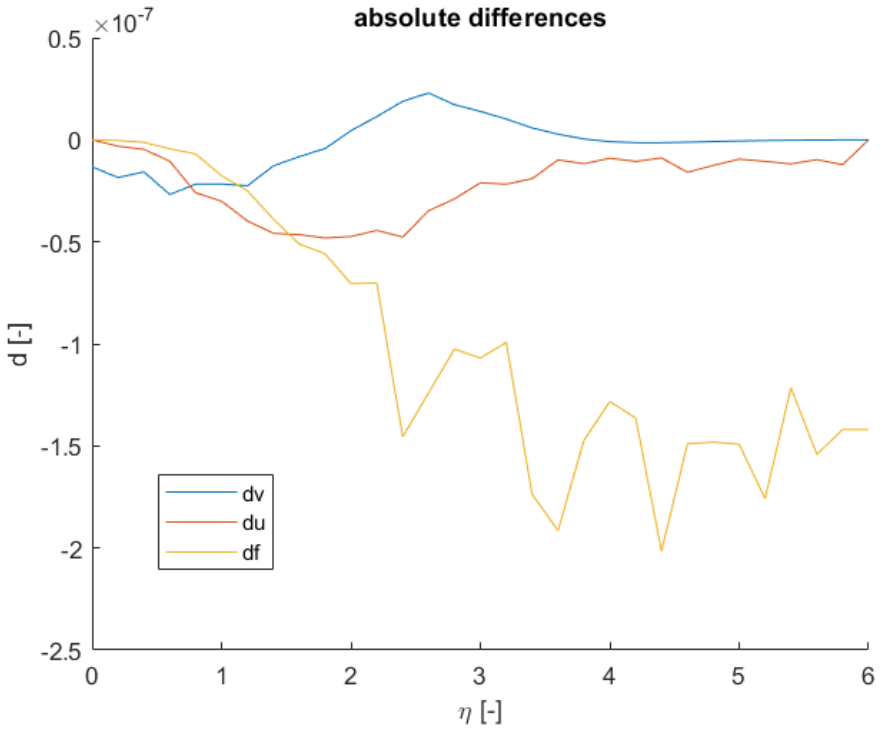

Figure A-1: Absolute differences of Blasius solution plotted as function of η-coordinate. Convergence criterion used was $\delta v < 1e-5$, which resulted in X iterations.

A-5 Verification Cases for Solver

Separation is indicated in the tables with 'sep'. In some cases separation is also predicted for (highly) favourable pressure gradients. In such cases, when the pressure gradient is favourable, 'sep' means that the solver is not able to find a solution, and not that flow separation has occured.

A-5-1 Verification with Blasius' Solution for Zero Pressure Gradient

Take Cebeci (1974) as example.

A-5-2 Verification with Falkner-Skan Wedge Flows for Nonzero Pressure Gradient

Verification with Falkner-Skan similar flows in table A-2 with variable pressure gradient (constant density, constant fluid properties, adiabatic flow, verifying implementation of pressure gradient in momentum equation).

1. 6 or 7 accurate digits. results get less accurate towards separation, and they are most accurate around pressure gradient close to zero. at lowest beta Rogers predicts separation while CSM does not.
2. 2 accurate digits for PG infinity, not possible, therefore approached by one thousand;
3. (remember that bvp4c method adapts the grid to obtain a more accurate solution to the PDE's; and CSM adapts the grid according to PG through the transformation).
4. for C26 it seems (very subtle) that PG equal to one is more accurate
5. for C27 always sep for first three PGs; why? try turn of sep check and see what happens.
6. case C28 sep for first PG; EE less accurate? Why?;

A-5-3 Verification with Compressible Flows for Nonzero Pressure Gradient and Heat Transfer

Compressible flow cases from Rogers.

- similar trend as before with FS-flows: higher accuracy, more accurate digits, for pressure gradietn towards zero.
- separation is predicted earlier for heat transfer from the flow (to the plate), and later for heat transfer from the plate (to the flow); compare with FS case (sep not yet predicted);
- also here we have the substitution with PG one thousand;
- grid is adapted here to for every calculation, see caption;
- check FS-flow points again.
- grid is calculated with values from Rogers; assumed (see his Appendix of the code) that Rogers uses these values too;
- Table C-25: To simulate beta (arrow) infinity a value of one thousand was used fro mtwo, which is considered to be sufficiently large.
- add bold face to text in all latex table
- Table C-28 less accurate towards separation; what about close to zero PG?

Table A-1: Comparison with tabulated data of the Blasius' solution taken from Rogers [57] table 3-1. With uniform (vertical) grid spacing (in compressible Falkner-Skan transformed y-coordinate) of $\mathrm{d}\eta = \sqrt{\frac{2C}{m_2+1}}0.001$ and heigth of $\eta_\mathrm{e} = \sqrt{\frac{2C}{m_2+1}}6.0$.

η	f''		f'		f	
	Rogers	**CSM**	**Rogers**	**CSM**	**Rogers**	**CSM**
0.0	0.469 600 5	0.469 600 49	0	0.000 000 00	0	0.000 000 00
0.2	0.469 306 57	0.469 306 55	9.390 540 1e−2	0.093 905 40	9.391 422e−3	0.009 391 42
0.4	0.467 254 7	0.467 254 68	0.187 605 34	0.187 605 34	0.037 549 24	0.037 549 24
0.6	0.461 734 93	0.461 734 90	0.280 575 76	0.280 575 75	8.438 566 3e−2	0.084 385 66
0.8	0.451 190 49	0.451 190 47	0.371 963 65	0.371 963 62	0.149 674 68	0.149 674 67
1.0	0.434 379 58	0.434 379 56	0.460 633 07	0.460 633 04	0.232 990 35	0.232 990 33
1.2	0.410 565 75	0.410 565 73	0.545 247 09	0.545 247 05	0.333 657 74	0.333 657 72
1.4	0.379 692 52	0.379 692 51	0.624 386 97	0.624 386 92	0.450 724 1	0.450 724 06
1.6	0.342 487 37	0.342 487 36	0.696 700 22	0.696 700 17	0.582 956 92	0.582 956 87
1.8	0.300 445 5	0.300 445 50	0.761 058 08	0.761 058 03	0.728 873	0.728 872 94
2.0	0.255 669 29	0.255 669 29	0.816 695 4	0.816 695 35	0.886 797 74	0.886 797 67
2.2	0.210 579 98	0.210 579 99	0.863 305 01	0.863 304 97	1.054 948 2	1.054 948 13
2.4	0.167 560 36	0.167 560 38	0.901 066 25	0.901 066 20	1.231 528 9	1.231 528 75
2.6	0.128 612 83	0.128 612 85	0.930 602 06	0.930 602 03	1.414 825 6	1.414 825 48
2.8	9.511 338 6e−2	0.095 113 40	0.952 876 24	0.952 876 21	1.603 285 1	1.603 285 00
3.0	6.771 028 6e−2	0.067 710 30	0.969 055 38	0.969 055 36	1.795 569 6	1.795 569 49
3.2	4.637 036 1e−2	0.046 370 37	0.980 365 75	0.980 365 73	1.990 582 8	1.990 582 70
3.4	3.053 521 4e−2	0.030 535 22	0.987 971 22	0.987 971 20	2.187 469 3	2.187 469 13
3.6	1.932 869 4e−2	0.019 328 70	0.992 888 65	0.992 888 64	2.385 592 6	2.385 592 41
3.8	1.175 867 8e−2	0.011 758 68	0.995 945 02	0.995 945 01	2.584 501 1	2.584 500 95
4.0	6.874 085 3e−3	0.006 874 08	0.997 770 83	0.997 770 82	2.783 888 9	2.783 888 77
4.2	3.861 352e−3	0.003 861 35	0.998 819 04	0.998 819 03	2.983 557 9	2.983 557 76
4.4	2.084 074 7e−3	0.002 084 07	0.999 397 34	0.999 397 33	3.183 385 5	3.183 385 30
4.6	1.080 752 5e−3	0.001 080 75	0.999 703 94	0.999 703 92	3.383 298 9	3.383 298 75
4.8	5.384 839 9e−4	0.000 538 48	0.999 860 13	0.999 860 12	3.583 257 1	3.583 256 95
5.0	2.577 805 2e−4	0.000 257 78	0.999 936 59	0.999 936 58	3.783 237 7	3.783 237 55
5.2	1.185 650 8e−4	0.000 118 56	0.999 972 56	0.999 972 55	3.983 229 1	3.983 228 92
5.4	5.239 528 5e−5	0.000 052 40	0.999 988 82	0.999 988 81	4.183 225 4	4.183 225 28
5.6	2.224 621 1e−5	0.000 022 25	0.999 995 88	0.999 995 87	4.383 224	4.383 223 85
5.8	9.075 032 9e−6	0.000 009 07	0.999 998 83	0.999 998 82	4.583 223 5	4.583 223 36
6.0	3.556 875e−6	0.000 003 56	1.0	1.000 000 00	4.783 223 4	4.783 223 26

Table A-2: Comparison with tabulated data of the Falkner-Skan wedge flows (adiabatic incompressible similar flows with nonzero constant pressure gradients for calorically perfect ideal gas with constant fluid properties) taken from Rogers [57] table C-1. The values obtained with the CS-method (CSM) are transformed from the compressible Falkner-Skan transformed y-coordinate with uniform (vertical) grid spacing of $\mathrm{d}\eta = \sqrt{\frac{2C}{m_2+1}}0.0010$ and height of $\eta_\mathrm{e} = \sqrt{\frac{2C}{m_2+1}}6.0$ to the Illingworth-Levy coordinates ($\mathrm{d}\eta = 0.0010$ and $\eta_\mathrm{e} = 6.0$). Note that separation occurred when the table entry shows 'sep'.

β	m_2	$f''(0)$		**Rogers**	**CSM**	**Rogers**	**CSM**
		Rogers	**CSM**	I_1	$2J_\mathrm{x}$	I_2	$2J_2$
2.00	1000 *	1.687 218	1.686 430	0.497 433 1	0.497 137 5	0.230 783 1	0.230 870 3
1.60	4.000 000	1.521 514	1.521 514	0.544 021 4	0.543 521 9	0.250 414 7	0.250 414 9
1.20	1.500 000	1.335 721	1.335 721	0.606 897 7	0.606 398 2	0.276 110 4	0.276 110 7
1.00	1.000 000	1.232 588	1.232 588	0.647 900 2	0.647 400 6	0.292 343 4	0.292 343 5
0.80	0.666 667	1.120 268	1.120 268	0.698 680	0.698 180 3	0.311 846 1	0.311 846 3
0.60	0.428 571	0.995 836 5	0.995 836	0.763 971 1	0.763 471 9	0.335 907 6	0.335 908 2
0.50	0.333 333	0.927 680 1	0.927 680	0.804 584	0.804 048 7	0.350 269 3	0.350 270 4
0.40	0.250 000	0.854 421 3	0.854 421	0.852 633 4	0.852 134 2	0.366 690 3	0.366 690 9
0.30	0.176 471	0.774 754 6	0.774 755	0.910 992 9	0.910 493 7	0.385 734 9	0.385 735 5
0.20	0.111 111	0.686 708 3	0.686 708	0.984 157 6	0.983 658 2	0.408 229 6	0.408 230 0
0.10	0.052 632	0.587 035 4	0.587 035	1.080 319	1.079 819 1	0.435 456 2	0.435 456 4
0.05	0.025 641	0.531 129 9	0.531 130	1.141 735	1.141 235 5	0.451 467 5	0.451 467 6
0	0.000 000	0.469 600 5	0.469 600	1.216 778	1.216 276 7	0.469 598	0.469 596 9
−0.05	−0.024 390	0.400 323 3	0.400 324	1.312 358	1.311 854 7	0.490 460 1	0.490 457 9
−0.10	−0.047 619	0.319 269 8	0.319 273	1.442 697	1.442 174 6	0.515 043 9	0.515 029 8
−0.14	−0.065 421	0.239 736	0.239 747	1.599 02	1.595 338 1	0.538 560 7	0.538 527 0
−0.16	−0.074 074	0.190 779 9	0.190 804	1.706 649	1.706 016 6	0.552 194 7	0.552 134 6
−0.18	−0.082 569	0.128 636 2	0.128 709	1.871 575	1.870 690 1	0.567 707	0.567 574 4
−0.19	−0.086 758	0.085 700 37	0.085 884	2.006 757	2.005 304 1	0.576 522 5	0.576 283 7
−0.198 837 6	−0.090 429	0	0.009 411	2.358 848	2.310 984 2	0.585 435 2	0.584 633 5

* The solution does not converge for $m_2 = \infty$, and therefore $m_2 = 1000$ is taken as approach.

Table A-3: Comparison with tabulated data of laminar compressible similar flows with constant nonzero pressure gradients and heat transfer for calorically perfect ideal gas with $C = 1$ (constant) and $\mathrm{Pr} = 1$ taken from Rogers [57] table C-25. The values obtained with the CS-method (CSM) are transformed from the compressible Falkner-Skan transformed y-coordinate with uniform (vertical) grid spacing of $\mathrm{d}\eta = \sqrt{\frac{2C}{m_2+1}}0.0001$ and height of $\eta_\mathrm{e} = \sqrt{\frac{2C}{m_2+1}}8.0$ to the Illingworth-Levy coordinates ($\mathrm{d}\eta = 0.0001$ and $\eta_\mathrm{e} = 8.0$). Note that separation occurred when the table entry shows 'sep'.

g_w	$\hat{\beta}$	m_2	$f''(0)$		$g'(0)$		**Rogers**	**CSM**	**Rogers**	**CSM**	**Rogers**	**CSM**
			Rogers	**CSM**	**Rogers**	**CSM**	J_1	$2J_1$	J_2	$2J_2$	J_3	$2J_4$
0	2.00	1000 *	0.738 646	0.738 495	0.520 637	0.520 610	0.177 507	0.177 575	0.383 660	0.383 699	1.288 10	1.287 141
	1.50	3.000 000	0.698 714	0.698 708	0.514 758	0.514 749	0.204 855	0.204 845	0.391 414	0.391 438	1.326 33	1.326 315
	1.00	1.000 000	0.648 858	0.648 858	0.506 661	0.506 661	0.245 559	0.245 559	0.403 297	0.403 298	1.382 65	1.382 598
	0.50	0.333 333	0.581 143	0.581 143	0.494 220	0.494 220	0.314 630	0.314 631	0.423 825	0.423 826	1.476 91	1.476 875
	0.10	0.052 632	0.498 666	0.498 667	0.476 549	0.476 550	0.423 879	0.423 877	0.456 276	0.456 272	1.624 64	1.624 600
	0	0.000 000	0.469 600	0.469 603	0.469 600	0.469 603	0.469 598	0.469 585	0.469 597	0.469 585	1.686 38	1.686 311
	−0.10	−0.047 619	0.433 977	0.434 006	0.460 534	0.460 542	0.530 955	0.530 899	0.487 091	0.487 048	1.769 39	1.769 251
	−0.20	−0.090 909	0.387 508	0.387 552	0.447 715	0.447 740	0.620 116	0.619 860	0.511 527	0.511 378	1.890 70	1.890 267
	−0.30	−0.130 435	0.318 261	sep	0.426 305	sep	0.772 474	sep	0.550 002	sep	2.100 94	sep
	−0.326 419	−0.140 310	0	sep	0.247 790	sep	1.957 50	sep	0.638 924	sep	4.095 47	sep
0.20	2.00	1000 *	0.948 323	0.948 028	0.433 374	0.433 350	0.296 497	0.296 396	0.355 346	0.355 381	1.155 64	1.154 697
	1.50	3.000 000	0.869 491	0.869 488	0.426 683	0.426 678	0.335 632	0.335 605	0.366 047	0.366 057	1.206 14	1.206 095
	1.00	1.000 000	0.775 537	0.775 537	0.417 547	0.417 547	0.393 393	0.393 384	0.382 142	0.382 142	1.280 23	1.280 182
	0.50	0.333 333	0.654 961	0.654 961	0.403 591	0.403 591	0.490 937	0.490 927	0.409 493	0.409 492	1.404 42	1.404 373
	0.10	0.052 632	0.516 777	0.516 778	0.383 665	0.383 666	0.646 479	0.646 466	0.452 129	0.452 125	1.601 81	1.601 760
	0	0.000 000	0.469 600	0.469 603	0.375 680	0.375 682	0.712 953	0.712 930	0.469 597	0.469 585	1.686 37	1.686 311
	−0.10	−0.047 619	0.412 212	0.412 224	0.365 003	0.365 010	0.804 518	0.804 421	0.492 664	0.492 611	1.803 39	1.803 223
	−0.20	−0.090 909	0.336 409	0.336 484	0.349 022	0.349 055	0.945 504	0.945 008	0.525 510	0.525 276	1.985 31	1.984 626
	−0.30	−0.130 435	0.209 010	sep	0.315 893	sep	1.244 16	sep	0.582 260	sep	2.381 10	sep
	−0.308 622	−0.133 682	0	sep	0.226 014	sep	2.034 46	sep	0.627 824	sep	3.555 11	sep
0.6	2.00	1000 *	1.333 35	1.332 796	0.230 628	0.230 610	0.519 429	0.518 974	0.294 479	0.294 544	0.926 629	0.925 760
	1.50	3.000 000	1.185 36	1.185 355	0.225 837	0.225 835	0.582 101	0.582 065	0.312 187	0.312 195	0.996 556	0.996 501
	1.00	1.000 000	1.012 19	1.012 192	0.219 273	0.219 273	0.674 252	0.674 222	0.337 939	0.337 940	1.099 27	1.099 217
	0.50	0.333 333	0.795 193	0.795 193	0.209 134	0.209 134	0.830 082	0.830 058	0.380 151	0.380 152	1.272 88	1.272 839
	0.10	0.052 632	0.552 320	0.552 320	0.194 163	0.194 163	1.085 13	1.085 103	0.443 806	0.443 803	1.557 79	1.557 750
	0	0.000 000	0.469 600	0.469 603	0.187 840	0.187 841	1.199 66	1.199 621	0.469 597	0.469 585	1.686 37	1.686 311
	−0.10	−0.047 619	0.367 041	0.367 060	0.178 822	0.178 827	1.367 98	1.367 805	0.503 838	0.503 765	1.876 37	1.876 154
	−0.20	−0.090 909	0.218 417	0.218 692	0.162 575	0.162 629	1.681 07	1.679 246	0.554 631	0.554 014	2.234 09	2.232 005
	−0.247 561	−0.110 147	0	sep	0.125 095	sep	2.428 47	sep	0.601 196	sep	3.121 46	sep
1.0	Solution to the Falkner-Skan equations, see Table **??**											
2.0	2.00	1000 *	2.487 68	2.486 378	−0.661 455	−0.661 388	1.210 19	1.208 447	0.067 273 6	0.067 429	0.307 899	0.307 182
	1.50	3.000 000	2.140 34	2.140 343	−0.642 295	−0.642 295	1.351 75	1.351 612	0.112 716	0.112 714	0.426 665	0.426 590
	1.00	1.000 000	1.736 68	1.736 684	−0.615 585	−0.615 585	1.560 58	1.560 481	0.176 103	0.176 103	0.601 104	0.601 054
	0.50	0.333 333	1.234 81	1.234 806	−0.572 886	−0.572 886	1.920 36	1.920 282	0.274 623	0.274 624	0.898 878	0.898 838
	0.10	0.052 632	0.670 713	0.670 713	−0.503 755	−0.503 756	2.561 93	2.561 858	0.414 519	0.414 518	1.418 04	1.418 002
	0	0.000 000	0.469 600	0.469 603	−0.469 600	−0.469 603	2.903 15	2.903 037	0.469 597	0.469 585	1.686 38	1.686 311
	−0.10	−0.047 619	0.181 379	0.181 483	−0.403 222	−0.403 295	3.614 29	3.613 052	0.542 734	0.542 493	2.224 78	2.223 996
	−0.129 507	−0.060 815	0	0.003 995	−0.338 911	−0.340 967	3.614 29 ◇	4.352 296	0.542 734◇	0.565 474	2.772 61	2.751 062

* The solution does not converge for $m_2 = \infty$, and therefore $m_2 = 1000$ is taken as approach.
◇ Same value as in row above! Probably a wrong value is printed here considering the CSM result.

Table A-4: Comparison with tabulated data of laminar compressible similar flows with constant nonzero pressure gradients and heat transfer for calorically perfect ideal gas with $C = 1$ (constant) and $\mathrm{Pr} = 0.723$ and $\bar{\sigma} = 0.0 \quad (\mathrm{Ma} = 0)$ taken from Rogers [57] table C-26. The values obtained with the CS-method (CSM) are transformed from the compressible Falkner-Skan transformed y-coordinate with uniform (vertical) grid spacing of $\mathrm{d}\eta = \sqrt{\frac{2C}{m_2+1}}0.0001$ and height of $\eta_\mathrm{e} = \sqrt{\frac{2C}{m_2+1}}8.0$ to the Illingworth-Levy coordinates ($\mathrm{d}\eta = 0.0001$ and $\eta_\mathrm{e} = 8.0$). Note that separation occurred when the table entry shows 'sep'.

g_w	$\hat{\beta}$	m_2	$f''(0)$		$g'(0)$		**Rogers**	**CSM**	**Rogers**	**CSM**	**Rogers**	**CSM**
			Rogers	**CSM**	**Rogers**	**CSM**	J_1	$2J_1$	J_2	$2J_2$	J_3	$2J_4$
0	1.0	1.000 000	0.610 911	0.610 912	0.442 248	0.442 248	0.176 773	0.121 986	0.434 135	0.299 582	1.482 55	1.023 025
	0.5	0.333 333	0.555 599	0.555 600	0.433 994	0.433 995	0.221 500	0.187 205	0.444 849	0.375 964	1.548 31	1.308 518
	0.1	0.052 632	0.491 300	0.491 306	0.422 874	0.422 893	0.289 930	0.275 925	0.462 306	0.439 723	1.646 79	1.566 326
	0	0.000 000	0.469 600	0.469 603	0.418 711	0.418 744	0.317 768	0.310 420	0.469 600	0.458 268	1.686 38	1.645 671
	−0.1	−0.047 619	0.443 805	0.443 787	0.413 474	0.413 526	0.354 308	0.354 954	0.479 236	0.479 250	1.738 11	1.738 132
0.2	1.0	1.000 000	0.746 736	0.746 736	0.365 466	0.365 466	0.339 480	0.234 258	0.407 252	0.281 031	1.355 75	0.935 519
	0.5	0.333 333	0.635 300	0.635 301	0.355 072	0.355 072	0.417 659	0.352 982	0.426 468	0.360 431	1.458 94	1.232 994
	0.1	0.052 632	0.510 965	0.510 970	0.340 609	0.340 623	0.540 066	0.513 807	0.456 958	0.434 640	1.619 20	1.540 098
	0	0.000 000	0.469 600	0.469 603	0.334 969	0.334 995	0.591 493	0.577 470	0.469 600	0.458 268	1.686 38	1.645 671
	−0.1	−0.047 619	0.420 249	0.420 236	0.327 601	0.327 647	0.661 195	0.661 724	0.486 368	0.486 368	1.777 54	1.777 522
0.6	1.0	1.000 000	0.998 901	0.998 901	0.192 617	0.192 617	0.648 147	0.447 243	0.350 753	0.242 043	1.133 85	0.782 399
	0.5	0.333 333	0.785 196 3	0.785 964	0.184 493	0.184 493	0.794 456	0.671 408	0.388 746	0.328 546	1.298 16	1.097 097
	0.1	0.052 632	0.549 487	0.549 489	0.172 516	0.172 522	1.032 62	0.982 237	0.446 225	0.424 437	1.566 20	1.489 705
	0	0.000 000	0.469 600	0.469 603	0.167 485	0.167 498	1.138 94	1.111 571	0.469 600	0.458 268	1.686 38	1.645 671
	−0.1	−0.047 619	0.371 286	0.371 288	0.160 369	0.160 398	1.293 99	1.294 190	0.500 684	0.500 642	1.862 47	1.862 341
1.0	Solution to the Falkner-Skan equations, see Table **??**											
2.0	1.0	1.000 000	1.764 83	1.764 828	−0.543 733	−0.543 733	1.621 32	1.118 754	0.143 497	0.099 024	0.529 297	0.365 219
	0.5	0.333 333	1.254 80	1.254 799	−0.507 821	−0.507 821	2.003 76	1.693 413	0.252 921	0.213 757	0.845 913	0.714 892
	0.1	0.052 632	0.677 291	0.677 288	−0.448 540	−0.448 550	2.688 30	2.556 928	0.408 461	0.388 530	1.398 97	1.330 665
	0	0.000 000	0.469 600	0.469 603	−0.418 711	−0.418 744	3.054 99	2.980 922	0.469 599	0.458 268	1.686 38	1.645 671
	−0.1	−0.047 619	0.166 218	0.166 515	−0.358 628	−0.358 900	3.843 47	3.838 994	0.550 566	0.550 022	2.280 09	2.278 078

* The solution does not converge for $m_2 = \infty$, and therefore $m_2 = 1000$ is taken as approach.

Table A-5: Comparison with tabulated data of laminar compressible similar flows with constant nonzero pressure gradients and heat transfer for calorically perfect ideal gas with $C = 1$ (constant) and $\mathrm{Pr} = 0.723$ and $\bar{\sigma} = 2.0 \quad (\mathrm{Ma} = \infty)$ taken from Rogers [57] table C-27. The values obtained with the CS-method (CSM) are transformed from the compressible Falkner-Skan transformed y-coordinate with uniform (vertical) grid spacing of $\mathrm{d}\eta = \sqrt{\frac{2C}{m_2+1}}0.0001$ and height of $\eta_\mathrm{e} = \sqrt{\frac{2C}{m_2+1}}8.0$ to the Illingworth-Levy coordinates ($\mathrm{d}\eta = 0.0001$ and $\eta_\mathrm{e} = 8.0$). Note that separation occurred when the table entry shows 'sep'.

g_w	$\hat{\beta}$	m_2		$f''(0)$		$g'(0)$		**Rogers**	**CSM**	**Rogers**	**CSM**
				Rogers	**CSM**	**Rogers**	**CSM**	J_1	$2J_1$	J_2	$2J_2$
0	2.00	1.000 000e3	*	0.703 383	sep	0.381 550	sep	0.158 885	sep	0.385 545	sep
	1.50	3.749 995e−6		0.667 808	sep	0.378 406	sep	0.182 897	sep	0.393 422	sep
	1.00	2.499 994e−6		0.623 739	sep	0.374 173	sep	0.218 392	sep	0.405 31	sep
	0.50	1.249 995e−6		0.564 591	0.564 584	0.367 826	0.367 818	0.277 945	0.138 965	0.425 583	0.212 802
	0.10	2.499 988e−7		0.493 985	0.493 975	0.359 069	0.359 054	0.370 076	0.184 998	0.456 948	0.228 484
	0	0.000 000		0.469 600	0.469 603	0.355 695	0.355 677	0.407 694	0.203 774	0.469 576	0.234 793
	−0.10	−2.499 987e−7		0.440 236	0.440 240	0.351 368	0.351 332	0.457 202	0.228 412	0.485 874	0.242 946
	−0.20	−4.999 973e−7		0.402 921	0.403 000	0.345 370	0.345 338	0.526 534	0.262 809	0.508 226	0.254 029
	−0.30	−7.499 957e−7		0.350 892	0.351 209	0.336 001	0.335 962	0.635 111	0.316 323	0.541 345	0.270 427
	−0.426 121	−1.065 296e−6		0.20	0.211 444	0.299 382	0.302 351	1.028 92	0.490 867	0.638 379	0.314 304
	−0.433 244	−1.083 103e−6		0.15	0.190 290	0.282 659	0.295 802	1.188 67	0.520 736	0.664 923	0.319 948
0.2	2.00	1.000 000e3	*	0.935 595	sep	0.299 591	sep	0.294 040	sep	0.347 458	sep
	1.50	3.749 995e−6		0.856 740	sep	0.296 330	sep	0.331 515	sep	0.359 453	sep
	1.00	2.499 994e−6		0.763 643	sep	0.291 938	sep	0.386 447	sep	0.377 149	sep
	0.50	1.249 995e−6		0.645 825	0.645 820	0.285 286	0.285 277	0.478 214	0.239 096	0.406 675	0.203 350
	0.10	2.499 988e−7		0.513 748	0.513 737	0.275 785	0.275 768	0.621 538	0.310 718	0.451 563	0.225 793
	0	0.000 000		0.469 600	0.469 603	0.271 951	0.271 928	0.681 389	0.340 596	0.469 576	0.234 793
	−0.10	−2.499 987e−7		0.416 813	0.416 826	0.266 819	0.266 769	0.762 222	0.380 824	0.492 953	0.246 476
	−0.30	−7.499 957e−7		0.247 150	0.248 209	0.244 465	0.244 423	1.099 99	0.546 403	0.577 073	0.287 841
	−0.347 875	−8.696 824e−7		0.15	0.157 900	0.225 411	0.226 715	1.359 82	0.661 196	0.622 984	0.308 350
	−0.356 406	−8.910 098e−7		0.10	0.127 574	0.212 666	0.219 355	1.519 69	0.704 220	0.641 565	0.313 834
0.6	2.00	1.000 000e3	*	1.357 04	sep	0.107 090	sep	0.545 626	sep	0.265 708	sep
	1.50	3.749 995e−6		1.202 47	sep	0.107 365	sep	0.610 013	sep	0.287 392	sep
	1.00	2.499 994e−6		1.022 62	sep	0.107 543	sep	0.704 201	sep	0.318 359	sep
	0.50	1.249 995e−6		0.799 139	0.799 124	0.107 306	0.107 297	0.862 178	0.431 087	0.368 005	0.184 022
	0.10	2.499 988e−7		0.552 454	0.552 442	0.105 657	0.105 636	1.116 60	0.558 228	0.440 762	0.220 394
	0	0.000 000		0.469 600	0.469 603	0.104 462	0.104 430	1.228 78	0.614 241	0.469 576	0.234 793
	−0.10	−2.499 987e−7		0.368 145	0.368 183	0.102 284	0.102 199	1.390 87	0.694 876	0.507 147	0.253 549
	−0.20	−4.999 973e−7		0.225 638	0.226 158	0.097 096 0	0.096 887	1.677 87	0.836 298	0.561 138	0.280 199
	−0.257 071	−6.426 739e−7		0.05	0.065 694	0.084 337 5	0.085 074	2.188 24	1.054 580	0.612 477	0.302 986
	−0.257 341	−6.433 489e−7		0	0.063 978	0.078 211 4	0.084 891	2.394 11	1.057 384	0.616 050	0.303 111
1.0	2.00	1.000 000e3	*	1.741 24	sep	−0.112 440	sep	0.780 252	sep	0.180 671	sep
	1.50	3.749 995e−6		1.519 46	sep	−0.105 971	sep	0.871 042	sep	0.212 828	sep
	1.00	2.499 994e−6		1.262 07	sep	−0.097 183 7	sep	1.004 05	sep	0.257 949	sep
	0.50	1.249 995e−6		0.943 144	0.943 128	−0.084 743 6	−0.084 753	1.228 77	0.614 384	0.328 707	0.164 375
	0.10	2.499 988e−7		0.590 174	0.590 160	−0.068 886 9	−0.068 911	1.602 11	0.800 971	0.429 928	0.214 981
	0	0.000 000		0.469 600	0.469 603	−0.063 025 9	−0.063 067	1.776 18	0.887 887	0.469 576	0.234 793
	−0.10	−2.499 987e−7		0.316 480	0.316 557	−0.055 315 70	−0.055 449	2.049 71	1.023 886	0.521 370	0.260 623
	−0.196 056	−4.901 373e−7		0.05	0.056 105	−0.041 334 4	−0.042 592	2.777 70	1.367 857	0.594 526	0.295 510
	−0.200 221	−5.005 497e−7		0	0.024 239	−0.038 523 3	−0.041 135	2.989 18	1.427 223	0.598 439	0.296 794
2.0	2.00	1.000 000e3	*	2.604 97	sep	−0.743 636	sep	1.320 19	sep	−0.035 529 6	sep
	1.50	3.749 995e−6		2.235 17	sep	−0.713 347	sep	1.474 37	sep	0.023 542 5	sep
	1.00	2.499 994e−6		1.806 39	sep	−0.672 821	sep	1.701 32	sep	0.104 997	sep
	0.50	1.249 995e−6		1.275 08	1.275 076	−0.611 937	−0.611 948	2.090 72	1.045 340	0.229 650	0.114 841
	0.30	7.499 968e−7		1.009 27	1.009 265	−0.575 473	−0.575 487	2.354 01	1.176 974	0.303 011	0.151 527
	0.10	2.499 988e−7		0.680 817	0.680 803	−0.522 479	−0.522 509	2.779 94	1.389 862	0.402 781	0.201 412
	0	0.000 000		0.469 600	0.469 603	−0.481 746	−0.481 811	3.144 66	1.571 999	0.469 575	0.234 793
	−0.10	−2.499 987e−7		0.164 923	0.165 352	−0.406 427	−0.407 029	3.915 49	1.953 728	0.556 395	0.277 897
	−0.120 701	−3.017 509e−7		0.05	0.052 442	−0.368 047	−0.370 053	4.364 91	2.168 317	0.576 789	0.287 452
	−0.125 567	−3.139 158e−7		0	0.007 246	−0.347 846	−0.352 575	4.620 19	2.276 648	0.580 102	0.288 669
	−0.126 950	−3.173 733e−7		−0.05	sep	−0.324 007	sep	4.940 89	sep	0.577 192	sep

* The solution does not converge for $m_2 = \infty$, and therefore $m_2 = 1000$ is taken as approach.

Table A-6: Comparison with tabulated data of adiabatic laminar compressible similar flows with constant nonzero pressure gradients for calorically perfect ideal gas with $C = 1$ (constant) and $\mathrm{Pr} = 0.723$ and $\bar{\sigma} = 2.0 \quad (\mathrm{Ma} = \infty)$ taken from Rogers [57] table C-28. The values obtained with the CS-method (CSM) are transformed from the compressible Falkner-Skan transformed y-coordinate with uniform (vertical) grid spacing of $\mathrm{d}\eta = \sqrt{\frac{2C}{m_2+1}}0.0001$ and height of $\eta_\mathrm{e} = \sqrt{\frac{2C}{m_2+1}}8.0$ to the Illingworth-Levy coordinates ($\mathrm{d}\eta = 0.0001$ and $\eta_\mathrm{e} = 8.0$). Note that separation occurred when the table entry shows 'sep'.

$\hat{\beta}$	m_2	g_aw		$f''(0)$		**Rogers**	**CSM**	**Rogers**	**CSM**
		Rogers	**CSM**	**Rogers**	**CSM**	J_1	$2J_1$	J_2	$2J_2$
1.00	2.499 994e−6	0.814 388	sep	1.152 95	sep	0.866 815	sep	0.286 134	sep
0.50	1.249 995e−6	0.826 698	0.826 691	0.881 723	0.881 713	1.071 83	1.071 785	0.345 808	0.345 823
0.10	2.499 988e−7	0.843 270	0.843 233	0.575 496	0.575 486	1.412 975	1.412 747	0.434 199	0.434 209
0	0.000 000	0.849 464	0.849 389	0.469 600	0.469 603	1.570 195	1.569 703	0.465 967	0.469 585
−0.10	−2.499 987e−7	0.857 375	0.857 094	0.335 283	0.335 395	1.810 908	1.808 755	0.516 373	0.516 197
−0.15	−3.749 980e−7	0.862 319	0.861 761	0.246 432	0.246 848	2.002 835	1.997 853	0.546 857	0.546 338
−0.20	−4.999 973e−7	0.868 479	0.866 773	0.114 397	0.117 393	2.359 336	2.336 963	0.586 263	0.584 018
−0.215 957	−5.398 895e−7	0.870 973	0.867 209	0.01	0.038 176	2.745 153	2.597 303	0.602 836	0.597 049
−0.216 103	−5.402 545e−7	0.871 000	0.867 186	0	0.036 978	2.790 413	2.601 652	0.603 017	0.597 136

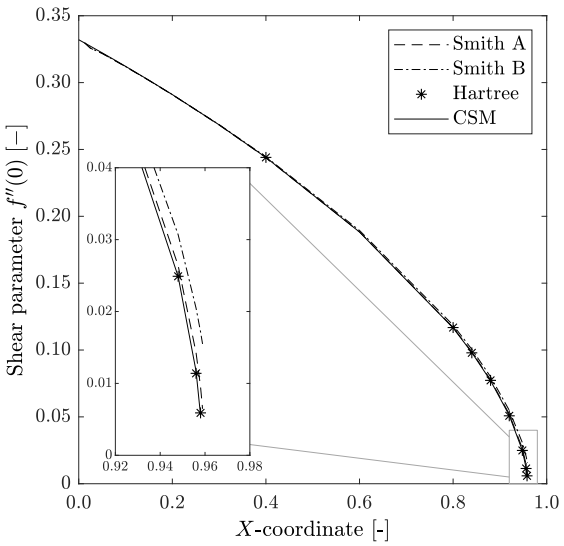

Figure A-2: Clutter (1961) comparison.

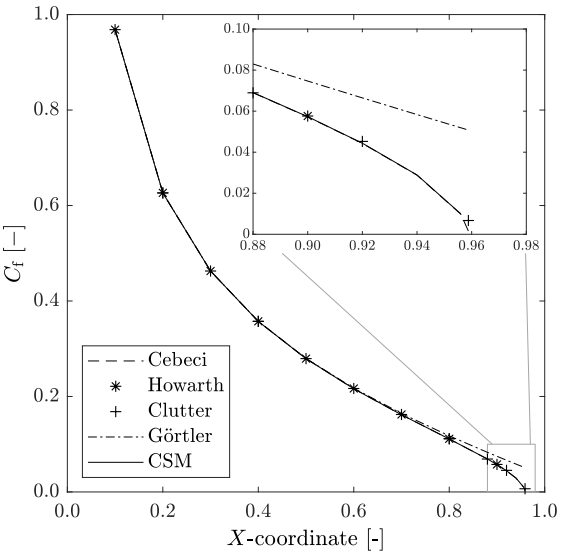

Figure A-3: Cebeci (1974) comparison.

A-5-4 Verification with Howarth's Flow

Nonsimilar case (first considered here), very suitable. Test case from Cebeci, according to Carlo from report by Clutter and Smith (1963) [22]. See also Clutter and Smith (1961) [21] and Cebeci (1974) [4] for the table.

1. put my results in last column (table Howarth 2)
2. I added first coordinate of 0, since Smith starts at 0.1. CSM program needs to start at zero.
3. Compared Rogers with first point: 6 accurate digits! Therefore, I doubt the accuracy of Smith's solution for 0.1.
4. close-up in MATLAB graph.
5. reference in table? fix question mark. add years? Mention complete table taken from Smith. add convergence criterion CSM, mention convergence criterion, and grid! unknown what grid was used by Smith. Change epsone to eps? Remove unit of meter, change to dimensionless (in table and graph!).
6. star in graph: explain, data point is missing.
7. conclude that it is interesting that CSM is closer to Hartree than Smith, add tolerances to legends (graph and table), and add a label such that graph and table can be related.
8. motivate why you plot data: you want the reader to appreciate the differences, they cannot be interpreted from the table alone. Reader cannot follow the conclusions from the table alone, which is the whole reason for graphs.

Graph Howarth's flow according to table 8-6 from Cebeci (1974):

1. (leave out later) first skin friction coeff used by cebeci was determined by plotting two definitions from the CSM program; was it clear from Cebeci literature? Or just state the definition of Cf used.
2. Then Gortler series towards the end deviate; Cebeci mentions it is because of the neglection of higher-order terms, which makes it less accurate towards the end
3. Zoom in is not needed, resuls are close: superimpose on Smith-Clutter and Howarth and Cebeci.

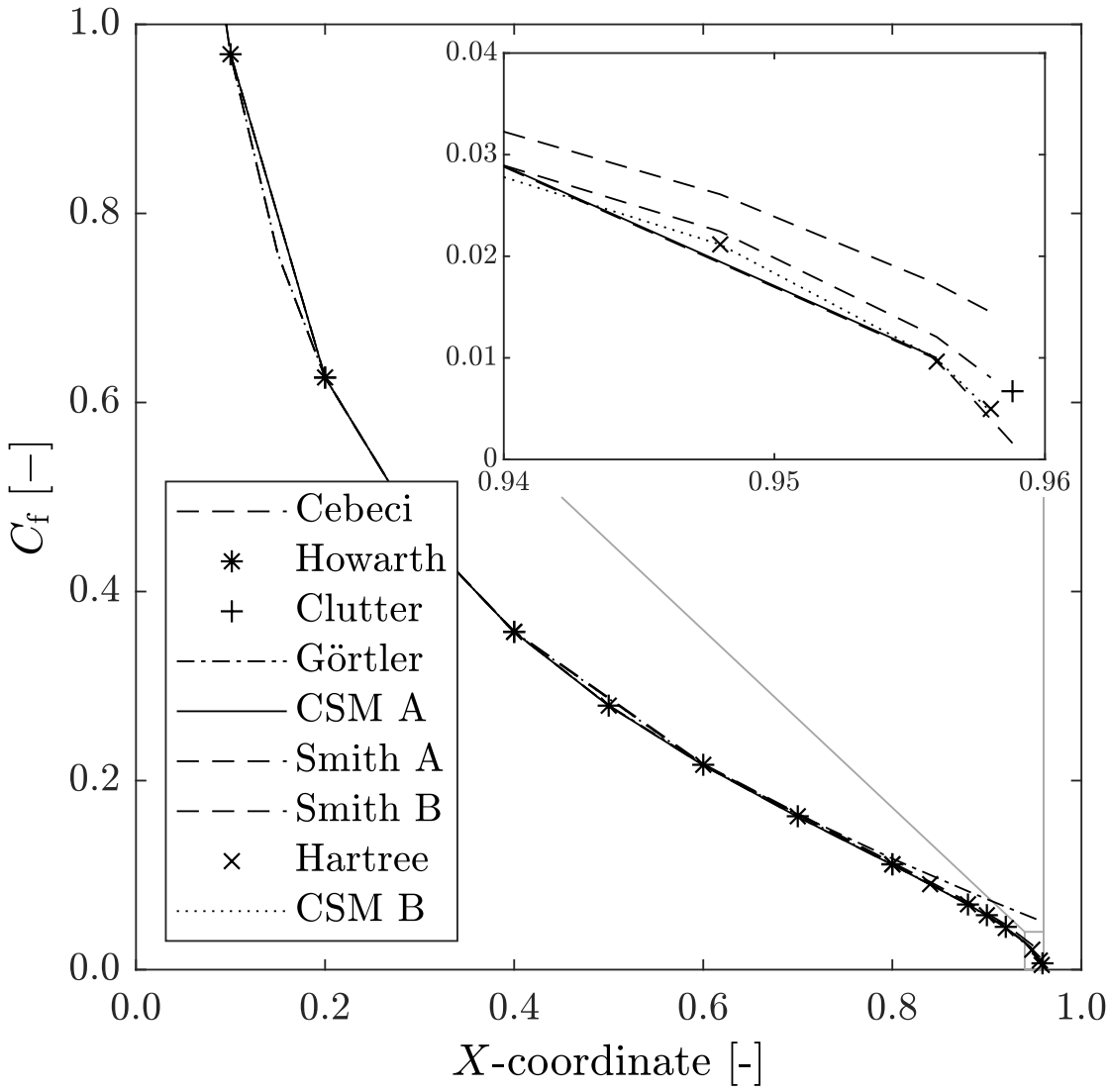

Figure A-4: comparison

Table A-7: Comparison with tabulated data of nonsimilar Howarths Flow: incompressible adiabatic decelarating flow (adverse pressure gradient) taken from Smith [21] table 6. All values in compressible Falkner-Skan transformed y-coordinate. Grid used by the CS-method (CSM): uniform (vertical) grid spacing of $\mathrm{d}\eta = 0.0100$ and height of $\eta_\mathrm{e} = 9.0$. Note that separation occurred when the table entry shows 'sep'.

X [-]	$f''(0)$ [-]			
	Douglas		Hartree	CSM
	$\epsilon = 0.000001$	$\epsilon = 0.00001$		$\epsilon = 0.00001$
0				0.332 057
0.0125	0.329 792	0.329 79		0.329 637
0.025	0.325 728	0.325 73		0.327 199
0.050	0.321 842	0.321 85		0.322 270
0.075	0.316 907	0.316 92		0.317 267
0.100	0.311 959	0.311 98		0.312 188
0.150	0.301 611	0.301 67		0.301 786
0.200	0.290 908	0.291 02		0.291 045
0.300	0.268 281	0.268 59		0.268 417
0.400	0.243 918	0.244 48	0.244 06	0.244 035
0.600	0.188 324	0.189 43		0.188 245
0.800	0.116 867	0.118 60	0.1168	0.116 523
0.840	0.098 627	0.100 57	0.0979	0.098 098
0.880	0.077 766	0.080 02	0.0773	0.077 081
0.920	0.052 064	0.054 93	0.0508	0.051 135
0.948	0.026 397	0.030 70	0.0249	0.024 884
0.956	0.014 267	0.020 47	0.0114	0.011 706
0.958	0.009 534	0.017 18	0.0059	0.005 566
0.9589	0.006 469	0.015 49		sep

Table A-9: Comparison with tabulated data of nonsimilar Howarths Flow: incompressible adiabatic decelarating flow (adverse pressure gradient) taken from Cebeci [4] table 8-1. All values in compressible Falkner-Skan transformed y-coordinate. Grid used by the CS-method (CSM): uniform (vertical) grid spacing of $\mathrm{d}\eta = 0.0100$ and height of $\eta_\mathrm{e} = 9.0$. Note that separation occurred when the table entry shows 'sep'.

$\bar{X}$ [-]	$f''(0)$ [-]	$\frac{\tau(0)}{\rho u_\infty^2}$ [-]				
	CSM		Cebeci	Howarth	Smith-Clutter	Görtler
0	0.332 057	Inf				
0.1	0.312 128	0.993 264	0.968 524	0.968 382		0.968 781
0.2	0.290 985	0.658 951	0.626 392	0.626 496	0.626 249	0.626 567
0.3	0.268 370	0.499 428	0.462 645	0.462 801		0.462 815
0.4	0.243 998	0.395 816	0.357 197	0.357 442	0.357 301	0.357 427
0.5	0.217 477	0.317 646	0.279 150	0.279 307		0.279 611
0.6	0.188 203	0.252 627	0.216 119	0.216 728		0.217 221
0.7	0.155 154	0.194 132	0.161 602	0.162 281		0.164 296
0.8	0.116 256	0.137 008	0.110 918	0.111 369	0.111 546	0.117 472
0.88	0.077 135	0.087 159	0.068 963		0.068 942	0.082 980
0.9	0.065 027	0.072 759	0.057 228	0.057 629		0.074 667
0.92	0.051 133	0.056 668	0.044 295		0.045 254	0.066 458
0.94	0.033 815	0.037 127	0.028 807			0.058 344
0.956	0.011 825	0.012 889	0.009 863			0.051 917
0.9588	sep	sep	0.001 602		0.006 717	0.050 798

A-6 Accuracy Study

NB subtle difference between accuracy (comparing with verified results) and accuracy of the solution based on your mesh size (mesh independent study).

1. last two columns in first table can be left out, since values are equal (limit is convergence criterion I guess);
2. in second table form factor is still changing, why?

Table A-10: Accuracy Study with Falkner-Skan wedge flows (adiabatic incompressible similar flows with nonzero constant pressure gradients for calorically perfect ideal gas with constant fluid properties) following the example of Cebeci [4] table 8-1. The convergence criterion used was $|\mathrm{d}f''(0)| < 1e-5$. The values obtained with the CS-method (CSM) are transformed from the compressible Falkner-Skan transformed y-coordinate with uniform (vertical) grid spacing and height of $\eta_\mathrm{e} = 8.0$ to the Illingworth-Levy coordinates.

β	m_2	$f''_\mathrm{w}(\mathrm{d}\eta = 1.0)$	$f''_\mathrm{w}(\mathrm{d}\eta = 0.5)$	$f''_\mathrm{w}(\mathrm{d}\eta = 0.2)$	$f''_\mathrm{w}(\mathrm{d}\eta = 0.1)$	$f''_\mathrm{w}(\mathrm{d}\eta = 0.01)$	$f''_\mathrm{w}(\mathrm{d}\eta = 0.001)$	$f''_\mathrm{w}(\mathrm{d}\eta = 0.0001)$	$f''_\mathrm{w}(\mathrm{d}\eta = 0.00001)$
1.0	1.000 000	1.155 489	1.210 943	1.228 986	1.231 682	1.232 579	1.232 588	1.232 588	1.232 588
0.5	0.333 333	0.902 464	0.921 149	0.926 624	0.927 416	0.927 677	0.927 680	0.927 680	0.927 680
0.3	0.176 471	0.761 054	0.771 294	0.774 199	0.774 616	0.774 753	0.774 755	0.774 755	0.774 755
0.1	0.052 632	0.581 351	0.585 644	0.586 815	0.586 980	0.587 035	0.587 036	0.587 036	0.587 036
0	0.000 000	0.466 862	0.468 960	0.469 502	0.469 578	0.469 602	0.469 603	0.469 603	0.469 603
−0.1	−0.047 619	0.319 142	0.319 320	0.319 305	0.319 301	0.319 299	0.319 299	0.319 299	0.319 299
−0.198 837 6	−0.090 429	0.044 220	0.031 080	0.025 278	0.024 304	0.023 973	0.023 969	0.023 969	0.023 969
$\mathrm{n}_\mathrm{points}$		9	17	41	81	801	8001	80001	800001

Table A-11: Accuracy Study of form factor H with Falkner-Skan wedge flows (adiabatic incompressible similar flows with nonzero constant pressure gradients for calorically perfect ideal gas with constant fluid properties) following the example of Cebeci [4] table 8-1. The convergence criterion used was $|\mathrm{d}f''(0)| < 1e-5$. The values obtained with the CS-method (CSM) are transformed from the compressible Falkner-Skan transformed y-coordinate with uniform (vertical) grid spacing and height of $\eta_\mathrm{e} = 8.0$ to the Illingworth-Levy coordinates.

β	m_2	$H(\mathrm{d}\eta = 1.0)$	$H(\mathrm{d}\eta = 0.5)$	$H(\mathrm{d}\eta = 0.2)$	$H(\mathrm{d}\eta = 0.1)$	$H(\mathrm{d}\eta = 0.01)$	$H(\mathrm{d}\eta = 0.001)$	$H(\mathrm{d}\eta = 0.0001)$	$H(\mathrm{d}\eta = 0.00001)$
1.0	1.000 000	1.2757	1.5968	1.9174	2.0565	2.1992	2.2145	2.2161	2.2162
0.5	0.333 333	1.5147	1.8228	2.0827	2.1852	2.2853	2.2958	2.2968	2.2969
0.3	0.176 471	1.6421	1.9398	2.1756	2.2655	2.3518	2.3607	2.3616	2.3617
0.1	0.052 632	1.8253	2.1109	2.3219	2.3995	2.4726	2.4801	2.4808	2.4809
0	0.000 000	1.9679	2.2475	2.4458	2.5172	2.5836	2.5904	2.5911	2.5911
−0.1	−0.047 619	2.2076	2.4842	2.6701	2.7350	2.7947	2.8007	2.8013	2.8013
−0.198 837 6	−0.090 429	3.1130	3.5024	3.7259	3.7925	3.8477	3.8530	3.8535	3.8535
$\mathrm{n_{points}}$		9	17	41	81	801	8001	80001	800001

Table A-12: Accuracy study with adiabatic laminar compressible similar flows with constant nonzero pressure gradients for calorically perfect ideal gas with $C = 1$ (constant) and $\mathrm{Pr} = 0.723$ and $\bar{\sigma} = 2.0 \quad (\mathrm{Ma} = \infty)$ based on tabulated data obtained from Rogers [57] table C-28 and the method following the example of Cebeci [4] table 8-3. The convergence criterion used was $|\mathrm{d}f''(0)| < 1e-5$. The values obtained with the CS-method (CSM) are in transformed compressible Falkner-Skan coordinates with grid height of $\eta_\mathrm{e} = 8.0$. Note that separation occurred when the table entry shows 'sep'.

$\hat{\beta}$	m_2	g_{aw} [-]						
		$\mathrm{d}\eta = 1.0$	$\mathrm{d}\eta = 0.5$	$\mathrm{d}\eta = 0.2$	$\mathrm{d}\eta = 0.1$	$\mathrm{d}\eta = 0.01$	$\mathrm{d}\eta = 0.001$	$\mathrm{d}\eta = 0.0001$
1.00	2.499 994e−6	sep	sep	sep	sep	sep	sep	sep
0.50	1.249 995e−6	0.847 676	0.831 986	0.827 540	0.826 903	0.826 693	0.826 691	0.826 691
0.10	2.499 988e−7	0.853 363	0.845 772	0.843 640	0.843 335	0.843 234	0.843 233	0.843 233
0	0.000 000	0.856 986	0.851 292	0.849 694	0.849 465	0.849 390	0.849 389	0.849 389
−0.10	−2.499 987e−7	0.862 353	0.858 410	0.857 305	0.857 147	0.857 095	0.857 094	0.857 094
−0.15	−3.749 980e−7	0.865 961	0.862 812	0.861 929	0.861 803	0.861 761	0.861 761	0.861 761
−0.20	−4.999 973e−7	0.869 918	0.867 575	0.866 902	0.866 806	0.866 774	0.866 773	0.866 773
−0.215 957	−5.398 895e−7	0.870 069	0.867 982	0.867 336	0.867 241	0.867 210	0.867 209	0.867 209
−0.216 103	−5.402 545e−7	0.870 052	0.867 962	0.867 313	0.867 218	0.867 187	0.867 186	0.867 186

Table A-13: Accuracy study with adiabatic laminar compressible similar flows with constant nonzero pressure gradients for calorically perfect ideal gas with $C = 1$ (constant) and $\mathrm{Pr} = 0.723$ and $\bar{\sigma} = 2.0 \quad (\mathrm{Ma} = \infty)$ based on tabulated data obtained from Rogers [57] table C-28 and the method following the example of Cebeci [4] table 8-3. The convergence criterion used was $|\mathrm{d}f''(0)| < 1e-5$. The values obtained with the CS-method (CSM) are in transformed compressible Falkner-Skan coordinates with grid height of $\eta_\mathrm{e} = 8.0$. Note that separation occurred when the table entry shows 'sep'.

$\hat{\beta}$	m_2	f_0'' [-]						
		$\mathrm{d}\eta = 1.0$	$\mathrm{d}\eta = 0.5$	$\mathrm{d}\eta = 0.2$	$\mathrm{d}\eta = 0.1$	$\mathrm{d}\eta = 0.01$	$\mathrm{d}\eta = 0.001$	$\mathrm{d}\eta = 0.0001$
1.00	2.499 994e−6	sep	sep	sep	sep	sep	sep	sep
0.50	1.249 995e−6	0.614 389	0.621 157	0.623 095	0.623 373	0.623 465	0.623 466	0.623 466
0.10	2.499 988e−7	0.403 793	0.406 173	0.406 811	0.406 901	0.406 930	0.406 930	0.406 930
0	0.000 000	0.330 122	0.331 604	0.331 988	0.332 041	0.332 059	0.332 059	0.332 059
−0.10	−2.499 987e−7	0.236 303	0.236 982	0.237 134	0.237 154	0.237 160	0.237 160	0.237 160
−0.15	−3.749 980e−7	0.174 324	0.174 542	0.174 550	0.174 549	0.174 548	0.174 548	0.174 548
−0.20	−4.999 973e−7	0.084 756	0.083 560	0.083 103	0.083 033	0.083 009	0.083 009	0.083 009
−0.215 957	−5.398 895e−7	0.034 723	0.029 419	0.027 409	0.027 099	0.026 996	0.026 995	0.026 995
−0.216 103	−5.402 545e−7	0.034 076	0.028 635	0.026 575	0.026 255	0.026 148	0.026 147	0.026 147

Table A-14: Accuracy study with nonsimilar Howarth's Flow: incompressible adiabatic decelarating flow (adverse pressure gradient) following the example of Cebeci [4] table 8-2. The convergence criterion used was $|\mathrm{d}f''(0)| < 1e-5$. The values obtained with the CS-method (CSM) are in transformed compressible Falkner-Skan coordinates with grid height of $\eta_e = 9.0$.

X [-]	$f''(0)$ [-]						
	$\mathrm{d}\eta = 1.0$	$\mathrm{d}\eta = 0.5$	$\mathrm{d}\eta = 0.2$	$\mathrm{d}\eta = 0.1$	$\mathrm{d}\eta = 0.01$	$\mathrm{d}\eta = 0.001$	$\mathrm{d}\eta = 0.0001$
0	0.330 121	0.331 604	0.331 986	0.332 040	0.332 057	0.332 057	0.332 057
0.0125	0.327 878	0.329 231	0.329 574	0.329 621	0.329 637	0.329 637	0.329 637
0.025	0.325 621	0.326 841	0.327 144	0.327 186	0.327 199	0.327 200	0.327 200
0.050	0.321 057	0.322 009	0.322 230	0.322 260	0.322 270	0.322 270	0.322 270
0.075	0.316 427	0.317 105	0.317 243	0.317 261	0.317 267	0.317 267	0.317 267
0.100	0.311 729	0.312 128	0.312 181	0.312 186	0.312 188	0.312 188	0.312 188
0.150	0.302 114	0.301 936	0.301 813	0.301 793	0.301 786	0.301 786	0.301 786
0.200	0.292 200	0.291 415	0.291 108	0.291 061	0.291 045	0.291 045	0.291 045
0.300	0.271 358	0.269 265	0.268 558	0.268 452	0.268 417	0.268 416	0.268 416
0.400	0.249 009	0.245 431	0.244 266	0.244 093	0.244 035	0.244 035	0.244 035
0.600	0.198 419	0.191 066	0.188 709	0.188 361	0.188 245	0.188 244	0.188 244
0.800	0.135 991	0.122 071	0.117 447	0.116 754	0.116 523	0.116 521	0.116 521
0.840	0.121 132	0.104 832	0.099 233	0.098 382	0.098 098	0.098 095	0.098 095
0.880	0.105 076	0.085 581	0.078 540	0.077 447	0.077 081	0.077 077	0.077 077
0.920	0.087 432	0.063 087	0.053 295	0.051 683	0.051 135	0.051 130	0.051 130
0.948	0.073 784	0.043 726	0.028 858	0.025 934	0.024 884	0.024 874	0.024 874
0.956	0.069 628	0.037 162	0.018 486	0.013 722	0.011 706	0.011 684	0.011 684
0.958	0.068 569	0.035 408	0.015 163	0.008 987	0.005 566	0.005 521	0.005 520
0.9589	0.068 089	0.034 601	0.013 485	0.006 023	sep	sep	sep
$n_{\eta_{\mathrm{points}}}$	10	19	46	91	901	9001	90001
$n_{\mathrm{X_{stations}}}$	19	19	19	19	19	19	19

Table A-15: Accuracy study with nonsimilar Howarth's Flow: incompressible adiabatic decelarating flow (adverse pressure gradient) following the example of Cebeci [4] table 8-3. The convergence criterion used was $|\mathrm{d}f''(0)| < 1e-5$. The values obtained with the CS-method (CSM) are in transformed compressible Falkner-Skan coordinates with grid height of $\eta_\mathrm{e} = 9.0$.

X [-]	$f''(0)$ [-]						
	$\mathrm{d}\eta = 0.01$ $\mathrm{d}X$	$\mathrm{d}\eta = 0.01$ $\mathrm{d}X/2$	$\mathrm{d}\eta = 0.01$ $\mathrm{d}X/4$	$\mathrm{d}\eta = 0.01$ $\mathrm{d}X/8$	$\mathrm{d}\eta = 0.01$ $\mathrm{d}X/16$	$\mathrm{d}\eta = 0.01$ $\mathrm{d}X/32$	$\mathrm{d}\eta = 0.01$ $\mathrm{d}X/64$
0	0.332 057	0.332 057	0.332 057	0.332 057	0.332 057	0.332 057	0.332 057
0.0125	0.329 637	0.329 637	0.329 638	0.329 638	0.329 638	0.329 638	0.329 638
0.025	0.327 199	0.327 200	0.327 200	0.327 200	0.327 200	0.327 200	0.327 200
0.050	0.322 270	0.322 271	0.322 272	0.322 272	0.322 272	0.322 272	0.322 272
0.075	0.317 267	0.317 269	0.317 270	0.317 270	0.317 270	0.317 270	0.317 270
0.100	0.312 188	0.312 190	0.312 191	0.312 191	0.312 191	0.312 191	0.312 191
0.150	0.301 786	0.301 791	0.301 793	0.301 793	0.301 793	0.301 793	0.301 793
0.200	0.291 045	0.291 052	0.291 054	0.291 055	0.291 055	0.291 055	0.291 055
0.300	0.268 417	0.268 435	0.268 440	0.268 441	0.268 442	0.268 442	0.268 442
0.400	0.244 035	0.244 064	0.244 071	0.244 073	0.244 074	0.244 074	0.244 074
0.600	0.188 245	0.188 267	0.188 274	0.188 276	0.188 276	0.188 276	0.188 276
0.800	0.116 523	0.116 325	0.116 258	0.116 240	0.116 236	0.116 234	0.116 234
0.840	0.098 098	0.097 993	0.097 950	0.097 938	0.097 935	0.097 934	0.097 934
0.880	0.077 081	0.076 999	0.076 964	0.076 954	0.076 952	0.076 951	0.076 951
0.920	0.051 135	0.051 018	0.050 968	0.050 955	0.050 951	0.050 950	0.050 950
0.948	0.024 884	0.024 519	0.024 385	0.024 347	0.024 338	0.024 335	0.024 335
0.956	0.011 706	0.011 012	0.010 747	0.010 671	0.010 652	0.010 647	0.010 646
0.958	0.005 566	0.004 132	0.003 469	0.003 259	0.003 203	0.003 189	0.003 185
0.9589	sep	sep	sep	sep	sep	sep	sep
n_{η_points}	901	901	901	901	901	901	901
$n_{\mathrm{X_{stations}}}$	19	37	73	145	289	577	1153

Table A-16: Accuracy study with nonsimilar Howarth's Flow: incompressible adiabatic decelarating flow (adverse pressure gradient) following the example of Cebeci [4] table 8-4. The convergence criterion used was $|\mathrm{d}f''(0)| < 1e-5$. The values obtained with the CS-method (CSM) are in transformed compressible Falkner-Skan coordinates with grid height of $\eta_e = 9.0$.

X [-]	$f''(0)$ [-]						
	$\mathrm{d}\eta = 1.0$ $\mathrm{d}X$	$\mathrm{d}\eta = 0.5$ $\mathrm{d}X/2$	$\mathrm{d}\eta = 0.2$ $\mathrm{d}X/4$	$\mathrm{d}\eta = 0.1$ $\mathrm{d}X/8$	$\mathrm{d}\eta = 0.01$ $\mathrm{d}X/16$	$\mathrm{d}\eta = 0.001$ $\mathrm{d}X/32$	$\mathrm{d}\eta = 0.0001$ $\mathrm{d}X/64$
0	0.330 121	0.331 604	0.331 986	0.332 040	0.332 057	0.332 057	0.332 057
0.0125	0.327 878	0.329 231	0.329 574	0.329 622	0.329 638	0.329 638	0.329 638
0.025	0.325 621	0.326 842	0.327 145	0.327 187	0.327 200	0.327 201	0.327 201
0.050	0.321 057	0.322 011	0.322 232	0.322 262	0.322 272	0.322 272	0.322 272
0.075	0.316 427	0.317 107	0.317 246	0.317 264	0.317 270	0.317 270	0.317 270
0.100	0.311 729	0.312 130	0.312 184	0.312 189	0.312 191	0.312 191	0.312 191
0.150	0.302 114	0.301 941	0.301 820	0.301 800	0.301 793	0.301 793	0.301 793
0.200	0.292 200	0.291 423	0.291 117	0.291 070	0.291 055	0.291 055	0.291 055
0.300	0.271 358	0.269 286	0.268 582	0.268 477	0.268 442	0.268 441	0.268 441
0.400	0.249 009	0.245 463	0.244 302	0.244 131	0.244 074	0.244 073	0.244 073
0.600	0.198 419	0.191 113	0.188 744	0.188 393	0.188 276	0.188 275	0.188 275
0.800	0.135 991	0.121 994	0.117 212	0.116 479	0.116 236	0.116 232	0.116 232
0.840	0.121 132	0.104 822	0.099 108	0.098 228	0.097 935	0.097 931	0.097 931
0.880	0.105 076	0.085 611	0.078 453	0.077 329	0.076 952	0.076 948	0.076 947
0.920	0.087 432	0.063 138	0.053 180	0.051 517	0.050 951	0.050 945	0.050 944
0.948	0.073 784	0.043 792	0.028 576	0.025 471	0.024 338	0.024 324	0.024 323
0.956	0.069 628	0.037 241	0.018 112	0.012 957	0.010 652	0.010 621	0.010 620
0.958	0.068 569	0.035 493	0.014 744	0.007 909	0.003 203	0.003 104	0.003 099
0.9589	0.068 089	0.034 689	0.013 034	0.000 000	sep	sep	sep
$n_{\eta_{\mathrm{points}}}$	10	19	46	91	901	9001	90001
$n_{\mathrm{X_{stations}}}$	19	37	73	145	289	577	1153

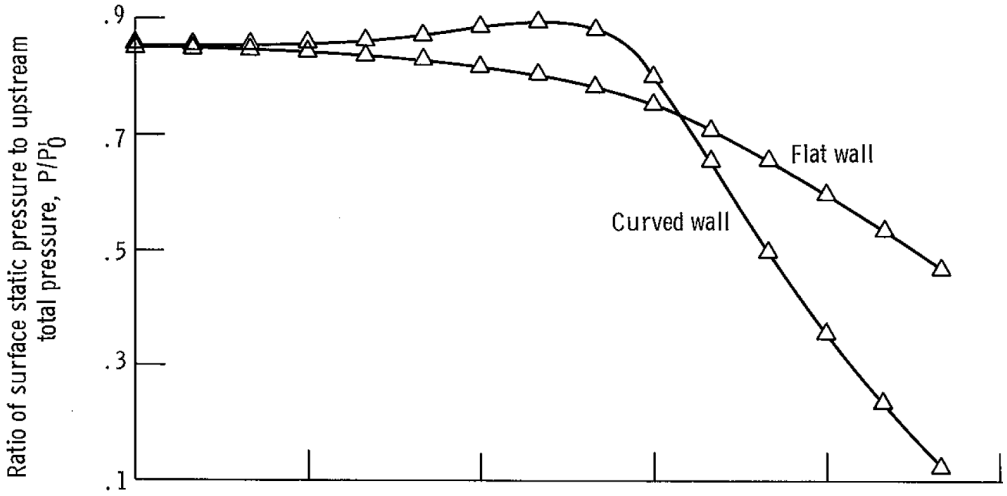

Figure A-5: Nozzle wall surface pressure distributions that serve as input. Note the maximum in pressure just before the rapid decrease in pressure in the converging wall section. This maximum is also present in the SU2 CFD predictions for the ORCHID nozzle, but was removed for simulation purposes. Taken from McNally [48].

A-7 Verification with the NACA0012 Airfoil Case

Include this case as an example of how to use the program. See Appendix F or the Addendum, for the example is included with the computer program online.

A-8 Validation with Nozzle Boundary Layer Thickness Measurements

Including added length to reach initial BL thicknesses and the wall surface pressure inputs.

A-9 Further Verification and Validation for Air

For further verification for cases with (ideal gas) air the reader is referred to the AGARDographs and the Stanford conferences that had the objective to build an extensive catalogue of reliable experimental data of turbulent flows for the validation of numerical codes. The AGARDographs by the Advisory Group for Aerospace Research & Development (AGARD) have been a very important source for the author, not only for obtaining experimental data but also for ideas and inspiration. Especially the compilations of compressible boundary layer data [101,102] which were meant as an extension to the Stanford conference on *Computation of turbulent boundary layers* [83]. The Stanford Conference

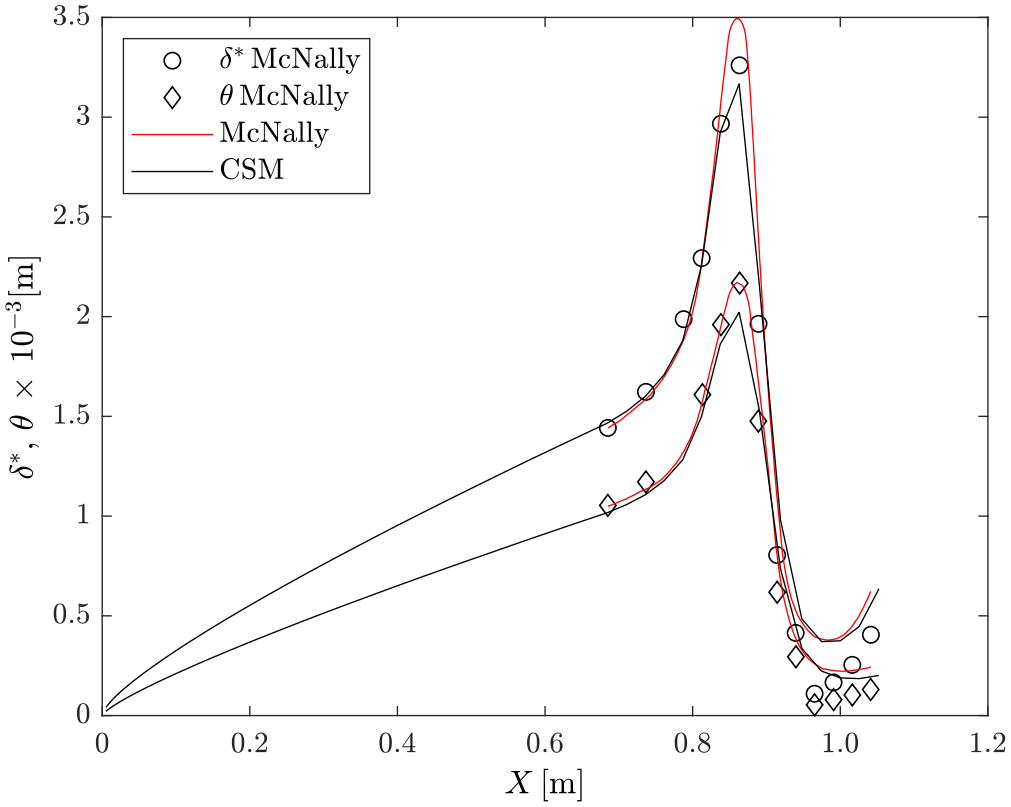

Figure A-6: Comparison with the curved walled nozzle with added length shown.

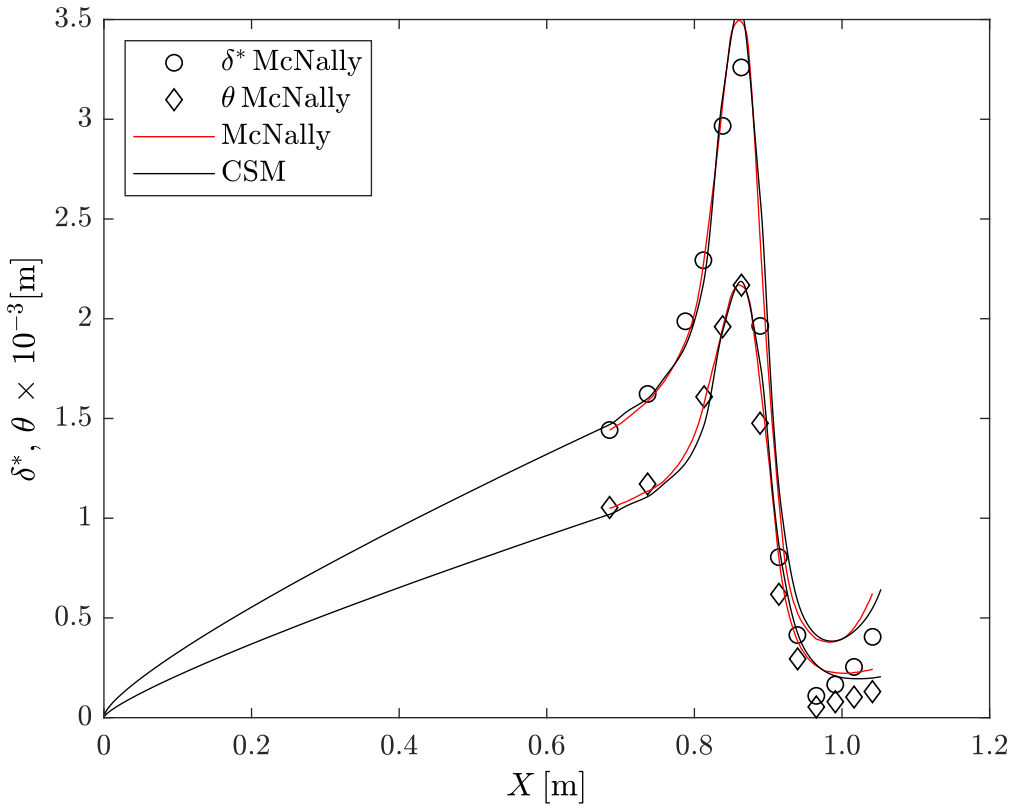

Figure A-7: Comparison with the curved walled nozzle with added length shown. Input interpolated, results are close to McNally, but a bit wavy because of the interpolation with scarce data points.

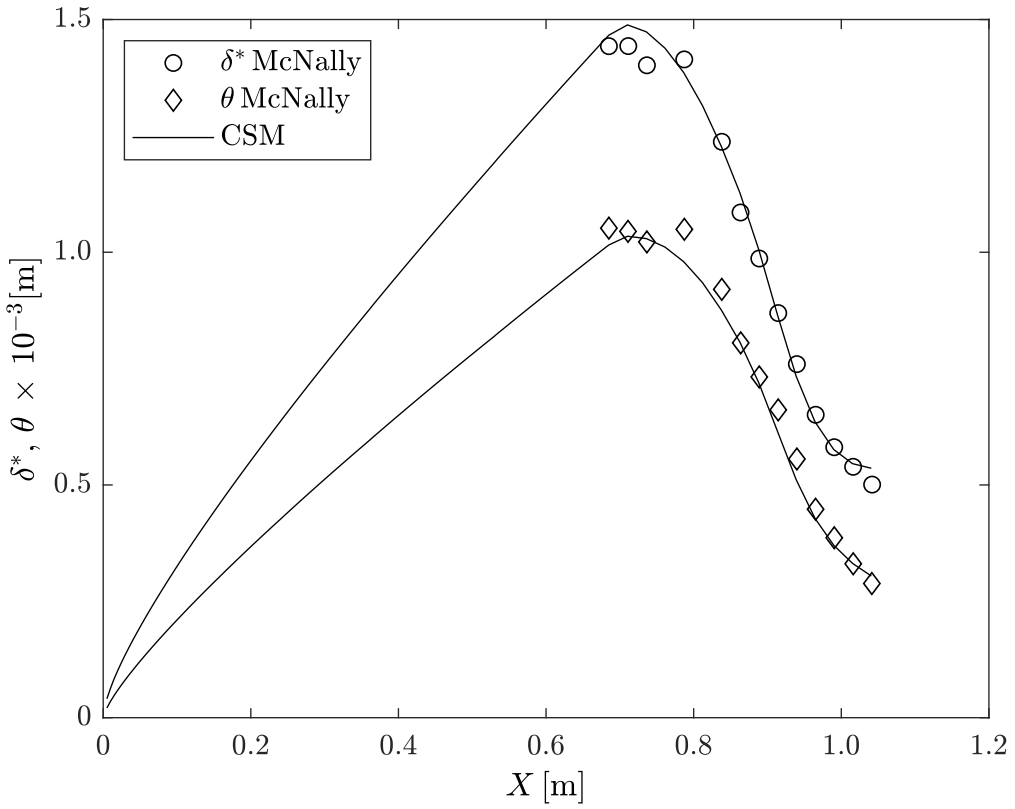

Figure A-8: Comparison with the flat walled nozzle with added length shown. Last three measured data points indicate a decrease in thicknesses not predicted by the program. This might indicate relaminarization, but at a later stage than on the curved wall.

on *Complex Turbulent Flows* by Kline [110] has not been studied yet and might give some inspiration for further validation or the design of experiments. All conferences had the objective of providing reliable experimental data for the validation of numerical models.

In future, add two reports (part 1 and part 2) that use conventional (at that time) measurements and LDV (part 2) to measure Reynolds-stresses. Same Mach-number range as Winter & Gaudet, highly suitable case to consider next. Sources: Measurements in the Turbulent Boundary Layer at Constant Pressure in Subsonic and Supersonic Flow part 1 [122] and part 2 [123].

Validation with nonideal gas flows is not possible yet. Taking in mind the catalogues mentioned above, it is highly recommended to plan and coordinate experimental measurement campaigns together with other researchers or research groups. Reliable data sets are difficult and expensive to generate. Matching these measurement campaigns and planning them in a smart way prevents double work. On top of that, it is certain that state-of-the-art researchers also include their model and measurement uncertainties (I cannot yet).

A-10 Take Into Account When Measuring a Boundary Layer

Extensive measurement campaigns for turbulent boundary layers were often focused on certain aspects and either measured not all circumstances, or did not include these conditions in the publication, which made a properly design and performed experiment useless for validation purposes of the boundary layer program. (the author does not know of any experimental laminar flow case data, please let him know if you know one, especially for supersonic Mach-number flows). A two-dimensional steady state boundary layer on a two-dimensional surface is a function of:

1. (Inlet) total conditions (P0, T0) and inlet velocity or Mach-number;
2. Initial (profile) conditions;
3. Free stream flow conditions at the BL edge (Mach-number, static pressure or velocity distribution);
4. Wall conditions (heat flux and or wall temperature);
5. Surface geometry (curvature, length, etc.);

The program input can be defined with the conditions above. Thus make sure to measure them. In literature the pressure history is often omitted and thus the build-up of a boundary layer cannot be simulated accurately (upstream history of the flow needs to be taken into account). To make sure the conditions are known, for example the start

of the boundary layer, it is advisable to insert a sharp-edged flat plate inside the test section. The start of the BL is then exactly known. The BL edge conditions, in this case the Mach-number, can be obtained with Schlieren. The plate can be considered adiabatic (flow on both sides, zero heat flux).

Take into account the surface coordinate which length is larger for a curved surface compared to the x-coordinate or straight length of a wind tunnel. Make sure that the radius of curvature is much larger than the boundary layer thickness.

A-11 Code listing

See Addendum Appendix G and/or Appendix F Code Listing.

A-11-1 Overview of Variables

Find Read-Me file online, see Addendum Appendix G and/or Appendix F Code Listing.

A-12 Code Nuances

This section highlights some parts of the code that need to be taken into account by the user for certain cases.

A-12-1 Implementation of the Intermittency Factor

The intermittency factor γ or $\gamma_{\text{intermittency}}$ or γ_{int} given by

$$\gamma = \left[1 + 5.5(y/\delta)^6\right]^{-1} \tag{A-1}$$

becomes in transformed form

$$y/\delta = \frac{\int_0^{\eta} c \, \mathrm{d}\eta}{\int_0^{\eta_e} c \, \mathrm{d}\eta} \tag{A-2}$$

$$\gamma = \left[1 + 5.5(y/\delta)^6\right]^{-1}. \tag{A-3}$$

Note that the implementation uses the edge of the grid instead of the edge of the boundary layer. Currently the solution is smooth, however, using the last option, the grid point closest to the boundary layer edge (or velocity thickness (which is ill defined) results in oscillations in the velocity thickness. Note also that the grid cannot be extended

arbitrarily, since the γ_{int} is in this way made a function of the boundary layer edge. Note also (number 3) that γ_{int} is not implemented in the inner eddy viscosity relation. The assumption that the laminar sublayer and logarithmic intermediate layer coincide at about 11.8 (and thus changing from inner EV to outer EV) means also that the gamma intermittency at this point is about 0.9999, which is practically equal to 1. Therefore, gam int is not taken into account in the code.

A-12-2 Implementation of Transition check

Due to reasons X and Y to Z the transition check is implemented differently in the MATLAB code compared to the/from the FORTRAN code of Cebeci (2002). First of all, there was not a transition check in the FORTRAN code, only the point of transition, the transition station, was specified. In the MATLAB code two methods for predicting transition were implemented: Wazzan and Michel. To implement this in a smooth and nice way one large difference is made with the FORTRAN code: where the FORTRAN code knows where and when transition occurs (it is specified beforehand), in the MATLAB code using Michel or Wazzan we don't know. We first have to run the BL calculation, and then calculate the BL characteristics and determine after the solution for the current station has converged if transition has occurred. Then, if transition has occurred, we use the laminar solution at the current station to restart the BL calculation, but now as a turbulent profile calculation. The difference with the FORTRAN code is this: FORTRAN code immediately starts calculating a turbulent solution at the transition station with a laminar (converged) profile solution from the previous station, the MATLAB code starts a turbulent calculation at the current station with a converged laminar profile solution of the CURRENT station. This results in a slightly different velocity profile in the transition region, from the station where transition is found to occur further downstream. The effect can be seen in the form factor. For verification purposes, the old FORTRAN method was kept in the code, making the code more complex than needed. Accuracy was reached up to 5-digits (more not checked), and thus both codes gave the same results. In a later version of the MATLA code this part has been removed. The differences in the transition region are assumed not to be of importance, since 1 transition region was calibrated for adiabatic flows only, 2 it is doubtful how well transition region can be predicted? 3 it is not that important 4 the turbulent (fully turbulent) solution is not that accurate either (within 10 percent would already be nice).

Note that when NTR is known beforehand, the transition check notices this one station before, and thus enabling the other two methods to be implemented in the code, which check after a converged solution at the current station for transition, and if so, iterate again now for turbulent flow at the same (current) station.

A-12-2-1 Calculation of $\gamma_{\text{transition}}$

For the calculation iof the γ transition factor (zero for laminar flow, and one for turbulent flow) Cebeci [27] calculates the Reynolds-number and uses fluid properties from the previous station, except for the use of νe which is used at the current station. Both reasons are unclear: 1) why use previous station properties? and 2) why only ν_e at current station? For airfoils, such as NACA0012 in ideal gas air this is probably not a problem since the viscosity does not change much. For our case however, we want the code to deal with large changes in fluid properties and thus it was assumed that ν_e from the previous station should also be used. (Why not use everything from current station?).

Implement Sutherland's Law in its original form in PRECAL-file and in FLDPRS-file. Note! that transition from laminar to turbulent flow does not change the edge flow properties! How does this work? Zero viscosity in the main flow. Inviscid flow. No losses. Thus turbulent (zero Eddy-Viscosity) and laminar flow behave the same for inviscid flows?

A-12-3 Implementation of Laminarization Check

A-12-4 Calculation of Velocity Thickness

with integral to take into account velocity peak. for normal profile still 0.99. With peak it is 0.99 of total disturbed flow velocity (THE quantity which we want to know). This calculation is fluently with appearing and disappearing velocity peaks. Linearisation between nodes. This results in an error of . . . ?

A-12-5 Pre-allocation of Maximum Grid Size and Extension During Run

201, must be enough. If not, warning message and extension with 20 points. Exceptional if it needs to be extended. If so, check if there are any errors in the input and if the solution is converging.

A-12-6 Changes Compared to FORTRAN Program

Added another call to FLDPRS after the final solution was calculated in order to update the Fluid Properties with the final solution. (The final solution is converged already). One case was found which showed the need for this.

One coefficient was missing in the FORTRAN code. It was added by the author.

A range of input-options was added.

Different types of thermophysical models were added, ranging from to. In addition, FluidProp was added to be able to simulate any fluid available through its library.

The Eddy Conductivity model from Cebeci [4] was added to the Eddy-file.

A PLOT-file was added.

A-12-7 Speed of program

Using MATLAB predefined functions in this program is generally slower than hard-coding simple functions. It has been found that implementing the coefficient matrices from 'Convective Heat Transfer' [27, p. 281] and using MATLAB's function $x = A\backslash b$ is slower than implementation of the solver obtained from the FORTRAN-code included with the book. Note that the book contains a misplaced 1 in one of these matrices! See Appendix D for details. Of course copying this misplaced 1 will result in a nonfunctional solver.

Also, it has been found that hardcoding the trapezium-rule is faster than using the MATLAB in-build function 'trapz'.

A-13 Extending the Functionality of the Program

Cebeci has rewritten 'Analyis of Turbulent Flows' which was published as a third edition [25] by Springer in 2013. It has become a nice overview for the properties of the CS-model and modifications accounting for specific flow types. This book can be used as a starting point to study what has been done with the CS-model in the past.

Cebeci [61] describes how the CS-model (and method) can be implemented in CFD codes impleemnting higher-order turbulence models. Basha [28] discusses the implementation of transition models in CFD software packages for improving the predicted drag. Abid [113] presents an improved CS-model for 3D boundary layer flows. And Cebeci [81] discusses a general method for arbitrary wings utilizing an adopted form of the CS-model.

The current MATLAB boundary layer program can be extended to include:

1. Program can be made faster with an order-of-magnitude by calling FluidProp only for the necessary thermophysical properties, or substitute for known fluid property relations in certain ranges, or table interpolation [111, 112]. Unnecessary calculations can be left out. When the calculation needs to be performed in a certain range with a-priori known behaviour, for example the ORCHID nozzle, then the calculations can be speed up. Furthermore, the implementation of Richardson Extrapolation (RE) [4] can make the program either much faster, or more accurate. The accuracy can easily be improved by two orders of magnitude with respect to the mesh spacing in the relevant variables by Richardson extrapolation on the nonuniform grid in one of two coordinate directions independently, or in both directions (not implemented here). The implementation of RE speeds up

the calculations even more, since less calls are needed to FluidProp, which is the limiting factor.

2. Transient simulations [add source];
3. A higher-order turbulence model (use 'Turbulence Models and Their Applications' by Cebeci (2004) [61]);
4. Surface roughness (use reference [27, p. 275]);
5. Surface mass transfer (change boundary conditions for suction or blowing [4]);
6. Fully developed duct or pipe flow and axisymmetric [4] nozzles. Source to start with: 'Convective Heat Transfer' by Cebeci (2002) [27]. Note that more experimental data is available for axisymmetric nozzles and pipe flow;
7. Centrifugal forces and non-negligible streamline curvatures ('Effects of Streamline Curvature on Turbulent Flow' by Bradshaw (1973) [124]);
8. Three-dimensional compressible laminar and turbulent boundary layers on arbitrary wings [81];
9. Transverse curvature (no information);
10. Low Reynolds-number effects (corrections for). Low-Reynolds-number effects exist in stagnation-point flows close to the leading edge or stagnation point, since the flow develops laminar first. Use Cebeci (2013) [25, pp. 161-162] and Cebeci [4] for EV-model, and Cebeci [4,64] (first paper eq. 41) for the eddy conductivity model.
11. High (adverse) pressure gradient (effects) Cebeci [4, 25];
12. Add the program CoolProp for fluid property retrieval (for comparison of different models and possible availability of different fluids);
13. Measured data, for example pressure, can be processed by a state variable filter (control engineering) to obtain a smooth and useful derivative.

Appendix B

Overview of Validation Cases Considered

The table on the next two pages shows a systematic overview of the validation cases listed in Fernholz & Finley [101, 102] as part of the AGARD library on compressible turbulent flows.

All cases have been listed and distinguished in the following categories:

1. Wind tunnel type: continuous or transient (blow-down);
2. Flow type (geometry): straight wall or plate, or curved surface;
3. Pressure Gradient (PG): adverse, zero or favourable;
4. Heat Transfer (HT): adiabatic or heat transfer;
5. Mach-number;
6. Re_θ;
7. Roughness;
8. Pressure history available; and,
9. Possibly any important remarks on the experimental data set.

The cases were selected based on the following criteria in this order:

1. Steady state flow;

2. Two-dimensional (flow) geometry;
3. Mach-number in range of the ORCHID nozzle ($0.3 < \text{Ma} < 2.0$); and,
4. Pressure history well documented (BL edge conditions);
5. Adiabatic flow, preferably complemented by heat transfer under the same conditions.

Validation case selection for compressible turbulent flows, including (non-)zero Pressure Gradients and heat transfer

Summary:
Both sources are studied and all cases were added to the tables below, dividing in 2D-flow (useful) and axisymmetric flow (not useful). The cases of both sources are added in a separate tables, such that they can still be distinguished.

Sources:	title	code	nr.	authors	year
1)	A critical compilation of compressible turbulent boundary-layer data	ADA045367	223	Fernholz and Finley	1977
2)	A further compilation of compressible boundary-layer data with a survey of turbulence data	ADA	263	Fernholz and Finley	1981

The goal of these documents is to be a reliable source of compressible supersonic experimental data for validation purposes.
An extension of the work of Coles and Hirsch (1968/1969), but then dealing with the compressible flows including heat transfer

1)	(Wind) Tunnel Type		Flow Type		Pressure Gradient			Heat Transfer			(smallest)			Remarks
Case	continuous	Blow-down	FP (Plate)	Nozzle	APG	ZPG	FPG	AW	HT	Mach	Re_theta	Roughness	pressure history available	
5301	X		X			X		X		2.0-4.5	2000-10000			
5501	X		X			X		X		1.7-2.5	6000-21000			
5502	X		X			X		X		2.0	11000-40000	X		
5503	X			X			X		X	5.0-8.2	5000-13000			
5801	X			X	X		(X)	X		1.9	11000-12000			
5802	X			X		X		X		1.75-3.75	2000-12000			
5803	X			X		X		X		1.7-4.8	26000-35000			
5804	X		X			X		X		2.2-2.7	8000-50000	X		
5805	X			X		X		X		2.0-3.5	6000-14000	Step		
5902	X		X			X			X	5.0	1000-4500			
6201		X	X			X		X	X	5.0	3000-7000			
6502		X				X		X		2.8	(57000)			
6504	X		X				X		X	1.0-3.0	3000-10000			
6505	X			X		X		X		1.6-2.2	9000-120000			
6506		X	X			X		X	X	4.95	4000-12000	X		
6601	X			X		X		X		2.4-3.4	55000			same case listed two times, only second time is complet
6602		X		X		X		X		2.5-3.5	14000-20000			
6702	X		X			X			X	6.5	1300-6000			
6800	X	X	X		X	X	X		X	1.6-3.25	7000		? Check!	No profile data available, but St-number measured
6902	X			X			X	X		1.4-3.0	4000-2000		Can't find source	
6903		X		X		X		X		2.0-5.0	85000-350000			
7003	X			X		X		X	X	1.75-3.00	4000-10000			
7006	X		X			X		X		4.0	2000-25000			
7007	X			X	X	X	?	X		4.0-2.95	35000-70000			
7101	X			X	X	X		X		3.5-2.8	18000-42000			
7202	X			X		X		X	X	4.9	7000-58000			
7301	X	?	X	X		X		X	X	4.0-4.9	8000-30000		Yes?	
7302	X			X		X		X		0.2-2.8	10000-160000			
7303	X			X		X		X		2.0-4.6	10000-80000			
7304	X	?		X			X	X	X	3.8-4.5	6000-50000		yes, but not from start.	See also case 7202
7401		X		X	X		X	X		2.56-3.00	14000-24000			With combined air injection
7402	X		X			X		X		2.5-4.5	5000-30000			Good/carefull dataset, best in this range
7403	X			X		X			X	9.4	40000			
7601		X		X		X		X		2.96-2.80	23000-415000			

Further compilation

2)	(Wind) Tunnel Type		Flow Type		Pressure Gradient			Heat Transfer			(smallest)			Remarks
Case	continuous	Blow-down	FP (Plate)	Nozzle	APG	ZPG	FPG	AW	HT	Mach	Re_theta	Roughness	pressure histroy available	
5806	X			X		X		X		1.77	16000			Large number of wires used. Data obtained from graphs
6002	X		X			X			X	5.1	2900-4300	X		with air injection
7404	X			X		X		X	X	4.9	6000-26000			These data are among the most carefully considered. T
7701	X		X			X		X		2.5-4.5	1000-8200			These data extend further the very large pool of carefully observed adiaba
7702	X		X			X			X	3.0	3000-4000	X		
7703	X			X		X			X	6.0	14000			response of BL on change in roughness
7801	X			X		X		X		0.1, 0.6-2.2	6000-40000			Compare to Winter and Gaudet! NB: deviation which is
7803	X			X	X			X		3.0-2.3	2700-5400			
7901	X			X		X		X		2.9	2700-58000	X		Blowing

1)	(Wind) Tunnel Type		Remarks
axisymme	continuous	Blow-down	
5901	X		
6001	X		
6401	X		Clutter (1964)
6501		X	
6503	X		
6701		X	blow-down but effectively continuous
6801			
6901			converging-diverging conical nozzle, subsonic to Ma 4.4
7001		X	
7002		X	
7004	X		
7005	X		
7102			
7103		X	
7105	X	X	
7201	X		
7203		?	
7204		X	
7205		X	
7206		X	
7207			
7208		X	
7209		X	
7305		X	

Further compilation (2)

axisymme	continuous	Blow-down	
5701	X		
7306		X	Shock wave BL interaction (SBLI) - Shock wave induced adverse pressure gradient
7405		X	
7501		X	SBLI
7802		X	
7804		X	
7902		X	
7903		?	
8001		X	SBLI

Appendix C

Assumptions Leading to the Final System of Equations

The assumptions that were made to obtain the final system of equations implemented in the computer program are listed below in a step-by-step manner (consider placing this as section in the appendix code report):

General assumptions (and principles) regarding the considered flow problem:

1. Two-dimensional flow geometry (no axial flow geometries considered in this thesis);
2. Steady state;
3. Single-phase fluid (gas/vapour or liquid (inlcuding supercritical fluid));
4. Uniform homogeneous composition, isotropic fluid;
5. Isentropic free stream (no losses in free stream, iso-energetic assumption [58]);
6. No heat sources inside the flow;
7. No body forces inside the flow (gravity (potential energy is neglected [27, p. 21]), centrifugal forces, electromagnetic forces or any other body forces are neglected);
8. No nuclear reactions (mass is neither created nor destroyed);
9. No relativistic effects (speeds are not even close to light speed, Lorentz factor equal to 1);

10. No fluid dissociation/recombination (for polyatomic molecules, $T > 2000$K), no ionization (all molecules, also monatomic) (these phenomena are part of real gas effects); and,

11. Principle of Parsimony (Law of Pasimony): the simplest solution (or model) is most likely to be the best solution to the problem (see also the dedication in the prematter of this thesis).

Regarding the derivation of the NS-equations [3, p. 74]:

1. Continuity hypothesis: the fluid is a continuum (Knudsen number is practically zero: $K = \bar{l}/L \gg 1$ (at least much smaller than 1));

2. Symmetric stress tensor: no torque acting on a fluid element;

3. Isotropic fluid: fluid properties are independent of coordinate axes direction;

4. Newtonian fluid: linear stress-strain relationship;

5. Fourier's law applies: the heat flux is a vector described by a linear relation between temperature gradient and thermal conductivity (transport property): $\vec{q} = -k\nabla T$ or in tensor notation: $\dot{q}_i = -k\frac{\partial T_i}{\partial x_i}$;

6. Stokes' hypothesis: bulk viscosity is assumed negligible (viscosity opposing dilatation/volume changes, it can be neglected when the time scale to reach local equilibrium is much shorter than deformation time scales; this results in: $\lambda = -\frac{2}{3}\mu$) (which results from taking the pressure equal to one third of the negative sum of the normal stresses);

7. The principle of local state [3], local equilibrium [76] or quasi-equilibrium/quasi-static [72] processes: 'even though the temperature and pressure may vary in a flowing fluid, as long as the changes are not as sharp as in a shock wave and the fluid internal relaxation times are rapid, the properties at each point in the fluid are interrelated by the same equations of state as for the equilibrium fluid.' (sentence taken from reference [76, p. 21]). This can be interpreted as: a process can be considered in quasi-equilibrium if departures from equilibrium are small, such as when molecular time scales are much smaller than the process (flow) time scales. Normally this is the case for large amounts of molecules with the intermolecular distance not too large (continuum hypothesis). In other words: departures from equilibrium are sufficiently small [125];

8. The local thermodynamic state is fixed by two state variables;

9. No radiative heat transfer; and,

10. There are no heat sources inside the flow (no radiation, no chemical reactions (combustion), no Joule's heat, etc.).

Regarding the boundary layer assumptions (of Prandtl [20]) (no second-order effects are considered in this thesis):

1. The boundary layer thickness δ is very thin compared to the length scale L of the flow geometry: $\delta \ll L$ or $\delta/L \ll 1$;
2. This results in (very) high Reynolds-number, together with (very) low viscosity: $\mathrm{Re_x} \gg 1$;
3. Diffusion in the x-direction can be neglected compared to diffusion in the y-direction (for example: no/negligible heat conduction in x-direction, see reference [27, p. 272]);
4. Constant pressure in y-direction: $\frac{\partial p}{\partial y} = 0$, and thus $\frac{\partial p}{\partial x} = -U_\mathrm{e}\frac{\partial U_\mathrm{e}}{\partial x}$, with U_e the velocity at the boundary layer edge. In words: an important consequence of this result is that the outer or free stream flow imposes the conditions (pressure distribution along the surface) on the boundary layer;
5. No slip at wall (no slip condition), which entails: velocity at the wall surface is zero in all directions (solid, nonporous wall surface), and there is no jump in temperature from wall surface to flow (this distinguishes the boundary layer equations from potential flows);
6. Flat wall: the effect of wall curvature can be neglected, which means: $\delta/R \ll L$ with R the radius of wall curvature, and L the length scale of the problem (wall curvature induces centrifugal forces on the boundary layer [57,125], and is a second-order effect, part of higher order BL theory, see reference [3]);
7. Two-dimensional, therefore no transverse curvature;
8. Assuming local and convective accelerations are equal in size (same time scale, results in: no sudden accelerations, which means no strong pressure waves [3, p147];
9. No shock waves or expansion fans;

Regarding the (Reynolds) averaging of the NS-equations (turbulence):

1. In turbulent steady state flow the velocity vector can be split in a (mass-weighted) time averaged part and a (mass-weighted) fluctuation part;
2. The fluctuations in the fluid properties viscosity μ, λ, thermal conductivity k, heat capacity c_p (and thus the Prandtl-number Pr) are neglected[1];

Regarding the turbulent boundary layer equations (adapted from reference [3, pp. 612-614]):

[1]This might become a problem close to the critical point R. Pecnik (personal communication, December 18, 2018)

1. 'It is found empirically that Prandtl's boundary layer approximations are also fairly good in turbulent cases and become better as Reynolds-number increases.' [4];

2. The diffusion terms in the x-direction (for example variation of the x-momentum flux in the x-direction) are neglected compared to those in the y-direction: $\left|\frac{\partial}{\partial x}\right| \ll \left|\frac{\partial}{\partial y}\right|$;

3. The velocity component $\tilde{v}$ is much smaller than the velocity component $\tilde{u}$. This yields for example: $\left|\frac{\partial \tilde{v}}{\partial x}\right| \ll \left|\frac{\partial \tilde{u}}{\partial x}\right| \ll \left|\frac{\partial \tilde{u}}{\partial y}\right|$. Therefore, the term $\tilde{v}^2/2$ was neglected compared to $\tilde{u}^2/2$ in the total energy equation (2-32) (normal velocity is neglected in rewriting the static enthalpy to total enthalpy). Also, the reduced y-momentum equation is a result of this assumption.

4. The normal stresses $\overline{\rho u'' u''}$ and $\overline{\rho v'' v''}$ are neglected compared to the pressure $\bar{p}$. This results in: $\frac{\partial \bar{p}}{\partial x} = \frac{\mathrm{d}p_\mathrm{e}}{\mathrm{d}x}$ and $\frac{\partial \bar{p}}{\partial y} = 0$, as in the laminar case, but the assumption leading to this relation in the turbulent case is 'weaker', since the pressure term is now of order $O(1)$ instead of $O(\delta)$. However, integration of the pressure derivative in y-direction gives the pressure variation across the boundary layer to be of order δ ($O(\delta)$). Note that the normal stresses can become more important close to separation. Therefore, a Howarth's flow simulation including bulk viscosity would be interesting to find the influence/importance of these normal stresses on the dissipation coefficient.

5. Fluid property fluctuations are assumed negligible for viscosity μ, λ, thermal conductivity k, heat capacity c_p (and thus the Prandtl-number Pr) (see also the assumption in the RANS list above). These assumptions result in the following approximations: $\overline{\mu \frac{\partial u}{\partial y}} \sim \bar{\mu} \frac{\partial \tilde{u}}{\partial y}$ and $\overline{\lambda \frac{\partial T}{\partial y}} \sim \bar{\lambda} \frac{\partial \bar{T}}{\partial y}$, which are equivalent to $\left|\overline{\mu \frac{\partial u''}{\partial y}}\right| \ll \left|\bar{\mu} \frac{\partial \tilde{u}}{\partial y}\right|$ and $\left|\overline{\lambda' \frac{\partial T'}{\partial y}}\right| \ll \left|\bar{\lambda} \frac{\partial \bar{T}}{\partial y}\right|$. It turns out that these assumptions are valid at Mach-numbers below 5 (Ma < 5) [4];

6. According to the scaling procedure we can take inside the boundary layer: $\tilde{h}_0 \sim \bar{h}_0$, $\tilde{u} \sim \bar{u}$ and $\bar{\rho}\tilde{v} = \overline{\rho v} = \bar{\rho}\bar{v} + \overline{\rho' v'}$. Because the fluctuations v'' in v are of the same order as $\tilde{v}$ itself, they cannot be neglected compared to the mean v-velocity component (in other words: $\overline{\rho' v'}$ cannot be neglected to the equally small quantity to $\bar{\rho}\bar{v}$);

7. Morkovin's hypothesis: the turbulence structure with variable fluid properties is the same as that for constant fluid properties as long as fluctuations in Mach-number remain below 1 (Ma$' < 1$). This is the case for adiabatic boundary layers below Mach 5 (taking previous assumptions into account: flat wall (6), and no shock waves (9) (no strong pressure gradients)). In short: the effects of density fluctuations on the turbulence is small: $\left|\overline{\rho' u' v'}\right| \ll \left|\bar{\rho}\overline{u' v'}\right|$. This assumption results in a simplification of the turbulent stress: $\tau_\mathrm{T} = -\overline{\rho u'' v''} = -\overline{\bar{\rho} u'' v''} - \overline{\rho' u'' v''} \sim -\bar{\rho}\overline{u' v'}$.

Regarding simplifications to the system of equations:

1.

Regarding the turbulence model:

1. Isotropic turbulence in free stream;
2. γ_{tr} is only valid for (calibrated to) adiabatic (ideal gas) flows. Include this in range instead? Parameter that simulates and smooths the transition region by gradually increasing the eddy viscosity. Coefficients here are calibrated for adiabatic flows.
3. intermittency concept used from Klebanoff? (1956). Cebeci 2013 also uses this, in 2004 a gaussian bell was introduced, but is more complicated?
4. This is a range! Not an assumption. Remove here, and add to range-section. PrT: $0.02 < PrT < 14.3$
5. In the CS-model the N-parameter (for taking into account (compressible) pressure gradients and heat transfer) contains the constant 11.8. The value of 11.8 is approximately the dimensionless distance where the lines of the linear law of the wall and the log law layer intersect for incompressible flat plate flow (obtained from measurements) [4]. It is assumed that the same value applies to nonzero compressible flows [4].
6. etc.

Regarding the numerical method:

1. The BL edge velocity is taken as the free stream velocity

Regarding the range of validity of equations of state and fluid property relations:

1. Sutherland's law for viscosity: temperature range for coefficients from air 170-1900 K for 2% error; error ? plusminus 4 percent in smaller range? White [54]; CO2 etc. (used in gas model 2)
2. Sutherland's law for thermal conductivity: temperature range for coefficients from air 160-2000 K for 2% error; error ? plusminus 3 percent in smaller range? White [54]; CO2 etc. (used in gas model 2)
3. $\mathrm{Pr_T} : 0.02 < \mathrm{Pr_T} < 14.3$
4. Wazzan's method for prediction of transition from laminar to turbulent flow:

- Valid for form factor values in the range of $2.1 <= H <= 2.8$;
- Valid for (heating rates with) wall temperatures of $T_w - T_{aw} <= 23K$ (or, see Cebeci [27, p. 177], free stream temperature instead of adiabatic wall temperature? But then how do we quantify free stream T? as total? (in book: Tinf). Then without losses Tinf is Taw);
- applicable only to flows over smooth surfaces or slender bodies of revolution (negligible radius of curvature) (own words?); and,
- free stream turbulence is not taken into account.

5. Michel's method for prediction of transition from laminar to turbulent flow:
6. Transitional flow region modeling by the γ_{tr} transition factor: only valid for adiabatic flows with $Ma < 5$ (see [27, p. 274]); CHECK source! how does it appear?

Chapman-Rubesin parameter? Assumption made here? Or just convenient way of writing in SoE, and determining the value in fluid properties file (with current model(s)? Assumption can be: $w = 1$, see Cho (2004) [58].

Note on bulk viscosity: BL assumptions (note! bulk viscosity is assumed to be proportional to dynamic viscosity, and thus is being removed when scaled [3] p65! See reference of Van Dyke (1962c, p. 50) (bulk viscosity is not even a second order effect?) and chapter 14! Also, White [54] points out that BL flows for compressible fluids have negligible normal stresses (p67) and thus only the first coefficient of viscosity, dynamic viscosity, is important. This is not the case however for normal shock waves, where the second coefficient of viscosity λ cannot be neglected. Also sound wave attenuation and absorption are involved. See White p67!) But, we have assumed: 'no sudden accelerations', see item ... above. Add my scaling procedure that show that bulk viscosity might become nonnegligible for high values (second-order size of ratio λ_e/μ_e), for example for CO2 (see Cramer). Not much known yet about values of bulk viscosity as transport property. Use scaling analysis to show if/how/when we can(not) neglect λ? Put in appendix.

Appendix D

Errata and Suggestions to used Literature

To help the reader (prevent him from confusion and getting lost) some errata has been included here for some imperfections and omissions that I encountered during my studies. This made me realize that human work, even how excellent it might be, will never be free of mistakes, and even with a few flaws a great work can help progress multiply.

First I would like to mention that the books dealt with in this Appendix do not have a nomenclature section. A nomenclature section would be a great improvement, also to the advanced reader, since nomenclature varies among different authors. Please, always follow (the conventions!) Schlichting [3]. Therefore, a modest nomenclature section is included in this work, and let us hope it is consistent and free of mistakes.

D-1 Errata to *Convective Heat Transfer* by Cebeci (2002)

This is a great book: it helped me understand two-dimensional steady state boundary layer flows including heat transfer. The FORTRAN program on the included DVD is the basis of the MATLAB computer program presented in this thesis. Note that the author Cebeci has introduced slightly different nomenclature for the eddy viscosity and for fluctuation terms than is commonly accepted. Especially the last can confuse the 'sloppy' reader. A great improvement would be the inclusion of a nomenclature section, as mentioned already above. The following list contains suggestions, possible improvements and errata:

Regarding the FORTRAN code:

1. Regarding the FORTRAN code on the DVD: the d-coefficient is not updated with the turbulent Prandtl-number in case of turbulent flow. This is believed to be a coding error (omission). The influence on the results is expected to be small.
2. Regarding the Flow-chart of the FORTRAN code (Fig. 11.1) on page 285: the Flow-chart of Fig. 11.1 on page 285 is not entirely corresponding with the FORTRAN program for Compressible Boundary-Layer Flows discussed in Sec. 11.2.

Regarding the book:

1. p0: please add nomenclature section;
2. p7: replace 'wich' with 'with';
3. p8: replace 'that' with 'heat';
4. p10: replace 'und' with 'and';
5. p23: replace $\frac{\partial u}{\partial x}\mathrm{d}u$ with $\frac{\partial u}{\partial x}\mathrm{d}x$;
6. p24: remove minus sign in equation 2.4.10 (since negative work on left face, and positive work on right face, thus positive derivative of normal stress);
7. p33: replace 'througnout' with 'throughout' in problem 2.1 (c);
8. p34: replace 'cquetion' with 'equation' in problem 2.7;
9. p35: replace 'neglectcd' with 'neglected' in problem 2.9;
10. p42: replace the dot after 'the special case of axisymmetric flow' with a comma (text in middle of lower page);
11. p70: the use and definition of g and S are mixed in this book; for example in Fig. 4.4 and 4.5 where g is equal to S but different from g as used in Chapter 10, where $g = h_0(j)/h_{0,\mathrm{e}}$, since g varies in Fig. 4.4 and Fig. 4.5 between 0 and 1. Therefore, replace symbol g with $S = (g(j) - g_\mathrm{w})/(g_\mathrm{e} - g_\mathrm{w})$ in Fig. 4.4 and 4.5 (according to [62] for example) to prevent confusion. Furthermore, not that in the last definition the temperature can also be used instead of enthalpy, which is not the same in some cases. In addition, do not use S in Chapter 10 Eq. 10.2.11 and 10.2.14a since a few pages later g again is used in Eq. 10.4.1e;
12. p196: about halfway down the page the text refers to 'Eq. (7.1.6)' which does not exist. Instead refer to Eq. ?;
13. p254: replace dot after 'Eq. (9.2.12)' and before ' locating' with comma;
14. p254: substitute double apostrophe (") by number '2' (in first part of Eq. (9.2.13), see for an example the second part of this equation);

15. p255: k_n misses inside Fig. 9.4;
16. p262: replace matrix entry $A(5,6) = (s_2)_J$ in the A-matrix in equation 9.2.26 with $A(5,6) = (s_1)_J$;
17. p262: replace delta vector entry $\delta(6,1) = p_j$ with p_J (bottom of page);
18. p263: replace A_j on the right bottom corner of the A-matrix in eq. 9.2.29 with A_J;
19. p264: remove bracket after first γ (entry $\Gamma(1,1)$) in Eq. on top of page;
20. p264: replace reference to Eq. 5.1.5 with Eq. 5.1.3 in the second line of Sec. 9.3 (wrong Eq. reference, since Eq. 5.1.5 refers to the mean average velocity);
21. p272: replace reference to Eq. 10.1.8 with Eq. 10.2.8;
22. p272-273: m_1 and m_2 are not given here (not defined in the entire book. The rest of the coefficients/parameters is defined on page 273);
23. p273: remove square from absolute brackets in Eq. 10.3.1;
24. p274: Eq. reference number 10.3.3 has been defined two times;
25. p274: replace G (2x) with G_{tr} to be consistent with page 289;
26. p281: replace entry $A_J(4,1) = 1$ in Eq. 10.4.14a with $A_J(4,1) = 0$ (this took me a lot of debugging time to find out! Since I used this as an example);
27. p282: replace 'In term of' with 'In terms of';
28. p285: flow-chart is not matching the FORTRAN code discussed in Sec. 11.2 entirely;
29. p288: Remark about γ might be removed from equation 11.2.7a. NB not necessarily. Since, analytically it should be there, but numerically it does not matter (practically equal to one) and thus it can be left out. Probably, for this reason it is not present in the FORTRAN code. The question is: is this justified for all cases?
30. p288: Remark about absolute value of the derivative. Uncertain about this. The absolute term of the derivative is omitted here, while it is present in all other references. The presence of the absolute term here is unclear to me, since the derivative is always positive as far as I know, for all cases up to separation, where the calculation stops. NB the absolute function is NOT present in any form in the FORTRAN code;
31. p288: Region of validity of inner and outer Eddy Viscosity should be defined (is noramlly defined) in terms of wall-coordinates y: $0 \leq y \leq y_c$ for inner, and $y_c \leq y \leq \infty$ for outer EV.

32. p289: Eddy Viscosity relations:
    (a) $(\epsilon^+)_i$: v^2 needs to be v; and why not abs() here? (compare with Eq. 11.2.7a);
    (b) $(\epsilon^+)_i$: $1 + exp()$ needs to be $1 - exp()$;
    (c) y/A: C_w needs to be $\sqrt{C_w}$;
    (d) N^2: C_w^2 needs to be c_w^2 (small c, density ratio);
33. p290: in the 3rd row of the table (of entries) replace $(bv)^n_{j-1/2}$ with $(bv)^n_{j-1}$ (should be $j - 1$ instead of $j - 1/2$);
34. Appendix B: t needs to be capital T; move $\times 10^6$ into upper row (text) as in other columns; what is κ? (units of viscosity).

General note: Cebeci uses a different notation for fluctuations (single prime instead of double prime as is the convention, see Schlichting [3, p. 611]). In addition, the symbol ϵ has been used instead of the symbol μ for the Eddy Viscosity. Therefore, it would be more appropriate to write μ_T instead of ϵ.

D-2 Errata to *Analysis of turbulent flows with computer programs*, 3rd edition, by Cebeci (2013):

1. p34: unnecessary comma between ij in τ_{ij} (eq. 2.2.2);
2. p37: rho-tilde: replace tilde by bar (eq. 2.3.13) (see 1st edition from 1974);
3. p38: u-bar: replace bar by tilde (eq. 2.3.14) (see 1st edition from 1974);
4. p39: replace bar by tilde for H and H' (see 1st edition from 1974);
5. p39: replace tilde by bar (two times) in eq. 2.4.1;
6. p40: u1(xi,t) needs to be u1(x1,t), and triple bar instead of equal sign (by definition, see Cebeci (1974) [4]);
7. p40: next relation: replace tildes (2) by bar above density terms; in following text one more time;
8. p42: on top of page, h-bar (second-last h) should be h-tilde.

D-3 Errata to *Laminar Flow Analysis* by Rogers (1992)

1. In tables C-25, C-26, C-27 and C-28 the values of J_1 and J_2 correspond to $2J_1$ and $2J_2$ respectively as found with the CS-method after transformation. See the comparisons of these values in Tables A-3 through 4-4.

2. The values of tabulated J_3 in tables C-25 and C-26 correspond to $2J_4$ as found with the CS-method after transformation.

3. Table C-25 on page 341: note that for $g_w = 2.0$ with $\hat{\beta} = -0.129507$ (fifth and sixth column in third last row) the values of J_1 and J_2 are equal to the ones in the row above (for $\hat{\beta} = -0.10$). Since the input is different, it is expected that these values are incorrect, which is supported by the simulation results tabulated in table A-3 in this work.

Appendix E

Implementation of Verification and Validation Cases

The verification and validation cases in chapter 4 cannot be implemented directly. Parameters need to be rewritten or transformed such that they can be compared in the same transformed coordinate system. This Appendix especially gives a detailed background in adapting the implemented cases obtained from Rogers [57].

E-1 Transformations for Coordinate Transformations

Several authors and sources use different variants of transformations. Transformations for converting a simulation result from one transformed coordinate system to the other are needed for comparison of simulation results between systems of equations transformed differently. This section discusses a few transformations. The compressible Falkner-Skan transformation is used in this work (probably Cebeci is the only person that uses this name, so we might even call it the 'Cebeci' transformation):

$$\mathrm{d}\eta = \sqrt{\frac{u_\mathrm{e}}{\nu_\mathrm{e} x}}\frac{\rho}{\rho_\mathrm{e}}\mathrm{d}y \tag{E-1}$$

$$\psi(x,y) = \sqrt{\rho_\mathrm{e}\mu_\mathrm{e}u_\mathrm{e}x}f(x,\eta) \tag{E-2}$$

Starting from the beginning, we can consider the transformations used for the Blasius' equation and the Falkner-Skan equation to finally arrive at the completely different 'compressible Falkner-Skan transformation'.

Remember the Blasius' equation for zero pressure gradient adiabatic incompressible flow with constant fluid properties:

$$f''' + ff'' = 0 \tag{E-3}$$

The transformation used here is:

$$\mathrm{d}\eta = \sqrt{\frac{u_\mathrm{e}}{2\nu_\mathrm{e} x}}\mathrm{d}y \tag{E-4}$$

$$\psi(x,y) = \sqrt{2\nu u_\mathrm{e} x} f(\eta) \tag{E-5}$$

where fluid properties are constant and u_∞ is the (constant) free stream velocity. The factor 2 in the transformation prevents the factor $\frac{1}{2}$ from appearing in the equation itself, that would otherwise have the form:

$$f''' + \frac{1}{2}ff'' = 0 \tag{E-6}$$

The well known Falkner-Skan equation for adiabatic incompressible wedge flows (nonzero pressure gradients) is:

$$f''' + ff'' + \beta\left[1 - \left(f'\right)^2\right] = 0 \tag{E-7}$$

has the following transformation (note the appearance of 2 in the transformation):

$$\mathrm{d}\eta = \sqrt{\frac{m_2+1}{2}}\sqrt{\frac{u_\mathrm{e}(x)}{\nu x}}\mathrm{d}y \tag{E-8}$$

$$\psi(x,y) = \sqrt{2\nu u_\mathrm{e}(x) x} f(\eta) \tag{E-9}$$

$$\beta = \frac{2m_2}{1+m_2} \tag{E-10}$$

$$u_\mathrm{e} = cx^{m_2} \tag{E-11}$$

Therefore, it is somewhat peculiar to call the transformation from equations E-1 and E-2 (our transformation) the compressible Falkner-Skan transformation, since it both lacks a factor 2 and a pressure gradient term. We might call it therefore the 'Cebeci' transformation from now on to be consistent.

Note that the factor 2 in the ME results in factor $\sqrt{2}$ in the transformation. Furthermore, note that:

$$\beta = \frac{2m_2}{m_2 + 1} \qquad m_2 = \frac{\beta}{2 - \beta} \tag{E-12}$$

The next section elaborates on the more complex derivation of transforming the Illingworth-Levy transformed coorindate system to our 'Cebeci' coordinate system (compressible Falkner-Skan transformation) and vise versa for comparison of simulation results with Rogers [57].

E-2 Compressible Laminar Flow Verification Tables from Rogers (1992)

The verification cases listed in tables C-25, C-26, C-27 and C-28 in the book 'Laminar Flow Analysis' by Rogers [57] cannot be implemented directly since a different coordinate transformation is used (the Illingworth-Levy transformations while Cebeci uses the compressible Falkner-Skan transformation) resulting in two similar, but slightly different transformed systems of equations. Also, the tabulated pressure gradient is expressed in a different way, and cannot be used directly as input to the CS-method. This section describes how the input can be transformed for use in the CS-method, and how the results from the CS-method can be transformed to match the tabulated results from Rogers [57] for a comparison. All tables considered involve compressible flow with nonzero pressure gradient and heat transfer. The Chapman-Rubesin parameter is assumed constant, and the ideal gas model with constant specific heats (calorically perfect ideal gas) is applied. The Prandtl-number can be taken equal to 1 (similarity case) or equal to 0.723 (for air), but then the Mach-number is zero or reaches infinity (since Rogers only considers similar cases).

E-2-1 System of Equations Solved by Rogers

The system of equations that is solved by Rogers [57] is:

$$f''' + ff'' + \hat{\beta}\left(g - f'^2\right) = 0 \tag{E-13}$$

$$g'' + \mathrm{Pr} f g' = \bar{\sigma}\left(1 - \mathrm{Pr}\right)\left(f' f''\right)' \tag{E-14}$$

Where:

$$\bar{\sigma} = \frac{(\gamma - 1)\,\mathrm{Ma}_\mathrm{e}^2}{1 + \frac{(\gamma-1)}{2}\mathrm{Ma}_\mathrm{e}^2} \tag{E-15}$$

$$\hat{\beta} = \frac{2\xi}{U_\mathrm{e}}\frac{\mathrm{d}U_\mathrm{e}}{\mathrm{d}\xi}\left(1 + \frac{\gamma - 1}{2}\mathrm{Ma}_\mathrm{e}^2\right) \tag{E-16}$$

Similar solutions of the above set of equations exist if $\hat{\beta}$ is constant, and if one of the following two conditions is met (in case of tables C-25, C-26, C-27 and C-28):

1. $\bar{\sigma} = 0$ or $\bar{\sigma} = 2$ (which corresponds to $\mathrm{Ma}_\mathrm{e} = 0$ and $\mathrm{Ma}_\mathrm{e} \to \infty$ respectively)
2. $\mathrm{Pr} = 1$

The similar cases of $\gamma = 1$ and $\mathrm{Ma}_\mathrm{e} =$ constant (other than zero) are not considered here (since they are not used for setting up the compressible flow tables considered).

E-2-2 System of Equations Solved by Keller's Box-Method

Recall the system of equations solved by the program (equations 3-1 and 3-4):

$$(bf'')' + m_1 f f'' + m_2\left[c - (f')^2\right] = x\left(f'\frac{\partial f'}{\partial x} - f''\frac{\partial f}{\partial x}\right) \tag{E-17}$$

$$(eg' + df'f'')' + m_1 f g' = x\left(f'\frac{\partial g}{\partial x} - g'\frac{\partial f}{\partial x}\right) \tag{E-18}$$

With parameters f and g defined as before:

$$f = \frac{u}{u_\mathrm{e}}, \tag{E-19}$$

$$g = \frac{h_0}{h_{0,\mathrm{e}}}, \tag{E-20}$$

and the coefficients (equations 3-7 to 3-14, in case of laminar flow, remind the book title: '*Laminar* Flow Analysis' [57]):

$$b = C, \qquad C = \frac{\rho\mu}{\rho_\mathrm{e}\mu_\mathrm{e}} \tag{E-21}$$

$$c = \frac{\rho_\mathrm{e}}{\rho} \tag{E-22}$$

$$d = \frac{Cu_\mathrm{e}^2}{h_{0,\mathrm{e}}}\left[1 - \frac{1}{\mathrm{Pr}}\right] \tag{E-23}$$

$$e = \frac{C}{\mathrm{Pr}} \tag{E-24}$$

$$m_1 = \frac{1}{2}\left[1 + m_2 + \frac{x}{\rho_\mathrm{e}\mu_\mathrm{e}}\frac{\mathrm{d}}{\mathrm{d}x}\left(\rho_\mathrm{e}\mu_\mathrm{e}\right)\right] \tag{E-25}$$

$$m_2 = \frac{x}{u_\mathrm{e}}\frac{\mathrm{d}u_\mathrm{e}}{\mathrm{d}x} \tag{E-26}$$

E-2-3 Rewriting the System of Equations

Now the coefficients in the system of equations solved by the CS-method (equations E-17 and E-18) and their solution need to be rewritten in such a way that the solutions can be compared with the similar cases tabulated by Rogers [57]. For this the input pressure gradient m_2 must be written as function of pressure gradient $\hat{\beta}$ which is tabulated. At the same time the solution needs to be transformed to the other coordinate system (from compressible Falkner-Skan to Illingworth-Levy). Writing down the conditions for the coefficients by comparing the two systems of equations and the coordinate transformations then gives (for similar cases the right side of the equations is zero):

$$\left(bf''\right)' + m_1 f f'' + m_2\left[c - \left(f'\right)^2\right] = 0 \tag{E-27}$$

$$\left(eg' + df'f''\right)' + m_1 f g' = 0 \tag{E-28}$$

$$b = C \tag{E-29}$$

$$c = \frac{\rho_\mathrm{e}}{\rho} \tag{E-30}$$

$$d = \frac{Cu_\mathrm{e}^2}{h_{0,\mathrm{e}}}\left[1 - \frac{1}{\mathrm{Pr}}\right] \tag{E-31}$$

$$e = \frac{C}{\mathrm{Pr}} \tag{E-32}$$

$$m_1 = \frac{1}{2}\left[1 + m_2\right] \tag{E-33}$$

$$m_2 = \frac{x}{u_\mathrm{e}}\frac{\mathrm{d}u_\mathrm{e}}{\mathrm{d}x} \tag{E-34}$$

A derivation follows in the next section.

E-2-4 Derivation

Rogers [57] implements the Illingworth-Levy coordinate transformations (note that Cebeci (2002) does not use a coordinate transformation in the x-direction):

$$\xi(x) = \int_0^x C\rho_e \mu_e U_e \, dx \tag{E-35}$$

$$\eta = \frac{U_e(x)}{\sqrt{2\xi}} \int_0^y \rho \, dy \tag{E-36}$$

For similarity cases with nonzero pressure gradient the velocity at the boundary layer edge can be written as:

$$U_e = \text{constant}\, x^{m_2} \tag{E-37}$$

The second pressure gradient term in the momentum equation is written by Rogers [57] as:

$$\beta \left(\frac{\rho_e}{\rho} - f'^2 \right) = \hat{\beta} \frac{h_{0,e}}{h_e} \left(g - f'^2 \right) \tag{E-38}$$

Resulting in:

$$\hat{\beta} = \frac{2\xi}{U_e} \frac{\partial U_e}{\partial \xi} \frac{h_{0,e}}{h_e} \tag{E-39}$$

For the last term, note that with calorically perfect ideal gas the static to total enthalpy ratio (which for constant heat capacity c_p is equal to the static to total temperature ratio):

$$\frac{h_0}{h} = \frac{T_0}{T} = \left(1 + \frac{\gamma - 1}{2} \mathrm{Ma}^2 \right) \tag{E-40}$$

Using the transformation and the boundary layer edge velocity function to find the following two derivatives

$$\frac{\partial U_e}{\partial \xi} = \frac{\partial U_e}{\partial x} \frac{\partial x}{\partial \xi}, \tag{E-41}$$

and rewriting the enthalpy ratio, we can now rewrite the pressure gradient $\hat{\beta}$ as a function of pressure gradient m_2, specific heat ratio γ and Mach-number Ma:

$$\hat{\beta} = \frac{2m_2}{m_2 + 1}\left(1 + \frac{\gamma - 1}{2}\mathrm{Ma}^2\right) \tag{E-42}$$

Which gives:

$$m_2 = \frac{\hat{\beta}\left(1 + \frac{\gamma-1}{2}\mathrm{Ma}^2\right)^{-1}}{2 - \hat{\beta}\left(1 + \frac{\gamma-1}{2}\mathrm{Ma}^2\right)^{-1}} \tag{E-43}$$

From equation E-43 the input pressure gradient m_2 can be calculated as a function of pressure gradient $\hat{\beta}$, which is tabulated in tables C-25, C-26, C-27 and C-28 in Rogers [57].

Note that the Chapman-Rubesin parameter is included inside the x-coordinate transformation in equation E-35, and thus it is also present in the y-coordinate transformation in equation E-36.

The fluid properties inside the integral in equation E-35 depend on the boundary layer edge static temperature, which in turn depends on the constant total enthalpy and the velocity at the boundary layer edge:

$$U_\mathrm{e} = c_0 x^{m_2} \tag{E-44}$$

$$h_{0,\mathrm{e}} = h_\mathrm{e} + \frac{U_\mathrm{e}^2}{2} \tag{E-45}$$

$$T_\mathrm{e} = \frac{h_{0,\mathrm{e}}}{c_\mathrm{p}} - \frac{U_\mathrm{e}^2}{2c_\mathrm{p}} \tag{E-46}$$

The integral can be simplified since the factor $\rho_\mathrm{e}\mu_\mathrm{e} = \text{constant}$ is a constant, which follows from its dependency on temperature:

$$\frac{\rho}{\rho_0} = \frac{T_0}{T} \quad \text{from the Ideal Gas law} \tag{E-47}$$

$$\frac{\mu}{\mu_0} = C\left(\frac{T}{T_0}\right)^{\omega} \tag{E-48}$$

Taking $\omega = 1$ we get:

$$\rho_e \mu_e = \rho_0 T_0 \frac{1}{T_e} \quad \mu_0 C \frac{1}{T_0} T_e = \text{constant} \tag{E-49}$$

The density ratio depends linearly on temperature, while the viscosity depends linearly on the inverse of temperature, and thus they cancel out each other and a constant remains). And thus the integral can be simplified:

$$\xi = \int_0^x C \rho_e \mu_e U_e \, \mathrm{d}x \tag{E-50}$$

$$= C \rho_e \mu_e \int_0^x U_e \, \mathrm{d}x \tag{E-51}$$

$$= \frac{C \rho_e \mu_e U_e x}{m_2 + 1} \tag{E-52}$$

Note here also that the pressure gradient parameter m_1 becomes:

$$m_1 = \frac{1}{2} \left[1 + m_2 + \frac{x}{\rho_e \mu_e} \frac{\partial \rho_e \mu_e}{\partial x} \right] \tag{E-53}$$

$$= \frac{1}{2} \left[1 + m_2 \right] \tag{E-54}$$

Now the Illingworth-Levy (y-coordinate transformation) can be rewritten to a factor times the compressible Falkner-Skan transformation:

$$\eta = \frac{U_e}{\sqrt{2\xi}} \int_0^y \rho \, \mathrm{d}y \tag{E-55}$$

$$= \frac{\rho_e U_e}{\sqrt{\frac{2C \rho_e \mu_e U_e x}{m_2 + 1}}} \int_0^y \frac{\rho}{\rho_e} \, \mathrm{d}y \tag{E-56}$$

$$= \sqrt{\frac{m_2 + 1}{2C}} \sqrt{\frac{U_e}{\nu_e x}} \int_0^y \frac{\rho}{\rho_e} \, \mathrm{d}y \tag{E-57}$$

Where the last two terms equal the compressible Falkner-Skan transformation. And thus, the solution of the momentum and energy equations need to be corrected with this factor $\sqrt{\frac{2C}{(m_2+1)}}$ for comparison with the data tabulated by Rogers:

$$f''(0) = v(1) \sqrt{\frac{2C}{(m_2 + 1)}} \tag{E-58}$$

$$g'(0) = p(1) \sqrt{\frac{2C}{(m_2 + 1)}} \tag{E-59}$$

E-2-5 Verification parameters

The parameters used in the verification tables (tables A-3 through A-6) are listed below:

$$
\begin{aligned}
J_1 &= \int_0^\infty \left(g - f'^2\right)\, \mathrm{d}\eta \\
J_2 &= \int_0^\infty f'\left(1 - f'\right)\, \mathrm{d}\eta \\
J_3 &= \int_0^\infty \left(1 - g\right)\, \mathrm{d}\eta \\
J_4 &= \int_0^\infty \left(1 - f'^2\right)\, \mathrm{d}\eta \\
J_\mathrm{x} &= \int_0^\infty \left(1 - f'\right)\, \mathrm{d}\eta \qquad \text{defined by author}
\end{aligned}
$$

In reality one integrates from zero to the value of η at the boundary layer edge: η_e.

Note that the values obtained from the CS-method need to be transformed to Illingworth-Levy transformed coordinates. On top of that, a factor 2 needs to be introduced for all J-values, and in Table A-2 a different J is used (J_x).

Note also that some values for high $\hat{\beta}$ and low g_w show 'sep' in the table entries, since they could not be calculated with the applied step-size and η_e. Lowering η_e to 2 in Illingworth-Levy coordinates makes it possible to let the program converge, but the results will not be accurate.

E-3 Validation with Experimental Data by Winter & Gaudet (1973)

What data did they list, what did I use, and how. Smart rewriting of the data to dimensionless coordinates for turbulent velocity profiles.

E-4 Simulation of the ORCHID Nozzle

Fluid properties as predicted with different models.

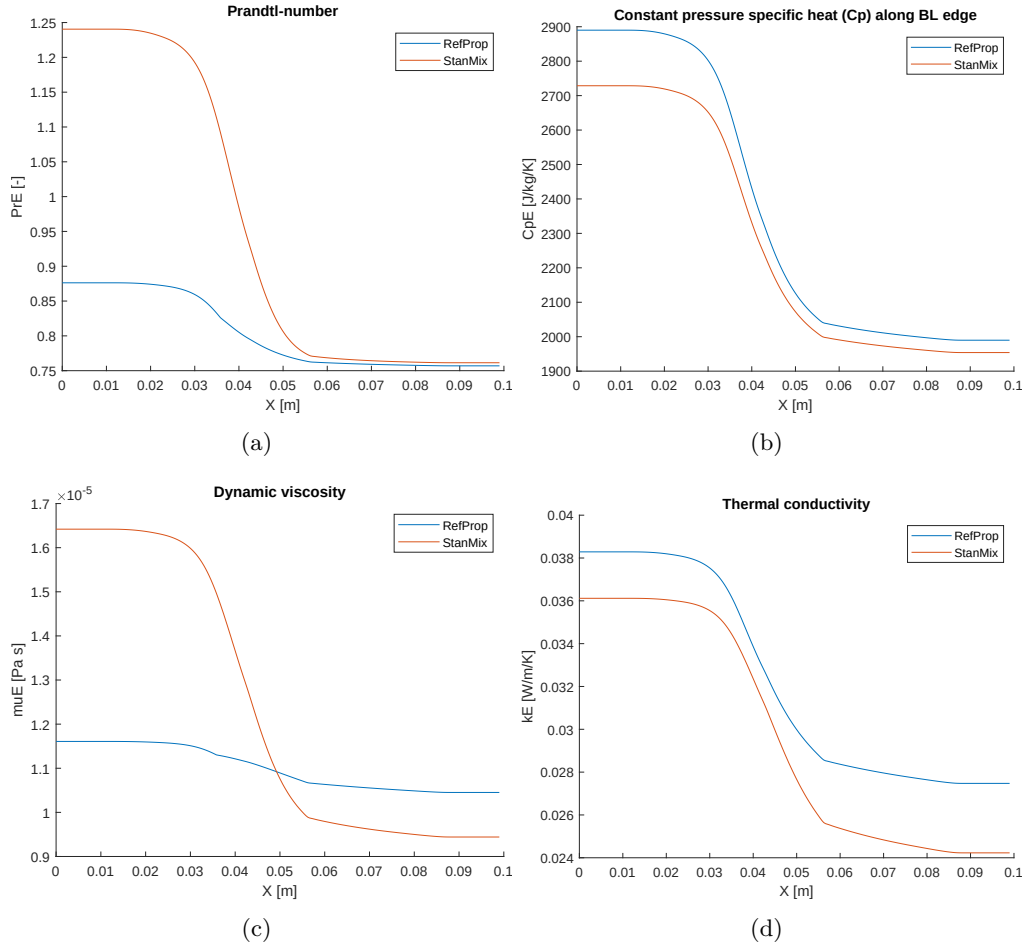

Figure E-1: Fluid properties as predicted with different models.: (a) Prandtl-number, (b) Constant pressure specific heat, (c) Dynamic viscosity, and (d) Thermal conductivity. Note how the differences affect the Prandtl-number, which converges for Z converging to 1. Note the discontinuity in the derivative of the dynamic viscosity at $0.36\,\mathrm{m}$ for the RefProp model.

Appendix F

Code Listing

The entire computer program consisting of MATLAB-files (m-files) can be found here:

- https://data.4tu.nl/authors/Dominic_Dijkshoorn/9706136
- https://doi.org/10.4121/21728249.v1

Cite as:

Dijkshoorn, Dominic (2022): Boundary-Layer-Program underlying the master thesis: Simulation of Two-Dimensional Steady State Boundary Layers Applied to Nonideal Gas Flows. 4TU.ResearchData. Software. https://doi.org/10.4121/21728249.v1

Appendix G

Addendum

This addendum has been added on March 6th, 2023 to include a reference to the computer program, which has been published on December 19th, 2022. In addition, the following has been changed compared to the master thesis version of August 10th, 2020:

1. This thesis has been re-uploaded to the TU-Delft repository, 3me faculty (Mechanical, Maritime and Materials Engineering) in March 2023;
2. This addendum has been added to include a reference to the computer program, which was finally published at December 19th, 2022;
3. A (complete) list of errata has been added, superseding former Appendix D (see Appendix D;
4. The report number was omitted on the cover of the previous version; and,
5. Errata have been taken into account, e.g. in referencing, numbering, spelling and a few small suggestions from Adam.

Many thanks to Federico Pizzi and Adam Head for their feedback on the 2020 version.

G-1 Computer program

The computer program can be found here (a descriptive read-me file is included):

- https://data.4tu.nl/authors/Dominic_Dijkshoorn/9706136

- https://doi.org/10.4121/21728249.v1

The computer program has been verified before publishing in 2021/2022 to guarantee the functionality of parts which have not been used fir the simulations presented in this master thesis.

Cite as:

Dijkshoorn, Dominic (2022): Boundary-Layer-Program underlying the master thesis: Simulation of Two-Dimensional Steady State Boundary Layers Applied to Nonideal Gas Flows. 4TU.ResearchData. Software. https://doi.org/10.4121/21728249.v1